Alma Mater Studiorum · Università di Bologna

FACOLTÀ DI SCIENZE MATEMATICHE, FISICHE E NATURALI
DOTTORATO DI RICERCA IN FISICA, XXIV CICLO
Settore Concorsuale di afferenza: 02/A1
Settore Scientifico disciplinare: FIS/04 - Fisica Nucleare e Subnucleare

Identified primary hadron spectra with the TOF detector of the ALICE experiment at LHC

Dr.ssa Barbara Guerzoni

Coordinatore Dottorato:
Prof.
Fabio Ortolani

Relatore:
Chiar.ma Prof.ssa
Luisa Cifarelli

Esame Finale anno 2012

Contents

Introduction

The theory of strong interactions, the Quantum ChromoDynamics (QCD), predicts a phase transition at high temperature between hadronic matter, where quarks and gluons are confined inside hadrons, and a deconfined state of matter, the Quark-Gluon Plasma (QGP).

The QGP formation can be reproduced in the laboratory thanks to ultra-relativistic heavy-ion collisions. A new energy frontier was opened in November 2010, with the first Pb-Pb collisions at a centre-of-mass energy for pairs of interacting nucleons of $\sqrt{s_{NN}} = 2.76$ TeV at the Large Hadron Collider (LHC) at CERN.

The LHC experiment designed to study Pb-Pb collisions is the ALICE experiment. Its main difference with respect to the other LHC experiment is its excellent Particle IDentification (PID) capability. Thanks to it, ALICE is able to investigate the formation and the properties of the QGP through a large variety of signatures.

One of these signatures is the transverse momentum spectrum of identified pions, kaons and protons that provides information on two evolution stages of the QGP: the chemical and kinetical freeze-out. It is in these two stages that the particle ratios and their kinematical properties are respectively fixed.

To have a useful reference for the understanding of heavy-ion data the ALICE experiment studies identified particle spectra not only in Pb-Pb collisions but also in pp interactions. The study of pp collisions is also important for the tuning and the optimization of the Monte Carlo generators that are commonly used for the description of particle production in high energy collisions.

One of the main detector involved in this analysis is Time of Flight (TOF) detector, since it is able to identify primary particles in the transverse momentum interval $0.5 < p_t < 4.0$ GeV/c, where most of them are produced.

In this thesis, the analysis I performed to reconstruct the primary transverse momentum spectra for pions, kaons and protons with the TOF detector in pp Minimum Bias collisions at $\sqrt{s} = 7$ TeV will be reported. In detail, this thesis is organized as follows.

In the first chapter a brief description of the main stages of the QGP formation and evolution in the heavy-ion collisions will be reported, in addition to the first ALICE results obtained with the study of Pb-Pb collisions at a centre-of-mass energy for pairs of interacting nucleons of $\sqrt{s_{NN}} = 2.76$ TeV at the LHC.

In the second chapter, after an introduction about the LHC, some details on the ALICE experiment will be given, putting emphasis on the Time Of Flight (TOF) detector, as this is the detector that is mainly used in the analysis reported in this thesis.

In the third chapter details on the event simulation and reconstruction procedures will be given. In addition, due to their importance in the TOF PID performance, the TOF calibration and alignment procedures will be described.

In the fourth chapter details about the two main factors that define the TOF PID performance, other than the time resolution of the TOF detector, will be reported. These are the TOF matching efficiency and the determination of the absolute time of the collision ("time zero").

In the fifth chapter, after a description of the general TOF PID performance, details will be given concerning the PID unfolding procedure that was used to reconstruct the identified transverse momentum spectra with the TOF detector. A comparison with a more "traditional" PID approach, the so-called 3σ cut, will be also reported.

Finally, in the last chapter, all the efficiency corrections that have to be applied to the TOF raw spectra will be described, together with an estimate of the systematic uncertainties. In addition, the K/π and p/π ratios obtained from the TOF spectra will be reported and compared to the Monte-Carlo predictions from different event generators and to the particle ratios obtained in pp collisions at $\sqrt{s} = 0.9$ TeV.

In ALICE, the identified transverse momentum spectra analysis is based not only on TOF, but makes also use of other PID detectors and techniques that are complementary to TOF in terms of momentum coverage, allowing to extend the particle identification on a wider p_t range. A comparison between all the results obtained with these independent analyses will be provided, showing, in particular, the excellent agreement between the TOF spectra and those from the others ALICE PID detectors.

Chapter 1

Ultrarelativistic heavy-ion collisions: the QGP

The theory of strong interaction, the quantum chromodynamics (QCD), predicts a phase transition at high temperature and/or energy density between hadronic matter, where quarks and gluons are confined inside hadrons and a deconfined state of matter, the so-called quark-gluon plasma (QGP). A new frontier in the study of QCD matter opened with the first Pb-Pb collisions in November 2010 at the Large Hadron Collider (LHC) at CERN. These collisions are expected to generate matter at unprecedented temperatures and energy densities in the laboratory. The main LHC experiment devoted to the study of the QGP is the ALICE experiment which, with its great Particle IDentification (PID) capability, can probe the QGP formation. In this chapter a brief description of the main stages of the QGP formation and evolution in the heavy-ion collisions will be reported. In addition the first ALICE results obtained with the study of Pb-Pb collisions at a centre-of-mass energy for pairs of interacting nucleons of $\sqrt{s_{NN}} = 2.76$ TeV at the LHC will be reported.

1.1 Introduction

The Standard Model predicts a phase transition when a certain energy density, namely the critical energy, is reached and, as a consequence, a symmetry is broken. Within this framework, the QCD predicts a phase transition between hadronic matter (where quarks and gluons are confined inside hadrons) and the QGP if the energy density is larger than $\varepsilon_c \sim 1$ GeV/c and the temperature is higher than $T_c \sim 170$ MeV. Since it is really short-lived, the QGP can not be studied directly and it is necessary to develop theoretical models

that predicts the properties of the final state of the interaction that prove the QGP formation, namely the QGP signatures. Many theoretical models have been developed and tuned on the results of the first heavy-ion experiments. The LHC experiments will provide the necessary information to select the model which better describes the interaction and the QGP evolution, since they have different prediction at the LHC energies. The main LHC experiment designed to analyze Pb-Pb collisions is the ALICE experiment. To be sure that the physical observables detected in Pb-Pb collisions are due to the QGP formation, the same analyses have to be done in collision systems in which the QGP can not be produced, and the results have to be compared. For this reason the ALICE experiment studies also pp interactions.

1.2 Heavy-ion collisions: general definitions

Since at ultra-relativistic energies the de Broglie wavelength ($\lambda = h/p = h/(mv\gamma)$) of the nucleus is smaller than its dimensions, the nuclear collisions can be considered as a combination of interactions between nucleons. Moreover, since the interaction range between nucleons is 1-2 fm, smaller than the radius of the nucleus, the simplified model in Fig. 1.1 can be assumed to define some general parameters of the nuclear collisions.

Due to the fact that nuclei are extended objects, in nucleus-nucleus (A-A) collisions the impact parameter b, that is the distance between the center of the two interacting nuclei in the transverse plane respect to the beam direction, can be defined. The A-A collisions are generally classified by the centrality, that is related to the impact parameter b. A collision is central if b is about zero, while is peripheral if $b_{max} \sim R_2 + R_2$, that is the maximum value that b can assume to have an interaction between nucleus 1 and nucleus 2, being R_1 and R_2 their radii. Obviously, more central the collision is, higher is the energy density, higher is the probability to produce the conditions for the QGP formation and lower is the number of nucleons that don't take part to the interaction (named spectators).

Finally, the motion of the particles is described in terms of the rapidity:

$$y = \frac{1}{2} \ln \frac{E + p_L}{E - p_L} \quad , \tag{1.1}$$

where E is the energy and p_L the longitudinal momentum. In the ultra-relativistic limit the rapidity can be approximated by the pseudorapidity

$$\eta = \frac{1}{2} \ln \frac{p + p_L}{p - p_L} = -\ln[\tan(\theta/2)] \quad , \tag{1.2}$$

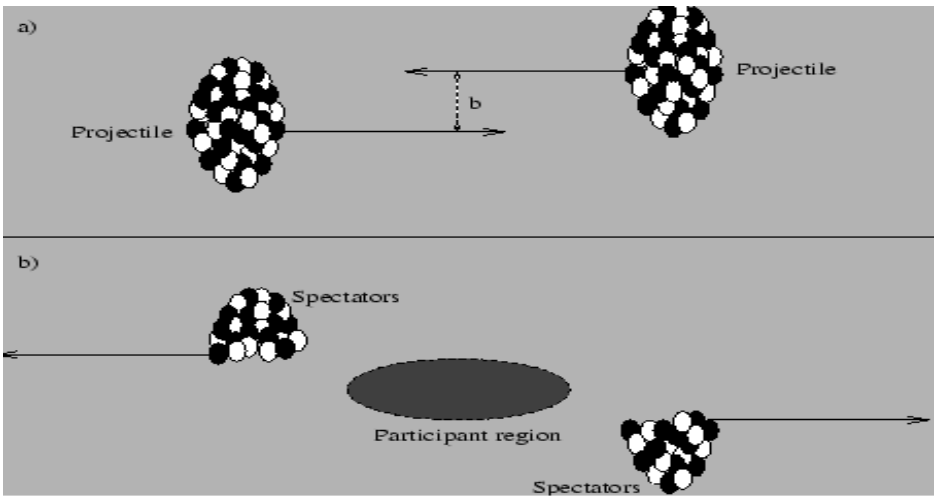

Figure 1.1: A collision between two heavy nuclei in the spectator-participant model. a) The two Lorentz contracted nuclei before the collision. The centrality is determined by the impact parameter b. b) After the collision a participant region with high temperature and density is created (fireball) while the spectators continue their motion in the beam direction.

where θ is the angle between the momentum of the particle and the beam axis. We notice that the particles produced with high transverse momentum (p_t), that are the particles produced with hard scattering, have $|\eta| \sim 0$.

1.3 Heavy-ion collisions: time evolution

In Fig. 1.2 a schematic view of the time evolution of A-A collisions is shown. After the interaction, a thermalized phase takes place, with the formation of the QGP. Than the fireball expands, giving rise to the hadronization process that ends with the freeze-out. A brief description of these phases will be given in the next sections.

Before the QGP formation

Before the formation of the QGP, heavy quarks and jets that are particles with heavy mass or high transverse momentum ($p_t \gg 1$ GeV/c) are produced[1], in addition to direct photons radiated by the means in which many

[1]If the collision energy is high enough (like at RHIC[2] and at LHC[3]) heavy quarks and jets can also be produced in the subsequent phases of the interaction.

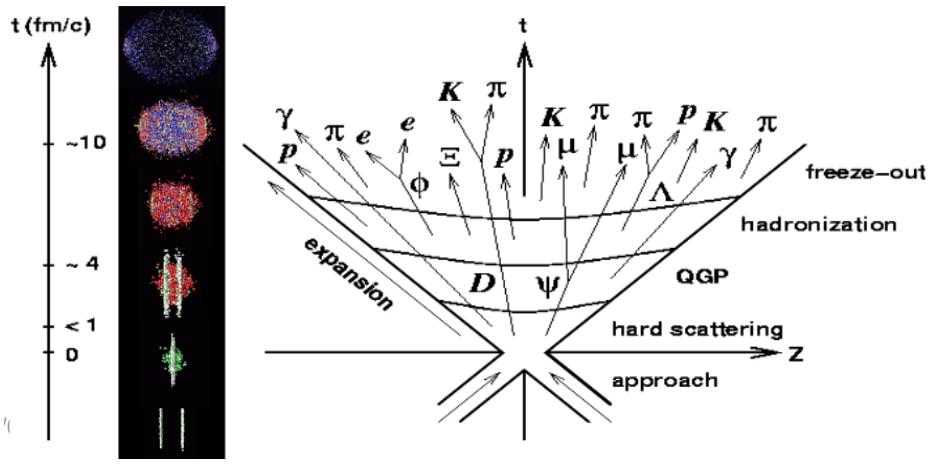

Figure 1.2: Schematic view of the time evolution of A-A collisions.

charges (quark/antiquark) are present. These photons can be real or virtual. In the last case they can be detected through their decay in dileptons, i.e. two leptons of opposite charge. Since direct photons are generated in the first stage of the interaction, they can be used to reconstruct the momentum distribution of the quarks from which they were produced even if to decouple them from the other photons and leptons produced in the later stages of the collision may be quite difficult.

Thermalization, expansion and hadronization

In heavy-ion interactions, the particles produced in the primary collisions continue to mutually interact, giving rise to a region of high matter and energy density at the thermal equilibrium from which the QGP can be produced in less than 0.1-0.3 fm/c (thermalization).

Thanks to inelastic scattering, the relative abundance of gluons, up, down and strange quarks changes. We have to take into account also of the strange quark since at the QGP formation energy, due to the chyral symmetry restoration, its mass is the running mass ($m_s \sim 150\,\mathrm{MeV/c^2}$) and not the constituent one ($m_s \sim 450\,\mathrm{MeV/c^2}$). This means that in heavy-ion collisions the production of the s quark and, as a consequence, of the strange hadrons should increase with respect to the pp collisions.

At this stage, due to the internal pressure, the termalized system expands and the energy density decreases. When it reaches again the critical density $\varepsilon_c \sim 1\,\mathrm{GeV/fm^3}$, the hadronization phase starts and the formation of the first bound states begins. In this phase, while the temperature has a small

variation (it is still $\sim T_c$), the energy density quickly decreases and the volume of the fireball increases.

Chemical and kinetical freeze-out

The relative abundance of hadron species can change until the hadron gas is able to interact inelastically. When the collisions have a too small energy to be inelastic, the abundance are fixed and the chemical freeze-out is reached. As a consequence, the ratios between particle species (e.g. K/π and p/π) can provide information on the system at the chemical freeze-out.

At this time elastic interactions are still present and continue to modify the kinetic properties of the hadrons. When the distances between hadrons are larger than the range of the interaction, also elastic collisions stop and the kinetical freeze-out is reached. Now, also the kinematical distribution of the hadrons are fixed hence from the hadron momentum spectra, information on the kinetic freeze-out temperature can be obtained.

1.4 QGP signatures: ALICE results

Since the QGP can not be studied directly, the theoretical models have to predict which properties of the final state of the interactions could provide information on the QGP formation. That is, they have to predict which properties are expected to be different in colliding systems where the QGP is or is not produced (i.e. A-A and pp interactions). These properties have hence to be experimentally investigated (signature of the QGP). Depending on the phase of the collision when they are produced, these signatures are grouped in soft and hard probes:

- *hard probes*: signals produced in the first stages of the collision by the interaction of high momentum partons. They are e.g. production of heavy quarks and of their bound states (charmonium and bottomonium), jet quenching, thermal photons and dileptons;

- *soft probes*: signals produced in the later stage of the collision. Even if they are produced during the hadronization stage, they keep indirect information on the properties of the phase transition and on the QGP. They are e.g. momentum spectra, strangeness enhancement, elliptic flow, particle correlations and fluctuations.

Beside the QGP signatures, also the global properties of the A-A collisions like impact parameter, energy density and entropy have to be studied. Ex-

perimentally they can be obtained from charged particle multiplicity and transverse energy distribution.

The purpose of this section is not to give a detailed description of the all QGP signatures but just to report about the most recent results obtained by the ALICE experiment at the LHC from the study of the first Pb-Pb collisions at $\sqrt{s_{NN}} = 2.76$ TeV. In particular:

- charged-particle multiplicity density;
- suppression of charged particle production at large p_t;
- elliptic flow;
- identified hadron transverse momentum spectra and particle ratios;
- strangeness enhancement.

For more information on QGP experimental results from the previous experiments one can see e.g. [1]-[19].

As already said, the ALICE experiment studies not only Pb-Pb collisions but also pp interactions which provide reference values for Pb-Pb results, are fundamental to tune Monte Carlo generators and of course are of interest in themselves.

1.4.1 Charged-particle multiplicity density

The first step in characterizing the system produced in A-A collisions is the measurement of the charged-particle pseudorapidity density. It constrains the dominant particle production mechanisms, is essential to estimate the initial energy density and to tune model predictions. The dependence of the charged-particle multiplicity density on energy and system size, reflects the interplay between parton-parton scattering processes and soft processes for particle production and may provide hypothesis on the partonic structure of the projectiles.

In the following the primary charged-particle density ($dN_{ch}/d\eta$) measured by the ALICE experiment in central (for the most central 5% fraction of the hadronic cross section) Pb-Pb collisions at $\sqrt{s_{NN}} = 2.76$ TeV will be reported [21]. The comparison with the results provided by the previous experiments at lower centre-of-mass energies will also be shown. To compare particle production in different collision systems at different energies and to compare to model predictions, the charged-particle density is scaled by the number of nucleons participating at the interaction.

The density measured by ALICE is $dN_{ch}/d\eta = 1584 \pm 4(stat) \pm 76(syst)$. Normalizing per participant pair, $dN_{ch}/d\eta/(0.5 < N_{part}) >= 8.3 \pm 0.4(syst)$.

In Fig. 1.3 this value is compared to the measurements for Au-Au, Pb-Pb, pp and $\overline{p}p$ collisions for different collision energies. The energy dependence is steeper for A-A collisions than for pp and $\overline{p}p$ ones. A significant increase of a factor 2.2 is observed from RHIC to ALICE results for A-A collisions and a factor 1.9 from ALICE Pb-Pb collisions and pp collisions at similar energies.

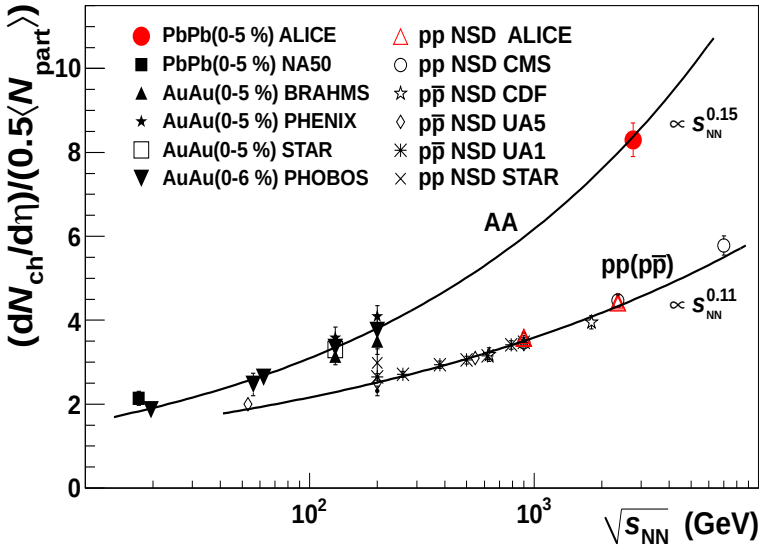

Figure 1.3: Charged-particle pseudorapidity density per participant pair for central A-A and pp ($\overline{p}p$) collisions as a function of $\sqrt{s_{NN}}$. The solid lines $\propto S_{NN}^{0.15}$ and $\propto S_{NN}^{0.11}$ are superimposed to the heavy-ion and pp data respectively.

In Fig. 1.4 the comparison between the ALICE result and the predictions at $\sqrt{s_{NN}} = 2.76$ TeV provided by the models able to describe RHIC measurements (obtained with Au-Au collisions at $\sqrt{s_{NN}} = 0.2$ TeV) is reported. As can be seen this new measurement provide new information and constraint to tune theoretical model and, indirectly, to understand the mechanism of particle interaction.

ALICE measured also the charged-particle density per participant pair as a function of the mean number of participants ($< N_{part} >$) that is related to the centrality of the collision (see [22])[4]. As can be seen in Fig. 1.5, $(dN_{ch}/d\eta)/(< N_{part} > /2)$ measured by ALICE (red points) increases with

[4]The average number of nucleons participating in the collision in a given centrality class reflect the collision geometry.

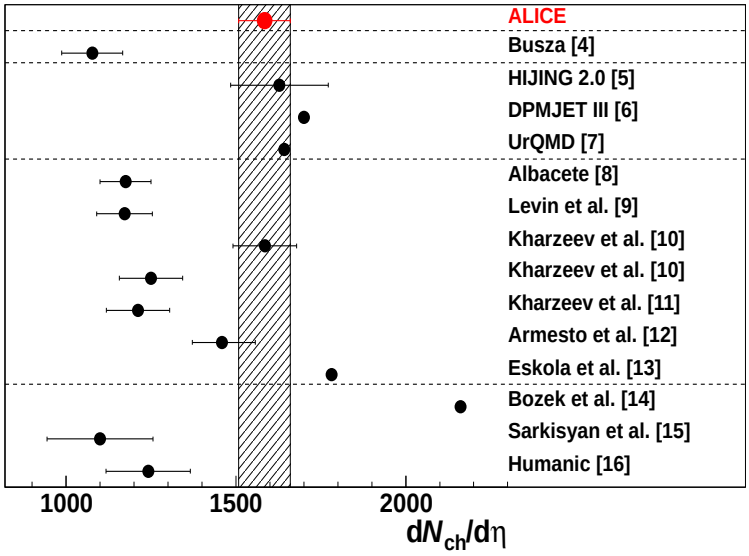

Figure 1.4: Comparison between the ALICE result and the predictions at $\sqrt{s_{NN}} = 2.76$ TeV provided by the models able to describe RHIC measurements obtained with Au-Au collisions at $\sqrt{s_{NN}} = 0.2$ TeV.

$< N_{part} >$ from 4.4 ± 0.4 for the most peripheral collisions to 8.4 ± 0.3 for the most central collision class. In the same figure, also the values for Au-Au collisions at $\sqrt{s_{NN}} = 0.2$ TeV averaged over the RHIC experiments are shown (white markers) artificially rescaled by a factor 2.1 in order to compare the dependence on $< N_{part} >$. It is evident that the centrality dependence of the multiplicity is very similar for the two energies.

In Fig. 1.6 the same ALICE data are compared with theoretical predictions. One again it is clear that the new LHC results are fundamental to select the better theoretical models and to provide constraints on the particle production mechanism.

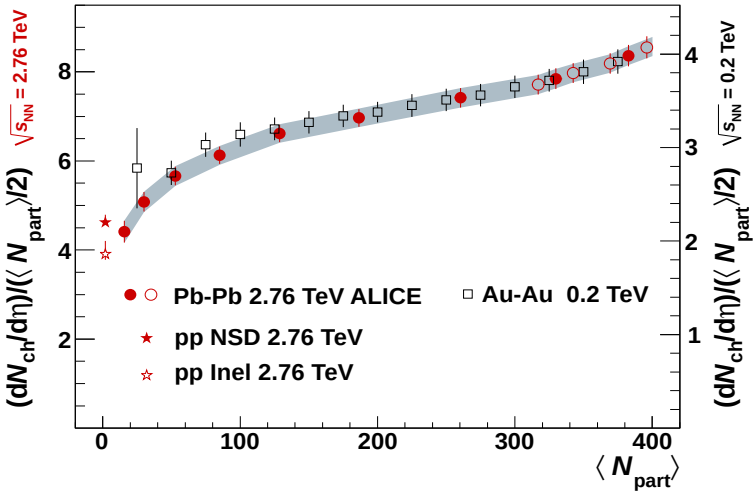

Figure 1.5: Dependence of $(dN_{ch}/d\eta)/(< N_{part} > /2)$ on the number of participants for Pb-Pb collisions at $\sqrt{s_{NN}}$=2.76 TeV (red points) and Au-Au collisions at $\sqrt{s_{NN}}$=0.2 TeV (RHIC average, white markers). The scale is different for the two collisions energies by a factor 2.1. The value for non single diffractive and inelastic pp collisions are the results of interpolating between ALICE data at $\sqrt{s}$ = 2.36 and $\sqrt{s}$= 7 TeV. See [22] for more information.

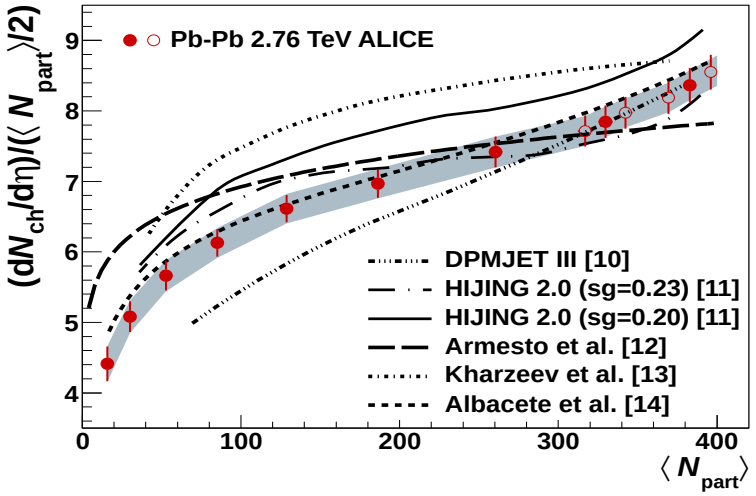

Figure 1.6: Comparison of the ALICE $(dN_{ch}/d\eta)/(< N_{part} > /2)$ measurement as a function of the event centrality compared to different models' predictions.

1.4.2 Suppression of charged particle production at large p_t

The RHIC experiments reported that hadron production at high transverse momentum in central Au-Au collisions at $\sqrt{s_{NN}} = 0.2$ TeV is suppressed by a factor 4-5 compared to expectations from an independent superposition of nucleon-nucleon collisions. The dominant production process for high p_t hadrons is the fragmentation of high p_t partons that originate in hard scattering in the early stage of the nuclear collision. Due to this, the observed suppression at RHIC is generally attributed to the energy loss of the partons as they propagate through the QGP. To quantify this effect, the so-called nuclear modification factor R_{AA} is used. It is defined as the ratio of the charged particle yield in Pb-Pb to that observed in pp collisions, scaled by the number of binary nucleon-nucleon collisions $< N_{coll} >$:

$$R_{AA}(p_t) = \frac{(1/N_{ev}^{AA}) d^2N_{ch}^{AA}/d\eta dp_t}{< N_{coll} > (N_{ev}^{pp}) d^2N_{ch}^{pp}/d\eta dp_t}. \tag{1.3}$$

If no nuclear modification is present, R_{AA} should tend to unity at high p_t. At the LHC energy the density of the medium is expected to be higher than at RHIC, leading to a larger energy loss of high p_t partons.

ALICE has measured the inclusive primary charged particle p_t distributions at mid-rapidity in central and peripheral Pb-Pb collisions at $\sqrt{s_{NN}} =$ 2.76 TeV (see [23]). In Fig. 1.7 R_{AA} for central and peripheral collisions is shown. It deviates from one in both samples. However, at high p_t, where production from hard processes is expected to dominate, there is a marked difference between peripheral and central events. In peripheral collisions R_{AA} reaches about 0.7 and shows no pronounced p_t dependence for $p_t > 2$ GeV/c indicating only weak parton energy loss. In central collisions, R_{AA} is again significantly different from one, reaching a minimum at $p_t = 6 - 7$ GeV/c and a maximum at $p_t = 2$ GeV/c, showing a strong dependence on p_t.

In Fig. 1.8 the ALICE result in central Pb-Pb collisions is compared to the ones by the PHENIX and STAR experiments at RHIC. The position and shape of the maximum at $p_t \sim 2$ GeV/c and the subsequent decrease are similar, while R_{AA} at $p_t = 6 - 7$ GeV/c is smaller at LHC compared to RHIC. This suggest an enhanced energy loss at the LHC with respect to RHIC, and therefore a denser medium production.

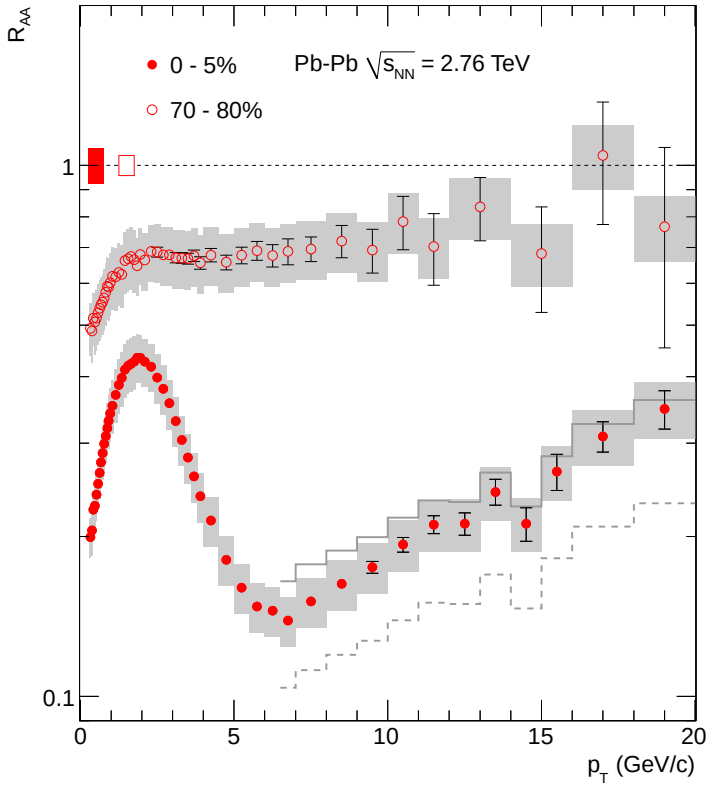

Figure 1.7: R_{AA} measured by the ALICE experiment in central and peripheral Pb-Pb collisions at $\sqrt{s_{NN}} = 2.76$ TeV. Error bars indicate the statistical uncertainties while the boxes contains the systematic errors (see [23] for more details).

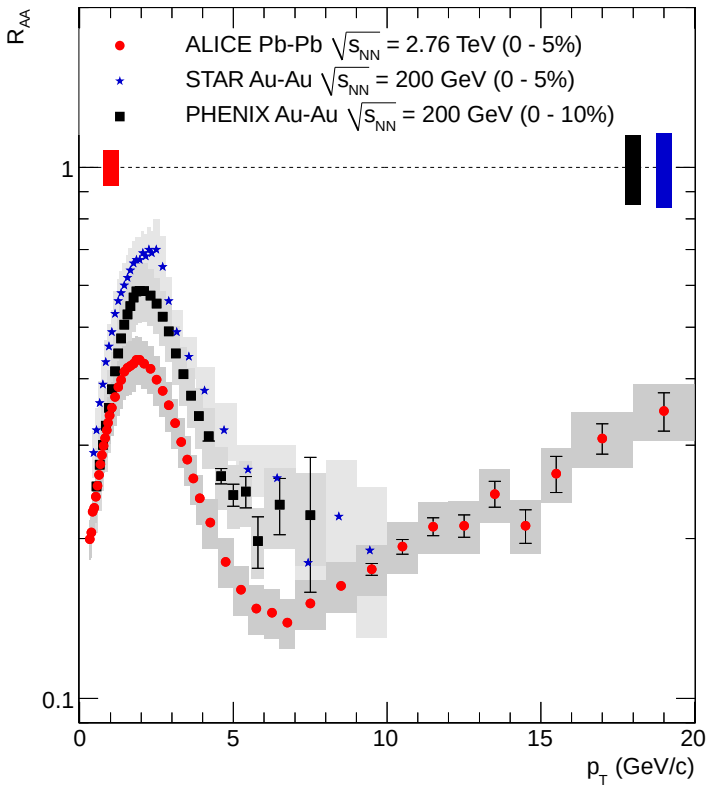

Figure 1.8: Comparison between R_{AA} measured by the ALICE experiment in central Pb-Pb collisions at $\sqrt{s_{NN}} = 2.76$ TeV and measurements performed by the PHENIX and STAR experiments at RHIC in central Au-Au interactions at $\sqrt{s_{NN}} = 0.2$ TeV. For the meaning of the errors see [23].

1.4.3 Elliptic flow

One of the experimental observables sensitive to the properties of the QGP is the azimuthal distribution of the particles in the plane perpendicular to the beam direction. When nuclei collide at finite impact parameter (non central collisions), the geometrical overlap region, and therefore the initial matter distribution, is anisotropic. If the matter is interacting, this spatial asymmetry is converted, via multiple collisions, into an anisotropic momentum distribution [24]. The second momentum of the final state hadron azimuthal distribution is called elliptic flow; it is a response of the dense system to the initial conditions and is therefore sensitive to the early and hot strongly interacting phase of the evolution. Since there are many theoretical models describing the RHIC data (but with different predictions at the LHC energies), a measurement of the elliptic flow at the LHC is crucial to test the validity of a hydrodynamic description of the medium and to measure its thermodynamic properties (in particular, shear viscosity and the equation of state). The azimuthal dependence of the particle yield can be written in the form of a Fourier series [25]:

$$E\frac{d^3N}{d^3p} = \frac{1}{2\pi}\frac{d^2N}{p_t dp_t dy}\left(1 + \sum_{n=1}^{\infty} 2v_n \cos[n(\phi - \Psi_R)]\right) \tag{1.4}$$

where E is the energy of the particle, p the momentum, p_t the transverse momentum, ϕ the azimuthal angle, y the rapidity and Ψ_R the angle of the reaction plane that is the plane defined by the beam axis z and the impact parameter direction. In general, the coefficients $v_n =< \cos[n(\phi - \Psi_R)] >$ are p_t and y dependent and are referred as differential flow. The integrated flow is defined as an average evaluated with $d^2N/dp_t dy$ used as a weight. The first coefficient, v_1, is called direct flow and the second coefficient v_2 is called elliptic flow.

The ALICE experiment has measured the elliptic flow of charged particles in Pb-Pb collisions at $\sqrt{s_{NN}} = 2.76$ TeV [26]. It was found that the dependence of v_2 on the transverse momentum does not change from the RHIC to the LHC energies for the measured centrality classes.

In Fig. 1.9 the integrated elliptic flow measured in the 20%-30% centrality class is compared to results from lower energies. There is a continuous increase in the magnitude of the elliptic flow for this centrality region from RHIC to LHC energies. A difference of about 30% was found. This increase is larger than in current ideal hydrodinamic calculation at LHC multiplicities, but it is in agreement with some models that include viscous corrections[26]. The larger integrated elliptic flow at the LHC is caused by the increase in the mean p_t.

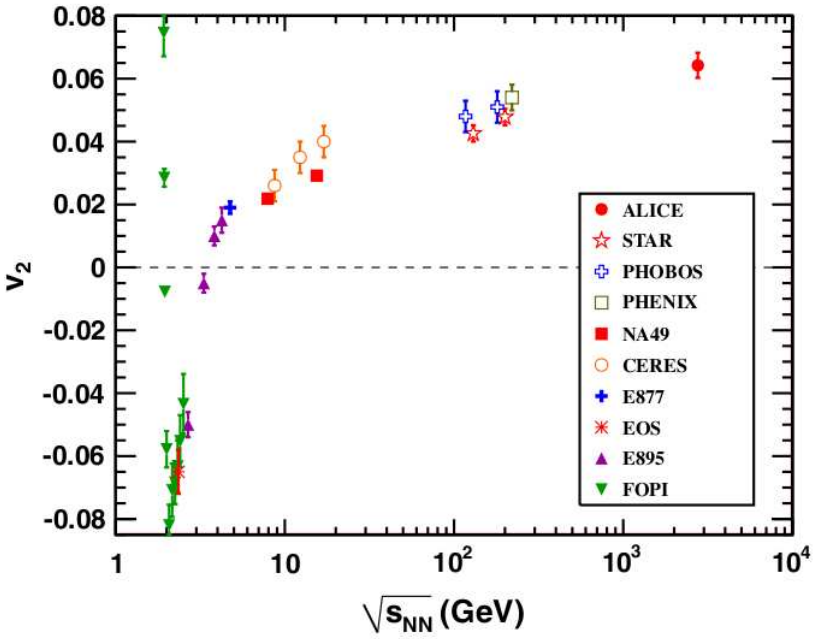

Figure 1.9: Integrated elliptic flow measured by the ALICE experiment in Pb-Pb data at $\sqrt{s_{NN}} = 2.76$ TeV in the 20%-30% centrality class compared with resuts from lower energies taken at similar centralities.

1.4.4 Identified primary hadron spectra and particle ratios

To extract the properties of the medium at the chemical and kinetical freeze-out, the ALICE experiment has studied the identified primary hadron spectra in Pb-Pb collisions at $\sqrt{s_{NN}} = 2.76$ TeV. In Fig. 1.10 Pb-Pb spectra for the most central bin are compared with STAR [28] and PHENIX [29] results at $\sqrt{s_{\rm NN}} = 200$ GeV. It can be seen that ALICE spectra are harder than RHIC ones and protons are flatter, probably due to stronger radial flow.

To determine integrated yields and average p_t, fits on individual particles with a Blast-Wave function [31] have been performed. In Fig. 1.11 (top panel) the K^-/π^- ratios obtained at ALICE and STAR are shown for different event multiplicity. An increase both with the centrality (same trend for STAR and ALICE) and going from pp to Pb-Pb collisions is evident. In the bottom panel the ALICE and RHIC [28, 29, 30] $\overline{p}/\pi^-$ ratios, constant for every centrality and respect to pp interactions, are shown. The results are compatible apart from STAR. It is partially due to the fact that STAR $\overline{p}$ are not feed-down corrected.

From Fig. 1.12, which shows the mean p_t for π, K and p as a function of $\mathrm{dN_{ch}}/\mathrm{d}\eta$, an increase of mean p_t with the particle mass and the collision centrality is present and at ALICE the mean p_t is higher than at STAR for the same value of $\mathrm{dN_{ch}}/\mathrm{d}\eta$.

In order to obtain information on the thermal properties of the medium at the kinetic freeze-out, a global fit of the spectra with a Blast Wave function in which the kinetic freeze-out temperature (T_{fo}) and the radial flow ($< \beta >$) are free parameters, is used. In Fig. 1.13 the fit parameters for ALICE and STAR in different centrality bins are shown. It can be noticed how the radial flow is $\sim 10\%$ higher at $\sqrt{s_{\rm NN}} = 2.76\,\mathrm{TeV}$ than at $\sqrt{s_{\rm NN}} = 0.2\,\mathrm{TeV}$.

1.5 Strangeness enhancement

One of the first signatures of the QGP was the strangeness enhancement in A-A collisions that is an increased production of strange hadrons with respect to pp interactions. In nucleon-nucleon collisions the s quark production is strongly suppressed due to its large mass (if compared with u and d quarks). If the QGP is formed, a large amount of gluons that can produce $s\overline{s}$ couples through gluon fusion processes ($gg \rightarrow s\overline{s}$) is present both because, due to the chyral symmetry restoration, the quark mass is set to the current one ($m_s \sim 150$ MeV, smaller than the critical temperature) and because the

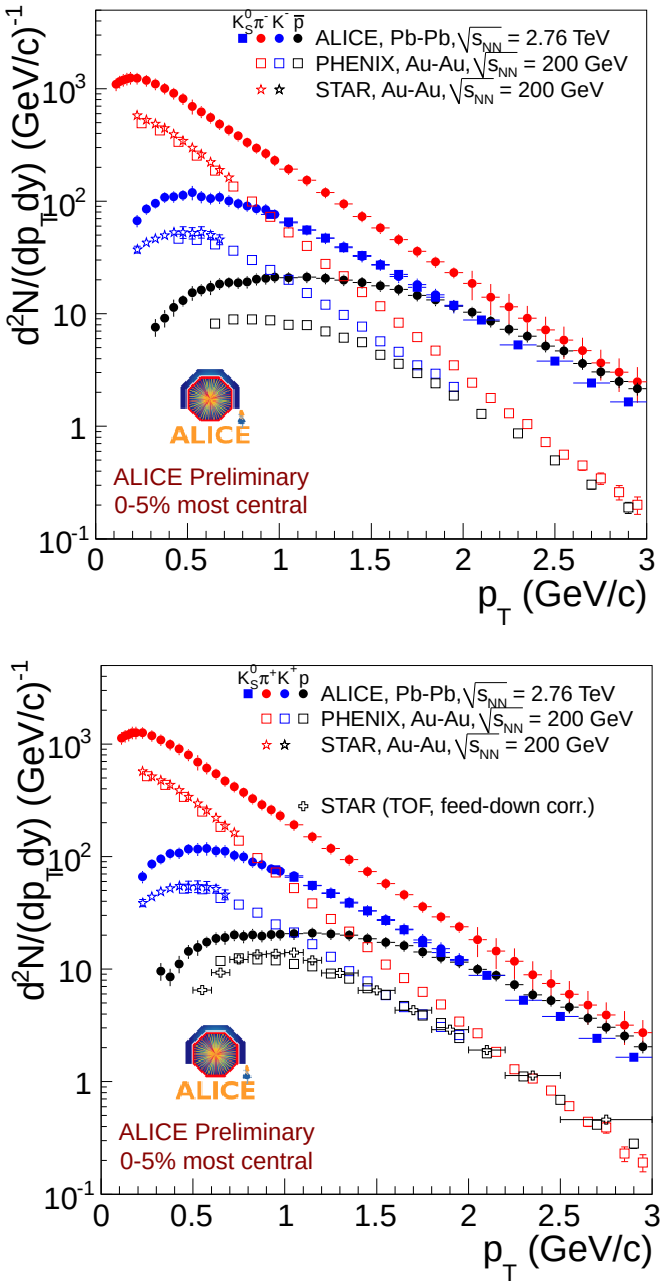

Figure 1.10: Transverse momentum spectra for π, K and p negative (top) and positive (bottom) in the most central bin. A comparison between results obtained by ALICE, STAR and PHENIX Collaborations is shown.

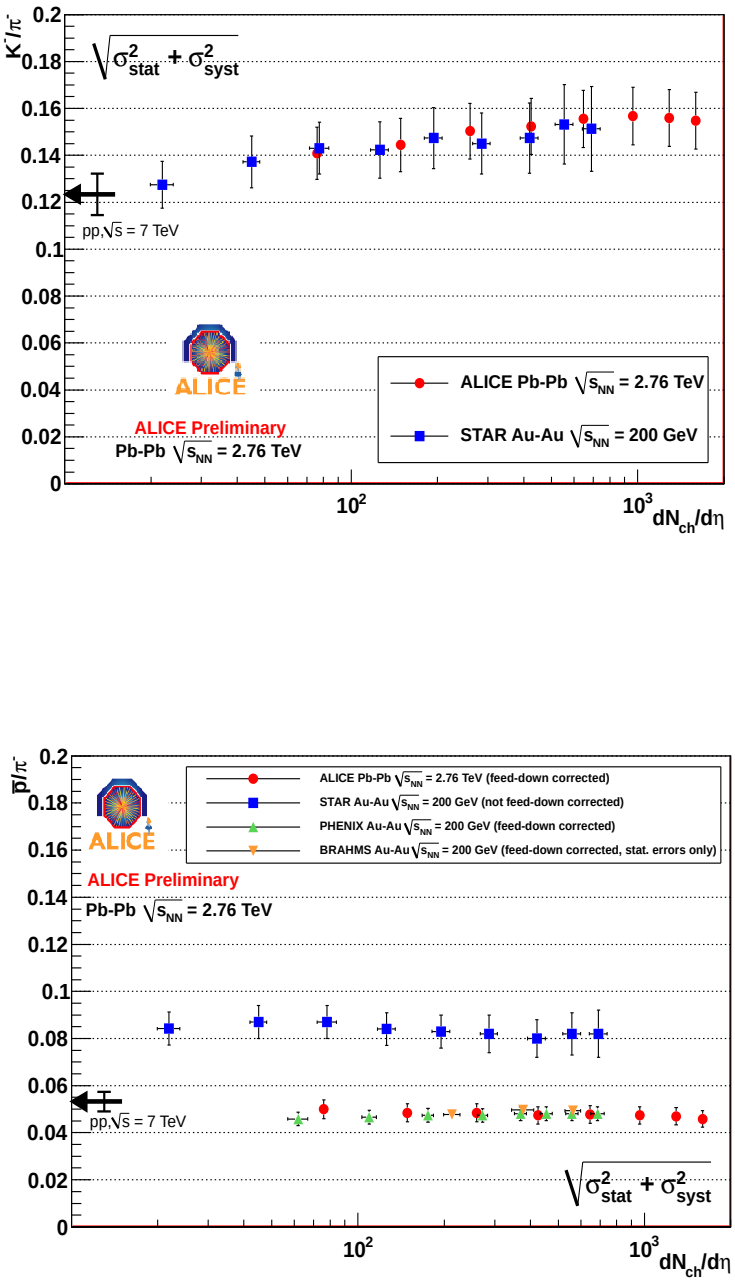

Figure 1.11: K/π (top) and p/π (bottom) density ratios as a function of $dN_{ch}/d\eta$.

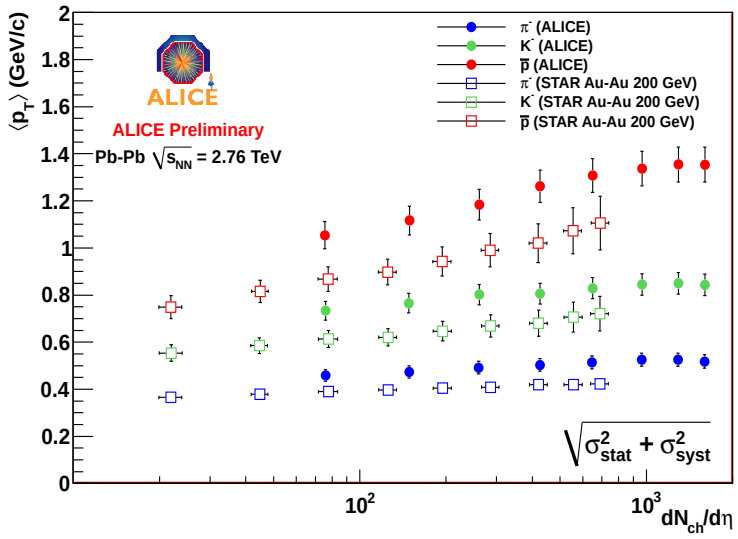

Figure 1.12: Mean p_t for π, K and p at different event multiplicity for ALICE and STAR.

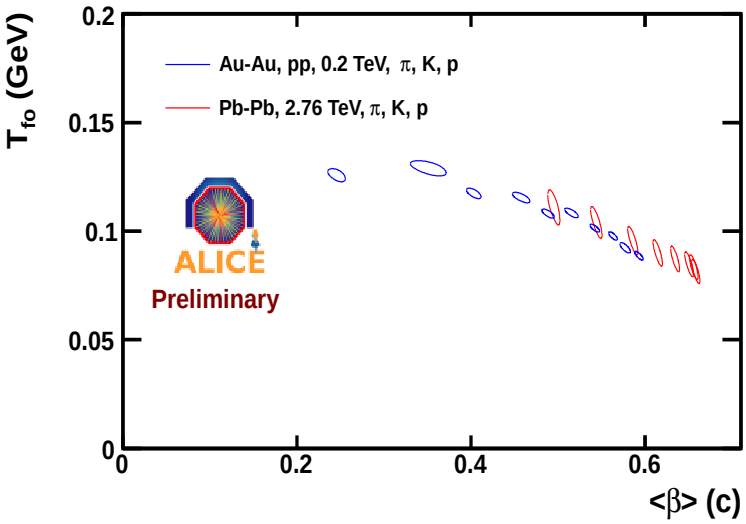

Figure 1.13: Kinetic freeze-out temperature and radial flow parameter as obtained from a global fit of the spectra with a Blast Wave function for increasing centrality.

Pauli principle become important in presence of the great amount of free u and d quark in the initial phase.

The ALICE experiments has measured the transverse momentum spectra of strange particle in Pb-Pb collisions at $\sqrt{s_{NN}} = 2.76$ TeV to get a precise determination of integrated yields, mean transverse momenta and particle ratios. For these studies the relevant particles are K, Λs, Ξs, Ωs.

As can be seen from the top panel of Fig. 1.11, as in the case of RHIC energies, the kaon production relative to pions increases with centrality in Pb-Pb collisions from approximately 0.125 in peripheral collisions to 0.16 in central collisions. To be noted the agreement between peripheral Pb-Pb collisions and the measurement in pp reactions. In addition, looking at the bottom panel of the same figure, in contrast to strange particles, the p/π ratio shows no dependence on the centrality. An interesting feature of strange particle production is the enhanced production in Pb-Pb relative to pp collisions. While the double ratio of p/π in pp to Pb-Pb collisions is close to unity, the K/π, Ξ/π, and Ω/π ratios show a significant increase proportional to the strangeness content (see [32]).

Chapter 2

The ALICE experiment at the LHC

The ALICE (A Large Ion Collider Experiment) collaboration has build a dedicated heavy-ion detector to exploit the unique physics potential of lead-lead (PbPb) interactions at the LHC (Large Hadron Collider) energies. The aim is to study the physics of strongly interacting matter at extreme energy densities, where the formation of a new phase of matter, the QGP (Quark-Gluon Plasma), is expected. The existence of such a phase and its properties are key issues in QCD (Quantum Cromo Dynamics) for the understanding of confinement and chiral-symmetry restoration. For this purpose, the ALICE experiment is carrying out a comprehensive study of the hadrons, electrons, muons and photons produced in the collisions of heavy nuclei. ALICE is also studying proton-proton (pp) collisions, that are fundamental not only as a comparison with PbPb collisions, but also to tune the Monte Carlo simulations and to study the physics of these collisions in themselves.

In this chapter, after a brief introduction about the LHC, some details on the ALICE experiment will be given, putting emphasis on one of its detectors, the Time Of Flight (TOF), as this is the detector that mainly used in the analysis reported in this thesis.

2.1 The Large Hadron Collider

2.1.1 Nominal parameters

The LHC [35], [33], [34] sits in a circular tunnel of 27 km circumference placed around 50 to 175 m underground. The LHC was aimed at colliding two counter-rotating beams of protons or heavy ions at $\sqrt{s} = 7\,\text{TeV}$ and

$\sqrt{s_{NN}} = 5.5\,\text{TeV}$ respectively. The accelerated particles are not uniformly distributed in the beams, but have a bunch structure. The nominal bunch spacing of 25 ns gives a peak crossing rate of 40 MHz. Since (for technical reasons) local larger bunch spacing are needed, the actual average crossing rate is 31.6 MHz. If we consider 19 interactions per crossing[1], at a nominal luminosity of $10^{34}\,\text{cm}^{-2}\text{s}^{-1}$ we get 600 millions inelastic events per second. At full intensity, each proton beam consists nominally of 2808 bunches where each bunch has 1.15×10^{11} protons at the start of a nominal fill, with a longitudinal dimension of 7.5 cm. If $\sqrt{s} = 7\,\text{TeV}$, the beam energy is 362 MJ. To bend the beams, 1232 superconducting dipole magnets are used. As a consequence, a huge cryogenic system is needed to produce the liquid helium that keeps the magnets cold. In Fig. 2.1 some of the LHC nominal parameters are reported.

• Circumference	26.7	km
• Beam energy at collision	7	TeV
• Beam energy at injection	0.45	TeV
• Dipole field at 7 TeV	8.33	T
• Luminosity	10^{34}	$\text{cm}^{-2}.\text{s}^{-1}$
• Beam current	0.58	A
• Protons per bunch	1.15×10^{11}	
• Number of bunches	2808	
• Nominal bunch spacing	24.95	ns
• Normalized emittance	3.75	μm.rad
• Total crossing angle	285	μrad
• Energy loss per turn	6.7	keV
• Critical synchrotron energy	44.1	eV
• Radiated power per beam	3.6	kW
• Stored energy per beam	362	MJ
• Stored energy in magnets	11	GJ
• Operating temperature	1.9	K

Figure 2.1: Some of the LHC nominal parameter.

Due to its very high complexity, the commissioning of the LHC is a long process and up to now, the LHC has not reached the designed parameters shown in Fig. 2.1 yet. We will see in $2.1.3 the best performance reached up to now by the LHC.

[1]Event rate = luminosity * cross section. If the inelastic pp cross section is 60 mb and the nominal luminosity is $10^{34}\,\text{cm}^{-2}\text{s}^{-1}$, the inelastic event rate is $600 \cdot 10^6/s$ so, for an average crossing rate of 31.6 MHz, we get 19 inelastic events per crossing.

2.1.2 Technical properties

To keep the luminosity high for long periods, a very stable orbit is required. The main limitation to this stability is the betatron oscillation [36] due to the different orientations of the angular momentum of the protons in the bunch: if in a single bunch the particles have momenta with different orientations, the beam is defocused when the bunch is deflected by a dipole. If the momenta of the particles have not the same direction we say that the bunch is hot; so, the colder the bunch is, the more stable the orbits are. To keep the beam focused, quadrupole magnets are used as they produce forces that act on particles that deviate from the stable orbit lead to that particles to oscillate around that stable orbit. Since it is impossible for a quadrupole to focus in both planes at the same time we have two types of quadrupoles: F quadrupoles which are focusing horizontally, but defocusing vertically, and D quadrupoles which are focusing vertically and defocusing horizontally. If D and F quadrupoles are placed at the correct distance, the overall effect is focusing in both planes. A lattice of quadrupoles can then be built, enabling the transport of the beam over long distances.

The result of the combined action of dipole and quadrupole magnets in the phase space in terms of x, that is the horizontal coordinate, and $x' = dx/ds$ (where s is the direction of the tangent to the beam pipe), is an ellipse described by the following equation:

$$\beta(s)x'(s)^2 + 2x'(s)x(s)\alpha(\sigma) + x^2(s)\gamma(s) = \varepsilon \tag{2.1}$$

The area of the ellipse is $\pi\varepsilon$. If we move along the orbit, the shape and the orientation of the ellipse change due to the presence of the quadrupoles, but its area remains costant. We define ε as the emittance of the beam, and $\beta(s)$ as the betatron amplitude which defines the characteristics of the trajectories of the beam particles. As already said, to focus the beam an alternating series of focusing and defocusing quadrupole magnets is needed. Indicating the dipoles with the letter "O" the basic cells used at the LHC is of type FODO: focusing + dipole + defocusing + dipole magnets[2]. The right configuration of the magnets is fundamental to keep $\beta(s)$ small in order to get a small transverse dimension and a high beam luminosity. An accelerator with low β along the whole circumference is highly unstable. As a consequence β is kept low only close to the Interaction Points (IP) that are shown in Fig. 2.2. Since the lower β is at the IP, the faster it grows going away from the IP so bigger magnets are needed just after the IP. This effect is obviously more important for large-sized experiments.

[2]Instead of the dipole, there can be a drift space

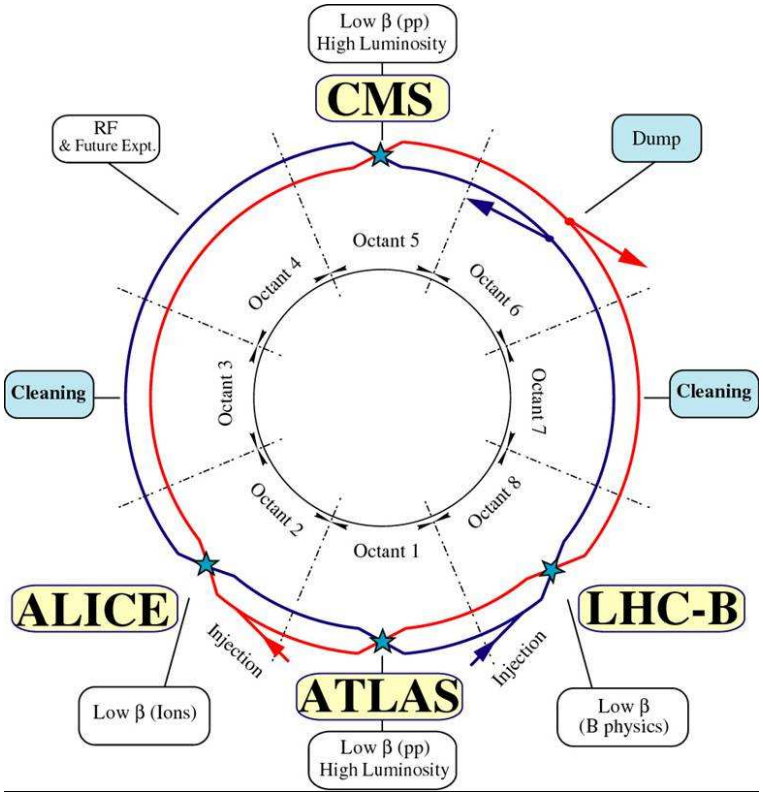

Figure 2.2: Schematic view of the IPs at the LHC.

To accelerate particles, a radiofrequency cavity is necessary [37] and the oscillation frequency f_{RF} has to be set so that it is an integer multiple h of the revolution frequency f_{rev}: $f_{RF} = h \times f_{rev}$. Since $f_{rev} = \beta c/2\pi R$ and $f_{RF} = 400\,\mathrm{MHz}$, $h \sim 35640$. The segments of the circumference centered on this points are called buckets.

Not all the particles in the beams have exactly the same energy. If a particle with lower (higher) energy is present, it arrives later (earlier) in the cavity and sees a higher (lower) voltage with respect to the synchronous particles. As a result, it accelerates (decelerates) while approaching synchronous particles after many turns. But what happens when the particle momentum increases? Taking into account that a particle with higher energy follows a longer path, since it is less bended by the magnet but has higher velocity, the frequency f varies as in eq. 2.2

$$\frac{df}{f} = \frac{dv}{v} - \frac{dr}{r} = \left(\frac{1}{\gamma^2 - \alpha_s}\frac{dp}{p}\right) \tag{2.2}$$

where v is the velocity of the particle, r its trajectory, and α_s the momentum compaction factor fixed by the quadrupoles. This means that in a constant magnetic field and at low momentum ($1/\gamma^2 > \alpha_s$), the revolution frequency increases with momentum, while at high momentum ($1/\gamma^2 < \alpha_s$) the revolution frequency decreases as momentum increases. The energy for which $1/\gamma^2 = \alpha_s$ is called transition energy. As a consequence, a particle not syncronized with the electromagnetic field has, after many turns, a full oscillation (called synchrotron oscillation) in the longitudinal plane around the synchronous particles: instead of being spread uniformly around the circumference of the accelerator, the particles get "clumped" around the synchronous particles in a bunch. This bunch is contained in a RF bucket.

The LHC might accelerate a beam made up of 35640 bunches, but not all LHC buckets need to be filled with bunches. The buckets are just virtual positions on the LHC circumference and the abort gap is the number of buckets in a row which are supposed to be never loaded with protons and form a gap in the circumference. The purpose of this gap is to be used during the dumping of the beam, when it takes a short but significant time to switch on the magnets which divert the beam from the LHC into the dump. On top of this, other factors make the presence of the abort gaps necessary, for example the long range beam-beam interactions, the total beam power and damage potential, the beam lifetime and cleaning efficiency of the collimation sections, the beam instabilities due to electron cloud effect, the required time for the injection (kiker rise time), the performance of the LHC injection chain. The bucket area is called longitudinal acceptance while the bunch area is named longitudinal emittance (see Fig. 2.3).

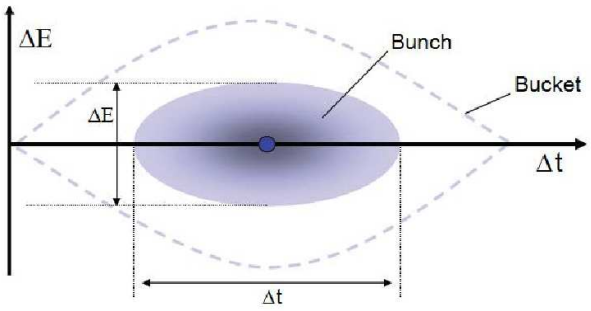

Figure 2.3: Bunch and bucket.

To accelerate protons up to $\sqrt{s} = 7\,\text{TeV}$ or PbPb up to $\sqrt{s_{NN}} = 5.5\,\text{TeV}$ it is necessary to use a complex system of accelerators working at increasing energies. As shown in Fig. 2.4, we can see that at CERN the accelerator chain is the following:

- Duoplasmatron which produces the H^+ beam with an energy of 92 keV.
- Radio-Frequency-Quadrupole (RFQ) which provides a transverse focusing of the beam, the bunch structure and an acceleration up to 750 keV.
- Linac2 which is a multichamber resonant cavity that makes the beam reach an energy of 50 MeV.
- Proton-Syncrotron-Booster (PSB) that boosts the protons up to 1.4 GeV.
- Proton-Syncrotron (PS) that is responsible for providing the 25 ns bunch separation and accelerates the protons up to 28 GeV.
- Super-Proton-Syncrotron (SPS) that accelerates up to 450 GeV.
- LHC that accelerates up to 7 TeV.

To move the beam from a transfer line to the accelerator, fast magnets that deflect the beam are necessary: the kikers. They are also used for beam cleaning (that is, to remove (dump) the protons out of the buckets before they generate magnet quenches). Certain materials undergo a phase transition and become superconducting if their temperature drops below the critical temperature. The virtue of superconducting materials is that they are capable of conducting very high current while having very low ohmic

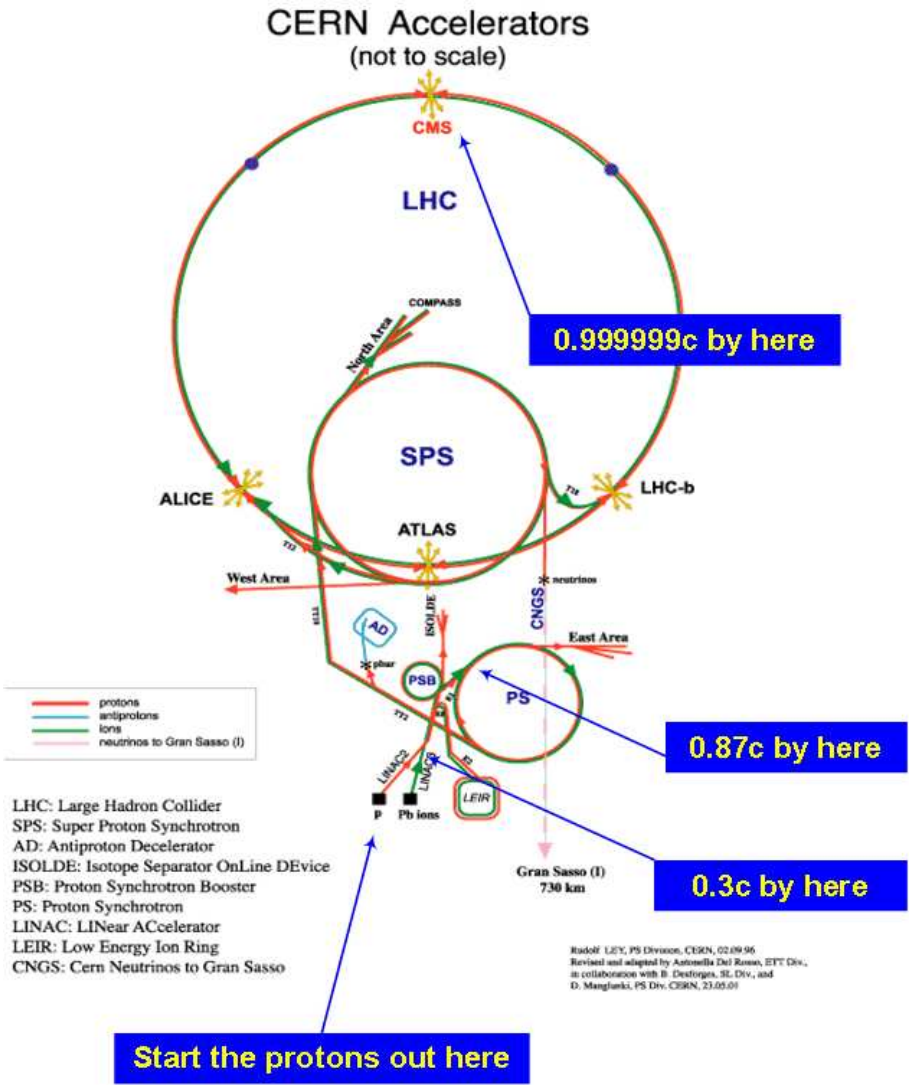

Figure 2.4: The CERN accelerator complex.

losses. But if the temperature, the current density or the magnetic field inside the material exceed some given limits, the material undergoes reversal phase transition, becoming a normal conducting material. This reverse phase transition is called quench. At the LHC, the loss of particles inside the magnets is considered the most critical source of magnet quenches. Due to this, the dump of the beam (when it is instable or the luminosity becomes too low) is a dangerous procedure.

Point 6 of the LHC is devoted to the Beam Dumping System. A gap of 3μs in the circulating bunch pattern is present to allow the horizontally deflecting extraction kikers (MKD) to switch on. The extracted beam is swept in a quasi-circular shape by two sets of orthogonally deflecting dilution kikers (MKB). Each beam dump absorber consists of a 7 m long segmented carbon cylinder with a 700 mm diameter contained in a steel cylinder. This is water cooled and surrounded by about 750 t of concrete and iron shielding.

In Fig. 2.5 the classical beam cycle from the injection to the dump is described.

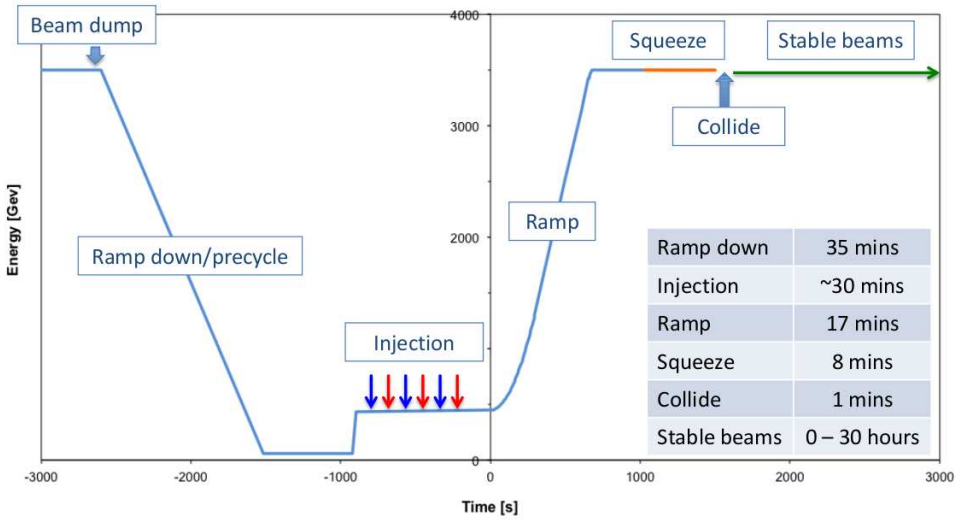

Figure 2.5: Usual LHC beam cycle.

2.1.3 LHC Performance

The first LHC injection tests occurred in august 2008 and the first beam was delivered on 10 september 2008. On 19 september 2008 the LHC underwent a long stop due to the quenching of a magnet. After this the first beam was

circulated on 29 november 2009. On 30 March 2010 the first pp collisions at $\sqrt{s} = 3.5\,\text{TeV}$ took place and on november 2010 PbPb collisions were performed. During 2011, about $10 fb^{-1}$ of integrated luminosity has been collected as can be seen in Fig. 2.6. Due to its different physical researches that don't look for rare signals but studies the QGP signatures, the ALICE experiment collected an integrated luminosity 3 order of magnitude lower than the one of ATLAS and CMS as can be seen in Fig. 2.7

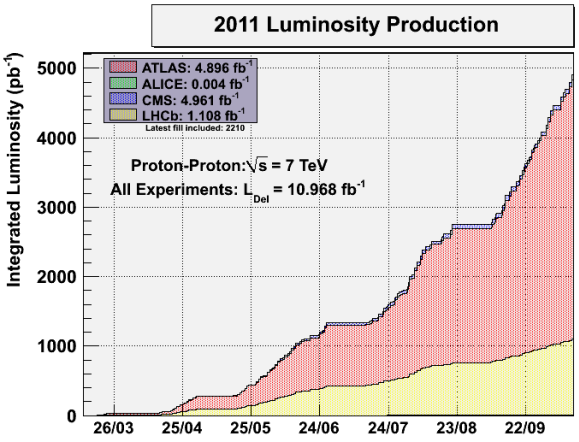

Figure 2.6: LHC delivered luminosity from March to september 2011.

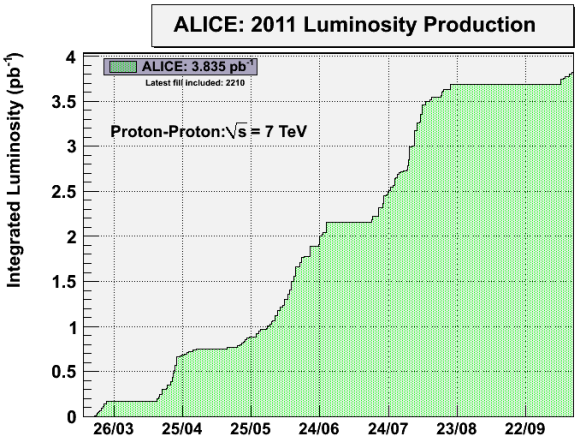

Figure 2.7: ALICE delivered luminosity from March to september 2011.

Despite its excellent performance, the LHC has not yet achieved the nominal ones. A comparison between the design performance and the achieved ones is shown in Tab. 2.1.

	Design	Achieved
Energy (TeV)	7.0	3.5
Number of bunches per beam	2808	1380
Bunch separation (ns)	25	50
Bunch intensity (10^{11})	1.15	1.3
Peak luminosity ($10^{33}\,\mathrm{cm}^{-2}\mathrm{s}^{-1}$)	10	3.2

Table 2.1: LHC designed parameters compared with actual ones.

Thanks to its stability, the LHC can maintain for a considerably long amount of time the so-called stable beam configuration, that is the phase in which the beam are declared stable and the experiments can take data in safe (for their detectors) conditions. Fig. 2.8 shows the LHC efficiency in terms of the fraction of time that was spent in the machine setup phase, the beam setup, the stable beam phase (useful time for data taking) and in the accesses needed to restore problems in the machine. The longest consecutive time in stable beams was 26 hours.

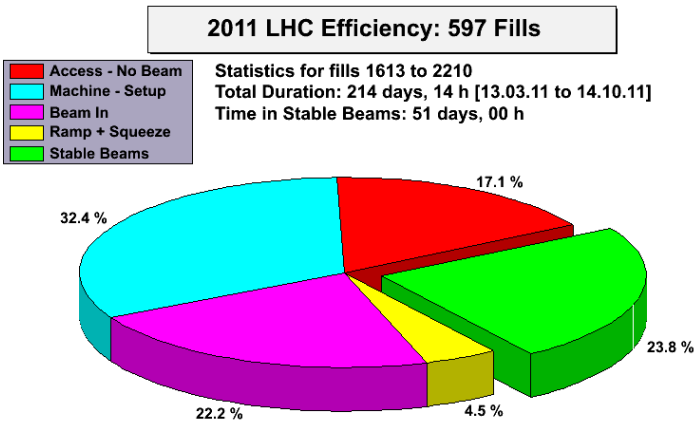

Figure 2.8: LHC efficiency

Fig. 2.9 exemplifies a typical screenshot of the LHC Page1 that displays as main information the status of the beam, the filling scheme, the beam energy and the intensity.

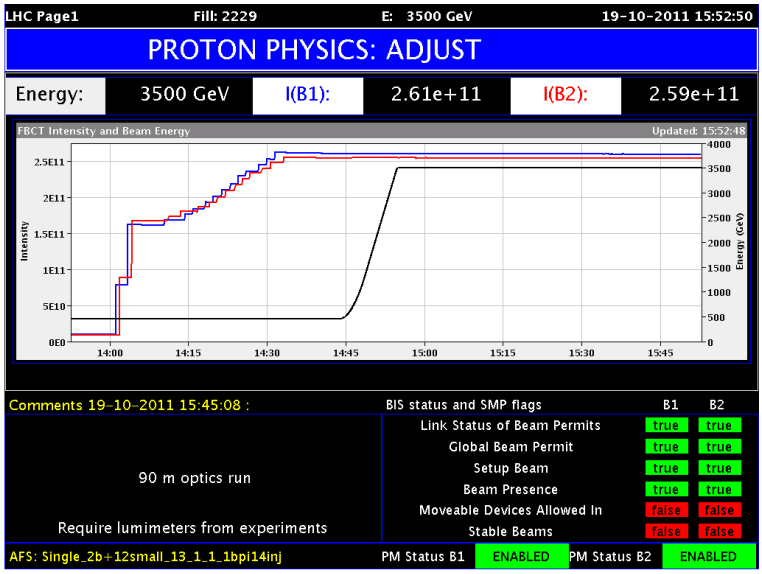

Figure 2.9: LHC page1 screenshot.

2.2 The ALICE experiment

The ALICE experiment at the LHC [38] has as main goal the study of nuclear matter under extreme conditions of temperature and energy density as those reached in ultrarelativistic heavy ion collisions. The aim is to verify the QCD prediction of the existence of a phase transition from the common hadronic matter to the so-called quark-gluon-plasma, in which quarks and gluons are free and not confined inside hadrons. Since ALICE is the only LHC experiment designed for PbPb collisions, it has to be able to measure as many observables as possible in the widest phase space region. ALICE is also interested in the study of pp interactions, that are crucial for a comparison with PbPb collisions, to tune Monte Carlo models and per se, like the other LHC experiments. With respect to these experiments, ALICE is endowed by an excellent Particle IDentification (PID) performance, obtained combining different PID techniques from different detectors that are optimized in different momentum (p) regions. In this section a brief description of the ALICE detectors will be given.

2.2.1 ALICE detectors

The ALICE detectors can be classified in three groups:

- *Barrel detectors*: they are housed in a solenoid magnet previously used in the L3 experiment at LEP which provides the experiment with a 0.5 T magnetic field and covers the pseudorapidity interval $-0.9 \leq \eta \leq 0.9$ (corresponding to a polar acceptance $\pi/4 \leq \theta \leq 3\pi/4$). The azimuthal ϕ acceptance is 2π. They are mainly dedicated to the vertex reconstruction, tracking, particle identification and momentum measurement. Starting from the interaction region and going outward, we find the following detectors:

  - Inner Tracking System (ITS);
  - Time Projection Chamber (TPC);
  - Transition Radiation Detector (TRD);
  - Time of Flight (TOF).

  In the mid-rapidity region there are also two detectors with limited acceptance:

  - High-Momentum Particle Identification Detector (HMPID);
  - PHOton Spectrometer (PHOS);

  In addition, the ElectroMagnetic CALorimeter (EMCAL) is present.

- *Muon spectrometer*: placed in the forward pseudorapidity region ($-4.0 \leq \eta \leq -2.5$), this detector consists of a dipole magnet and tracking and trigger chambers. It is optimized to reconstruct heavy quark resonances (such as J/ψ through their $\mu^+\mu^-$ decay channel) and single muons;

- *Forward detectors*: placed in the high pseudorapidity region (small angles with respect to the beam pipe) they are small and specialized detector systems used for triggering or to measure global event characteristics. They are:

  - Time Zero (T0) to measure the event time;
  - V0 to reject the beam-gas background and to trigger minimum bias events;
  - Forward Multiplicity Detector (FMD) to provide multiplicity information over a large fraction of the solid angle ($-3.4 \leq \eta \leq -1.7$ and $1.7 \leq \eta \leq 5$));

  - Photon Multiplicity Detector (PMD) to measure the multiplicity and the spatial distribution of photons on an event-by-event basis in the $2.3 \leq \eta \leq 3.7$ region;
  - Zero Degree Calorimeter (ZDC) to measure and trigger on the impact parameter.

- Besides the so far listed detector, an array of scintillators (ACORDE) is installed on top of the L3 magnet to trigger on cosmic rays.

In Fig. 2.10 and 2.11 a schematic view of the ALICE experiment is shown.

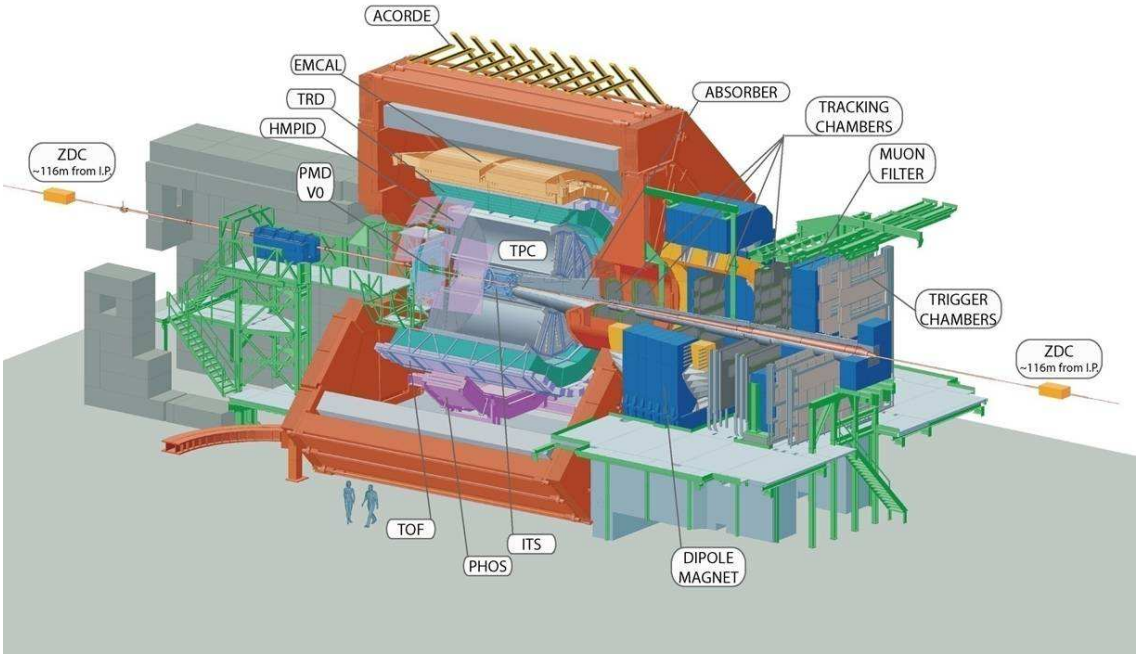

Figure 2.10: Schematic view of the barrel detectors and of the muon spectrometer of the ALICE experiment. The central barrel is housed inside the L3 solenoid magnet (red octogonal shape). From the IP outwards, we find the ITS, TPC, TRD and TOF detectors, together with the small acceptance detectors, (HMPID, PHOS) and EMCAL. On the right-hand side of the experiment, the muon spectrometer is composed of a dipole magnet, 14 planes of tracking and triggering chambers and absorber plates.

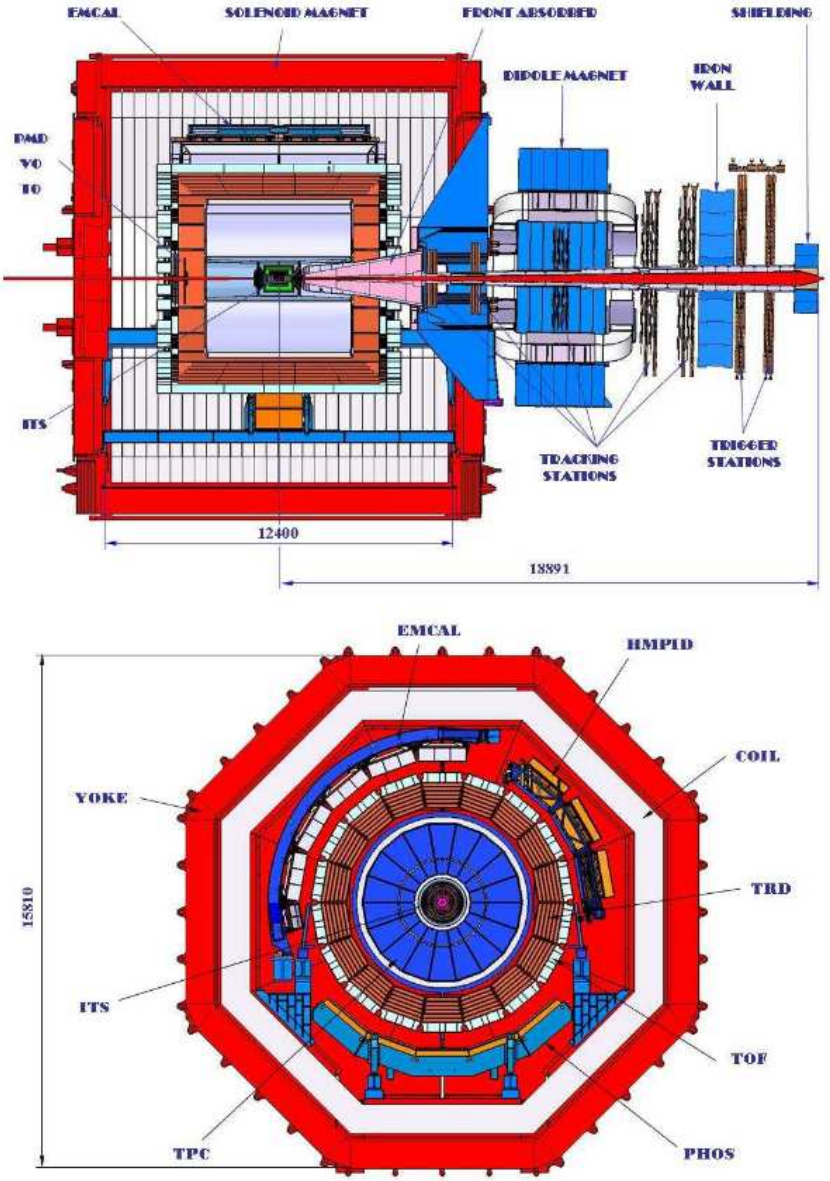

Figure 2.11: ALICE 2D cut views along the yz direction (top) and xy direction (bottom). The ALICE coordinate system is defined as follow: the x axis is perpendicular to the beam direction, pointing to the accelerator center; the y axis is perpendicular to the x axis and to the beam direction; finally the z axis is parallel to the beam direction. The positive z axis is pointing in the direction opposite to the muon spectrometer.

In Fig. 2.12 a summary of the ALICE detector subsystems is reported. In the following sections some details of the ALICE experiment will be given.

Detector	Acceptance (η, ϕ)	Position (m)	Dimension (m^2)	Channels
ITS layer 1,2 (SPD)	$\pm 2, \pm 1.4$	0.039, 0.076	0.21	9.8 M
ITS layer 3,4 (SDD)	$\pm 0.9, \pm 0.9$	0.150, 0.239	1.31	133 000
ITS layer 5,6 (SSD)	$\pm 0.97, \pm 0.97$	0.380, 0.430	5.0	2.6 M
TPC	± 0.9 at r=2.8 m ± 1.5 at r=1.4 m	0.848, 2.466	readout 32.5 m^2 Vol. 90 m^3	557 568
TRD	± 0.84	2.90, 3.68	716	1.2 M
TOF	± 0.9	3.78	141	157 248
HMPID	± 0.6, $1.2^\circ < \phi < 58.8^\circ$	5.0	11	161 280
PHOS	± 0.12, $220^\circ < \phi < 320^\circ$	4.6	8.6	17 920
EMCal	± 0.7, $80^\circ < \phi < 187^\circ$	4.36	44	12 672
ACORDE	± 1.3, $-60^\circ < \phi < 60^\circ$	8.5	43	120
Muon Spectrometer				
Tracking station 1	$-2.5 < \eta < -4.0$	-5.36	4.7	1.08 M
Tracking station 2		-6.86	7.9	
Tracking station 3		-9.83	14.4	
Tracking station 4		-12.92	26.5	
Tracking station 5		-14.22	41.8	
Trigger station 1	$-2.5 < \eta < -4.0$	-16.12	64.6	21 000
Trigger station 2		-17.12	73.1	
ZDC:ZN	$\lvert\eta\rvert < 8.8$	± 116	2×0.0049	10
ZDC:ZP	$6.5 < \lvert\eta\rvert < 7.5$ $-9.7^\circ < \phi < 9.7^\circ$	± 116	2×0.027	10
ZDC:ZEM	$4.8 < \eta < 5.7$, $-16^\circ < \phi < 16^\circ$ and $164^\circ < \phi < 196^\circ$	7.25	2×0.0049	2
PMD	$2.3 < \eta < 3.7$	3.64	2.59	2 221 184
FMD disc 1	$3.62 < \eta < 5.03$	inner: 3.2		
FMD disc 2	$1.7 < \eta < 3.68$	inner: 0.834 outer: 0.752	0.266	51 200
FMD disc 3	$-3.4 < \eta < -1.7$	inner:-0.628 outer:-0752		
V0A	$2.8 < \eta < 5.1$	3.4	0.548	32
V0C	$-1.7 < \eta < -3.7$	-0.897	0.315	32
T0A	$4.61 < \eta < 4.92$	3.75	0.0038	12
T0C	$-3.28 < \eta < -2.97$	-0.727	0.0038	12

Figure 2.12: Summary of the ALICE detector subsystems. The acceptance in η is calculated from the nominal IP. The position is the approximate distance from the interaction point to the face of the detector, corresponding to the radius for the barrel detectors or to the position along the beam for the others. The dimension corresponds to the total area covered by the active detector elements. Channels refers to the total number of independent electronic readout channels. In case a detector is subdivided into subdetectors, the numbers refer to the individual components.

The magnets

The ALICE experiment includes a solenoid magnet previously used in L3 experiment of LEP, and a dipole magnet situated next to the solenoid one, as a part of the forward muon spectrometer. The value of the uniform field provided by the solenoid magnet is variable up to 0.5 T which is a compromise between the momentum resolution, the acceptance al low p_t, and the efficiency in the track reconstruction. The dipole magnet is placed 7 m from the interaction vertex at 10 cm distance from the solenoid. The field produced by the dipole magnet is perpendicular to the beam direction with a nominal value of $B \sim 0.2$ T.

The Inner Tracking System

The ITS [40] is the barrel detector closest to the beam pipe. Its main goals are: to reconstruct the primary vertex and the secondary vertices from the decays of hyperons and D and B mesons, to track and identify particles with momentum below 200 MeV/c via dE/dx measurements, to improve the momentum and angular resolution for tracks reconstructed by the TPC, and to reconstruct tracks traversing dead TPC regions. The ITS surrounds the beam pipe (which is a 800 μm thick cylinder with an outer diameter of 6 cm) and consists of six cylindrical layers of silicon detectors located at radii between 4 cm and 43 cm. Due to the high track density, the two innermost layers are Silicon Pixel Detectors (SPD) which guarantee a high granularity. They are followed by two layers of Silicon Drift Detectors (SDD), while the two outmost layers are double-sided Silicon micro-Strip Detectors (SSD). The four outer layers have analogue readout and therefore can be used for particle identification via dE/dx measurement in the non-relativistic region ($dE/dx \sim 1/\beta^2$).

Since the momentum and impact parameter resolution for low-momentum particles are dominated by multiple scattering effects, the amount of material in the active volume has been kept to a minimum. The granularity of the detector was optimized to keep the occupancy low in all the layers. With the technology chosen, the ITS detectors reach a spatial resolution of the order of few tens of μm [3] resulting in a resolution on the impact-parameter better than 70 μm in the $r\phi$ plane for $p_t > 1$ GeV/c well suited for the reconstruction of heavy-flavour decays (see Fig. 2.13).

In Fig. 2.14 the resolution of the primary vertex reconstructed with global

[3] $r\phi$ spatial precision: SPD=12 μm, SDD=35 μm, SSD=20 μm; z spatial precision: SPD=100 μm, SDD=25 μm, SSD=830 μm

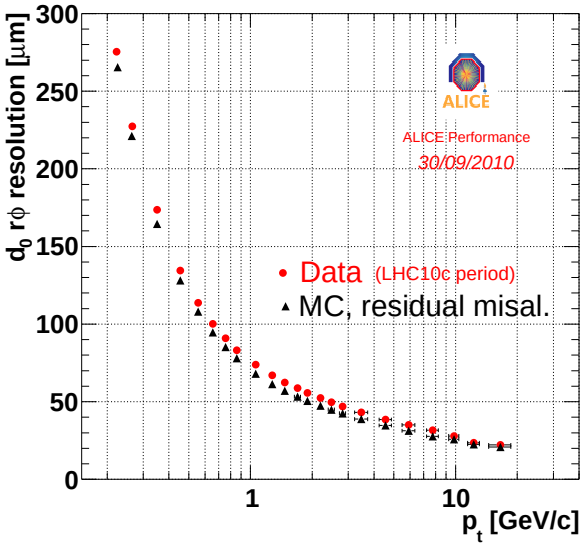

Figure 2.13: Transverse impact parameter resolution for pp collisions at $\sqrt{s} = 7\,\text{TeV}$ obtained for tracks well reconstructed in the TPC and having two measured points in the SPD. For each track its impact parameter was estimated with respect to the primary vertex reconstructed without using this track. The resulting impact parameter resolution is the convolution of the track-position and the primary-vertex resolutions. Also the resolution simulated in the Monte Carlo is reported.

tracks and SPD only tracks [4] for pp interactions at $\sqrt{s} = 7\,\text{TeV}$ is shown.

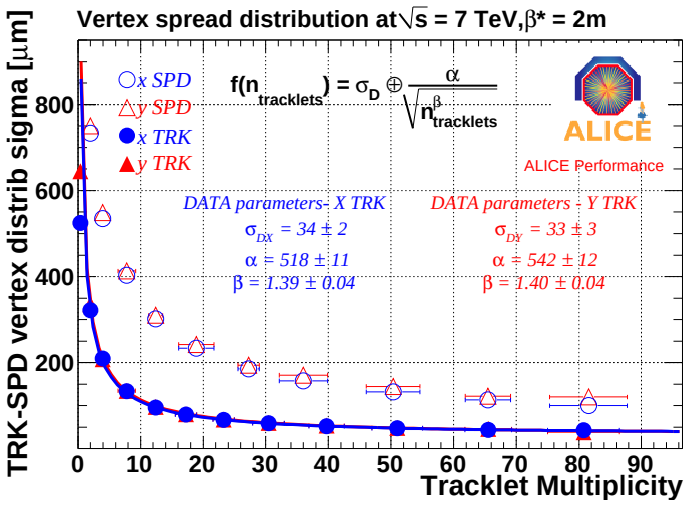

Figure 2.14: Resolution of the primary vertex reconstructed with tracks and SPD only for pp interactions at $\sqrt{s} = 7\,\text{TeV}$.

The Time Projection Chamber

The TPC [41] is the main tracking detector of the central barrel, optimized to provide, together with the other central barrel detectors, charged-particle momentum measurements with good two-track separation, particle identification and vertex determination. A large p_t range is covered from about $p_t \sim 0.1\,\text{GeV/c}$ up to $p_t \sim 100\,\text{GeV/c}$ with good momentum resolution. The TPC was designed for an excellent tracking performance in the high multiplicity environment of PbPb collisions. For this reason, it was chosen to be a drift chamber, cylindrical in shape, 5 m long, with the inner radius ($r_{in} \sim 85\,\text{cm}$) determined by the maximum acceptable track density, and the external one ($r_{ext} \sim 250\,\text{cm}$) by the minimum track length for which dE/dx resolution is $< 10\%$. The TPC volume is filled with $90\,\text{m}^3$ of $Ne/CO_2/N_2$ (90/10/5). The readout planes are divided in 18 sectors in which multiwire proportional chambers (with cathode pad readout) are housed. Because of its good dE/dx resolution, the TPC can identify particles with $p_t < 1\,\text{GeV/c}$. The TPC tracking efficiency is $> 90\%$ for $p_t > 100\,\text{MeV/c}$ where the limiting factor are the interactions in the ITS material. Measuring the deflection in

[4] If all the ITS and TPC information are used the tracks are named "global"; if only the SPD information are used they are named "SPD only".

the magnetic field, the ITS and the TPC are able to determine the momentum of the charged particles with a resolution better than 1% at low p_t and better than 20% for $p_t \sim 100\,\mathrm{GeV/c}$ (see Fig. 2.15).

Due to its huge size, the drift time in the TPC is $\sim 90\,\mu s$; this means that at high interaction rate the pile up effect becomes relevant. Tracks from pile up events can be rejected using the fact that they point to a different primary vertex. Another limiting factor is the long TPC dead time, that keeps down the readout frequency despite the fact that the slowest detector (in terms of readout electronics) is the SDD, with a busy time of 1 ms.

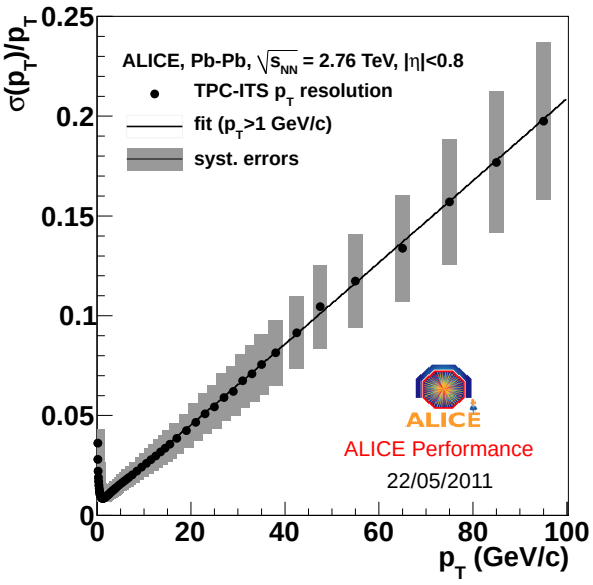

Figure 2.15: Momentum resolution in PbPb interactions at $\sqrt{s_{NN}} = 2.76\,\mathrm{TeV}$.

The Transition Radiation Detector

The other barrel detectors (TRD, TOF, HMPID, PHOS) are mainly dedicated to particle identification at higher momenta.

The main purpose of the TRD [42] is to provide electron identification with $p_t > 1\,\mathrm{GeV/c}$ (below this threshold electrons can be identified with the dE/dx method in the TPC). Above $1\,\mathrm{GeV/c}$, the transition radiation from electrons passing a radiator can be exploited in concert with the specific energy loss in a suitable gas mixture to obtain the necessary pion rejection capability. Using also the information from the ITS and the TPC, it is possible to study the production of vector meson resonances (like $J/\psi, \Upsilon, \Upsilon', \ldots$)

through their lepton decay channel e^+e^-. The TRD is segmented along the azimuthal angle in 18 sectors. Each sector contains 30 modules arranged in five stacks along z and six layers in radius. Each detector element consists of a radiator of 4.8 cm thickness, a drift section of 30 mm thickness and a multiwire proportional chamber with pad readout. At present 10 TRD modules are installed.

The Time Of Flight

The main target of the Time of Flight (TOF) detector [39][43][50] is charged particle identification. This detector was designed to identify pions and kaons up to 2.5 GeV/c and protons up to 4 GeV/c in the central pseudorapidity region ($|\eta| \leq 0.9$) and with full azimuthal coverage. To achieve this, a total time resolution better than 100 ps is needed. For this reason the TOF detector is based on Multi-gap Resistive Plate Chamber (MRPCs) [51]. These detectors have an intrinsic time resolution better than 50 ps (from test beam studies) dominated by the jitter in the electronics and the time resolution of the TDCs [52] [53]. The MRPC efficiency was measured to be close to 100%.

The TOF is made of 1638 MRPCs located in 90 gas-tight modules distributed over 18 azimuthal sectors (Super Modules-SMs). Since each MRPC is composed of 96 readout pads, the TOF detector consists of 152928 readout channels[5] ($2.5 \times 3.5\,\mathrm{cm}^2$ each) covering a total area of 141 m^2. Thanks to this highly segmented structure, the TOF occupancy can be kept low while the performance remains good also in a high multiplicity environment (like the one in PbPb collisions).

The information provided by TOF is the time that takes to a particle to travel from the interaction vertex to the TOF sensible layer. Together with the momentum information, the TOF time is used to identify particles. A more detailed description of the TOF detector will be given in \$2.3.

The High Momentum PID

The HMPID [44] is dedicated to the identification of charged hadrons at $p_t > 1$ GeV/c, extending the momentum range over which ALICE can perform PID. The HMPID was designed as a single-arm array with a geometrical acceptance of 5% of the central barrel and is based on proximity-focusing Ring Imaging Cherenkov (RICH) counters. It consists of seven modules of about $1.5 \times 1.5\,\mathrm{m}^2$ size each. The radiator, which defines the momentum range covered by the HMPID, is a 15 mm thick layer of low chromaticity C_6F_{14}

[5] 3 SMs have been installed without the central module in order to reduce the amount of material in front of the high resolution electromagnetic calorimeter (PHOS).

liquid with a refraction index $n = 1.2989$ at $\lambda = 175\,\text{nm}$, corresponding to $\beta_{min} = 0.77$ (i.e. a momentum threshold $p_{th} = 1.21m$, where m is the particle mass). Cherenkov photons emitted by a fast charged particle traversing the radiator are detected by a photon counter with a thin layer of CsI deposited onto the pad cathode of a MultiWire Pad Chamber (MWPC).

The PHOton Spectrometer

The PHOS [45] is a high-resolution electromagnetic spectrometer covering a limited acceptance ($|\eta| < 0.12$ and $\Delta\phi = 100°$) at central rapidity. The PHOS main physics objectives are the test of thermal and dynamical properties of the initial phase of the collision, that can be extracted from low p_t direct photon measurements, and the study of the jet quenching effect through the measurement of high-p_t π^0 and γ-jet correlations. Due to the high multiplicity in nuclear collisions, the calorimeter has to be dense, highly segmented, with small Moliere radius, and located at a large distance from the interaction point, in order to keep the occupancy at a reasonable level. Direct photons are discriminated against decay photons either through shower shape analysis at high p_t, or through invariant mass analysis at low p_t. A high energy resolution and granularity is obtained by using dense scintillator crystals ($PbWO_4$) of 20 X_0 with high photo-electron yield. A high spatial resolution is achieved by choosing the dimension of the individual detection cell of the order of the Moliere radius of the scintillator. The good timing resolution of about 2 ns is achieved by using a fast scintillator and preamplifier. The PHOS is divided into five independent modules positioned on the bottom of the ALICE setup at a distance of 460 cm from the interaction point.

The ElectroMagnetic CALorimeter

The ALICE EMCAL [46] is a large Pb-scintillator sampling calorimeter with longitudinal wavelength-shifting fibers readout via avalanche photo diodes with cylindrical geometry. It is located adjacent to the ALICE magnet coil at a radius of 4.5 m from the beam line. The EMCAL covers the pseudorapidity range $|\eta| \leq 0.7$, with a polar angle coverage of $\Delta\phi = 107°$ and is positioned approximately opposite in azimuth to the PHOS detector. It enhances the ALICE capabilities of measuring jet properties.

The Forward Muon spectrometer

The main interest of the muon spectrometer [47] is the detection of muons in the pseudo-rapidity region $-4.0 < \eta < -2.5$. With this detector the complete

spectrum of heavy-quark vector-mesons resonances (like $J/\psi, \psi', \Upsilon, \Upsilon', \Upsilon''$) as well as the ϕ meson can be measured in the $\mu^+\mu^-$ decay channel. The simultaneous measurement of all the quarkonia species with the same apparatus allows a direct comparison of their production rate as a function of different parameters such as the collision centrality and the transverse momentum. In addition to vector mesons, the unlike-sign dimuon continuum up to masses around $10\,\mathrm{GeV/c^2}$ can be measured. Since at the LHC energies the continuum is expected to be dominated by muons from the semi-leptonic decays of open charm and open beauty, this channel will allow to study the production of heavy flavours. This study is motivated by the QCD prediction of a reduction of the production of resonances with heavy quarks.

The spectrometer consists of the following components: a passive front absorber to absorb hadrons and photons from the interaction vertex; a high granularity tracking system of 10 detection planes; a large dipole magnet; a passive muon filter wall followed by four planes of trigger chambers; an inner beam shield to protect the chambers from primary and secondary particles produced at high rapidity. Besides, the muon spectrometer is provided with a cone shaped absorber made of carbon, covered by a thin layer of tungsten with a length of 3.5 m and placed at a distance of 0.9 mm from the collision point. Another absorber with a conical geometry and a length of 18.1 m and an angle of 2° made of a high Z material is present to screen the detector from particles produced in the interactions at high pseudorapidity. Moreover, a dipole magnet which produce a field of $3\,\mathrm{T}\cdot\mathrm{m}$ and an iron absorber are part of the spectrometer. The "active" detector consists of 4 plates which make up the muon triggering system. They use RPC chambers working in the streamer regime, whose aim is to select events with a $\mu^+\mu^-$ pair at high p_t. In addition to the trigger chambers, the muon spectrometer has 10 tracking chambers characterized by a high granularity, and with a spatial resolution of $100\,\mu$m. Four chambers are placed in front of, two inside and four after the dipole magnet.

Forward detectors

A number of small and specialized detector systems are used for triggering or to measure global event characteristics.

- The ZDC [48] detects spectator nucleons (and consequently measures the impact parameter and the collision centrality) by measuring the energy in the forward direction. It can also give an estimate of the reaction plane in nuclear collisions. Two sets of hadronic ZDCs are located at 116 m on either side of the IP. In addition, two small electromagnetic

calorimeters (ZEM) are placed at 7 m from the IP on both sides of the LHC beam pipe opposite to the muon arm. Spectator protons are spatially separated from neutrons by the magnetic elements of the LHC beam line. Therefore each ZDC set is made up of two distinct detectors: one for neutrons (ZN) placed between the beam pipe at 0° relative to the LHC axis and one for protons (ZP) placed externally with respect to the beam pipe. The ZDCs are quartz fiber sampling calorimeters with a very dense passive material. Since in Ultra Peripheral Collisions (UPC) the fragments (spectators) stay in the beam pipe, the ZDCs collect a small amount of energy both for central and UP events. To distinguish the two classes of events the ZEMs are used: as a matter of fact, by measuring the energy of the particles emitted at forward rapidity that increases with the collision centrality, they can discriminate events with different centralities.

- The PMD [49] measures the multiplicity and spatial distribution of photons in the region $2.3 < \eta < 3.7$. It consists of two planes of gas proportional counters preceeded by two lead converter plates.

- The FMD provides charged-particle multiplicity information in the pseudorapidity range $-3.4 < \eta < -1.7$ and $1.7 < \eta < 5.0$, extending the pseudorapidity region where the SPD is able to provide multiplicity information. Charged particles are counted in rings of silicon strip detectors located at three different positions along the beam pipe. FMD3 and FMD2 are located on either side of the ITS detector (at about 75 cm from the IP) while FMD1 is placed at 320 cm from the IP on the opposite side with respect to the muon spectrometer.

- The V0 is a small angle detector consisting of two arrays of scintillator counters, called V0A and V0C, located at 340 cm from the IP on the side opposite to the muon spectrometer (V0A) and 90 cm from the IP (V0C) on the other side. Each one is segmented into 32 individual counters distributed in four rings. It provides minimum bias trigger for the central barrel detectors. This trigger is given by particles originating from primary collisions and from secondary interactions in the vacuum chamber elements. Thanks to the dependence between the number of registered particles and the number of emitted particles, the V0 can provide information on the multiplicity of the event.

- The T0 is able to provide the start time of the event for the TOF that corresponds to the real time of the interaction and the vertex position. It consists of two arrays of cherenkov counters, 12 counters per array.

The T0C is placed at -72.7 cm from the IP ($-3.28 < \eta < -2.97$) and T0A at 375 cm from the IP on the opposite side ($4.61 < \eta < 4.92$).

2.3 The TOF detector

In this section a detailed description of the structure and performance of the TOF detector will be given [39][43][50]. Since the TOF detector is able to identify charged hadrons in the range $0.5 < p_t < 4.0\,\mathrm{GeV/c}$ (where most of particles are produced), in the central pseudorapidity range ($|\eta| \leq 0.9$) and with a full azimuthal coverage, the TOF performance is of great importance for the ALICE experiment.

2.3.1 RPC and MRPC

To reach the design PID performance (i.e. identify pions and kaons up to 2.5 GeV/c and protons up to 4 GeV/c), the total TOF time resolution should not be worse than 100 ps. Such resolution could be obtained using scintillators coupled with photomultipliers, a solution which would be too expensive for the ALICE TOF detector with its 141 m^2 active surface. To have a good compromise between costs and performance the TOF detector has been realized as a gaseous detector based on Multi-gap Resistive Plate Chambers (MRPCs).

Resistive Plate Chambers are ionization chambers whose parallel plates (the anode and cathod) produce an uniform electric field inside the whole sensible volume. When a charged particle goes through this volume, it produces a primary ionization that, if the field is strong enough, gives rise to an avalanche process. The signals read by the pick-up electrodes (pads) on the anode and the cathode plates are produced by the motion in the electric field of the electron-ion pairs created in the avalanche process.

The advantages of the parallel plate configuration with respect to a traditional wire chamber with a radial electric field is that the drift effect on electrons disappears: since the field is uniform, the electrons do not have to travel before to reach a volume where the field is strong enough to produce an avalanche. This means that we don't have any time uncertainty related to the point where the primary ionization is produced. This point determines only the amount of charges produced, and so it is strongly related to the efficiency. The only condition to generate a signal is that the avalanche has traveled enough to produce a signal over the detectable threshold. This length has no influence on the time resolution of the measurement but only on the time t_0 elapsed between the crossing of the particle and the arrival of the signal.

The uncertainty related to the signal formation has two components: on one side the fluctuation of the number of primary pairs, which has a poissonian distribution dependent only on the gas type and not on the electric field, and which has an influence only on the detector efficiency. On the other side there is the fluctuation on the development of the avalanche, which influences the time resolution. The detector intrinsic time resolution is, in fact, due to the fluctuation of the time necessary to create (in the avalanche) a sufficient number of electrons to produce a signal over threshold. This time resolution can be estimated in the following way:

$$\sigma_t \sim \frac{1}{(\alpha - \eta) v_D}, \tag{2.3}$$

in which α is the Townsend coefficient, η is the attachment coefficient and v_D is the electron drift velocity. All this parameters are related to the type of gas and to the strength of the electric field.

Despite their good performance, traditional RPCs are not satisfactory for the ALICE TOF detector. As already said, they are made of two parallel plane electrodes of high resistivity material mainteined at a defined ddp (to have a uniform electric field), between which there is a gas at atmospheric pressure. Since the two electrodes have high resistivity (to prevent the formation of a spark inside the detector), the applied potential can be high enough to work in the streamer region so the RPCs have an efficiency close to 100%. Despite all that, they can not be used for the ALICE TOF detector since, in case of a high rate as expected in PbPb collisions at the LHC, the efficiency and the time resolution would decrease due to the pile up of the charges induced on the resistive planes which reduces the electric field inside the gap.

The problem could be avoided decreasing the resistivity of the plate; in this way the induced charges would be dissipated faster but the efficiency would be lower since the signal would extend over a larger number of readout channels. Another solution could be to reduce the amount of charges produced by working in the avalanche region (instead of in the streamer one), making the gap thinner or the electric field lower. The disadvantages of such choice would be that in the first case the efficiency would decrease, since the first ionization process depends on the quantity of crossed gas, while in the second case the time resolution would worsen according to eq. 2.3.

To be able to work at high rate keeping the performance high in terms of both efficiency and time resolution, the MRPCs (Multi-gap Resistive Plate Chamber) have been developed. In the MRPCs, since the gap is smaller (as explained later in detail), the time uncertainty related to the point where the avalanche starts is reduced. Since the smaller the gap, the smaller the

probability for pair production, the use of high density gas is required. At the same time the presence of a large number of gaps is needed to increase the efficiency. A schematic comparison between RPC and MRPC is shown in Fig. 2.16.

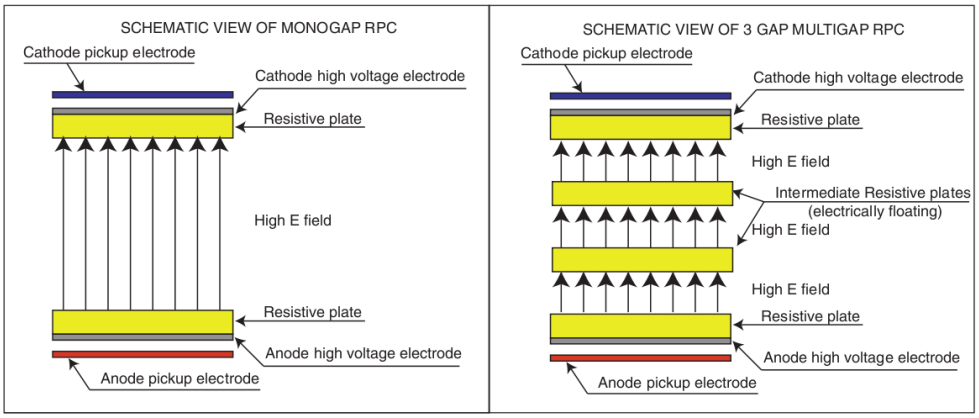

Figure 2.16: Schematic comparison between RPC (left) and MRPC (right).

MRPCs are RPCs whose gas volume has been divided in several identical gas gaps with equal width between resistive plates parallel and identical to the external ones. The voltage is applied by a resistive layer only to the external surface of the external plates; all the internal plates are electrically floating but their voltage is self-regulating. Pickup electrodes are located outside the stack and insulated from the high voltage electrodes. Signals on the pickup electrodes are induced by the movement of electrons towards the anode[6]. Since these resistive plates act as dielectrics, induced signals can be caused by the movement of charges in any of the gas gaps between the anode and cathode pickup electrodes, so that the observed induced signal is the sum of the charge movement in any of the gaps in the multigap RPC. In this way the active volume of the detector is the sum of the volume of every gap and it is possible to reach the RPC efficiency (100%) just increasing the number of gaps.

In this configuration, the MRPCs can work in the proportional region even if the ddp (and the produced electric field) is very high since the avalanche and the collected charge are limited by the small width of the gaps. The high electric field, and the consequent high drift velocity, allows to reach very good

[6]The electrons produced by the avalanche induce a fast signal as they move towards the anode. A much slower signal is produced by the positive ions as they drift towards the cathode.

time resolution, while the possibility of working in the proportional region (where there are less induced charges than in the streamer region) allows working at high rate.

Another advantage of the MRPCs compared to RPCs is that the amount of charge produced depends less on the applied voltage (see Fig. 2.17). As a results, the system is more stable and the risk of reaching the streamer region is smaller. This is due to the space charge that affects the growth of the gas avalanche decreasing the gain.

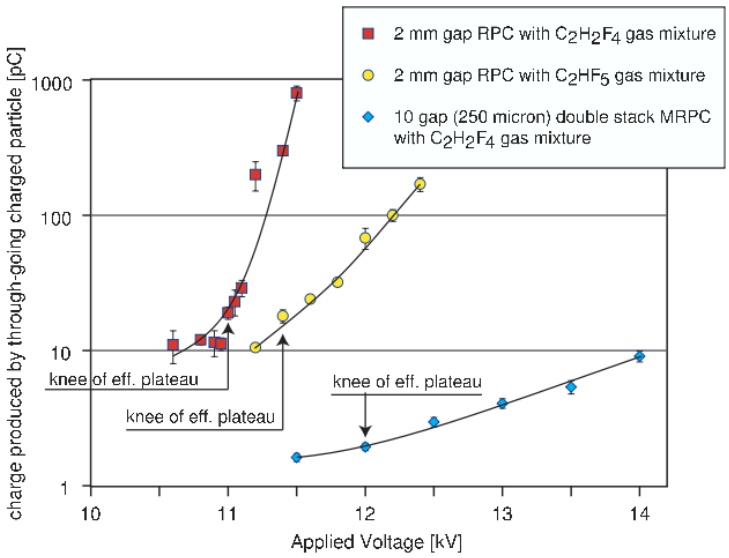

Figure 2.17: Total charge versus applied voltage for 2mm RPC and a TOF MRPC.

If we look at a signal produced by a TOF MRPC, it is clear that the slow voltage ramp due to the movement of positive ions towards the cathode is non-linear (the linear behavior is expected if the avalanche grows exponentially as defined by Townsend). This is because as the avalanche grows, the electrons at the head of the avalanche experience a reduced electric field due to the charge of the positive ions in the tail of the avalanche. Therefore the gas gain is reduced and the avalanche deviates from the exponential growth. The centre of gravity of the production of the electrons moves away from the anode so the ratio of fast charge versus the total charge grows.

To have an idea of the MRPCs performance, we have to take in account that, roughly, when a particle crosses the detector, it produces a primary ionization in every gap and, in every gap, the avalanche process takes place

according to the Townsend equation $N = N_0 e^{\alpha x}$. Here N_0 is the number of electrons in the initial ionization cluster, $\alpha = 1/\lambda$ is the Townsend coefficient, λ is the average distance between ionizing collisions and x the distance that the avalanche has traveled. The ratio of the fast signal to the total signal (due to the shape of the avalanch) is $1/\alpha D$ for a gap of width D. To work in the proportional region, the electron gain has to be less than 10^8 ($e^{\alpha L} < 10^8$) which corresponds to the value above which a transition to the streamer region happens. If the electric field is $E \sim 100\,\mathrm{kV/cm}$ ($\alpha \sim 100\,\mathrm{mm}^{-1}$), the gap thickness should be $L \sim 10^{-1}$ mm. Since for this electric field the drift velocity is $\sim 100\,\mu$m/ns, the time resolution is ~ 100 ps, corresponding to the ALICE TOF target. If the maximum gain is 10^8, the maximum value of αD is 18 and the ratio of fast to total signal is $1/\alpha D \sim 5\%$.

2.3.2 Properties of the TOF MRPCs

The TOF MRPCs have a double-stack configuration: a central anode plate and two cathode plates with a symmetrical position with respect to it (see Fig. 2.18).

The advantages of the double stack configuration compared to the one with one single cathode and anode, if the number and the width of the gaps are the same, are the following:

- half of the ddp is needed to reach the same electric field;
- the read-out signal is the sum of the signals induced in both stacks so that the amplitude is the same in the two configurations;
- the electrodes are closer so that the border effects between close pads are reduced.

In the TOF detector, the MRPCs are assembled in strips (see Fig. 2.19). Each strip has a total surface of $122 \cdot 13\,\mathrm{cm}^2$ while the active area is of $120 \cdot 7.4\,\mathrm{cm}^2$. The gaps are 5+5 (5 for each stack), each with a width of $250\,\mu$m filled with a gas mixture $C_2F_4H_2(90\%) - C_4H_{10}(5\%) - SF_6(5\%)$. Each stack is delimited by a cathode and an anode Printed Circuit Board (PCB) with 96 readout pads with an area of $3.5 \cdot 2.5\,\mathrm{cm}^2$ arranged in two raws. The gaps are delimited by glasses with a volume resistivity of $\sim 10^{13}\,\Omega$cm; the external glasses of each stack have a thickness of 550 μm and are painted on the external surface with a resistive paint; the inner ones are 400 μm thick. The High Voltage (HV) is applied through electrodes connected to the external surface of the outer glasses. All the internal plates are not connected to the HV and are electrically floating. The gap width is kept fixed by a fishing line

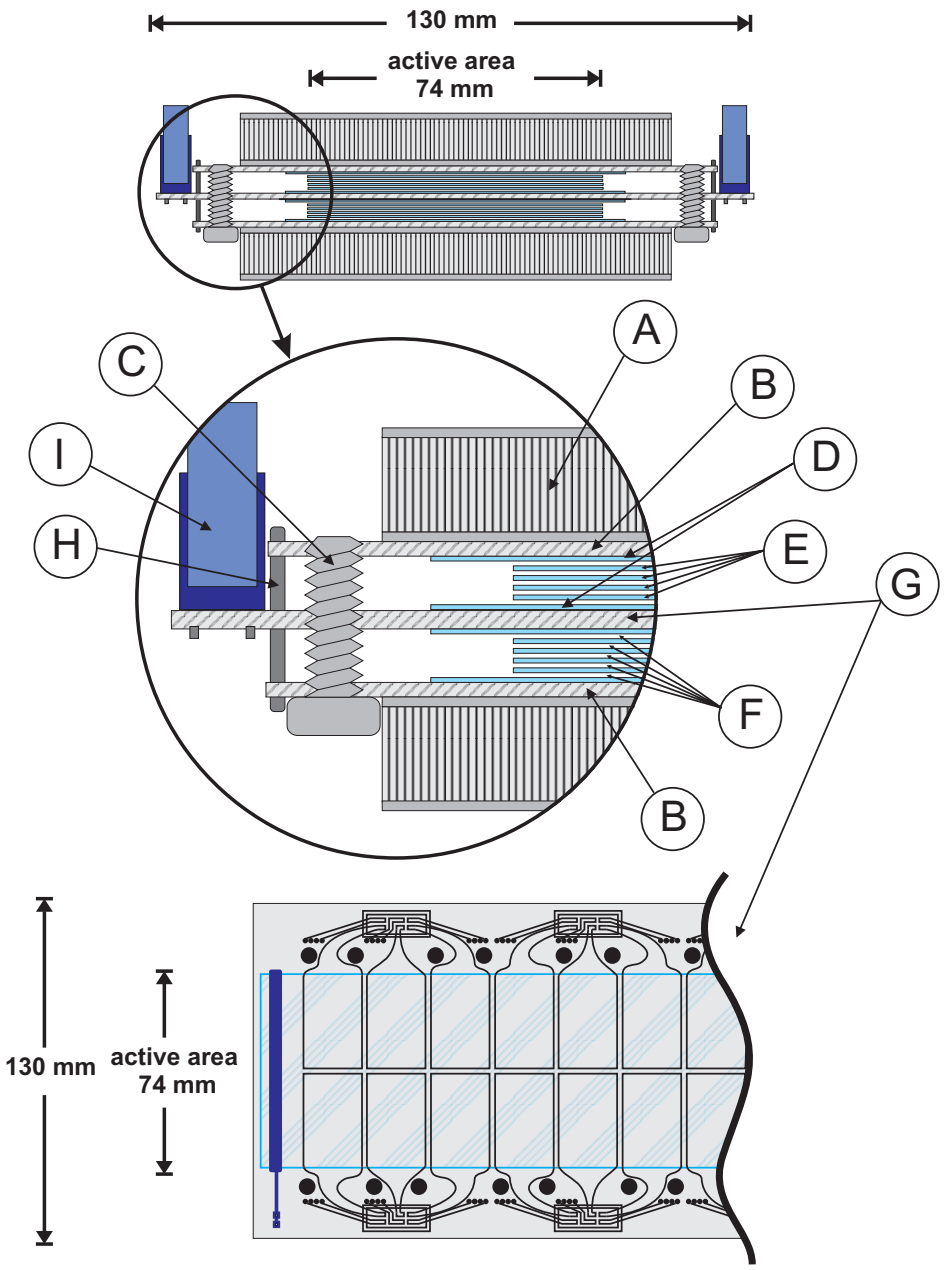

Figure 2.18: Schematic diagram of a double-stack MRPC. (A) honeycomb panel to guarantee good mechanical rigidity; (B) Printed Circuit Board (PCB) with the cathode pickup pads; (C) nylon pin to stretch the fishing line; (D) 550 μm glasses with resistive coating used to apply the voltage; (E) 400 μm glasses; (F) 250 μm gaps; (G) central PCB with the anode pickup pads; (H) metallic pin soldered to cathode and anode PCB; (I) 16 pin connector. On the bottom, layout of the readout pads.

stretched from pin to pin. Signals from the pads are brought to 36 16-pin connectors mounted on the anode PCB [54].

Figure 2.19: MRPCs production at Bologna-INFN laboratories.

2.3.3 Performance of the TOF MRPCs

The MRPCs performance was tested with test beam at CERN [56] [57]. In Fig. 2.20 the results obtained with the final readout chain are shown. Starting from 13.0 kV, the TOF MRPCs have an intrinsic time resolution better than 50 ps (including the contribution of the readout electronics, estimated to be $\sim$ 30 ps) and an efficiency close to 100%. All the tested MRPCs showed a very good uniformity and a long streamer-free plateau. In Fig. 2.21 the efficiency and time resolution distributions for 159 readout pads at a fixed applied voltage of 13 kV are shown.

The response of the detector to high rate and high radiation dose was tested at the Gamma Irradiation Facility (GIF) at CERN. Measurements have shown no degradation of the results up to about 1 kHz/cm^2 and for a radiation dose greater than 3.5 times the dose foreseen in the first 10 years of the LHC operation.

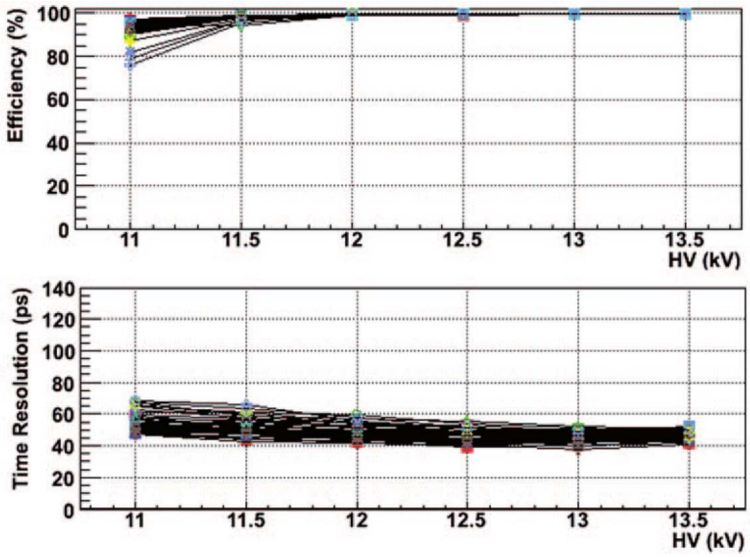

Figure 2.20: Efficiency (top) and time resolution (bottom) as a function of the applied voltage for 55 readout pads randomly distributed on 10 MRPCs.

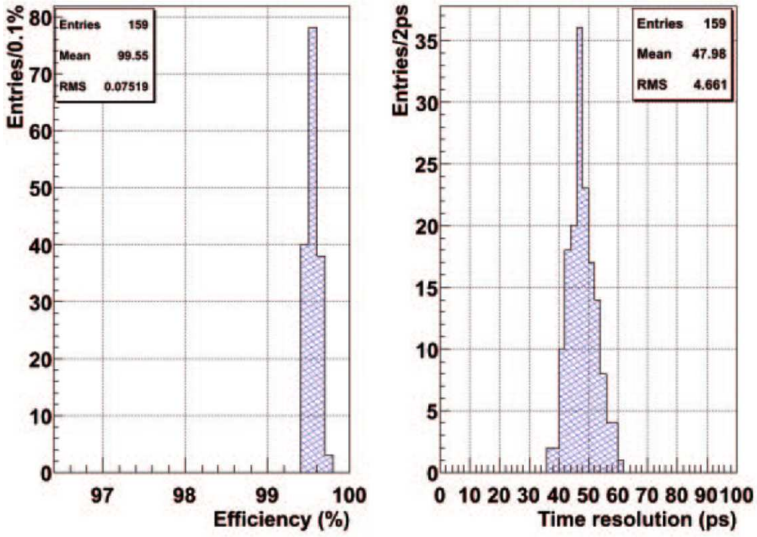

Figure 2.21: Efficiency (left) and time resolution (right) distributions for 159 readout pads working at a fixed applied voltage of 13 kV.

2.3.4 The TOF SuperModules

The TOF has a modular structure. In the azimuthal angle ϕ, the detector is segmented in 18 sectors, the so-called SuperModules (SMs), that are supported by a cylindrical shell (space-frame), with an internal radius of 370 cm and an external radius of 399 cm (see Fig. 2.22).

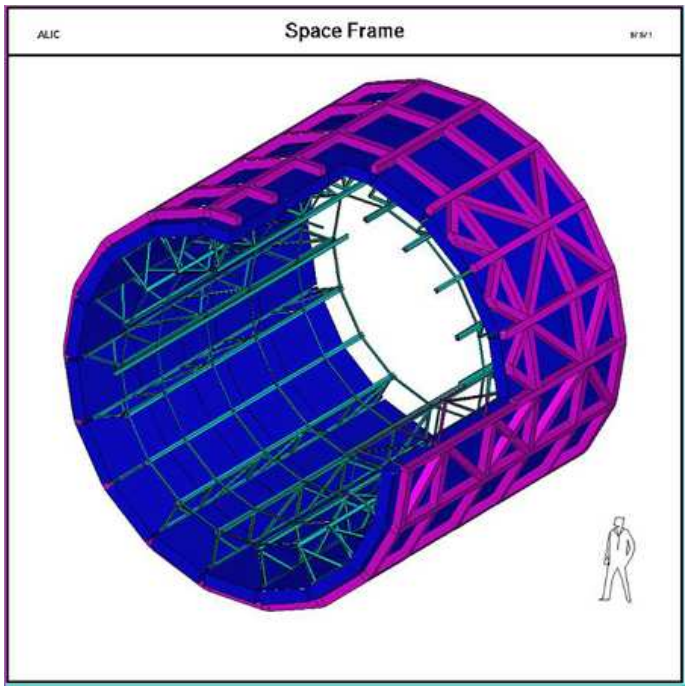

Figure 2.22: Space frame, the cylindrical structure that supports the SMs.

Each SM (see Fig. 2.23), with a total length of 927 cm and a weight of 1.45 metric tons, consists of 5 gas-tight modules placed along the beam axis, and two custom VME crates containing the readout electronics at both ends (see Fig. 2.24).

All the modules have the same width (128 cm) but an increasing length going from the centre to the end of the SM. The two external and two intermediate modules contain 19 strips each, while the central one includes 15 strips, for a total of 91 MRPCs per SM. Since each strip has 96 readout pads, the TOF has 152928 readout channels[7] covering a total area of 141 m^2. Each module can be considered as divided in two volumes, one containing gas and MRPCs and one containing the front-end electronics (FEA).

[7] 3 SMs have been installed without the central module in order to reduce the amount of material in front of the high resolution electromagnetic calorimeter (PHOS).

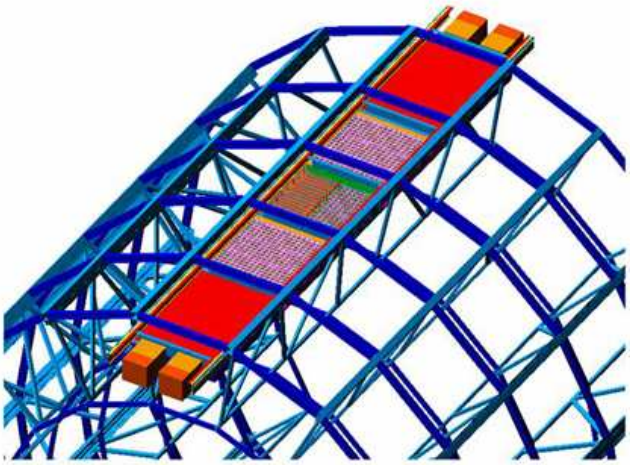

Figure 2.23: One SM inserted in the space-frame. We can see the 5 modules in which the SM is segmented and the two custom VME crates which contain the read-out electronics placed at both ends of the SM.

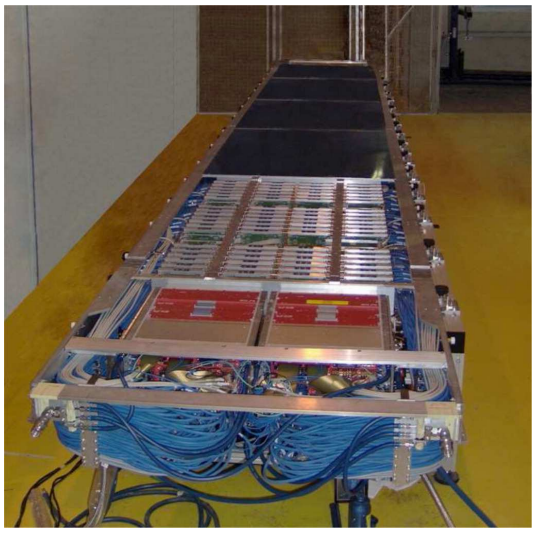

Figure 2.24: A TOF SM after the assembly of the 5 modules. Two of the four crates are visible (the other two are on the opposite side). These crates house the readout and control electronics. The top aluminium covers enclose completely the front-end electronics placed on the modules.

In Fig. 2.25 the section of a central module is reported. We can see the peculiar positioning of the strips: perpendicular to the beam direction, they are tilted so to be perpendicular to the trajectory of a particle coming from the interaction point. This aims at minimizing the number of particles that cross the detector with an oblique direction, and at reducing the occupancy and the time resolution (see also Fig. 2.26).

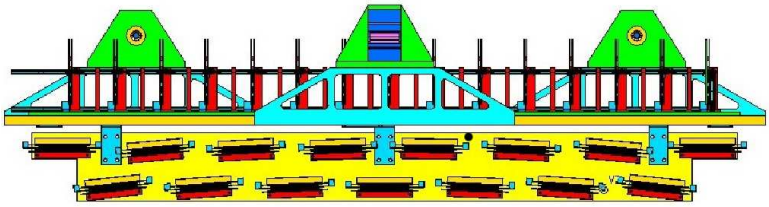

Figure 2.25: Position of the strips inside a module (a central module is reported here). The MRPCs are tilted to be, on average, perpendicular to the flight direction of the particles produced at the interaction point.

To avoid dead zones, the active zone of two adjacent strips overlaps by 2 mm. Besides, the modules are built in such a way to reduce the dead zone along the length of the SM at the boundaries between modules (see Fig. 2.27).

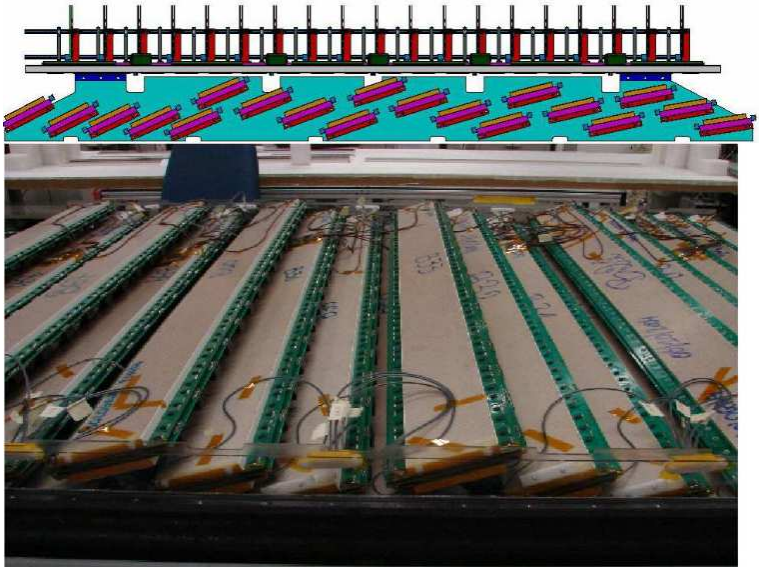

Figure 2.26: Scheme and picture of the tilted geometry for TOF MRPC strip, in an intermediate module.

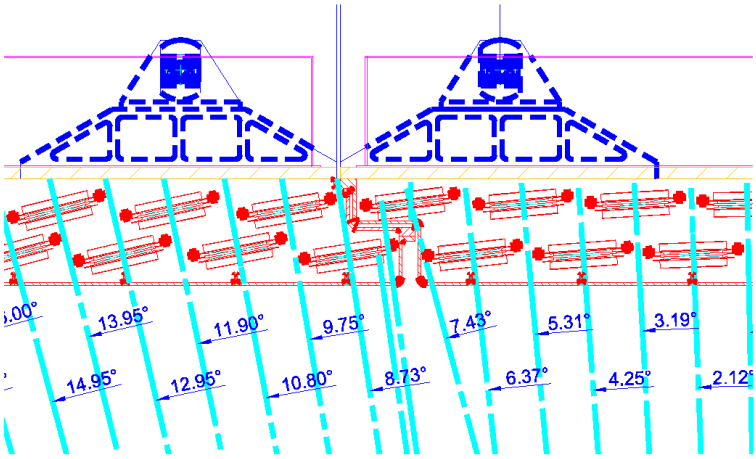

Figure 2.27: Detail of the shape of two adjacent modules, the central one and the intermediate one.

2.3.5 TOF Data Acquisition

The schematic layout of the TOF electronics is shown in Fig. 2.28.

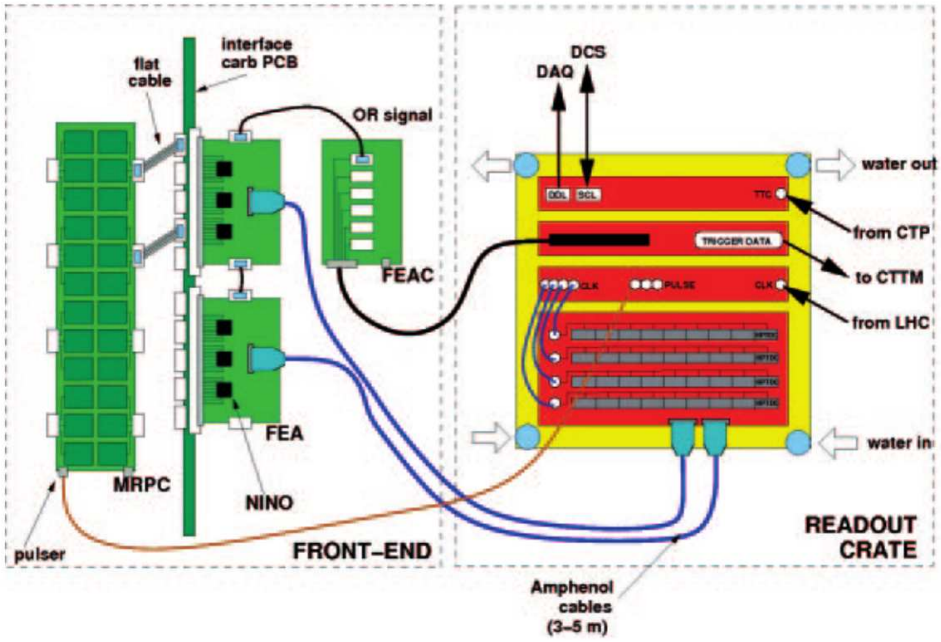

Figure 2.28: Schematic layout of the TOF electronics.

The MRPC differential signals are sent to the Front-End Analogue (FEA) cards which contain three ASICs (NINO) that are 8-channel amplifier/ discriminator devices with an output width correlated to the charge of the input signal, and with a minimum output width of 6 ns. Measuring this width allows the correction for time slewing.[8] Each strip is directly connected to four FEAs. The FEAs then send the signals to the High-Performance Time-to-Digital Converter (HPTDC) for digitization. The FEAs also provide a 24-channel OR signal for trigger purposes which is first collected in the FEAC (FEA control card) and then elaborated in the LTM. Data from the LTM are sent to the CTTM for further trigger processing. The FEAC, which serves a group of 10 or 12 FEAs (see Fig. 2.29), provides the low voltage (2.5 V) to power on the FEAs, monitors their temperature, sets the threshold voltages on the discriminator (sent by the LTM) and, as already said, collects the OR signal.

[8]The NINO ASICS encodes the charge of the input signal into the width of the output signal (Time-Over-Threshold).

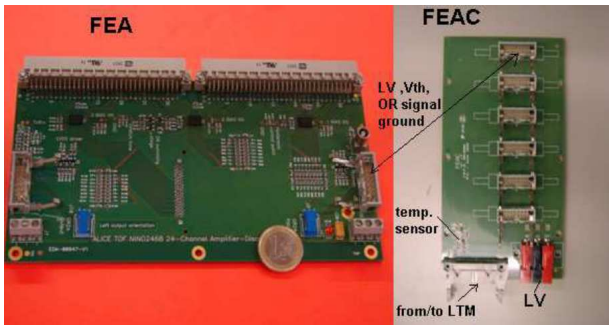

Figure 2.29: FEA and the FEAC service card.

The readout modules are placed in crates mounted at both ends of a SM (four crates per SM). Each crate contains DC-DC converters receiving 48 V from power supplies placed outside the magnet and providing the necessary voltage both to the FEAs and the readout modules. Each crate contains also a VME bus with 12 slots filled in the following way:

- 9 or 10 TDC Readout Modules (TRMs) that read time information digitized by the HPTDC housed in them. Each TRM hosts 10 piggy backs each with 3 HPTDC that can read 8 channels; as a consequence, each TRM hosts 30 HPTDCs that read 240 channels;
- a Data Readout Module (DRM) that receives trigger information from the Central Trigger Processor (CTP) and propagates it to the TRMs and the HPTDCs. Then it performs the readout of the data available in the boards and sends them to the central Data AcQuisition (DAQ) system. Moreover it interfaces with the Detector Control System (DCS) for electronic configuration and monitoring. To sum up, the DRM acts as the main interface between the central ALICE data acquisition/trigger system and the TOF electronics;
- a Local Trigger Module (LTM) to collect the FEA ORs, elaborate a local trigger and sent it to the Cosmic and Topology Trigger Module (CTTM). Moreover, it defines the thresholds and monitors the low voltages and temperatures of the FEAs;
- a Clock/Pulser Distribution Module (CPDM) to distribute the LHC clock signal to the other modules in the crate and to send the pulser signals to the MRPCs for calibration and monitoring purposes.

The readout system is completed by the CTTM which provides the TOF trigger to the ALICE CTP and by the pulse/busy distributor (ACM). Both

the CTTM and the ACM are placed outside the ALICE magnet. (busy signals from the DRMs are elaborated to generate the global bust signal to the CTP).

The DRM

The readout of the data stored in the TRM and LTM cards installed in each crate is done via the DRM (Data Readout Module). The DRM interfaces to the central ALICE DAQ system using the ALICE Detector Data Link (DDL). Several DDLs are collected into the LDCs (Local Data Collectors) of the central DAQ. The current number of DDLs per LDC has been set to 6, limiting the output rate to 5.7 KHz. Anyway this value is much higher than the current limitations imposed by other ALICE detectors such as the TPC. The DRM card is also equipped with an additional optical link to a commercial PC which provides extra Slow Control functionalities. In total, the 72 TOF crates are connected to 18 commercial PCs. Each DRM is also connected to an Auxiliary Control Module (ACM) that supplies the busy signal to the whole TOF detector (the busy signal inhibits further triggers from being generated by the ALICE central trigger processor during readout).

The LTMs

The LTM is an interface between the front-end electronics and the CTTM. Each LTM is connected to 8 FEACs of which it monitors the low voltages and temperatures. The LTM is also meant to provide the voltage thresholds to the FEAs. Each FEA recives, amplifies and discriminates the signals coming from 24 pads and produces an OR signal of these 24 channels. The ORs of two contiguous FEAs are chained and sent to the FEAC. The FEAC receives six ORs and sends them to the LTM. As a results each LTM gets 48 input signals. The architecture of the LTM allows to choose the trigger segmentation at software level with high flexibility. Data from the 72 LTMs are then sent to the CTTM which receives 3456 input signals.

In Tab. 2.2 the numbers, per SM and for the whole detector, of the TOF relevant electronic devices are reported.

Device	Quantity/SM	Total quantity
NINO	1092	19656
FEA	364	6552
FEAC	32	576
HPTDC	1140	20520
TRM	38	684
Custom crate	4	72
DRM	4	72
LTM	4	72
CPDM	2	36
ACM		5
CTTM		1

Table 2.2: Relevant TOF electronic devices. The amount installed on a SM and the total amount for the whole detector are quoted.

Chapter 3

Simulation, Reconstruction, Calibration and Alignment

The aim of the ALICE experiment is the study of PbPb collisions to verify the formation of a new phase of matter, the QGP. However it studies also pp collisions as a reference for the PbPb ones, to tune Monte Carlo simulations and to study the physics of these collisions in itself like the other LHC experiments (ATLAS, CMS, LHCb) do. This is a challenge not only for the hardware, but also for the software that has to be able to reconstruct events with high precision and to efficiently analyse the data for physics studies. For these purposes the ALICE offline software framework, AliRoot [60], has been developed. Being written in C++, its implementation is Object-Oriented. Besides, it is based on the ROOT [61] framework which provides common tools for the analysis of the high energy physics data. Another important feature of the AliRoot software is the possibility to interface with AliEn, the grid framework implemented by the ALICE collaboration[1].

AliRoot is used in all the offline processes like simulation, alignment, calibration, reconstruction, visualization and analysis. Some details related to the ALICE simulation and reconstruction procedures will be given in the first two sections of this chapter while details on TOF calibration and alignment will be reported in the last ones.

3.1 Event simulation

To evaluate the efficiency of the algorithms used to reconstruct and analyze events and to find out which are the physical signals that can be detected, it

[1]Due to the great amount of data that ALICE has to process, distributed computing (grid) is necessary.

is necessary to perform Monte Carlo simulations of the interactions that are espected to occur during a real collision. This includes the particles produced in the collisions, their propagation inside ALICE and the detector response. The problem is that the physical processes at the LHC energy are not completely understood, since the data available so far were obtained at lower energies. Many theoretical models have been developed but they bring to significantly different results (especially for PbPb collisions). At the simulation level this means that not only one Monte Carlo generator exists, but many, each of which is based on a different theoretical model producing different results. For this reason, by comparing real data with the simulations, we can tune the Monte Carlo models so that they are able to reproduce correctly the data.

Another issue in terms of simulations is that the simulation of events with small cross section needs long time and huge computing resources to have a statistics comparable with the real data. To solve these problems a dynamic simulation framework has been developed. It includes the following options:

- interface to several external generators like HIJING [62], DPMJET [63], PYTHIA [64], etc.;
- generation of underlying events, that are signal-free events in which the pseudorapidity[2] (η) and transverse momentum (p_t) distributions and the event multiplicity are external parameters to be set by the user. These events are useful if η and p_t distributions are known a priori or to study the effect of the variation of these parameters;
- production of rare signals through external generators or internal parametrized generators;
- combination of signals produced with different generators (cocktail);
- combination of underlying events and signal events on the primary particle level (cocktail) or on the Digit (signal induced by the particles on the detector) level (merging);
- generation of beam-gas and beam-halo events;

[2]The pseudorapidity is defined as follows:

$$\eta = \frac{1}{2} ln \frac{p + p_L}{p - p_L} = -ln[tg(\frac{\theta}{2})] \tag{3.1}$$

with θ = angle between particle momentum and beam axis and p_L = longitudinal momentum

- modification of the generated particles' momentum to introduce predefined particle correlations (afterburners).

After the particle generation, the simulation framework has to reproduce their propagation inside the detectors, the energy release in the active volumes and the corresponding readout signal. At this stage different events could be merged.

As already said, once the primary particles have been produced, it is necessary to simulate their transport inside ALICE and the detectors' response. This means that the geometry of the ALICE experiment has to be described in great detail and that also the particle decays have to be taken into account. A lot of different transport Monte Carlo packages are available such as GEANT3 [66], GEANT4 [67], FLUKA [68]. To be able to use them in the AliRoot framework, they have been interfaced with the ROOT Virtual Monte Carlo abstract interface. Moreover, their native geometry modellers have been replaced by the geometry modeller provided by ROOT. The simulation of the ALICE detector geometry is performed with any of these three transport codes defining appropriately the simulation configuration file[3].

To give a realistic description of what happens to the particles propagating inside the detectors, ALICE has to be described with great detail not only with respect to the active, sensible volumes, but also to the services, support structures, absorbers, beam pipe, etc. As a consequence, the modular and hierarchical structure typical of ROOT volumes is used for the ALICE simulation. When a geometry is created with ROOT, the first step is the definition of the so-called universe volume inside which all the necessary daughter volumes will be inserted. In ALICE, the top volume is named ALIC. The first strip of SM0 of TOF is an object identified by the path ALIC_1/B077_1/BSEGMO0_1/FTOA_0/FLTA_0/FSTR_1, where each element refers to a node (a volume) contained in the previous one up to the universe volume, ALIC.

In Fig. 3.1 a visualization of the ideal ALICE barrel structure, as described in the geometry file built during simulation, is shown. Going deeper in the hierarchical structure, the volumes inside ALIC_1/B077_1 are shown in Fig. 3.2, the ones inside ALIC_1/B077_1/BSEGMO02_1 in Fig. 3.3 and the ones in ALIC_1/B077_1/BSEGMO0_1/BTOF0_1 in Fig. 3.4. We can notice that adding elements in the path is equivalent to looking at inner volumes.

The last step of the simulation process is the simulation of the interactions

[3]The configuration file is a macro running before the simulation starts. Here, the generators, the classes managing the decays, the Monte Carlo, the magnetic field, the geometry and the fundamental parameters needed for the physical processes simulation are created and configured.

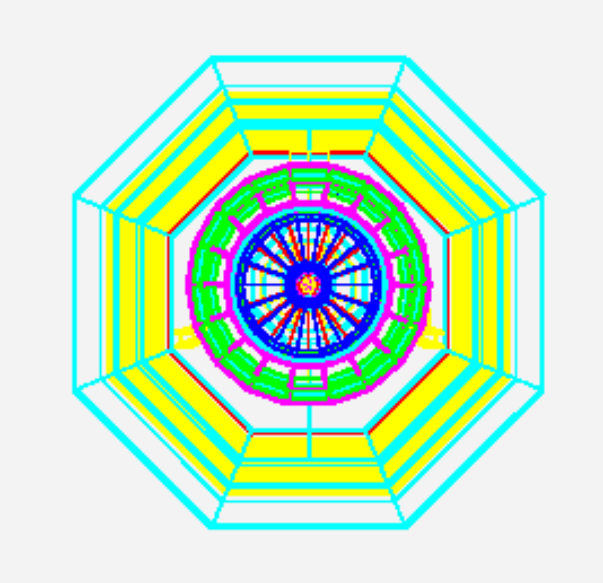

Figure 3.1: Global structure of the barrel of the ALICE experiment in the $r - \phi$ plane as defined during simulation processes. r is the radius while ϕ the angle respect to the x axis.

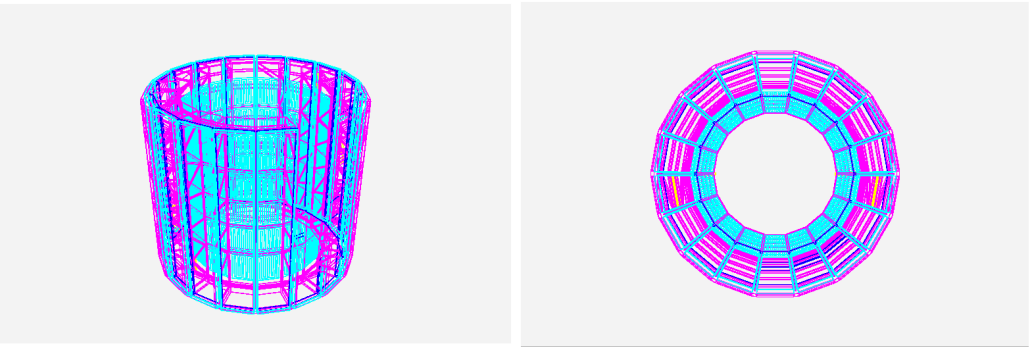

Figure 3.2: Visualization of the simulated volumes described by the path ALIC_1/B077_1: prospective view (left) and front view in the $r - \phi$ plane (right).

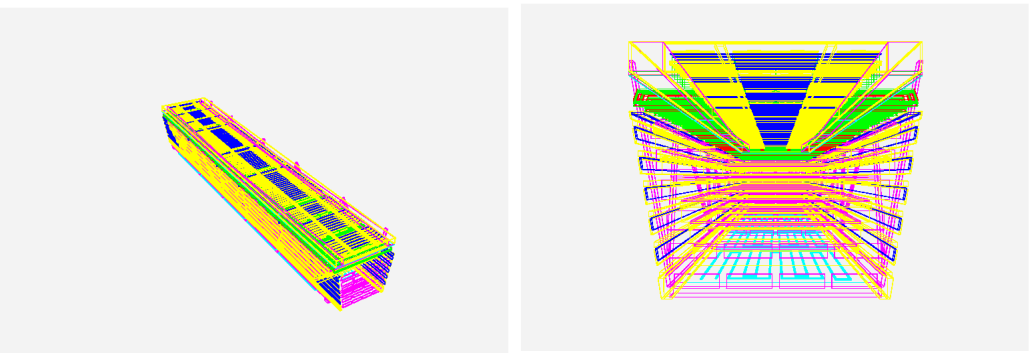

Figure 3.3: Visualization of the simulated volumes described by the path ALIC_1/B077_1/BSEGMO02_1. They correspond to a TOF and TRD SM: prospective view (left) and front view in the $r - \phi$ plane (right).

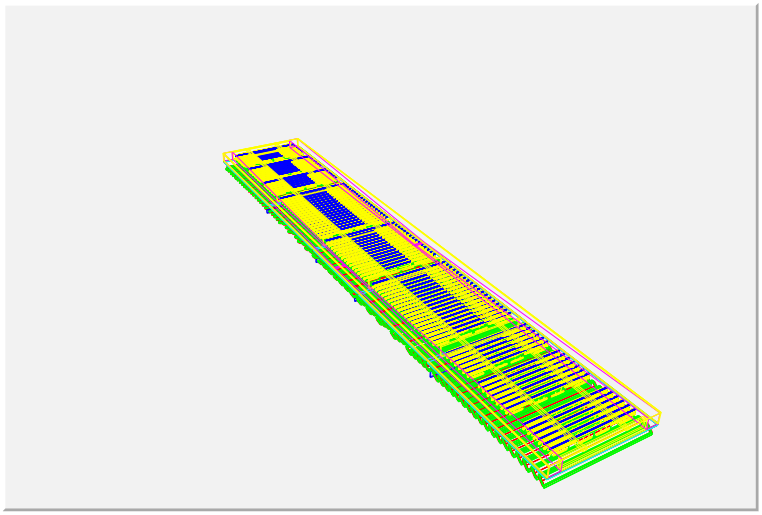

Figure 3.4: Visualization of the simulated volumes described by the path ALIC_1/B077_1/BSEGMO02_1/BTOF0_1. They correspond to the volumes inside a SM.

of the particles moving inside ALICE with the detectors, and in particular with their sensible volumes in terms of deposition of a certain amount of energy (Hit). At this stage, the detector response (Hit) is the ideal one, obtained before the conversion of the signal from analogue to digital by the front-end electronics. In this way SDigits are produced from Hits. They are digital signals still without noise and with unrealistic thresholds so that they can be summed up even when produced with different generators (merging processes). Once noise and realistic thresholds are applied, the signals are called Digits. The same physical information contained in the Digits can be expressed in the Raw Data format that is the one given by the front-end electronics during real data taking.

In the top part of Fig. 3.5 the schematic flow of the simulation process is shown.

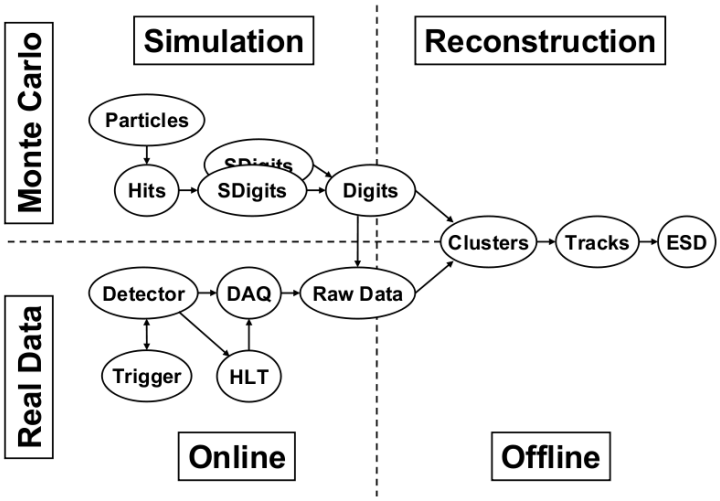

Figure 3.5: Schematic view of the simulation and reconstruction flow.

3.2 Event reconstruction

Both simulated and real events have to be reconstructed in order to extract the information needed for the physics analysis. The event reconstruction consists of different steps: cluster finding, primary vertex reconstruction, track reconstruction, particle identification and secondary vertex reconstruction[4]. The input data can be Digits or Raw Data and the output ones are

[4]The secondary vertex are from V^0, cascade, kink-dacay topologies

the so-called ESDs (Event Summary Data) containing reconstructed charged particle tracks, V^0 decays (i.e. $\Lambda \rightarrow p\pi$), kinks (i.e. $K \rightarrow \mu\nu$), and cascade topologies (i.e. $\Xi \rightarrow \Lambda\pi \rightarrow p\pi\pi$). Besides, the ESDs include the information on the global properties of the events. Before describing the reconstruction procedure here are some useful definitions:

- cluster: group of Digits close in space or time that are supposed to be produced by the same particle;
- space point: position where a particle is supposed to have crossed the sensible volume of the detector. It can be obtained computing the center of gravity of the corresponding cluster. When this is not possible, the space points correspond to the geometrical centre of the fired sensible volume. For example, in the TOF detector the space points are the centre of the pad matched with the track;
- reconstructed track: it is defined by a set of five parameters which characterize the trajectory, plus their covariance matrix;
- reference system: the ALICE global reference system (see Fig. 3.6) is a right-handed system with the z axis along the beam line pointing in the opposite side with respect to the muon spectrometer; the y axis is vertical pointing upwards with the origin at the intersection of the TPC middle plane with the z axis. In the reconstruction steps, the ITS, TPC, TRD clusters and tracks are always defined in the local reference frame of the volume they belong to (i.e. ITS module, TPC sector,...). These local reference systems follow the common convention to be right-handed system with the same origin and the same z axis as the global reference, and the x axis perpendicular to the sensible plane of the volume. In this way a rotation around the z axis allows to go from the local to the global reference system.

The first step of the reconstruction procedure is the local reconstruction. During this stage, each detector can not exchange information with the others and looks for clusters in its sensible volumes. The second step is the primary vertex reconstruction using the clusters in the two ITS inner layers (see Fig. 2.14). Finally the third one is the track reconstruction. Actually, tracking and cluster finding are two interactive steps: the number and the final position of the clusters are defined at the end of the tracking procedure when superimposed clusters can be distinguished. This last step includes also particle identification and secondary vertex reconstruction.

The track reconstruction methods are classified in two groups: the global methods and the local ones, depending on how the information are used.

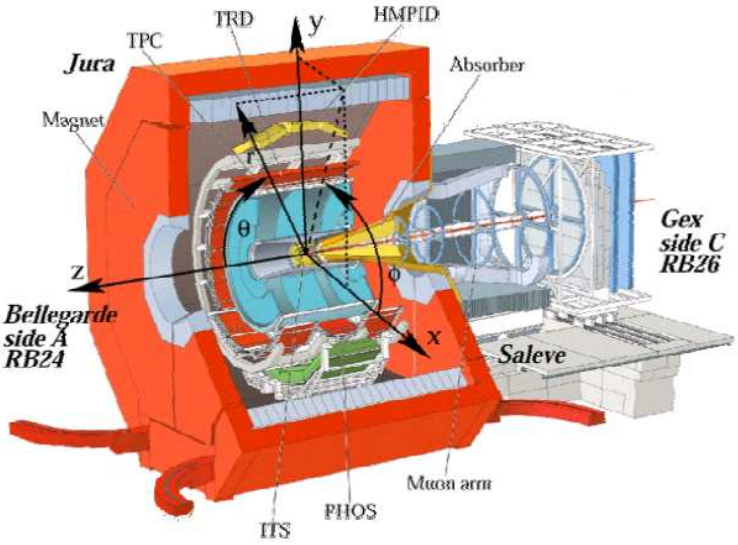

Figure 3.6: ALICE global reference system with polar (θ) and azimuthal (ϕ) angles.

In the global methods, all the measures are used at the same time and the decision to include or not a measure is taken when all the information on the track are known. Hough transform, templates and conformal mappings are examples of global algorithms. The advantages of these kind of procedure are the stability with respect to the noisy of the detectors and the easy assessment of the space point errors. The disadvantage is that a theoretical model able to describe with great precision the trajectories of the particles is needed. Such model is often not available since stochastic processes that can not be described analytically (like multiple scattering, unpredictable energy loss due to disomogenity in the material, deflection of trajectory due to disomogenity in the magnetic field,...) are present. In the local reconstruction procedures a global model for the tracks description is not needed since the track parameters are estimated locally and the decision whether to accept or not a measure is taken using the information coming from the points previously associated to the track. The advantage of such methods is that local peculiarity can be taken into account in a easier way. The disadvantages are that these are time demanding and considerably cpu consuming algorithms, highly sensible to noise, to wrong measures and to wrong parametrizations of the errors associated to a point. The ALICE tracking is based on one of the most advanced local reconstruction methods: the kalman filter [69]. This

algorithm has many advantages, among which:

- the recognition and fitting of a track can be done at the same time;
- wrong points (due to noise or coming from other tracks) can be excluded directly during the tracking procedure (while in other methods this has to be done in a subsequent step);
- multiple scattering and energy loss can be taken into account in a simpler way than with global methods;
- the extrapolation of a track from a detector to another is easier.

In more details, the ALICE track reconstruction procedure based on Kalman Filter, is made of the following steps: search of probable tracks in the outer layer of the TPC (seeds); inner propagation to the TPC inner layers and to the ITS towards the primary vertex; re-propagation in the outer direction towards, eventually, TRD, TOF and the other central detectors (HMPID, PHOS); final inner extrapolation towards the primary vertex. In the following, some details concerning these steps are given.

- At first, only the TPC clusters close to the outer layer are taken into account and the possible tracks (seeds) are reconstructed as groups of clusters that are supposed to have been produced by the same particle. From these seeds, a first estimate of the track parameters is done but it would be too rough to extrapolate in the outer detectors. At this stage only the reconstruction of primary tracks is possible, imposing that they point towards the primary vertex (as it was reconstructed by the SPD after the local reconstruction).
- The next step is the propagation of the seeds found in the TPC towards its inner radius, taking into account multiple scattering and energy deposition in the hypothesis that all the particles are pions (being this the most abundant particle specie that is expected to be produced). In this phase more clusters are associated to the tracks, improving the quality of their parameters. To decide which cluster to add, at each propagation step a window is defined around the point where the track is expected to be according to the parameters describing it (assuming them to be correct), with size depending on the uncertainty on the track position. Among all the clusters inside this window, the one with the highest probability to belong to the track is added to it.

- After the extrapolation to the inner TPC radius, the reconstruction in the ITS starts, ending at the point which is the closest to the primary vertex (in Fig. 3.7 the ITS prolongation efficiency is reported). During this phase some ITS clusters are associated to the track improving again the knowledge of its parameters. Due to the p_t acceptance and the dead zones of TPC detector, not all the ITS clusters are associated to these tracks that have crossed the TPC. Hence an independent tracking algorithm is then used to deal with the remaing ITS clusters. The tracks reconstructed in this way are called ITS Stand-Alone (ITSsa) tracks [70];

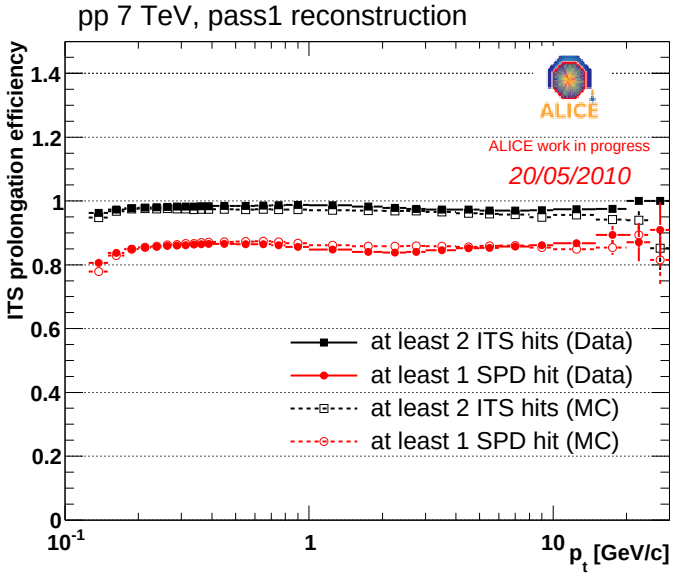

Figure 3.7: ITS prolongation efficiency defined as the probability to prolong a TPC track to ITS. The tracks that are prolonged in ITS are signed with the flag ITSrefit. In other words, the plot shows the fraction of tracks successfully prolonged to ITS over the total number of tracks that satisfy TPC only quality cuts ($|\eta| < 0.8$, number of TPC clusters > 70, χ^2/cluster< 4, DCAxy< 2.4 cm and DCAz< 3.2 cm where DCA is the distance of closest approach in the transverse plane (DCAxy) and in the z direction (DCAz) defined using ony TPC information). By definition, due to these cuts, the ITSsa tracks are excluded from this plot.

- To further improve the track parameters, a back-propagation to the outermost layer of the ITS and then to the outermost radius of the TPC is performed.

- After reaching the outer TPC radius, the tracks are extrapolated in the TRD where eventually other clusters are added to the track and in this case an update of the track parameters is also done (for tracks with $p_t > 200\,\mathrm{MeV/c}$).
- The tracks are then matched with TOF, HMPID and PHOS which provide PID information but don't update the track parameters.
- As last step, reconstructed tracks are re-fitted inwards to TRD, TPC and ITS and are propagated towards the primary vertex reconstructed by the SPD. Also the ITSsa tracks are re-fitted from the outer ITS layer to the primary vertex (or the innermost point, if they are secondary tracks);
- Once all the tracks have been reconstructed, they are used to find secondary vertices. In fact, secondary verices can be defined also during the tracking procedure to avoid that secondary particles are uselessly prolonged till the primary vertex.

We have seen that the general track reconstruction procedure includes ITS-TPC and ITSsa configurations. The ITSsa tracking capability is important both for the reconstruction of low-momentum particles that do not reach TPC and for high-momentum particles that pass through the TPC dead zones or decay between the ITS and the TPC. Optionally, the ITSsa tracker can be configured to take into account all ITS points (also those already used by the ITS-TPC tracker). In this case the tracks are flagged as ITSpureSA. These tracks are useful for the ITS/TPC relative alignment procedure which is based on the comparison of the track parameters computed for both the ITS and the TPC stand-alone track segments. In the following, we will refer to the tracks reconstructed with both ITS and TPC as "global tracks", and to the ones reconstructed by the ITSsa algorithm as "ITSsa tracks".

3.3 TOF calibration and alignment

During the outer propagation step of the tracking procedure, the tracks are extrapolated until the TOF sensitive layer and a track matching window (on the TOF layer) of 3 cm in PbPb interactions and 10 cm in pp collisions is open around this crossing point[5]. All TOF clusters inside the track matching

[5]The difference between the two window sizes is related to the different track multiplicity in pp and PbPb collisions

window are collected and the one closest to the crossing point between the track prolongation and the TOF sensitive layer is associated to the track. At this moment, the time-of-flight measured by the TOF detector is associated to the track. To improve the TOF performance, the TOF track matching efficiency[6] has to be as high as possible, while keeping the number of mismatched tracks[7] as small as possible. At the same time, the definition of the time-of-flight has to be know with the best possible resolution. To reach this goal, the calibration and alignment of the TOF detector are of fundamental importance.

3.3.1 TOF Calibration

If TOF was an ideal detector, the distribution of the difference $\Delta\widetilde{t} = \widetilde{t}_{TOF} - t_{exp}$ between the time-of-flight measured by TOF ($\widetilde{t}_{TOF}$) and the expected time defined during the track reconstruction (t_{exp}) [8] should be centered at zero. In reality, such distribution is shifted from zero due to a number of reasons. The LHC clock and the bunches circulating in the accelerator are perfectly synchronized in the radiofrequency cavity, but since the first one propagates in the optical fibre, while the second travels in vacuum and the radiofrequency cavity is quite far from ALICE, they are no more synchronized when they reach ALICE. The difference in the arrival times is not constant but it is function of the temperature[9]. Since the TOF times are measured with respect to the LHC clock, they have to be realigned with the bunch crossing, to be then compared to the expected times t_{exp}. This shift, which we refer to as $t0_{Fill}$, is common to all the TOF channels and has to be defined for each fill from the $\widetilde{t}_{TOF} - t_{exp}$ distribution. In practice, the $t0_{Fill}$ corresponds to the mean of the gaussian fit to the $\widetilde{t}_{TOF} - t_{exp}$ distribution.

In addition to this common phase, other factors contribute to the desynchronization of the TOF time signals coming from different channels, biasing the measured times-of-flight. They are for example related to delays in the front-end cards, the clock time distribution on each sector, etc. Some of this shifts (t_{calib1}) are known a-priori (i.e. the delays due to the different length of the cables were measured in laboratory before the TOF assembly) and can be easily subtracted to the $\widetilde{t}_{TOF}$ of the corresponding channel. To take into account any other unknown deviations of the $\widetilde{t}_{TOF}$ with respect to the actual time, a global correction t_{calib2} is applied to every readout channel. Since

[6]The TOF track matching efficiency is defined as the number of tracks matched with TOF over the number of tracks reconstructed by the TPC.

[7]Mismatched tracks are tracks matched with a wrong TOF hit.

[8]For a detailed definition of t_{exp} see \$5.2, eq. 5.2.

[9]A change of the temperature produces a change of the speed in the optical fibre.

the corrected value for the time-of-flight measurements can be expressed as $t_{TOF} = \widetilde{t}_{TOF} - t0_{Fill} - t_{calib1} - t_{calib2}$, t_{calib2} can be determined getting the mean value of the gaussian fit of the $\Delta t = t_{TOF} - t_{exp}$ distribution.

Another channel by channel factor which needs to be considered is the time slewing effect caused by the finite amount of charge necessary to trigger the discriminator (signal over threshold). This is done fitting with a 5-th order polynomial function the distribution of $\widetilde{t}_{TOF}$ versus the time over threshold (ToT).

After the above mentioned calibration steps, the distribution of $\Delta t = \widetilde{t}_{TOF} - t0_{fill} - t_{calib1} - t0_{calib2} - t_{time-slewing} - t_{exp}$ should be centered at zero for each channel[10]. In the following sections and chapters we will name t_{TOF} the calibrated TOF signal.

3.3.2 TOF alignment

Since one of the main tools for the ALICE physics program is particle identification, all the parameters that influence the experiment PID performance have to be optimized. Among these, as far as the TOF detector is concerned, there are the matching efficiency, the computation of the expected times and obviously the measurement of the TOF time-of-flight. Both the first two parameters are affected by the TOF misalignment, that is the displacement of the TOF sensible volumes with respect to their ideal position. If during the reconstruction procedure the true TOF geometry is not known, and the ideal one or a wrong one is used, the tracks will be likely to be extrapolated to the wrong TOF volume, resulting in a decrease in the matching efficiency[11], while, obviously, the matching with wrong TOF hits will increase. Moreover the computation of the track length will be wrong and consequently also the definition of the expected times. Due to this the alignment of the TOF detector is fundamental to guarantee an optimal performance of the TOF PID. In this section some details and results about the TOF alignment will be presented.

Ideal and real geometry

The actual positions of the TOF volumes are different from the ideal ones defined at the planning stage mainly because of the deformation of the space frame (due to the ALICE weight) and the mechanical tolerances. Hence it

[10]The TOF resolution will be further improved once also the time walk effect will be taken into account in the calibration procedure.

[11]To give a feeling of the scale of the effect, on simulated events it was found that a z misalignment of 1 cm causes a 5% decreasing in the matching efficiency.

is necessary to determine these real positions or, equivalently, the misalignments with respect to the ideal ones, to be able to use the correct geometry in the event reconstruction procedure. These displacements are defined by six parameters: three translations $(\Delta x, \Delta y, \Delta z)$ in the x, y, z directions and three Euler angles $(\Delta\psi, \Delta\theta, \Delta\phi)$ that define a rotation in the "active roll-pitch-yaw" convention[12] (see Fig. 3.8). This procedure is simplified by the use of the ROOT geometry package which describes complex volumes with a modular and hierarchical structure: the single parts of an object are dealt with as simple volumes, and positioned inside or with respect to each other. As a results, when moving a volume the positions of all the ones inside it will change accordingly.

In this context, a volume for which it is possible to define the real position or better the displacements with respect to the ideal one (thanks to the alignment procedure) in global or local coordinates[13] is called "alignable".

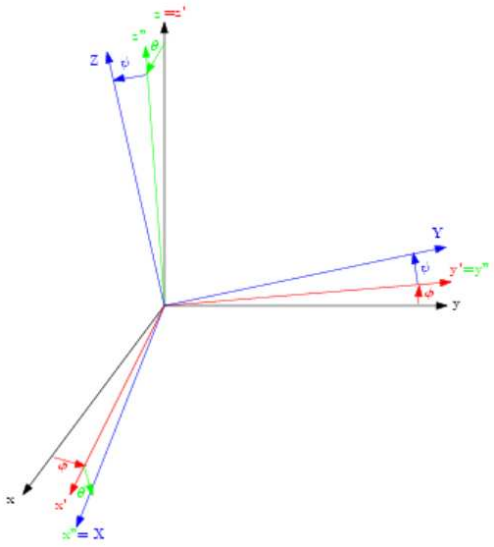

Figure 3.8: Euler angles in the "roll-pitch-yaw" convention.

The TOF alignable volumes are 1611: 18 SMs (alignable non sensitive volumes) and 1593 strips (alignable sensitive volumes).

[12] $\Delta\psi$ (yaw) is a rotation around the z axis, $\Delta\theta$ (pitch) is a rotation around the new y axis and $\Delta\phi$ (roll) is a rotation around the last x axis. "Active" means that if the rotation matrix is applied to the ideal coordinates of a point, the misaligned position is obtained (local-to-global transformation).

[13] Global coordinates are defined with respect to the global ALICE reference system while local ones refer to the mother coordinate system.

Track alignment procedure

The TOF alignment procedure is track based and developed within the ALICE software alignment framework. With this method it is possible both to align strip by strip (each strip can have a different misalignment matrix) to take into account the relative displacement between them, and to align groups of strips (all the strips belonging to the group have the same misalignment matrix) considered as a single rigid object. For example we can suppose that only the SMs can move, while the strips inside them are fixed with respect to it. As already said, the alignment algorithm is based on the track reconstruction and gives the possibility to define misalignment matrices from the residuals between the extrapolated track-point on the sensitive TOF layer and the matched TOF space point. In this way, the TOF becomes aligned with respect to the inner tracking detectors that are supposed to have been previously aligned. In general, once the volumes we want to align and those with respect to which we align are defined, the procedure steps to be run for every volume or group of volumes to be aligned are the following:

- loading of the most updated ALICE geometry configuration (if it is the first time that we align a detector, its geometry is the ideal one);
- selection of the reconstructed tracks with at least one track-point in the volume to be aligned and which satisfy the user requirements (e.g. minimum and maximum momentum, minimum number of ITS clusters,...);
- fast reconstruction of the selected tracks using only the track-points belonging to the volumes respect to which we want to align;
- extrapolation of the fast reconstructed tracks till the TOF layer. At the end of this step two TOF points are associated to each track: one is the extrapolated point and the other one is the TOF space-point matched with the track during the global tracking procedure;
- computation for each track of the distance between the couple of points associated to it during the previous step(residual);
- looking for the displacement of the volume to be aligned that minimizes these residuals. These are the alignment parameters associated to the volume.

It is evident that the performance of this algorithm are deeply connected with the precision of the reconstruction and extrapolation procedures. In the alignment framework the track reconstruction in presence of a magnetic

field is performed with a dedicated track fitting algorithm, the Riemann Fitter, based on the Riemann sphere formalism [71, 72, 73]. For the residuals' analysis and minimization, three different methods are available: Fast, Linear and Chi2. They all minimize the χ^2 function in eq. 3.2; the differences among them are related to the level of approximation of the solution.

$$\chi^2(\Delta x, \Delta y, \Delta z, \Delta\psi, \Delta\theta, \Delta\phi) = \sum_{i=1}^{N} \frac{(y_e - f(y_i, \Delta x, \Delta y, \Delta z, \Delta\psi, \Delta\theta, \Delta\phi))^2}{\sigma(y_e)^2 + (df/dy)^2\sigma(y_i)^2}. \tag{3.2}$$

The Chi2 method allows to find a numerical solution to the alignment equation relying on the MINUIT package [74]. The other methods make the approximation of small rotations and traslations, hence reducing the rotation roll-pitch-yaw matrix:

$$\begin{pmatrix} \cos\theta\cos\phi & -\cos\theta\sin\phi & \sin\theta \\ \sin\psi\sin\theta\cos\theta + \cos\psi\sin\phi & -\sin\psi\sin\theta\sin\phi + \cos\psi\cos\phi & -\cos\theta\sin\psi \\ -\cos\psi\sin\theta\cos\phi + \sin\psi\sin\phi & \cos\psi\sin\theta\sin\phi + \sin\psi\cos\phi & \cos\theta\cos\psi \end{pmatrix}$$

to the following one:

$$\begin{pmatrix} 1 & -\phi & \theta \\ \phi & 1 & -\psi \\ -\theta & \psi & 1 \end{pmatrix}$$

The Linear procedure uses a ROOT-based method that fits points with a linear combination of known functions. Actually the function is an hyperplane in six dimensions. The Fast method is instead based on simple matrix calculations. The comparison of the three different methods[14] led to the conclusion that the best-performing minimization algorithm is the Linear one. For this reason, the track based TOF alignment was chosen to use the Riemann algorithm for the track reconstruction and the Linear approach for residuals minimization[15].

TOF alignment: some details

The first TOF alignment was performed in November 2009 with cosmic ray data. Due to the particular topology of these events where tracks come mostly

[14]The check was done by introducing a known misalignment in the TOF SMs. Events were simulated with this new geometry, reconstructed with the ideal one and the alignment procedure was applied to determine which minimizing method computes the alignment parameters the closest to the introduced ones.

[15]All the results reported later in this chapter were obtained with a procedure based on these algorithms.

from the vertical direction, the statistics on SM 0-17-8-9 was not enough to determine reliable alignment parameters on these SMs. We hence decided to complete the alignment with pp data. In January 2010 the TOF alignment procedure was optimized and applied to $\sqrt{s} = 900\,\text{GeV}$ pp data. Due to the fact that, after that, the ITS and TPC detector (with respect to which the TOF needs to be aligned) produced new alignment objects, we needed to re-align the TOF detector taking into account the new geometry of the inner tracking systems. On 27 January 2010 two SMs were moved to recover some front-end cards, so a further alignment was done using the $\sqrt{s} = 7\,\text{TeV}$ pp data. Since on January 2012 other SMs will be moved and other TRD SMs will be installed, with the consequent modification of the space frame geometry, a new alignment will be carried out with the first 2012 pp data. A more frequent alignment procedure is not necessary because the TOF detector does not undergo significant displacements apart from what mentioned above. Indeed, on 2011 data where no alignment was performed, it was found that the residuals between the matched TOF space points and the extrapolated track-points were stable and very limited.

In the following, the alignment results from spring 2010 are reported. These results were obtained with $\sim$ 430000 Minimum Bias events collected in pp collisions[16] at $\sqrt{s} = 7\,\text{TeV}$ in April 2010. The tracks were selected requiring a matched space point in the TOF volume, at least 2 points in the ITS, at least 80 clusters in the TPC, a maximum DCA to the vertex in both z and xy directions of 3 cm and $0.5 < p < 5$ GeV/c. A wide momentum range can be accepted since the alignment performance has small dependence from the track momentum[17].

Since it is more probable to have a displacement of a whole SM (especially in the z direction) from its ideal position in the space frame, rather than a shift of a strip inside the module, I decided to align SM by SM. This means that I treated the SM as a rigid object. Consequently, the alignment matrices of all the strips belonging to are the same.

To sum up, the alignment procedure was performed 18 times (one for each SM) selecting tracks with a matched hit on the TOF SM to be aligned, reconstructing them using only the TPC clusters, extrapolating them till the TOF layer, and finally getting the SM alignment matrix minimizing the residuals.

As already said, I used the Riemann fitting procedure and the Linear

[16]Due to the low multiplicity environment, pp collisions are more suited for alignment purposes than PbPb collisions.

[17]Actually a small improvement of the performance with increasing track momentum was observed since the multiple scattering becomes less important at higher p and the extrapolation procedure is more reliable. The effect is anyway small.

minimizing algorithm. This was done in an iterative way: at each cycle the alignment matrices computed in the previous ones were applied to the volumes and the residual parameters were found out after a new extrapolation and minimization step. The final alignment matrix is hence the product of all the ones computed during each cycles. Fig. 3.9, 3.10 and 3.11 show the cumulative parameters (top) and the residual ones (bottom) versus the iteration cycle, where the *cumulative parameter* at interation i is the one obtained from the product of the matrices computed in the $i-1$ previous cycles, and the *residual parameter* is the one computed at cycle i. The parameters refer to SM0, but similar results were obtained for all the other SMs. As one can see, after 10 iterations the cumulative parameters reach a plateau value and the residual ones are consistent with zero. This means that after 10 iterations the x, y and z residuals have a distribution perfectly centered on zero. In Fig. 3.12, 3.13 and 3.14 the x, y and z residuals are shown as a function of the strip number before the alignment procedure (left) and after 10 cycles (right).

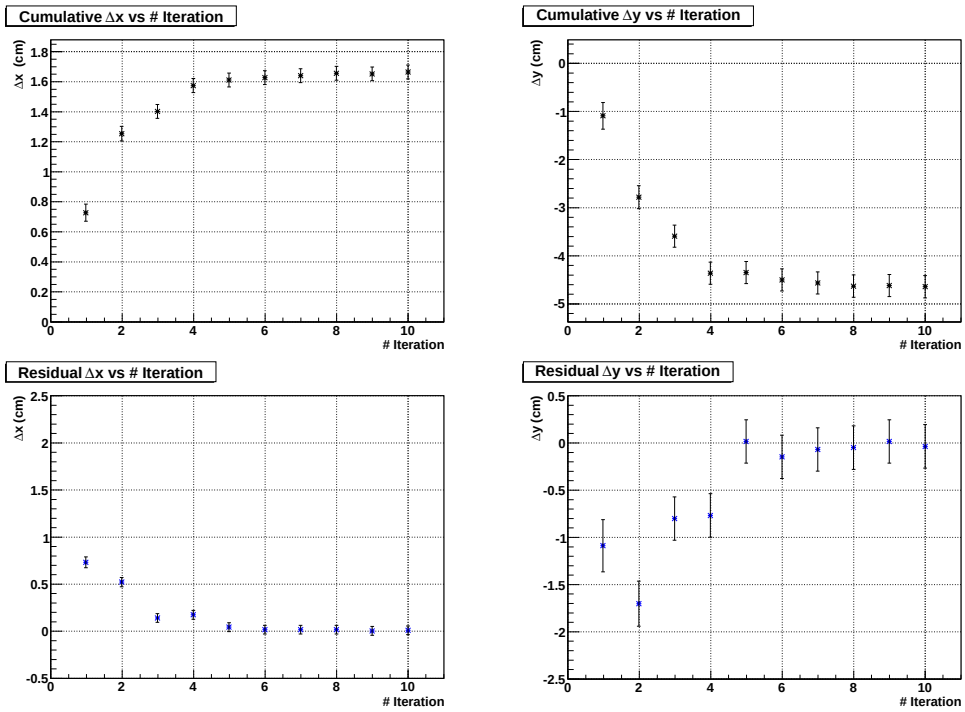

Figure 3.9: Δx (left) and Δy (right) cumulative parameters (top) and residual parameters (bottom) as a function of the number of iterations.

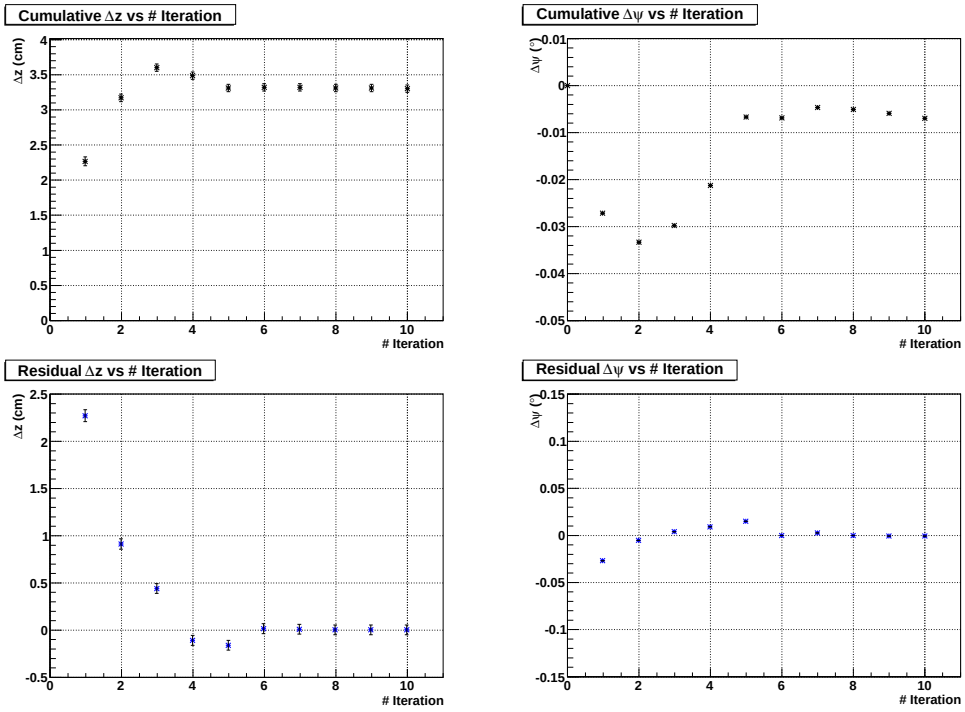

Figure 3.10: Δz (left) and $\Delta\psi$ (right) cumulative parameters (top) and residual parameters (bottom) as a function of the number of iterations.

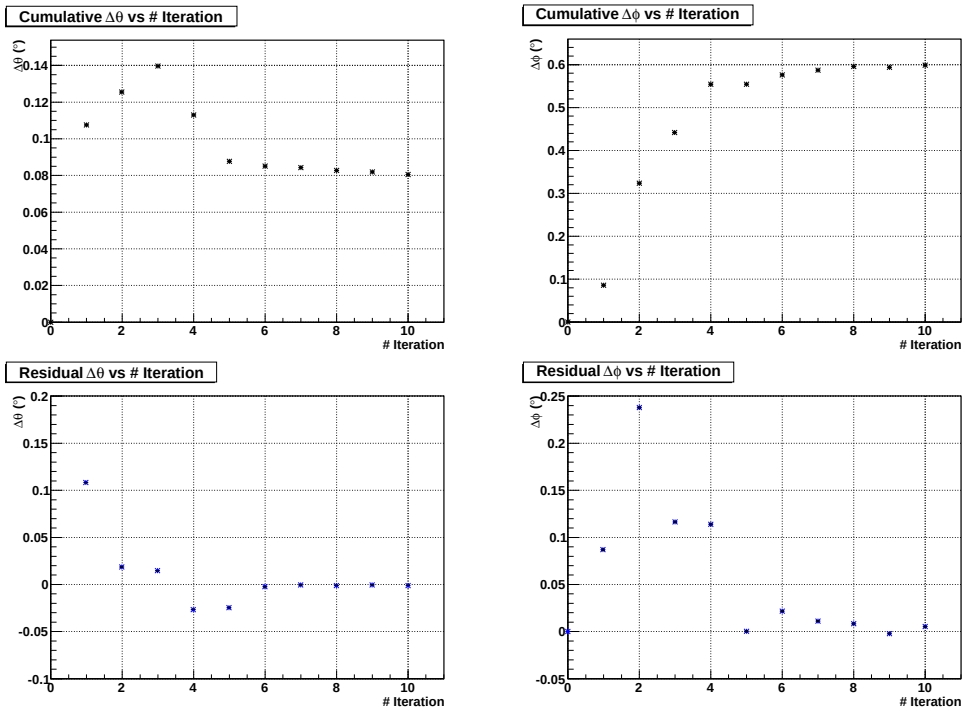

Figure 3.11: $\Delta\theta$ (left) and $\Delta\phi$ (right) cumulative parameters (top) and residual parameters (bottom) as a function of the number of iterations.

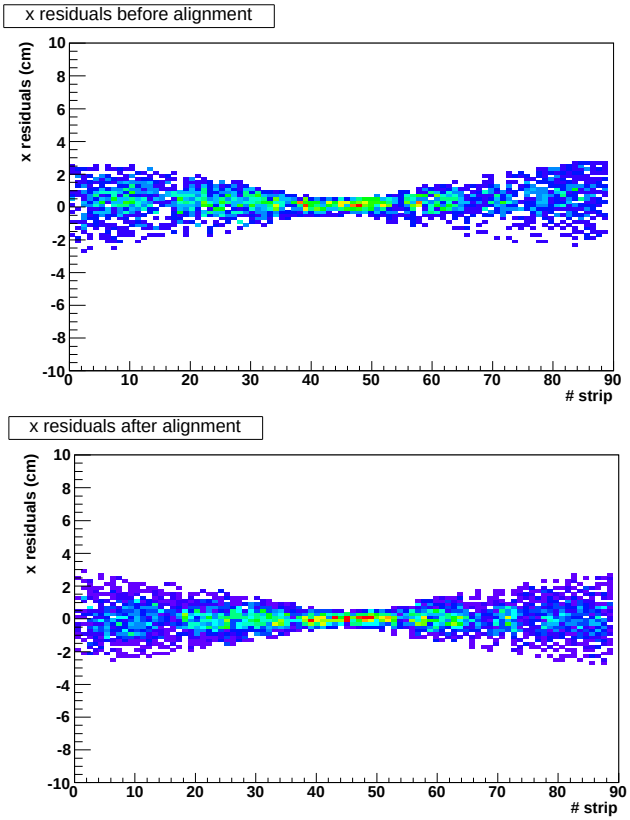

Figure 3.12: Residuals between the extrapolated point and the TOF track-point in the x direction before the alignment procedure (left) and after 10 iterations (right) as a function of the strip number.

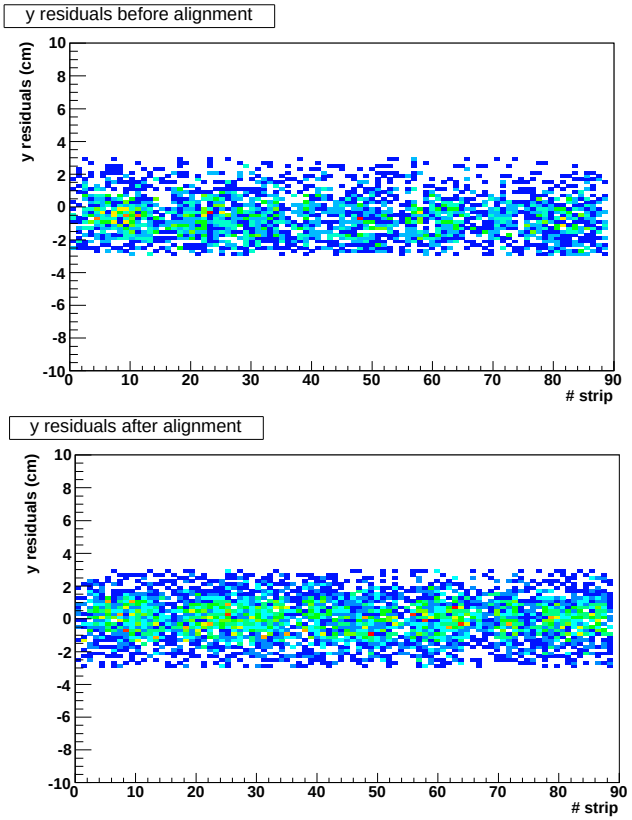

Figure 3.13: Residuals between the extrapolated point and the TOF trackpoint in the y direction before the alignment procedure (left) and after 10 iterations (right) as a function of the strip number.

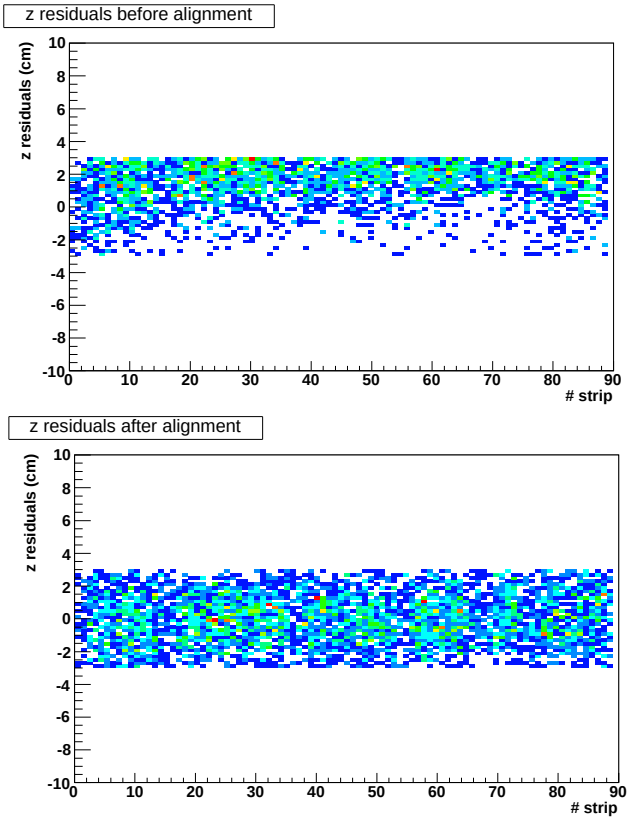

Figure 3.14: Residuals between the extrapolated point and the TOF trackpoint in the z direction before the alignment procedure (left) and after 10 iterations (right) as a function of the strip number.

At the end of the alignment procedure we have 18 aligned matrices, one for each SM. We can apply these matrices to the SM volumes to get the aligned geometry. Infact, the TOF alignment objects obtained during the alignment procedure are used as part of the AliRoot software every time the geometry is used for simulation / reconstruction purposes: these objects have to be applied to the ideal geometry in order to describe the real one.

To have an idea of the TOF misalignment with respect to the ideal conditions, in Fig. 3.15, 3.16 and 3.17 a frontal (z $\sim$ +360 cm), central (z = 0 cm) and back (z $\sim$ -360 cm) TOF sections are shown in the $x-y$ plane projection. The black points represent the ideal pad positions, while the red ones are the positions in the real geometry. To emphasize the difference, the red points are magnified by 10, following the expression: ideal+(misaligned-ideal)*10. The effect due to the deformations induced in the space frame by the weight of the ALICE detectors is clearly visible.

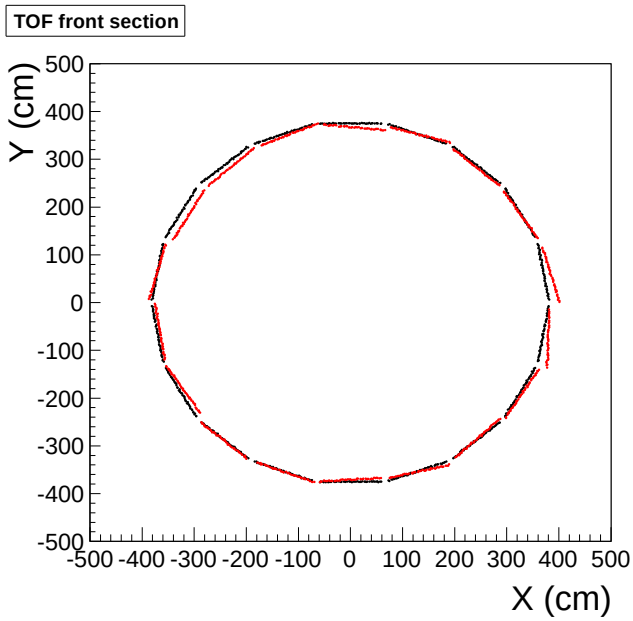

Figure 3.15: Frontal TOF section (z $\sim$ +360 cm). The black points are the pad positions in the ideal geometry while the red ones are the true positions in the real geometry. They are magnified by 10 according to the expression: ideal+(misaligned-ideal)*10.

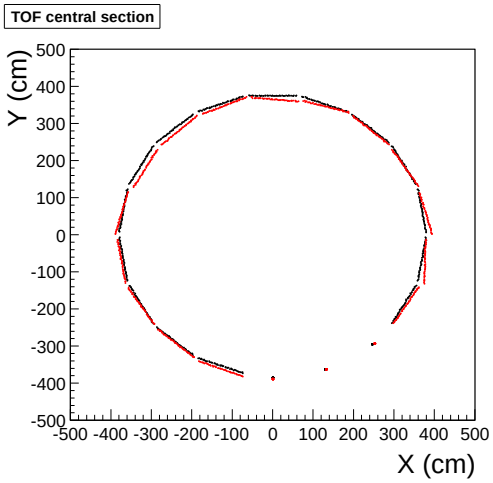

Figure 3.16: Central TOF section (z = 0 cm). The black points are the pad positions in the ideal geometry while the red ones are the true positions in the real geometry. They are magnified by 10 according to the expression: ideal+(misaligned-ideal)*10. The missing points correspond to the three missing central modules in the PHOS region.

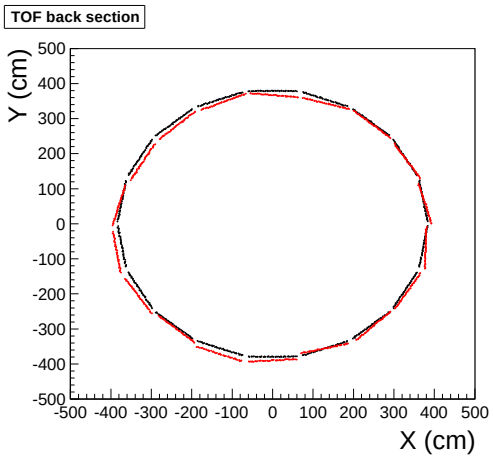

Figure 3.17: Back TOF section (z $\sim$ - 360 cm). The black points are the pad positions in the ideal geometry while the red ones are the true positions in the emphasize real geometry. They are magnified by 10 according to the expression: ideal+(misaligned-ideal)*10.

In Fig. 3.18, 3.19 and 3.20 the displacements of the aligned positions (computed with the alignment algorithm) of the central pad of each strip of a SM in x, y and z direction with respect to the ideal ones are shown. Each color corresponds to a SM. It is evident that the main displacements are in z direction. Their size varies SM by SM, with a miximum deviation of $\sim 4\,\mathrm{cm}$.

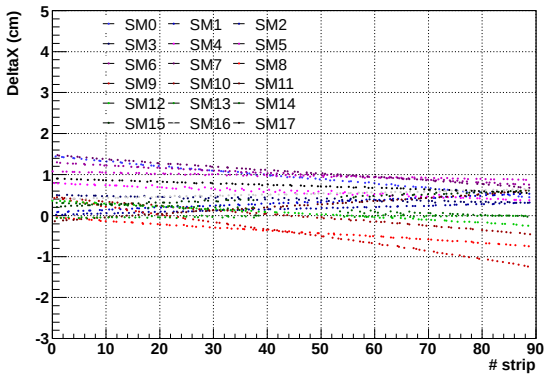

Figure 3.18: Displacements along the x direction of the aligned positions computed with the alignment algorithm with respect to the ideal ones. Each point represent the central pad of each strip of a SM . Each color correspond to a different SM.

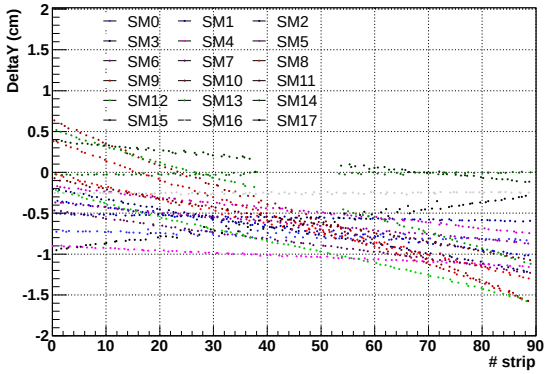

Figure 3.19: Displacements along the x direction of the aligned positions computed with the alignment algorithm with respect to the ideal ones. Each point represent the central pad of each strip of a SM . Each color correspond to a different SM.

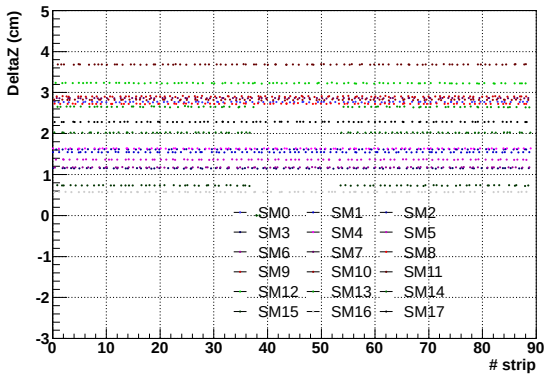

Figure 3.20: Displacements along the x direction of the aligned positions computed with the alignment algorithm with respect to the ideal ones. Each point represent the central pad of each strip of a SM . Each color correspond to a different SM.

Chapter 4

TOF PID: matching efficiency and time-zero of the event

The reconstruction of particle spectra, necessary to access the thermal parameters of the system created in heavy-ion collisions at the kinetic and chemical freeze-out, relys on the capability of the ALICE experiment to identify particles following three different approaches: topological identification, invariant mass fit and use of dedicated PID detectors. The first two approaches are mainly used for weak decays, resonances and kaons decaying in the active volume of the tracking system ("kinks"). In these cases the PID detectors can be used to improve the signal over background ratio, without any loss of the actual signal, by means of "compatibility cuts" with the PID signal (e.g. requiring that the dE/dx signals of the kaons in a $\phi \to KK$ candidate are within 3 sigmas from the expected value). The ALICE barrel detectors for particle identification are ITS, TPC, TRD, TOF and HMPID, which exploit different PID techniques over complementary p_t ranges. Usually, for all detectors, in the regions where a clean separation between different particles species is possible, a track-by-track PID is feasible. On the other hand, a statistical unfolding procedure has to be used in the regions of limited separation (e.g. in the relativistic rise of the TPC signal or at high momenta in the case of TOF).

An example of the ALICE PID is kaon identification. This can be done in three different ways:

- direct PID of charged K using one of the PID detectors
- topological reconstruction of neutral K in $K^0 \to \pi^+\pi^-$ decays, which are called "V^0 decays"
- charged K decays, as $K^\pm \to \mu^\pm\nu$, which are called "kinks"

All these analyses provide compatible results in terms of kaon identification, as can be seen in Fig. 4.1. Here, the charged kaon spectra obtained from the combined ITS, TPC and TOF analysis, the one from the kink topology reconstruction and the K^0_s spectra obtained in pp collisions at $\sqrt{s} = 900\,\mathrm{GeV}$ are shown (see [75]).

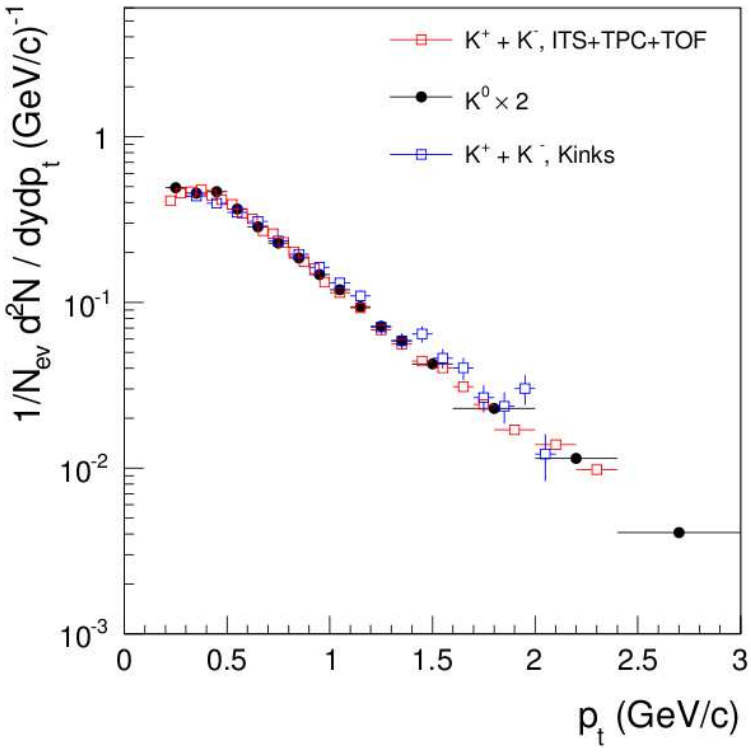

Figure 4.1: Comparison between the K^0_s spectra, the charged kaon spectra obtained with the combined ITS, TPC and TOF analysis, and the one from the kink topology study.

In this chapter some information on the PID performance of the detectors used for the ALICE spectra analysis (ITS, TPC, TOF and HMPID) will be given. We will focus our attention on the TOF detector, giving details on the two main factors, after the TOF detector time resolution, that define its PID performance, namely the matching efficiency and the computation of the time-zero of the events.

4.1 Particle identification with the ITS detector

The four outer layers of the ITS detector are characterized by analogue readout and can therefore be used for PID. In particular, with these detectors we can identify charged particles on the basis of up to 4 measurements of the specific energy loss (dE/dx) in the non-relativistic ($1/\beta^2$) region, with a resolution of $\sigma_{dE/dx} \sim 10 - 15\%$. In Fig. 4.2 the dE/dx information of charged particles provided by the ITS detector is shown as a function of the momentum as reconstructed by the ITS. Here only ITSsa tracks are taken into account. The black lines correspond to the Bethe-Bloch parametrization of the detector response. The bands for charged hadrons are clearly visible.

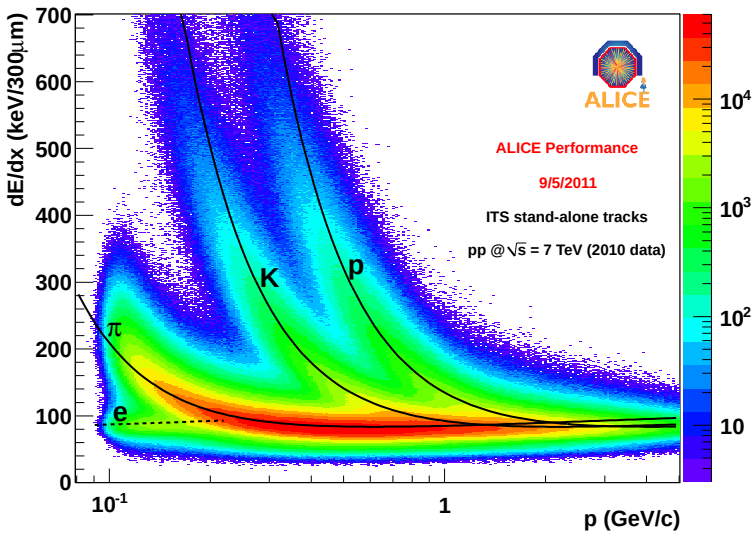

Figure 4.2: ITS dE/dx of charged particles (from ITS standalone tracks) as a function of their momentum reconstructed by the ITS. The results correspond to pp collisions at $\sqrt{s} = 7\,\text{TeV}$. The black lines are the Bethe-Bloch parametrization of the detector response.

4.2 Particle identification with the TPC detector

The TPC detector can provide up to 159 measurements of the specific energy loss dE/dx with a resolution of $\sigma_{dE/dx} \sim 5\%$, extending the particle identification to momenta higher than those covered by the ITS detector. Moreover, PID with the TPC can be carried out in the relativistic rise region up to $50 - 100$ GeV/c in momentum, on a statistical basis. In Fig. 4.3 the TPC dE/dx distribution as a function of momentum is shown. Global tracks have been analyzed. The lines are the Bethe-Bloch parametrization of the detector response. The bands for e, π, K and p and deuterons are clearly visible.

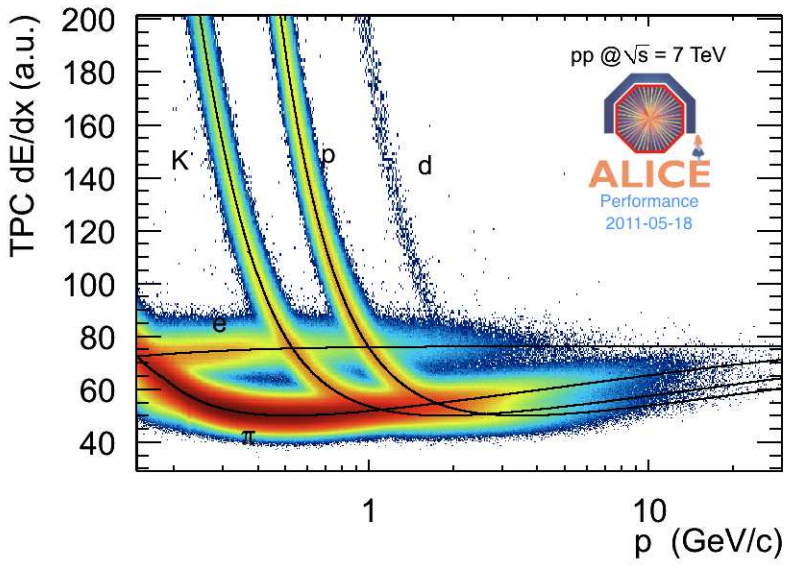

Figure 4.3: TPC dE/dx distribution as a function of momentum in pp collisions at $\sqrt{s} = 7$ TeV. The black lines are the Bethe-Bloch parametrization of the detector response.

4.3 Particle identification with the HMPID detector

The HMPID detector detects the Cherenkov photons emitted by fast charged particles traversing the radiator. The reconstruction of the cherenkov angles allows to provide charged hadrons PID for momenta higher than 1.5 GeV/c.

In Fig. 4.4 the Cherenkov angle as a function of momentum for global tracks in pp collisions at $\sqrt{s} = 7\,\text{TeV}$ is shown. The black lines are the theoretical values of the Cherenkov angles as a function of the track momentum for pion, kaon and proton mass hypotheses.

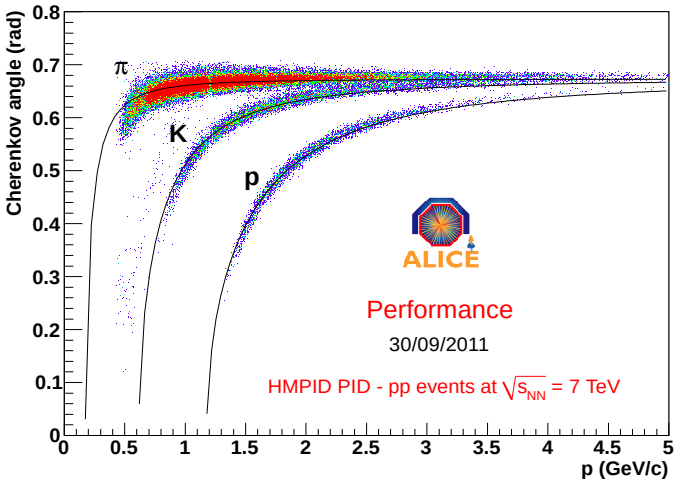

Figure 4.4: HMPID Cherenkov angle as a function of momentum in pp collisions at $\sqrt{s} = 7\,\text{TeV}$. The black lines are the theoretical values of the angles for the pion, kaon and proton mass hypotheses.

The HMPID is able to distinguish kaons from protons within 3σ (2σ) up to $p_t = 5\,\text{GeV/c}$ ($p_t = 6\,\text{GeV/c}$) and pions from kaons within 3σ (2σ) up to $p_t = 3\,\text{GeV/c}$ ($p_t = 4\,\text{GeV/c}$), extending the reach in p_t of the ALICE particle identification with respect to using the ITS, TPC and TOF detector only. This can be seen from Fig. 4.5 where the HMPID π/K and K/p $n\sigma$ separation as a function of transverse momentum is shown.

4.4 Particle identification with the TOF detector

To identify a particle it is necessary to know both its charge and its mass. The mass can be computed using at least two kinematic variables which depend on it. Usually, one of these is the momentum that, in ALICE, is determined by ITS and TPC from the radius of curvature of the track in the magnetic field. The second variable can be the energy loss (dE/dx), the Cherenkov

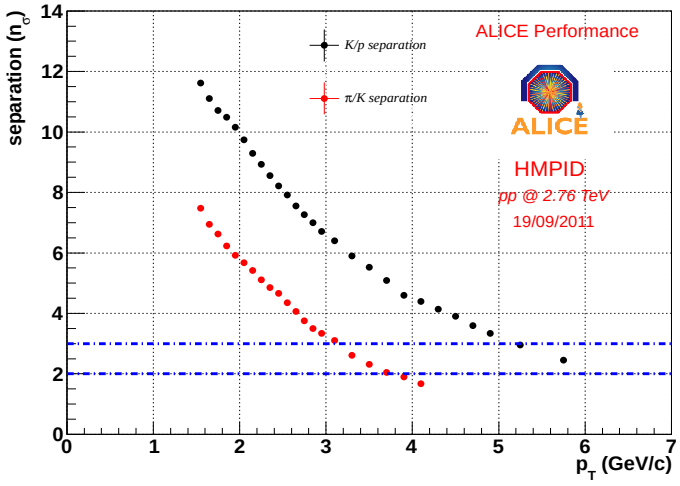

Figure 4.5: HMPID π/K and K/p $n\sigma$ separation as a function of transverse momentum. The σ's have been estimated performing the fit with 3 gaussian functions (for pions, kaons and protons) of the Cherenkov angle distribution in each p_t bin.

angle or the velocity of the particle defined as the ratio between the length of the trajectory L and its time-of-flight t. In the latter case, for example, being p the momentum associated to the track, then its mass m is:

$$m = p\sqrt{\frac{t^2}{L^2} - 1} \tag{4.1}$$

The resolution of the mass depends on three terms, that are functions of the resolution on the momentum, on the time-of-flight and on the track path length:

$$\frac{\partial m}{\partial p}\frac{1}{m} = \frac{\delta p}{p} \tag{4.2}$$

$$\frac{\partial m}{\partial t}\frac{1}{m} = \left(\frac{E}{m}\right)^2 \frac{\delta t}{t} \tag{4.3}$$

$$\frac{\partial m}{\partial L}\frac{1}{m} = \left(\frac{E}{m}\right)^2 \frac{\delta L}{L} \tag{4.4}$$

Square-summing these three terms we get

$$\delta m^2 = (\frac{m}{p})^2 \delta p^2 + \frac{p^2 + m^2}{t^2}\delta t^2 + \frac{p^2 + m^2}{L^2}\delta L^2 \tag{4.5}$$

from which we can see that, if $p \gg m$, the mass resolution is mainly determined by the resolution on the time-of-flight and on the track length.

By definition and from eq. 4.1, if we want to distinguish two particles with the same p and L but with different masses, it is necessary that the difference between the two time-of-flights is larger than the resolution. The difference between the time-of-flight of two different particles with same p and L is:

$$\Delta t = \frac{L}{2c}\frac{m_1^2 - m_2^2}{p^2} \tag{4.6}$$

The capability to distinguish these two particles can be expressed in terms of number of sigma:

$$n = \frac{\Delta t}{\delta t} = \frac{L(m_1^2 - m_2^2)}{2cp^2\delta t}. \tag{4.7}$$

where δt is the time resolution. Fig. 4.6 shows the Δt difference as a function of p between the π and K and between the K and p time-of-flights for a track path length of 4 m. We can see that in order to have a 3σ π/K separation up to 2.5 GeV/c the overall time resolution has to be better than 100 ps.

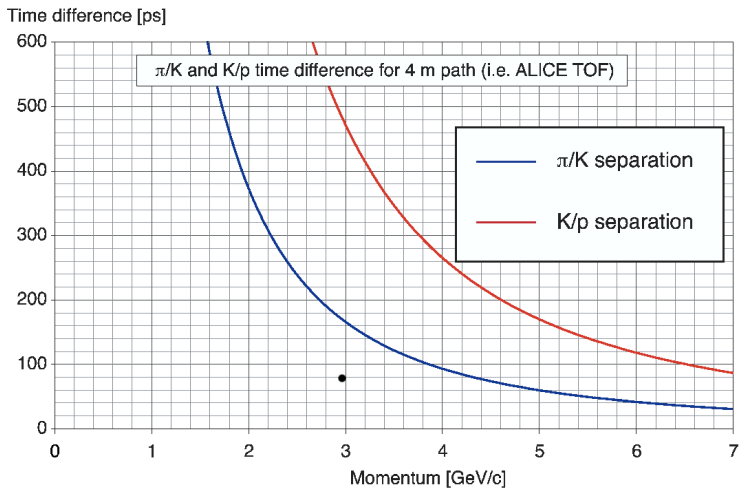

Figure 4.6: Difference between the time-of-flights for π/K and K/p with the same p and a track length of 4 m, as a function of momentum.

The ALICE TOF detector identifies particles using their time-of-flight i.e. the time it takes them to travel from the primary vertex to the TOF sensible layer. The TOF total time resolution σ_{TOF} is the sum of different

contributions:

$$\sigma^2_{TOF} = \sigma^2_{MRPC} + 2\sigma^2_{TDC} + \sigma^2_{Clock} + 2\sigma^2_{ClTRM} + \sigma^2_{FEE} + \sigma^2_{Cal} \tag{4.8}$$

where σ_{MRPC} is the MRPC intrinsic time resolution ($\sigma_{MRPC} \sim 45$ ps), σ_{TDC} is the TDC resolution ($\sigma_{TDC} \sim 20$ ps), σ_{Clock} e σ_{ClTRM} are the resolutions related to the fluctuation of the clock signal ($\sigma_{Clock} \sim 15$ ps) and its distribution towards the front-end cards ($\sigma_{ClTRM} \sim 10$ ps), σ_{FEE} is related to the jitter of the front-end electronics ($\sigma_{FEE} \sim 10$ ps) and σ_{cal} is defined by the uncertainty on the residual channel calibration and on the time slewing effect.

As said before, the time-of-flight used to identify a particle is the time it takes it to travel from the primary vertex to the TOF sensible layer. On top of this, one should have in mind that the TOF detector measures the time with respect to the LHC clock. Since the bunches have a small but finite size and we don't know which of the particles in the bunches have collided, the actual time of the collision may differ from the nominal beam crossing by a time that is related to the size of the bunches[1]. Therefore, the event time has to be measured on an event-by-event basis and subtracted to the measured TOF time t_{TOF}. In the following, we will refer to the event time as time-zero ($t0$) of the event. The time-of-flight t taken to travel from the primary vertex to the TOF layer is actually $t_{TOF} - t0$ and the total time resolution is therefore:

$$\sigma^2_t = \sigma^2_{TOF} + \sigma^2_{t0} \tag{4.9}$$

Obviously, the smaller the total time resolution, the better the PID performance. This means that both the TOF time resolution (σ_{TOF}) and the time-zero resolution (σ_{t0}) have to be as small as possible. Once the TOF detector has been built, all the hardware contributions to the resolution are fixed and σ_{TOF} can be reduced only improving the calibration (see eq. 4.8). σ_{T0} is instead deeply related to the way it is computed and to the multiplicity of the event.

Due to its fundamental role in the PID procedure, I will show some properties of the $t0$ in \$ 4.6. In \$ 4.5 I will describe another important parameter for the TOF PID performance, i.e. the matching efficiency, which is the fraction of global tracks matched with a TOF signal and on which the TOF PID can be applied.

It is important now to point out that, since the TOF can measure the time only with respect to the LHC clock (or to the event time when the $t0$

[1]This would be true even if the bunch crossing would be synchronized with the LHC clock.

is subtracted), it can identify only particles produced at the primary vertex, that is both primary particles and particles coming from the decay of resonances with really short mean life time (like $\Delta^{++}, \phi, \ldots$). Since these resonances decay in the beam pipe, the decay products can not be distinguished from primary particles.

All the results I will show in the next sections of this chapter were obtained from pp data. The events I selected and analyzed were triggered by the BPTXs on bunch crossing, they were not flagged as beam-gas by either V0A or V0C, they were not flagged as beam-gas from the correlation between the SPD clusters and tracklets and they are Minimum Bias (MB) events. In addition, I required also that the selected events have a primary vertex reconstructed with global tracks or, if it is not available, using only the SPD information. This additional cut removes $\sim 10\%$ of the MB events that satisfy the previous requirements. In each event, quality cuts were applied on the tracks, so that only primary particles in the TOF acceptance (central pseudorapidity region) were selected and used in the analysis. In detail, the following track cuts were defined:

- $|\eta| < 0.9$;
- at least 70 clusters in the TPC;
- χ^2 per TPC cluster smaller than 4;
- no kink daughters;
- succesfull inward ITS and TPC refit in the reconstruction procedure;
- p_t-dependent transverse impact parameter (DCA_{xy}) cut (smaller than 7σ from the current vertex resolution);
- at least 1 cluster in SPD;
- impact parameter in the beam direction (DCAz) smaller than 2 cm.

In the following sections I will name "standard cuts" the ones listed above. The results shown hereafter were obtained from ~ 3.5 millions events. The same was anyway found on the full pp statistics at 7 TeV used for the identified particle transverse momentum spectra analysis.

4.5 TOF matching efficiency

To improve the TOF PID performance, the number of particles that can be identified through the time-of-flight procedure has to be maximized. This

means that the matching efficiency (Eff_{match}) defined as the number of tracks matched with a TOF hit over the number of tracks reconstructed by the TPC has to be as high as possible. At the same time, the number of mismatched tracks, that is the tracks matched with a wrong TOF hit, has to be minimized.

As already explained in $ 3.3.2, during the outer propagation step of the reconstruction procedure, the tracks are extrapolated till the TOF sensible surface and a matching window (on the TOF layer) of 3 cm in PbPb interactions[2] and 10 cm in pp collisions is opened around this crossing point. All the TOF clusters inside this matching window are collected. As a first step the algorithm checks if the extrapolated track-point on TOF is inside a pad which gave a signal. If this condition is not satisfied it looks for the closest fired pad within the matching window to be matched with the global track. It is easy to understand that Eff_{match} depends on the quality of the tracking and of the extrapolating procedure, on the correct alignment of the TOF detector (see $ 3.3.2), on the noise level of the TOF readout electronics (fake hits due to the noise can be associated to real tracks) and on the fraction of readout TOF channels that are not enabled during data taking.

A first estimate of the quality of the matching algorithm can be obtained looking at the distance between the extrapolated track-point at the TOF layer and the center of the pad containing the matched hit (TOF space point). Fig. 4.7 and 4.8 show such distance in the x and z directions in the pad local reference frame[3] (ΔX_{pad} and ΔZ_{pad}). The red lines correspond to the pad size in x and z. The fact that the residuals are mainly distributed within the pad size means that the tracks are mainly matched with hits on the TOF pad that was crossed by the track extrapolation. We notice also that the residuals are centered at zero and have a symmetrical distribution showing that the detector is correctly aligned and that the reconstruction procedure works correctly. In Fig. 4.9 ΔZ_{pad} is shown as a function of ΔX_{pad}. The pad shape between [-1.25;1.25] cm in x and [-1.75;1.75] cm in z is clearly visible, with few entries around it (note the color scale), within a radius of 10 cm.

In the top panel of Fig. 4.10 the matching efficiency as a function of the transverse momentum for positive (red), negative (blue) and total (green) particles is shown. Due to the presence of the magnetic field which deflects charged particles, Eff_{match} at $p_t < 0.5\,\mathrm{GeV/c}$ drops quickly. At higher momenta where the multiple scattering becomes less important, it increases smoothly. Since at $p_t < 0.5\,\mathrm{GeV/c}$ Eff_{match} is quite low and a little varia-

[2]For ultra-peripheral events (defined as those events with no more than 10 tracks reconstructed in the TPC) the matching window is increased up to 10 cm.

[3]In the pad local reference frame the x direction is along the pad shortest side while the z direction is along the longest one.

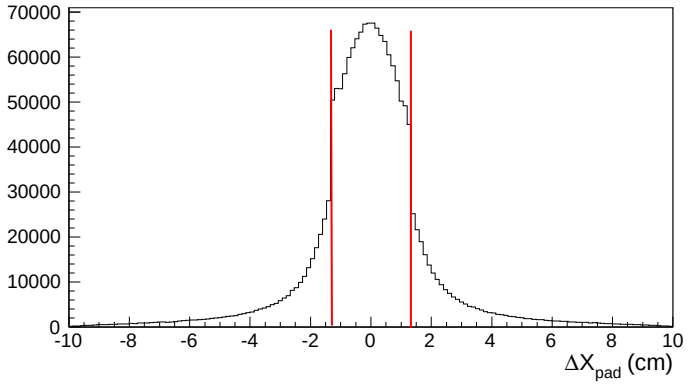

Figure 4.7: Distance in the x direction in the pad reference frame between the extrapolated track-point on the TOF layer and the TOF space point. The red lines correspond to the pad size along x.

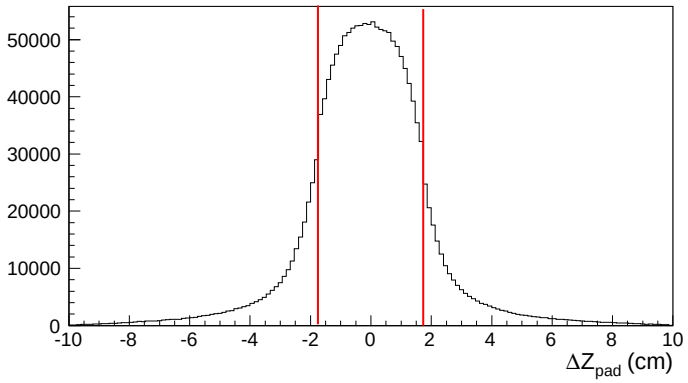

Figure 4.8: Distance in the z direction in the pad reference frame between the extrapolated track-point on the TOF layer and the TOF space point. The red lines correspond to the pad size along z.

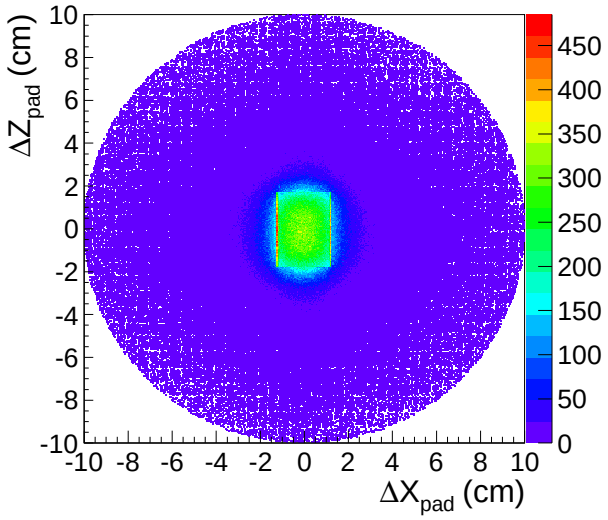

Figure 4.9: Distance along the x and z direction in the pad reference frame between the extrapolated track-point on the TOF layer and the TOF space point. The pad shape (2.5×3.5 cm) is clearly visible.

tion in the track momenta can cause a significant variation in Eff_{match}, only tracks with $p_t > 0.5\,\mathrm{GeV/c}$ are considered for the TOF analyses.

We remind here that the value of the matching efficiency is not only due to the efficiency of the matching algorithm that is larger than 95% but it is also due to the magnetic field at low p_t, the interaction of the particles with the material in front of the TOF detector, the dead and noisy channels, the dead zones in the detector which limit the geometrical acceptance and the intrinsic MRPC efficiency.

In the bottom panel of Fig. 4.10, the ratio between the matching efficiency for positive and negative particles is shown. Since for $p_t > 0.5\,\mathrm{GeV/c}$ it is flat, the systematic effects related to the charge of the particles can be neglected.

In the top panel of Fig. 4.11 Eff_{match} as a function of η is shown. The left panel illustrate the case when no cuts on the track momentum were applied, while in the right one only tracks with $p_t > 0.5\,\mathrm{GeV/c}$ were taken into account. As a results, the distributions on the left side are characterized by values that are systematically lower than those on the right side. The dip in Eff_{match} in the central rapidity region is due to the absence of three central TOF modules in front of the PHOS spectrometer, while at higher η values the matching efficiency drops as a consequence of the barrel geometrical acceptance. In the bottom panels the ratio between the matching efficiency

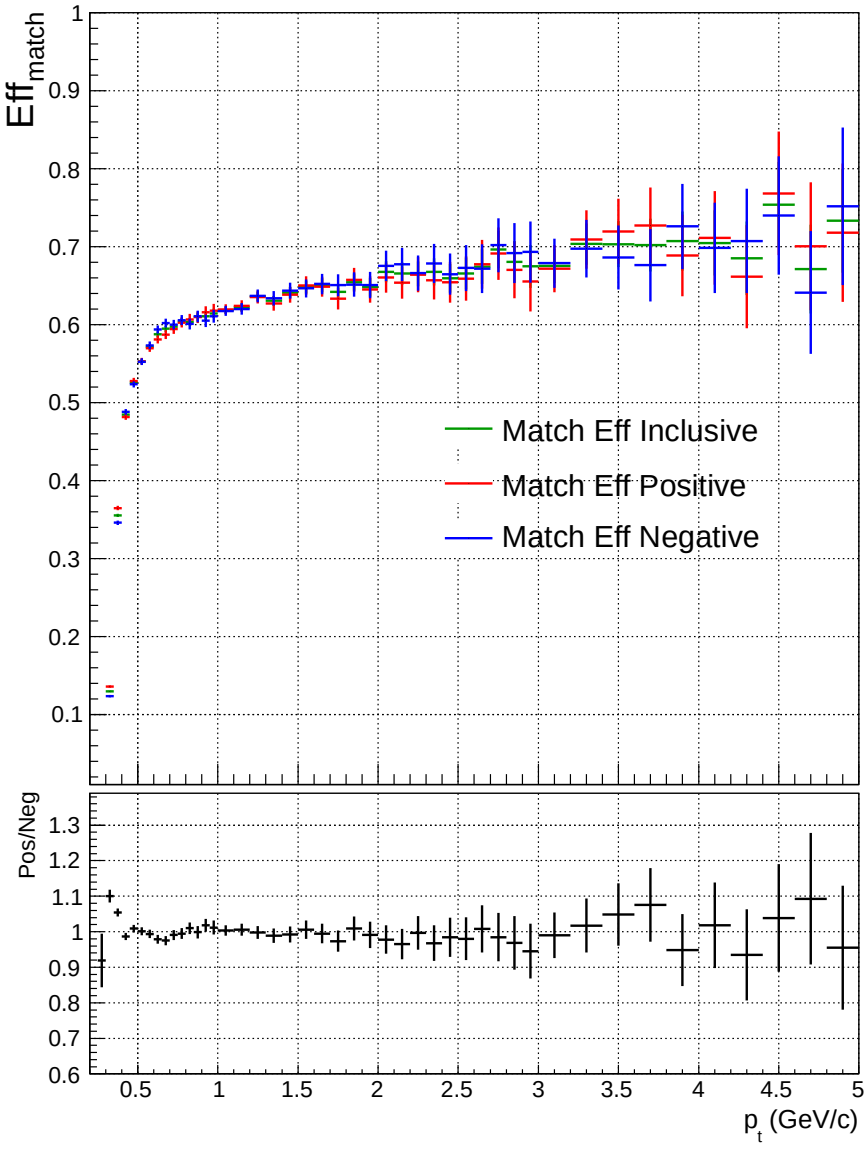

Figure 4.10: Top: matching efficiency for positive (red), negative (blue) and all positive and negative (green) particles as a function of p_t. Bottom: ratio between the matching efficiency of positive and negative particles.

of positive and negative particles is shown.

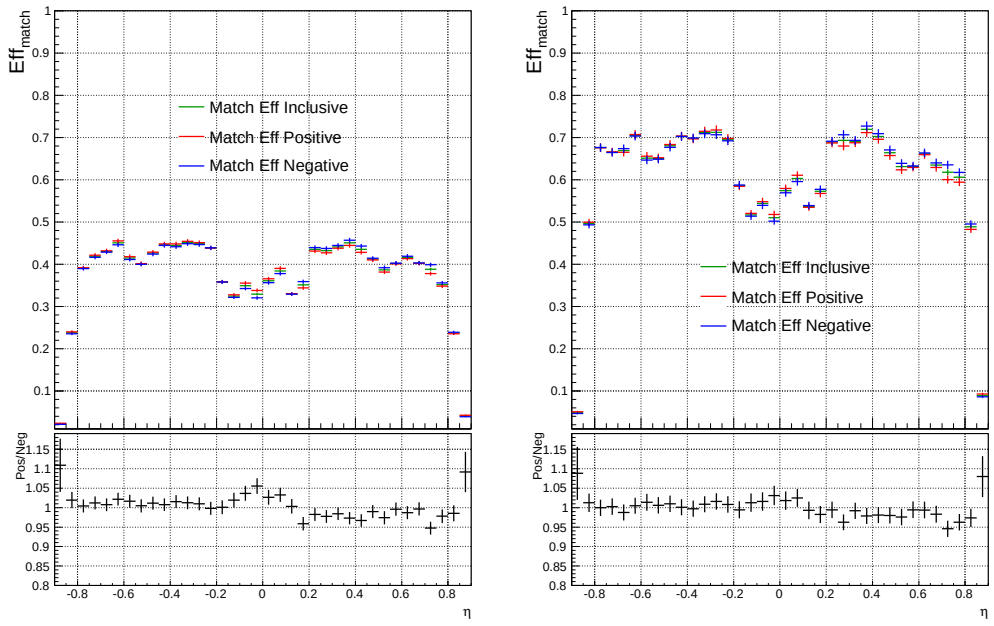

Figure 4.11: Eff_{match} as a function of η. The left panel includes all the tracks passing the quality cuts, while for the right panel, a cut on $p_t > 0.5\,\mathrm{GeV/c}$ was applied. In the bottom panels the ratios between the matching efficiency of positive and negative particles are shown.

An important check to evaluate the effect of the material budget (and so of the multiple scattering) would be the comparison of the matching efficiency in the TOF sectors where the TRD modules are present (in such case the material budget that the tracks have to cross to reach the TOF is higher) and in the ones where they are absent[4]. Since the global track parameters are computed at the primary vertex and because of the presence of the magnetic field, there is no correspondence between the azimuthal angle ϕ of a track (at the primary vertex) and the ϕ at TOF which would allow to determine the TOF sector used for the matching. The only information that can be used are the parameters computed at the last track-point inside a tracking detector (ITS or TPC). In the following we will refer to the azimuthal angle at this point as ϕ_{out}. In Fig. 4.12 Eff_{match} as a function of ϕ_{out} is shown. The violet lines divide the regions with and without TRD modules[5]. An

[4]At the time when these data where taken, only 7 TRD modules were installed. They were SM 0, 1, 7, 8, 9, 10, 17.

[5]This separation would be exact if ϕ_{out} was computed at the inner TOF surface.

increasing/decreasing trend in the region with/without TRD is visible but, due to the magnetic field and the distance between the last track space-point inside a tracking detector and the TOF layer, as already said, the correspondence between ϕ_{out} and the TOF SM is not perfect. These are also the reasons for the difference observed in Eff_{match} between negative and positive particles. We note finally that the low values of Eff_{match} for $260 < \phi_{out} < 320$ are due to the fact that they correspond to SMs 13, 14 and 15, that are the ones without the TOF central module (in correspondence of the PHOS region).

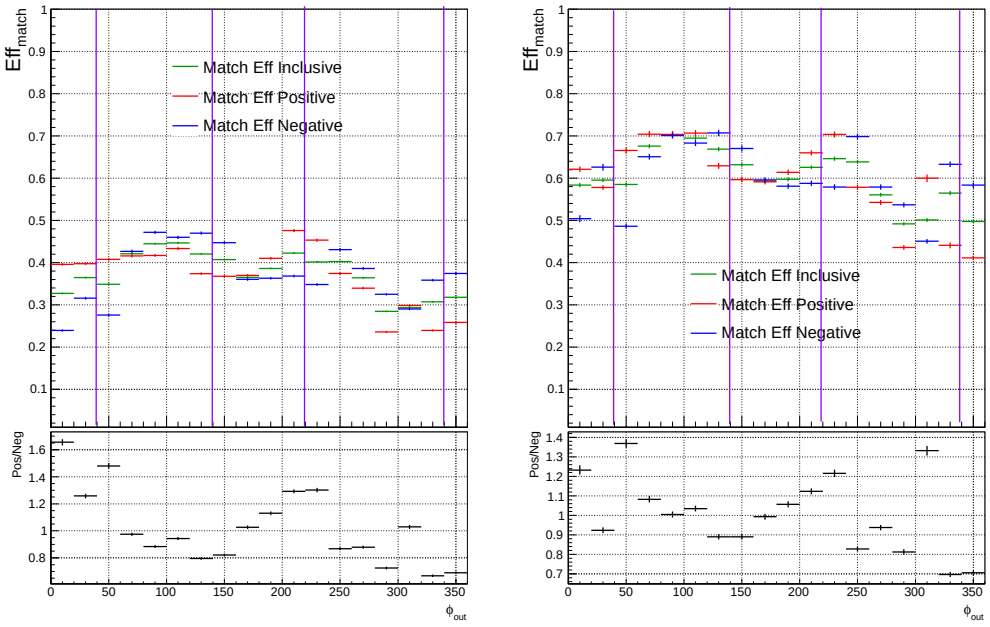

Figure 4.12: Eff_{match} as a function of ϕ_{out}. The violet lines guide the eye to the regions with and without TRD modules.

To verify that the matching efficiency is correctly reproduced in the Monte Carlo, in Fig. 4.13 Eff_{match} for positive, negative and inclusive particles both in data and Monte Carlo is shown. As we can see from the bottom plot, the Eff_{match} on data is a few percent $(2 - 4\%)$ higher than the Monte Carlo one. This is due to the fact that the pad efficiency was simulated as 2% lower than the real one.

If we compare Eff_{match} in data and Monte Carlo as a function of η and ϕ_{out} the same level of agreement is observed. One can conclude that the Monte Carlo matching efficiency for positive, negative and inclusive particles, reproduces the measured one within a few percent. This residual difference

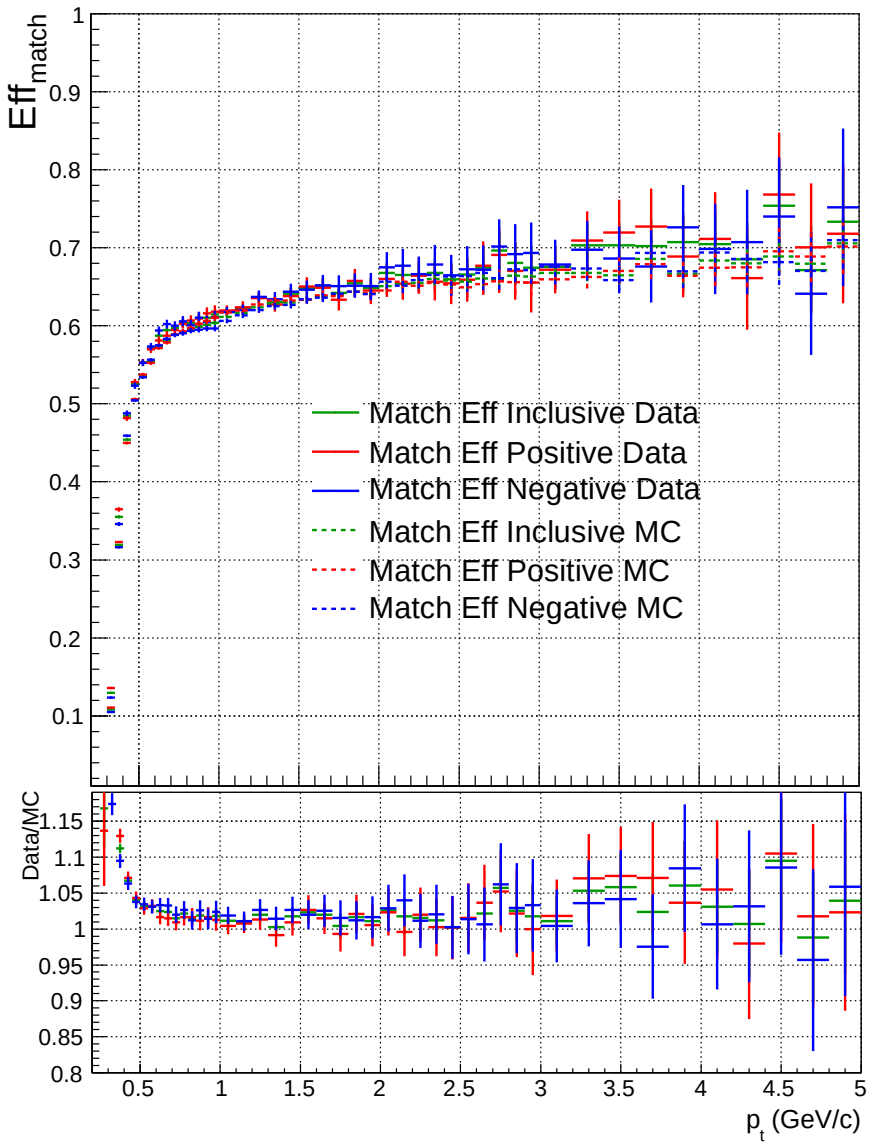

Figure 4.13: Comparison between the matching efficiency obtained from data (solid line) and Monte Carlo (dotted line) for positive (red line), negative (blue line) and inclusive (green line) particles.

can be considered as part of the systematic error. Since in pp collisions the most aboundant particle specie are the pions, this difference can also be considered as the difference in the pion matching efficiency between data and Monte Carlo. However, at low p_t, using the TPC PID is possible to compare Eff_{match} in data and Monte Carlo separately for π, K and p.

From the Monte Carlo simulation we can also check the performance of the matching algorithm. If we define N_{TOF} the number of tracks matched with a signal on TOF, $N_{TOF,t}$ the number of tracks matched with the right TOF signal, $N_{TOF,f}$ the number of tracks matched with the wrong TOF signal and N_{TPC} the number of tracks reconstructed by the TPC, the matching efficiency Eff_{match}, the right matching efficiency $Eff_{match,good}$ and the contamination $Cont_{match}$ can be expressed in the following way:

$$Eff_{match} = \frac{N_{TOF}}{N_{TPC}}; \quad Eff_{match,good} = \frac{N_{TOF,t}}{N_{TPC}}; \quad Cont_{match} = \frac{N_{TOF,f}}{N_{TOF,t} + N_{TOF,f}}. \tag{4.10}$$

In Fig. 4.14 Eff_{match} (blue), $Eff_{match,good}$ (gray) and $Cont_{match}$ (black) are shown. We can see that the contamination at $p_t > 0.5\,\mathrm{GeV/c}$ is flat and less than 10%.

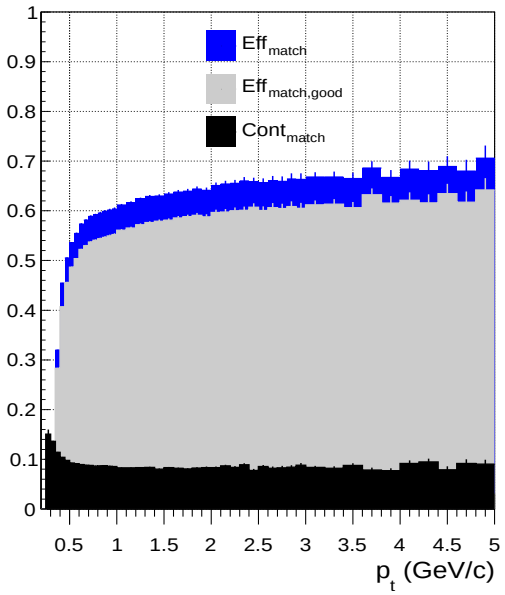

Figure 4.14: Eff_{match} (blue), $Eff_{match,good}$ (gray) and $Cont_{match}$ (black) obtained from Monte Carlo simulations.

Finally, in the analyses based on particle identification, the matching

efficiency defined for each hadron species (π, K, p) are necessary since they are not expected to be the same due to the different interaction cross-section in the material. Eff_{match} can be derived from Monte Carlo simulations where we know a priori the true identity of the particles[6]. In Fig. 4.15 the matching efficiency for positive (solid line) and negative (dotted line) pions (red), kaons (blue) and protons (green) is shown.

From Fig. 4.15 it is clear that Eff_{match} for K^+ and p is higher than the one for K^- and $\overline{p}$, especially at low p_t. As mentioned above, a slight difference between protons and anti-protons and between kaons and anti-kaons is expected due to their different cross sections. This would anyway not explain the differences observed here which was found to be due to the fact that the cross sections for $\overline{p}$ and K^- in GEANT3 (the ALICE simulation transport code) are not correctly reproduced while Fluka is expected to provide a more accurate prediction. For this reason, a comparison between the GEANT3 and Fluka simulations was done and the two correction factors reported in Fig. 4.16 were extracted.

The final matching efficiency can be obtained scaling the Monte Carlo predictions by the GEANT/Fluka correction factors, as shown in Fig. 4.17. After the correction factors have been applied, the ratio between Eff_{match} for positive and negative particle is flat and close to unity for $p_t > 1\,\mathrm{GeV/c}$. At lower momenta some differences are still present.

[6]For each collected run, a Monte Carlo sample is produced with the same geometry, hardware and readout configuration to be as realistic as possible.

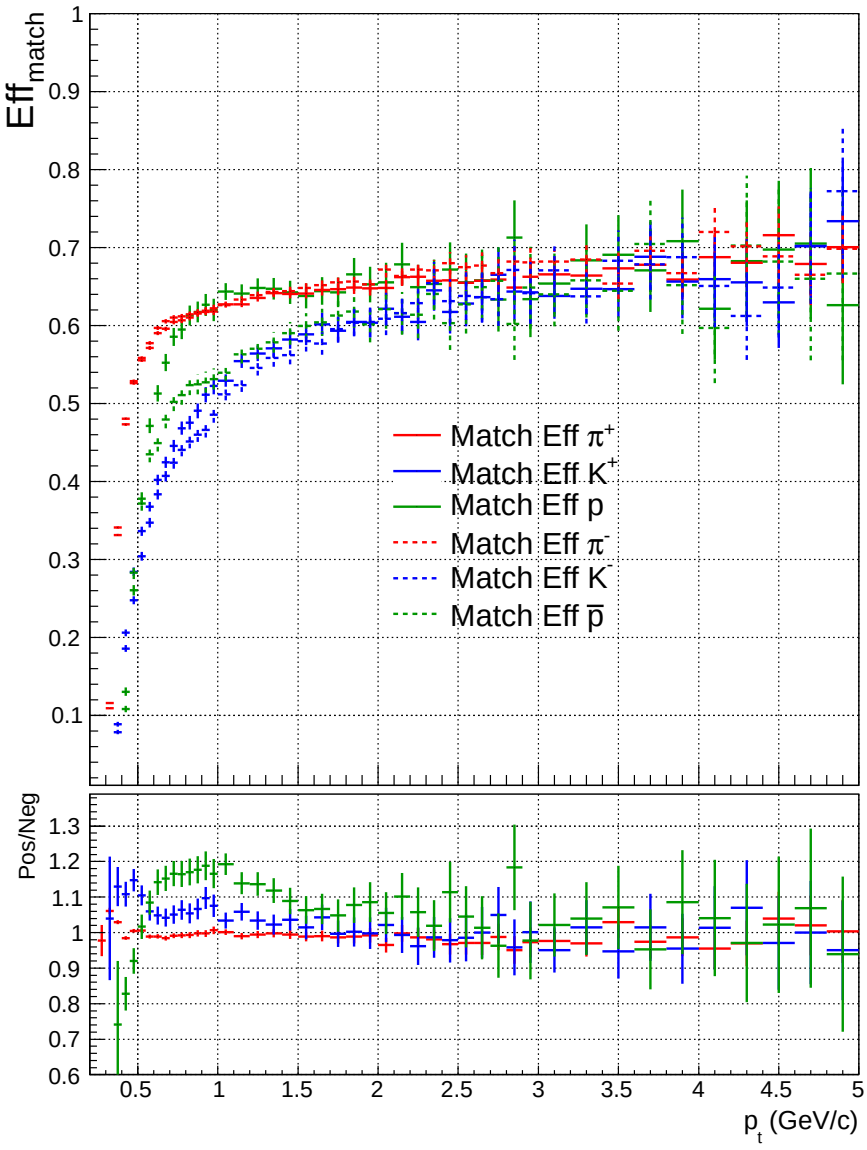

Figure 4.15: Matching efficiency for pions (red), kaons (blue) and proton (green) (positive (solid line) and negative (dotted line)) as obtained from Monte Carlo simulations.

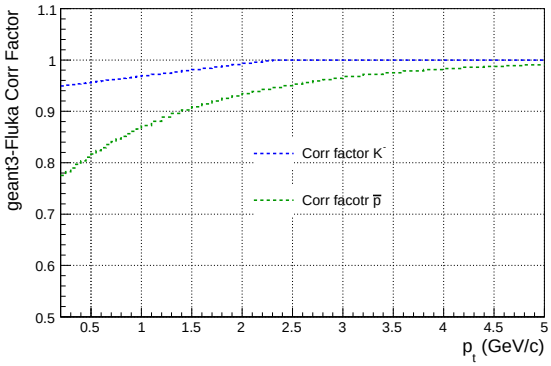

Figure 4.16: Correction factors for the $\overline{p}$ and K^- matching efficiency derived from the comparison of GEANT3 and Fluka simulations.

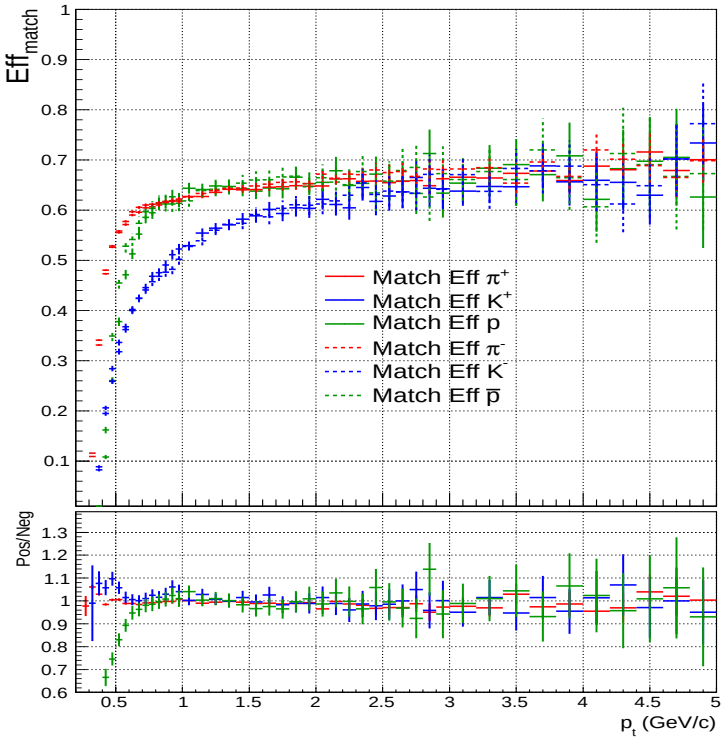

Figure 4.17: Final matching efficiency (after GEANT/Fluka correction) for pion (red), kaon (blue) and proton (green). Positive (solid line) and negative (dotted line) tracks are shown.

4.6 Event Time

As said before, the time-of-flight used to identify a particle is the time it takes it to travel from the primary vertex to the TOF sensible layer. On top of this, one should have in mind that the TOF detector measures the time with respect to the LHC clock. Since the bunches have a small but finite size and we don't know which of the particles in the bunches have collided, the actual time of the collision may differ from the nominal beam crossing by a time that is related to the size of the bunches[7]. Therefore, the event time has to be measured on an event-by-event basis and subtracted to the measured TOF time t_{TOF}. In the following, we will refer to the event time as time-zero ($t0$) of the event. The time-zero can be provided in three different ways: by the calibration procedure only, by the T0 detector, by the TOF detector. These different methods to provide the time-zero and its resolution will be described in $ 4.6.1, $ 4.6.2 and $ 4.6.3.

4.6.1 Time-zero provided by $t0_{Fill}$

During the calibration procedure (see $ 3.3.1) the $t0_{Fill}$, that is the average start time of the events collected in a given fill, is always subtracted from each TOF time measurement to realign with respect to the LHC clock. If for some events it is not possible to calculate the time-zero, only the $t0_{Fill}$ is used to correct the measured time. The uncertainty associated to the time-zero is, in this case, $t0_{Spread}$ that is related to the average bunch size in the fill, and is estimated as the sigma of the fit performed to calculate the $t0_{Fill}$ or form the longitudinal spread of the vertex. To summarize, if the computation of the time-zero is not possible $t0 = 0$ and $\sigma t0 = t0_{Spread}$. Of course the $t0_{Spread}$ can be different fill by fill, depending on the beam conditions; for the data used for the identified transverse momentum spectra analysis that will be reported in the next chapters the $t0_{Spread}$ was quite uniform and rather small ($\sim$ 120 ps) thanks to the limited size of the bunches.

4.6.2 Time-zero provided by the T0 detector

The ALICE detector designed to provide the time-zero information is the T0. It consists of two arrays of 12 cherenkov counters each, T0A and T0C, placed at 375 cm and -72.7 cm from the interaction point along the beam axis. We define t_{T0A} and t_{T0C} the first signal in time among the ones detected by the 12 counters of T0A and T0C respectively. If the T0 detector is properly

[7]This would be true even if the bunch crossing would be synchronized with the LHC clock.

calibrated, the time it takes to a particle produced in an event synchronous with the LHC clock to travel from the IP to each T0 PMT (photomultiplier) is known, hence the interaction time can be extracted from t_{T0A} and t_{T0C}. Depending on the multiplicity of the event and the efficiency and the noise rate of the T0 detector, it could be that only t_{T0A} or t_{T0C} is available. In the following, we will call $t0_{T0A}$ the time-zero computed from the t_{T0A} only, $t0_{T0C}$ the time-zero computed from the t_{T0C} only, and $t0_{T0AC}$ the one defined as the average of both measurements, $t0_{T0AC} = (t0_{T0A} + t0_{T0C})/2$. If only t_{T0A} or t_{T0C} is available, in order to have an accurate measure of the event time, the z position of the primary vertex has to be taken into account. In order to reject $t0$ values coming from various effect such as noise and satellite collisions, an upper cut ($T0Cut$) on the measured $t0$ has to be applied. This cut is equal to three times the $t0_{Spread}$ and is such that only the values smaller than this are accepted and can be subtracted to the t_{TOF} to compute the actual time-of-flight. This cut was applied for all the following plots.

In Fig. 4.18 the distributions of $t0_{T0A}$, $t0_{T0C}$ end $t0_{T0AC}$ are shown. As one can see, they are all centered at zero, as expected.

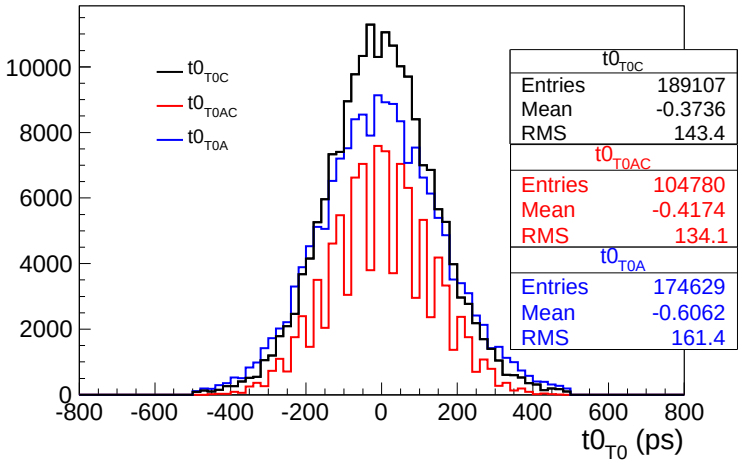

Figure 4.18: Distribution of $t0_{T0A}$, $t0_{T0C}$ end $t0_{T0AC}$. Only the values satisfying the $T0Cut$ are shown.

The resolution on $t0_{T0AC}$ ($\sigma t0_{T0AC}$) is $\sqrt{2}$ times better than the one on $t0_{T0A}$ and $t0_{T0C}$, assuming that they have the same resolution. Moreover, $\sigma_{t0_{T0AC}}$ can be derived from the $(t0_{t0A} - t0_{t0C})/2$ distribution. Here, both $t0_{T0A}$ and $t0_{T0C}$ are corrected for the primary vertex position. Fig. 4.19 shows the $(t0_{t0A} - t0_{t0C})/2$ distribution. From the superimposed gaussian fit, one

can see that $\sigma t0_{T0AC} \sim 50$ ps. The T0 detector is also able to give an estimate of the primary vertex position via the $(t_{T0A} - t_{T0C})/2$ distribution.

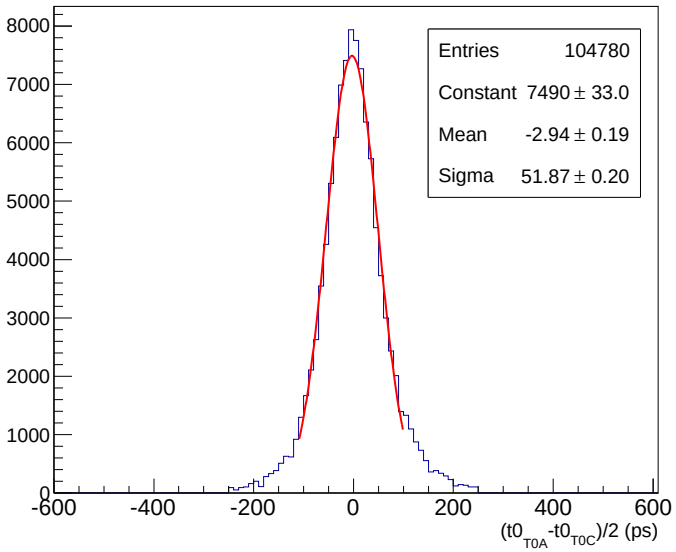

Figure 4.19: Distribution of $(t0_{t0A} - t0_{t0C})/2$. The sigma of the fit (σ = 51.87 ps) corresponds to the resolution on $t0_{T0AC}$.

In Fig. 4.20 the resolution of $t0_{T0AC}$ as a function of the event multiplicity (defined as the number of tracks satisfying the standard cuts listed in \$4.4 but in $|\eta| < 0.8$ (instead of $|\eta| < 0.9$) and with $p_t > 0.15$ GeV/c) is shown. Due to the analyzed statistics, only events with a multiplicity smaller that 30 are shown. The expected decreasing trend is clearly visible.

In Fig. 4.21 the mean value of $t0_{T0AC}$ as a function of the event multiplicity is shown. A slight decrease is visible going from low to high multiplicities even if the time-zero should be independent. Anyway the effect is limited to $\sim 10 - 20$ ps.

The inclusive efficiency on Minimum Bias events for the T0 detector to provide a time-zero measurement via $t0_{T0A}$, $t0_{T0C}$ or $t0_{T0AC}$ is respectively $\sim 51\%$, $\sim 56\%$ and $\sim 31\%$. In Fig. 4.22 the $t0_{T0AC}$, $t0_{T0A}$ and $t0_{T0C}$ efficiency as function of event multiplicity is shown. As one can observe the efficiency increases with the event multiplicity. As already said in the previous section, if the time-zero is not available, it is set to zero and its resolution is set to $t0_{Spread}$.

As it was shown, the T0 detector can provide time-zero information in a large fraction of events with a good time resolution, but it was in the

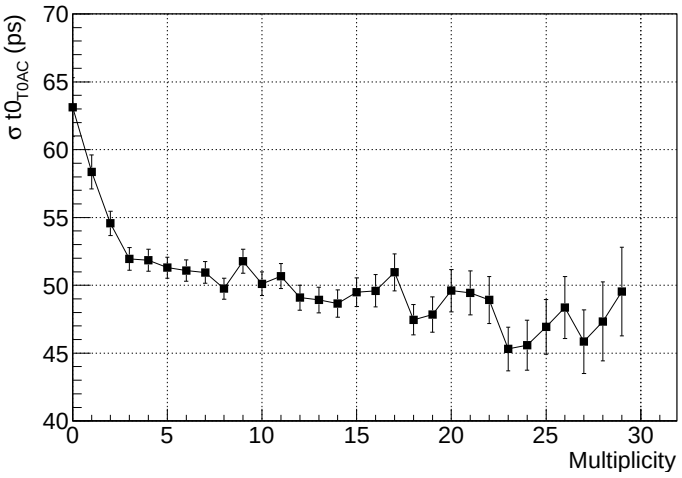

Figure 4.20: $t0_{T0AC}$ resolution of as a function of the event multiplicity.

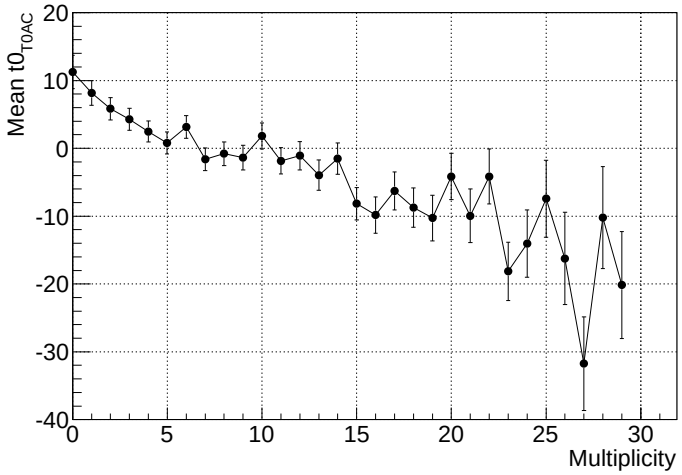

Figure 4.21: $t0_{T0AC}$ mean value as a function of the event multiplicity.

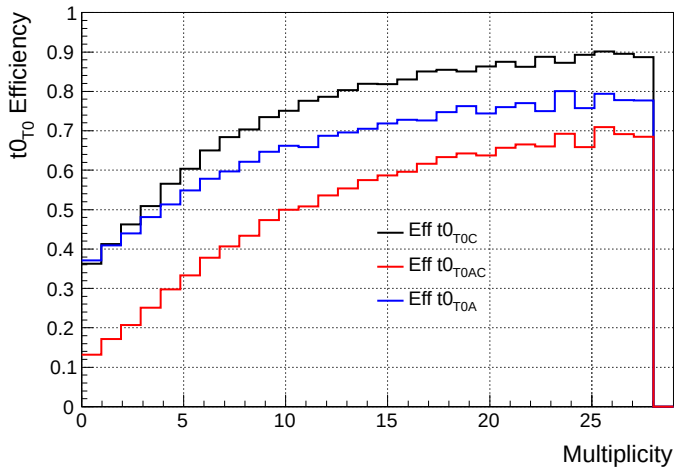

Figure 4.22: $t0_{T0AC}$, $t0_{T0A}$ and $t0_{T0C}$ efficiency as a function of the event multiplicity.

data acquisition configuration only in a small fraction of the events used for the transverse momentum spectra analysis (LHC10b and LHC10c periods). For this reason and since in the corresponding Monte Carlo the T0 detector information was not correctely simulated, I decided to not use the time-zero provided by the T0 detector in the spectra analysis.

4.6.3 Time-zero provided by the TOF detector

The TOF detector is able to compute the time-zero of the events using a combinatorial algorithm. For each event it selects the tracks matched with TOF hits that satisfy the standard cuts (see \$4.4) and divides them in subsets of maximum 10 tracks each. Since every track can be a pion, a kaon or a proton (which are the most abundant species reaching TOF), each set has 3^n possible combinations of mass hypothesis, where n is the number of tracks in the set. The algorithm looks for the one which minimizes the value of χ^2 defined as:

$$\chi^2 = \sum_i \frac{(t0[i] - \overline{t0})^2}{\sigma t0[i]^2} \tag{4.11}$$

where i is the track index in the set[8]. If we define $t_{TOF}[i]$ the time-of-flight measured by the TOF detector, $t_{exp}[i]$ the expected time for the mass hy-

[8]If a track with a too high χ^2 value is present, it is removed from the set and the total χ^2 is calculated again.

pothesis assumed in that combination and $\sigma t0[i]$ the expected sigma for the track i (see \$5.2 for the definitions), we have:

$$t0[i] = t_{TOF}[i] - t_{exp}[i] \tag{4.12}$$

$$\overline{t0} = \sum_i \frac{t0[i]}{\sigma^2 t0[i]} / \sum_i \frac{1}{\sigma^2 t0[i]} \tag{4.13}$$

$$\sigma\overline{t0} = \sqrt{\frac{1}{\sum_i \frac{1}{\sigma^2 t0[i]}}} \tag{4.14}$$

The search of the combination of the mass hypotheses that minimize the χ^2 function is done for all the sets and the final time-zero of the event ($t0_{TOF}$) is set to the mean of the $\overline{t0}$ computed in each set weighted on its error $\sigma\overline{t0}$. As usual, if the procedure is not able to compute the time-zero, $t0$ is set to zero and $\sigma t0$ to $t0_{Spread}$.

To avoid to introduce any bias on the PID procedure, for each event the time-zero is calculated as a function of p. In detail, defining 10 p intervals[9], the time-zero in a given p bin is derived with the algorithm described above using all the selected tracks in the event, except those with a momentum belonging to that p interval. In other words, for a track with momentum p, the time-zero that will be subtracted to its t_{TOF} is the one computed with all tracks in the event except the ones in the corresponding p interval. In this way a track is never used to compute the time-zero that has to be subtracted to its own t_{TOF}, avoiding any bias on the PID[10].

Of course, depending on the number of tracks and on their p spectra, it can happen that the $t0_{TOF}$ can be computed only for some p intervals. For all the others the $t0_{Spread}$ is assumed. In the following plots only events for which the $t0_{TOF}$ is available are taken into account.

In Fig. 4.23 and in Fig. 4.24 the $t0_{TOF}$ and the $\sigma t0_{TOF}$ for each p interval are shown. As expected the shape of the distributions is the same for each range. This means that the algorithm does not depend on the transverse momentum of the tracks it uses.

The only difference between different p ranges is the fraction of events for which it was possible to derive the $t0_{TOF}$, as can be seen in Fig. 4.25. The red line takes into account all the MB events with a reconstructed primary vertex

[9]The 10 p ranges are defined by the following intervals: bin 1: $0.3 < p < 0.5$, bin 2: $0.5 < p < 0.6$, bin 3: $0.6 < p < 0.7$, bin 4: $0.7 < p < 0.8$, bin 5: $0.8 < p < 0.9$, bin 6: $0.9 < p < 1.0$, bin 7: $1.0 < p < 1.2$, bin 8: $1.2 < p < 1.5$, bin 9: $1.5 < p < 2.0$, bin 10: $2.0 < p < 3.0$ where all the values are in GeV/c.

[10]As an example, the $t0_{TOF}$ of a track with $p = 1.25$ GeV/c is the one associated to the 8^{th} p interval that is computed with all the tracks of the event but those with $1.2 < p < 1.5$.

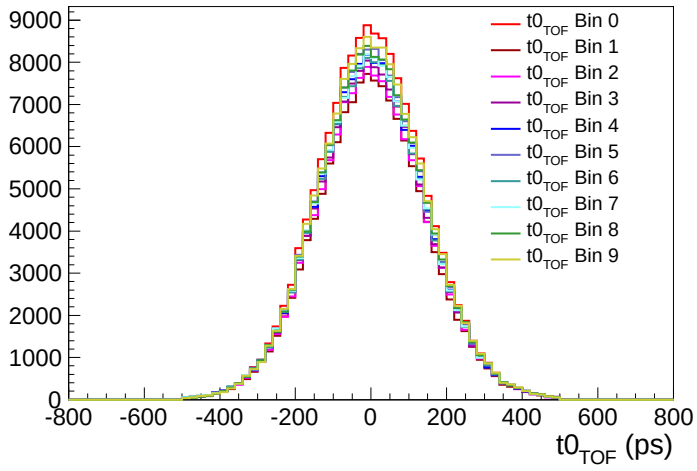

Figure 4.23: $t0_{TOF}$ for each p interval.

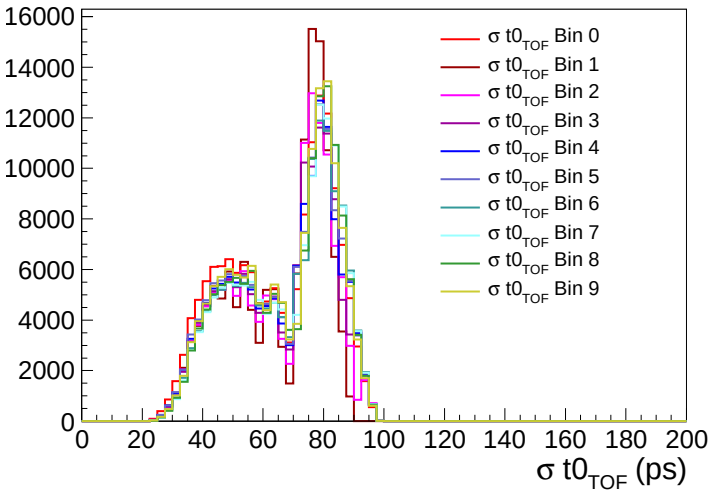

Figure 4.24: $\sigma t0_{TOF}$ for each p interval.

while the blue one requires that they have also at least one track matched with TOF that satisfies the standard cuts. The increasing trend from bin1 to bin9 is due to the fact that the p distribution of the tracks reaching the TOF detector has an exponential shape. It is hence less probable to be able to compute the $t0_{TOF}$ in lowest p ranges where most tracks are. We can also see that for more than 55% of events with at least one track reaching TOF, the TOF detector is able to compute the time-zero.

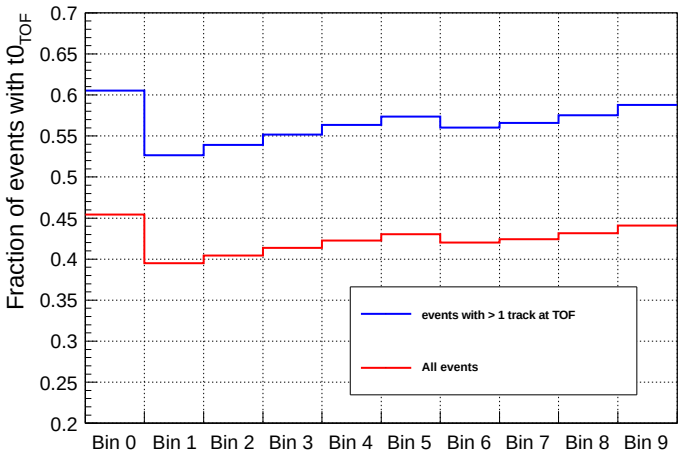

Figure 4.25: Fraction of events with $t0_{TOF}$ for each p interval. The red line corresponds to all the MB events with a reconstructed primary vertex while the blue one requires that they have also at least one track matched with a TOF hit and satisfying the standard cuts.

In Fig. 4.26 the efficiency for each p range of the $t0_{TOF}$ computation as a function of the multiplicity of the MB events is shown. The black line represents the fraction of events for which it was possible to calculate the $t0_{TOF}$ in at least one p interval. As expected, for all p ranges the efficiency increases with the multiplicity.

In Fig. 4.27 the mean value of $\sigma t0_{TOF}$ as a function of the number of selected tracks n used in the algorithm is shown. This distribution can be fitted with a function $f(n) = A/\sqrt{n-1}$ where A is ~ 110 ps. The plot was obtained for the p interval $1.5 < p < 3.0$ GeV/c.

In Fig. 4.28 we can see that the mean value of $t0_{TOF}$ does not depend on the multiplicity of the event and on the number of tracks n used in the algorithm.

Comparing the properties of the time-zero computed by the TOF detector

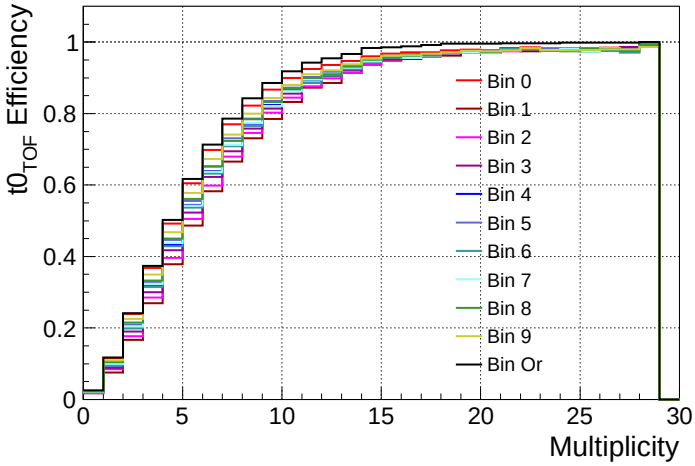

Figure 4.26: $t0_{TOF}$ efficiency computation in the different p ranges as a function of the multiplicity for MB events with a reconstructed vertex. Each color represents a p interval. The black line is the fraction of events in which the computation of the $t0_{TOF}$ was possible in at least one p range.

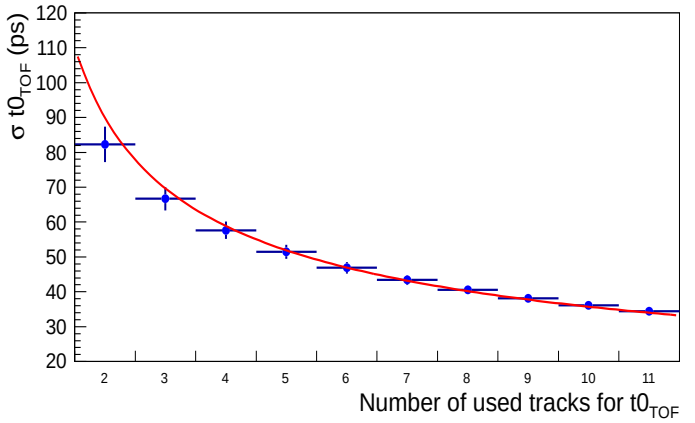

Figure 4.27: $\sigma t0_{TOF}$ mean value as a function of the number of tracks n used in the $t0_{TOF}$ algorithm. The p range $1.5 < p < 3.0$ GeV/c was considered. The red line is the fit with a function of the form $f(n) = A/\sqrt{n-1}$.

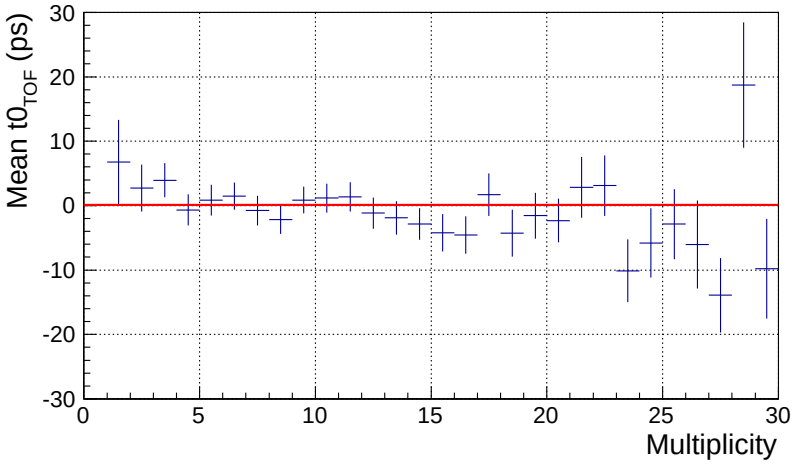

Figure 4.28: $t0_{TOF}$ mean value as a function of the multiplicity of the event.

in data and Monte Carlo we find that the distributions of $t0_{TOF}$ and $\sigma t0_{TOF}$ for each p range are the same. What is different is the fraction of events for which the $t0_{TOF}$ can be computed in each interval as can be seen in Fig. 4.29 where the solid lines correspond to data and the dotted ones to Monte Carlo. The red lines take into account all the MB events with a reconstructed primary vertex. For the blue ones the additional requirement to have at least one track matched with a TOF hit that satisfies the standard cuts is included.

The $t0_{TOF}$ efficiency as a function of the multiplicity for events with at least 1 track matched with TOF shows some differences between data (red line) and Monte Carlo (blue line), as shown in Fig. 4.30.

We have seen that the time-zero can be provided by the T0 detector in three different configuration ($t0_{T0A}$, $t0_{T0C}$ and $t0_{T0AC}$) and by the TOF detector in all p intervals (TOFAND) or only in a subset of them (TOFOR). In Fig. 4.31 the relative importance of these configurations is shown. If we consider all the MB events with the reconstructed primary vertex and at least one track matched with TOF, the $t0_{TOF}$ can be computed at least in one p interval in more than 60% of the events while the $t0_{T0}$ in more than 80%. In only less than 10% of the events the TOF is able to compute the time-zero when the T0 is not. If we had the possibility to use both the $t0_{TOF}$ and the $t0_{T0}$ we would be able to compute the $t0$ in 90% of the events, having to rely on the $t0_{Spread}$ only in the remaining $\sim$ 10%. This would result in a better mean time resolution (see eq. 4.9) and, as a consequence, in an improved PID performance. As already explained, in the spectra analysis presented in this

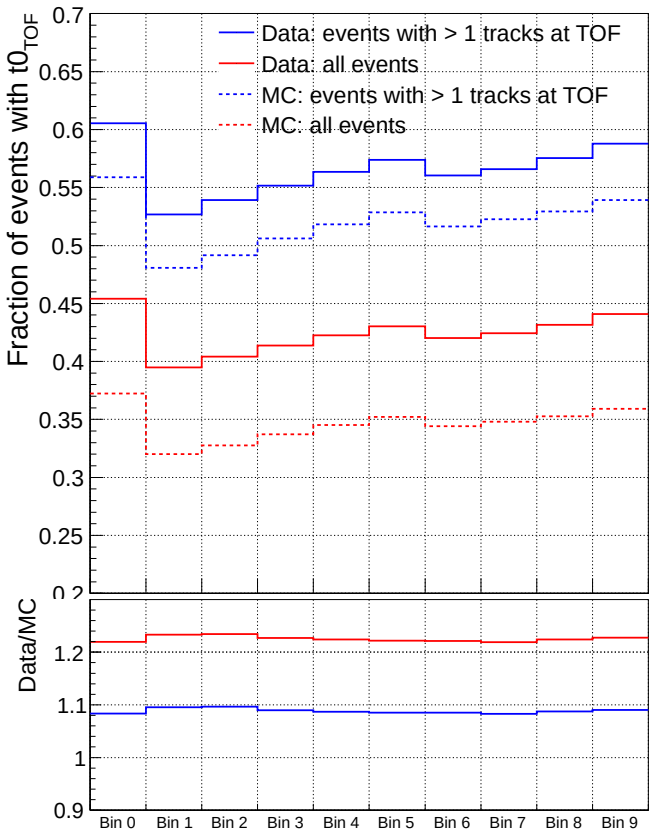

Figure 4.29: Fraction of events with $t0_{TOF}$ for each p range in data (solid lines) and Monte Carlo (dotted lines). The red lines refer to all the MB events with a reconstructed primary vertex while the blue ones require in addition that they have at least one track matched with a TOF hit that satisfies the standard cuts.

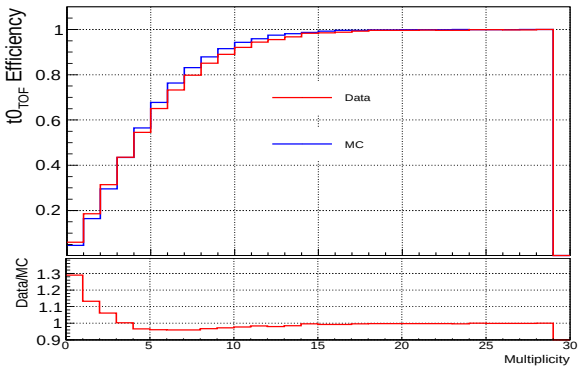

Figure 4.30: $t0_{TOF}$ efficiency as a function of the multiplicity for events with at least 1 track matched with a TOF hit for data (red line) and Monte Carlo (blue line).

thesis the $t0_{T0}$ could not be used. Therefore we will have a sample of events with good time resolution (for which the $t0_{TOF}$ was used) and a smaller one with worse time resolution (for which the $t0_{Fill}$ was used). The consequences of the presence of these two samples with different time resolution on the PID method and on the final transverse momentum spectra results will be clear in the next chapter.

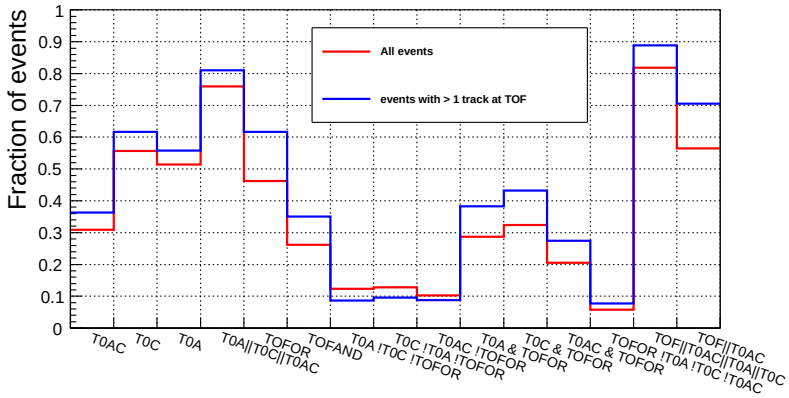

Figure 4.31: Fraction of events with the time-zero provided by different combination of $t0_{T0}$ and $t0_{TOF}$ (see text for more details).

Chapter 5

Identified hadron spectra with the TOF detector: analysis details

As already said in the previous chapters, the ALICE experiment has been designed to study ultrarelativistic Pb-Pb collisions in order to understand the properties of a new state of matter, the QGP, predicted to be formed at high temperature ($T \sim 170\,\mathrm{MeV}$) or energy density by lattice QCD calculations. To access the thermal parameters of the system created in heavy-ion collisions at the kinetic and chemical freeze-out, the measurement of identified particle transverse momentum spectra is necessary. In the ALICE experiment, particle spectra are studied not only in Pb-Pb collisions but also in pp interactions which provide a useful reference for the understanding of heavy-ion data and are crucial to tune Monte Carlo models.

In this chapter, after a brief description of the general TOF PID performance, details concerning the PID unfolding procedure will be given. This is the method that was used to reconstruct the identified transverse momentum spectra in pp collisions at $\sqrt{s} = 7\,\mathrm{TeV}$ with the TOF detector. Finally, a comparison with a more "traditional" PID approach, the so-called 3σ cut, will be reported.

5.1 TOF PID performance

The ALICE TOF detector identifies particles using their time-of-flight, i.e. the time it takes them to travel from the primary vertex to the TOF sensible layer (see §4.4). The mass m of a particle, and as a consequence its identity, can infact be determined on the basis of eq. 5.1:

$$m = p\sqrt{\frac{t^2}{L^2} - 1}, \tag{5.1}$$

from the measurement of its time-of-flight t, its track length L and its momentum p (here $c = 1$). The reconstructed mass distribution is shown in Fig. 5.1 where the time-of-flight was measured with the TOF detector, and L and p were determined by the tracking system. As one can see, the three particle species π, K and p can be clearly distinguished, together with a hint of deuterium particles, as narrow peaks superimposed on a continuous distribution that represents the tracks matched with a wrong TOF hit (mismatch contribution).

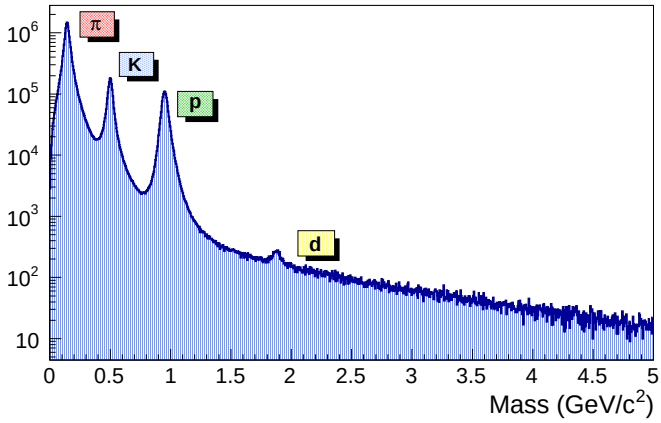

Figure 5.1: Mass spectrum as obtained by the TOF detector in pp collisions at $\sqrt{s} = 7\,\text{TeV}$. Signals from π, K, p and deuterons (d) are clearly visible as narrow peaks superimposed on a continuous distribution that represents the tracks matched with a wrong TOF hit.

In Fig. 5.2 the β of the particles, defined as $\beta = L/t \times c$ (where c is the speed of light) is shown as a function of the rigidity (i.e. momentum times charge). Once again, the TOF PID capability is evident from the clear separation of the bands, corresponding to different particle species. The entries between the bands are due to the mismatch.

5.2 TOF PID methods

Following an approach which is conceptually equivalent to the one outlined in the previous section, in ALICE the particle identification with the TOF

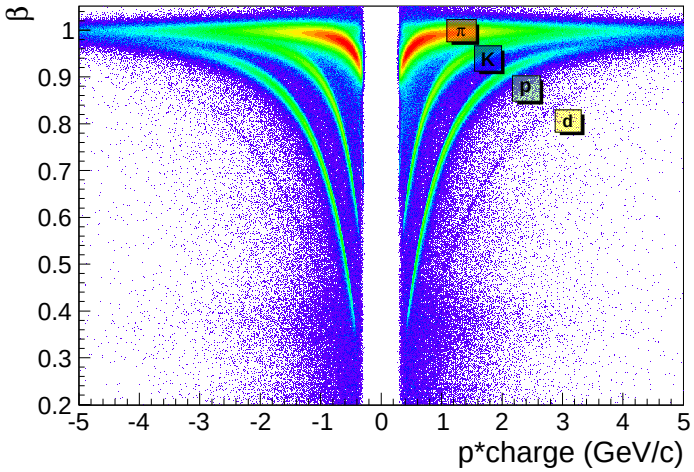

Figure 5.2: β of reconstructed tracks as a function of the momentum times charge. The bands corresponding to π, K, p and d are clearly visible. All the points that do not follow the band distribution are due to the mismatch.

detector is actually based on the comparison between the time-of-flight measured by TOF (t_{TOF}) and the corresponding expected time ($t_{exp,i}$), that is calculated from the momentum p and the track length L for each mass hypothesis i (i.e. hypothesis on the particle identity) considered in the analysis. In other words, the expected time is the time it would take to a particle of mass m_i to go from the interaction point to the TOF. This approach has the advantage of including more accurately the energy loss a particle may experience along its path to the TOF. Infact, in order to take into account the energy loss and the consequent variation in the track momentum, $t_{exp,i}$ is calculated as the sum over k of the small time increments $\Delta t_{i,k}$, each of which is the time a particle of mass m_i and momentum p_k spends to travel along each propagation step k (of Δl_k length) during the track reconstruction procedure (see eq. 5.2):

$$t_{exp,i} = \sum_k \Delta t_{i,k} = \sum_k \frac{\sqrt{p_k^2 + m_i^2}}{p_k} \Delta l_k. \tag{5.2}$$

Therefore, the fundamental variable to perform PID with the TOF detector is $t_{TOF} - t0 - t_{exp,i}$ (here the time-zero $t0$ is subtracted). Its expected resolution $\sigma_{PID,i}$ for the mass hypothesis i is the combination of the TOF detector time resolution σ_{TOF}, the time-zero resolution σ_{t0} and the tracking

resolution $\sigma_{t_{exp}}$ as shown in eq. 5.3

$$\sigma^2_{PID,i} = \sigma^2_{t_{exp}} + \sigma^2_{TOF} + \sigma^2_{t0}, \tag{5.3}$$

where $\sigma_{t_{exp}}$ is defined as in eq. 5.4, in the hypothesis that the resolution on the length of the track is negligible with respect to the one on the momentum, and Δp is the momentum resolution:

$$\sigma^2_{t_{exp}} = \left(\frac{\Delta p \cdot t_{exp,i}}{1 + \frac{p^2}{m_i^2}} \right)^2 . \tag{5.4}$$

As can be seen, the term where the mass hypothesis dependence is present is the tracking term $\sigma_{t_{exp}}$.

The TOF information can be used to perform PID in different ways. In this thesis, two methods have been considered: the unfolding technique and a 3σ cut "traditional" analysis. Details on these methods will be given in the next sections.

For the spectra analysis presented herein the unfolding technique has been chosen since it allows to extend the PID p_t coverage with respect to the other methods, without having to rely on any Monte Carlo information and simulation. To validate the unfolding method, thorough studies with the 3σ cut method have been performed and the spectra obtained with it have been compared with those obtained with the unfolding.

Despite the fact that the two PID approaches are conceptually different, their performance depend on the same total time resolution, which, for pp collisions at $\sqrt{s} = 7\,\text{TeV}$, is about 120 ps on average. This can be seen in Fig. 5.3 where the $t_{TOF} - t0 - t_{exp,\pi}$ distribution together with a gaussian fit is shown for all the tracks that satisfied the standard cuts (see §4.4), were associated with a TOF hit and had transverse momentum in the range $0.9 < p_t < 1.1$. This p_t range has been chosen since here the separation between π, K and p is good enough that we can correctly suppose that all the particles in the plot are pions and hence we can compare the measured time-of-flight with $t_{exp,\pi}$. For these tracks the time-zero is $t0_{TOF}$ when available and $t0_{Fill}$ in all the other cases.

In Fig. 5.4 the same fit is performed only for the tracks with $t0_{Fill}$. Since, as one can see, the total resolution is 157 ps, and since for these data $\sigma_{t0} = t0_{Spread} = 120$ ps, this provides an estimate of ~ 100 ps for the TOF resolution convoluted with the tracking resolution (see eq. 5.3).

In Fig. 5.5 the same fit is shown taking into account only the tracks with $t0_{TOF}$. Since, as shown in the previous chapter, $\sigma t0_{TOF} < t0_{Spread}$ the total time resolution of this sample is smaller, as expected.

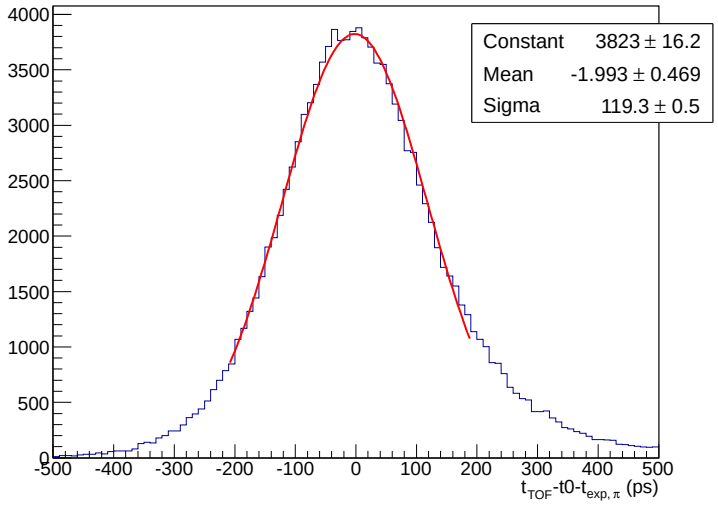

Figure 5.3: $t_{TOF} - t0 - t_{exp,\pi}$ for tracks matched with TOF, satisfying the standard cuts and with $0.9 < p_t < 1.1$ in pp collisions at $\sqrt{s} = 7\,\text{TeV}$. The total time resolution is ~ 120 ps, corresponding to the standard deviation of the gaussian fit in the range $|t_{TOF} - t0 - t_{exp,\pi}| < 200$ ps.

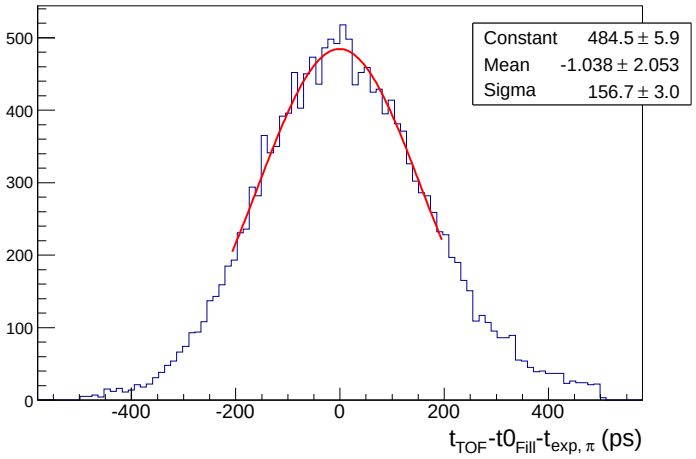

Figure 5.4: $t_{TOF} - t0_{Fill} - t_{exp,\pi}$ for tracks matched with TOF, satisfying standard cuts with $0.9 < p_t < 1.1$ and with $\sigma_{t0} = t0_{Spread}$. For these tracks the total time resolution is 157 ps, corresponding to the standard deviation of the gaussian fit in the range $|t_{TOF} - t0_{Fill} - t_{exp,\pi}| < 200$ ps.

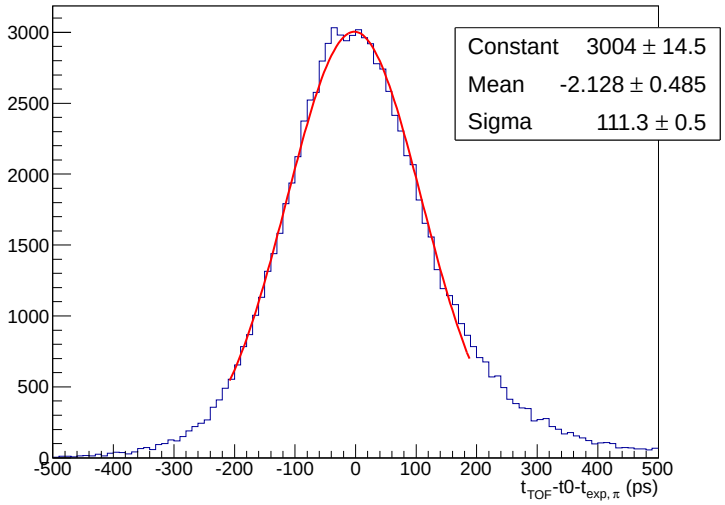

Figure 5.5: $t_{TOF} - t0_{TOF} - t_{exp,\pi}$ for tracks matched with TOF, satisfying standard cuts with $0.9 < p_t < 1.1$ and with time-zero computed with TOF. For these tracks the total time resolution is 111 ps, corresponding to the standard deviation of the gaussian fit in the range $|t_{TOF} - t0_{TOF} - t_{exp,\pi}| < 200$ ps.

5.3 Identified hadron spectra with the unfolding procedure

The PID method used for the transverse momentum spectra analysis is based on the unfolding procedure. This choice was driven by the fact that, contrary to other methods, it does not need any comparison with the Monte Carlo samples to extract the PID efficiency. As a consequence, the fact that the Monte Carlo simulations do not reproduce perfectly the fraction of events with the event time calculated by the TOF detector ($t0_{TOF}$) becomes irrelevant. The same holds true for the potential discrepancies between the real and the simulated time resolution. The other advantage of the unfolding procedure is the possibility to identify particles up to higher p_t with respect to the other methods.

In order to be able to use the PID unfolding method, the best variable to fit and the best function that is able to reproduce the data should be found. The variables that can be fitted are the time difference $\Delta t_i = t_{TOF} - t0 - t_{exp,i}$ and the number of sigma $n\sigma_{PID,i} = (t_{TOF} - t0 - t_{exp,i})/\sigma_{PID,i}$, for the mass hypothesis i. For an ideal detector, the signal shape, in terms of both the $n\sigma_{PID,i}$ and Δt_i variables would be distributed following a gaussian shape. In reality, due to residual miscalibration, the TOF signal is not purely gaussian but it is described by a function that includes a gaussian term with an exponential tail on its right-end side ($f_{Gaus+Exp}(x)$).

In the folowing section a detailed description of the unfolding procedure I used to reconstruct the primary hadron spectra will be reported. All the results are based on the analysis of about 55 millions pp events at $\sqrt{s} = 7$ TeV[1]. The event selection is the same as the one described in \$4.4, with the further requirement that the distance between the centre of the experiment and the z coordinate of the reconstructed primary vertex was smaller than 10 cm. Only primary tracks in the central pseudorapidity region ($|y| < 0.9$), satisfying the standard cuts (see 4.4 for more details), matched with a TOF hit and with a reliable associated expected time were selected. Since the T0 detector was included in the data acquisition only for a subsample of the data and it was not always properly calibrated, I decided to not use the information from the T0 detector and to require only the time-zero computed by the TOF detector when possible (see \$4.6 for more information on the time-zero definition). As a consequence, the analysis was carried out on two sub-samples of data, which in terms of tracks, result in having ∼70% of the tracks with the $t0_{TOF}$ available with $\sigma t0 = \sigma t0_{TOF}$, while for the remaining 30% $\sigma t0 = t0_{Spread}$. Since, as already said, $\sigma t0_{TOF} < t0_{Spread}$, these two

[1]They belong to the LHC10b and LHC10c periods.

subsamples have different total time resolutions (see eq. 5.3).

5.3.1 Fitting the Δt_i variable with analytic functions

To analyze events with a uniform time resolution, the tracks were divided into two sub-samples: the one containing the tracks (∼70% of the total) for which the $t0_{TOF}$ could be obtained and the one with the tracks (∼30% of the total) for which this value was not available. In each subsample the three $\Delta t_i = t_{TOF} - t0 - t_{exp,i}$ distributions, one for each mass hypothesis ($i = \pi, K, p$), have been analyzed since they can be better fitted with respect to the $n\sigma_{PID,i}$ distributions.

In detail, the unfolding method applied in each subsample and for each mass hypothesis is the following. All the selected tracks are supposed to be of type i. With this mass hypothesis the rapidity defined as:

$$y = ASinH(\frac{\sqrt{p^2 - p_t^2}}{\sqrt{m_i^2 + p_t^2}}) \tag{5.5}$$

is calculated and only tracks with $|y| < 0.5$ are accepted. Then the Δt_i distribution is computed in each p_t interval. Of course, only for some tracks the mass hypothesis i is correct, hence the Δt_i distribution is composed by three sub-distributions, one for each particles types[2]. One subdistribution is centered at zero and is due to the tracks of type i for which the mass hypothesis was correct (signal), one is due to the particles of type $j \neq i$ (background 1) and one is due to the particles of type $k \neq i$ (background 2) where e.g. i are pions, j are kaons and k are protons. As a consequence, in each p_t interval, the Δt_i distribution is fitted with three functions $f(x)$ (one for the signal and two for the background), each of which is the combination of a gaussian function plus an exponential tail on its right-end side, so that:

$$x \leq \overline{x} + t \rightarrow f(x) = Gaus(x, \overline{x}, \sigma) \tag{5.6}$$

$$x > \overline{x} + t \rightarrow f(x) = Gaus(\overline{x} + t, \overline{x}, \sigma) \times Exp(-s(x - t - \overline{x}))$$

As one can see, each function $f(x)$ is described by 4 parameters: the mean ($\overline{x}$) and the sigma (σ) of the gaussian part, the tail (t) that is the point where the exponential tail starts, and its slope (s). Taking into account also the three yields for the signal, and the two backgrounds, the total number of parameters is 15. The yields are constrained to be between zero and the total number of analyzed tracks. For what concerns the other parameters, in the lower p_t regions where the signals from different hadron species are well separated,

[2]We are assuming that only pions, kaons and protons are present.

they are allowed to vary within very loose bounds. In the high p_t regions, they are than fixed to the saturation values that could be determined in the lower p_t bins. In addition, the slopes of the three exponential tails are constrained to be the same. The free parameters, at low p_t are hence 13. In Fig. 5.6 an example of the fit of the $t_{TOF} - t0 - t_{exp,\pi}$ distribution for the sample of tracks with (top) and without (bottom) the $t0_{TOF}$ in logarithmic (left) and linear (right) scale is shown for the $1.00 < p_t < 1.10$ GeV/c interval. It is clear that, due to the better time resolution in the cases when the $t0_{TOF}$ is available, the separation between the species is better for the sample with the $t0_{TOF}$. This behaviour is more evident in Fig. 5.7 where the same as in Fig. 5.6 is drawn but for the $2.40 < p_t < 2.50$ GeV/c interval. Since the tracks with $t0_{TOF}$ available are $\sim$70% of the total, the p_t reach of this PID method can be defined as the highest p_t interval, in this sample, where the signal and the backgound can be reliably fitted and the systematic uncertainties are kept under control. With such definition, one gets $p_{t,reach} = 2.5$ GeV/c for pions and kaons and $p_{t,reach} = 4.0$ GeV/c for protons. Fig. 5.8, 5.9, 5.10 and 5.11 show the same fits as in Fig. 5.6 in the kaons and protons mass hypothesis in $1.00 < p_t < 1.10$ GeV/c and $2.40 < p_t < 2.50$ GeV/c intervals for kaons and in $2.00 < p_t < 2.10$ GeV/c and $3.80 < p_t < 4.00$ GeV/c intervals for protons.

The raw yields of pions, kaons and protons are extracted from the integral of the signal fit function, separately for each sample, and finally summed together to obtain the total raw spectra. This is reported in Fig. 5.12 for negative (left) and positive (right) pions (red), kaons (blue) and protons (green). These spectra are normalized to the number of analyzed events. We mention that, in the case of protons, p_t spectra are reported starting from $p_t = 0.8$ GeV/c since, below this threshold, the estimate of $t_{exp,p}$ suffers from imperfections in the corrections for energy loss in the material. This causes the signal distribution to be unsatisfactorely described by the fit function used in the procedure, and the result of the interpolation may be not reliable.

To summarize, the best way to identify particles with the unfolding procedure in pp collisions at $\sqrt{s} = 7$ TeV is to fit the Δt_i distributions separately for the sample of tracks with $t0_{TOF}$ available and for the sample of tracks where only the $t0_{Fill}$ is subtracted as time-zero of the event with three functions $f(x)$ each of which is defined by a gaussian part plus an exponential tail on its right-end side. All the results that will be shown in the next chapter are based on this PID procedure.

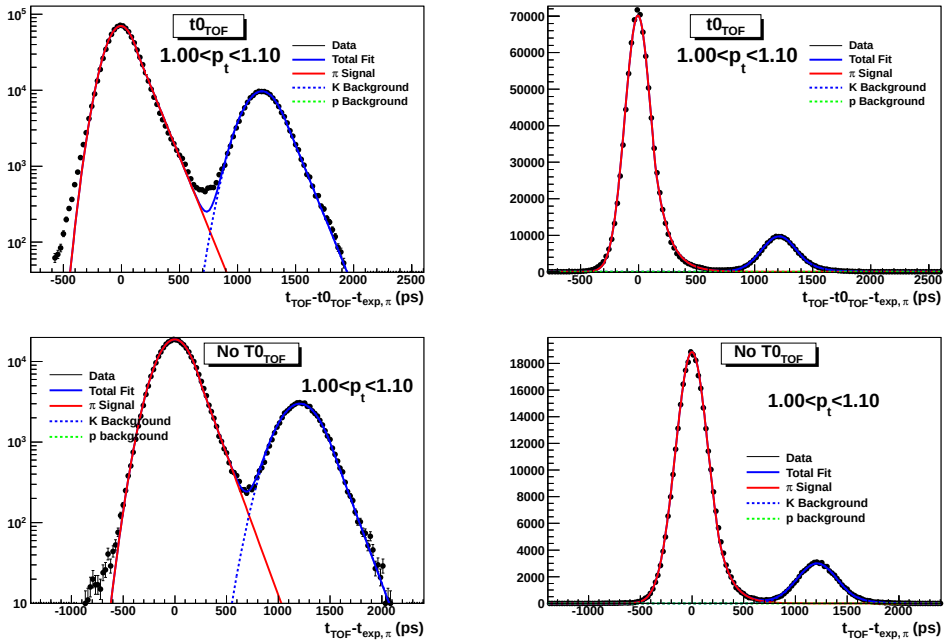

Figure 5.6: $t_{TOF} - t0 - t_{exp,\pi}$ distribution for tracks with (top) and without (bottom) $t0_{TOF}$, in logarithmic (left) and linear (right) scale. The $1.00 < p_t < 1.10$ GeV/c interval was considered. The red line corresponds to the fit of the signal, while the dotted blue and green lines are the fits of the background. Each fit function consists of a gaussian part and an exponential tail on its right-end side, see text for more details. Here the protons are not visible since they are centered at ~ 4200 ps, out of the range of these histograms.

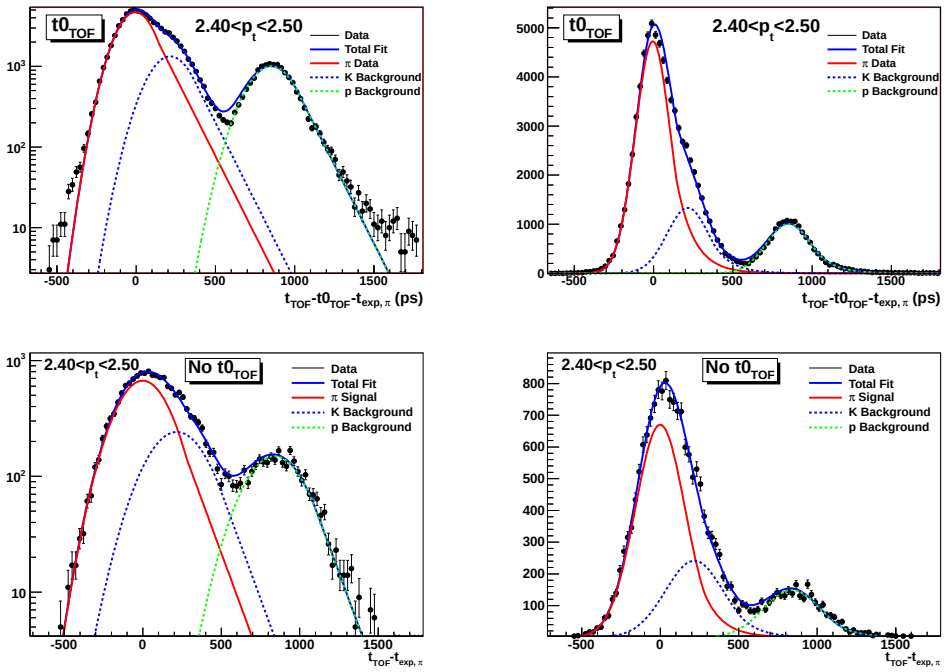

Figure 5.7: $t_{TOF} - t0 - t_{exp,\pi}$ distribution for tracks with (top) and without (bottom) $t0_{TOF}$, in logarithmic (left) and linear (right) scale. The $2.40 < p_t < 2.50$ GeV/c interval was considered. The red line corresponds to the fit of the signal, while the dotted blue and green lines are the fits of the background. Each fit function consists of a gaussian part and an exponential tail on its right-end side, see text for more details.

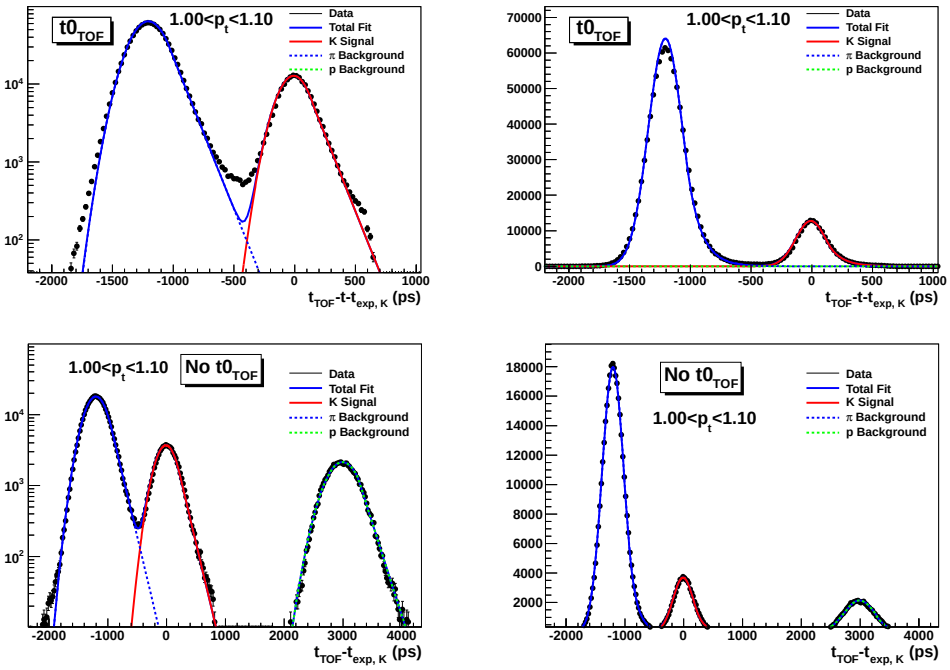

Figure 5.8: $t_{TOF} - t0 - t_{exp,K}$ distribution for tracks with (top) and without (bottom) $t0_{TOF}$, in logarithmic (left) and linear (right) scale. The $1.00 < p_t < 1.10$ GeV/c interval was considered. The red line corresponds to the fit of the signal, while the dotted blue and green lines are the fits of the background. Each fit function consists of a gaussian part and an exponential tail on its right-end side, see text for more details. In the top plots the protons are not visible since they are centered at ~ 3000 ps, out of the range of these histograms.

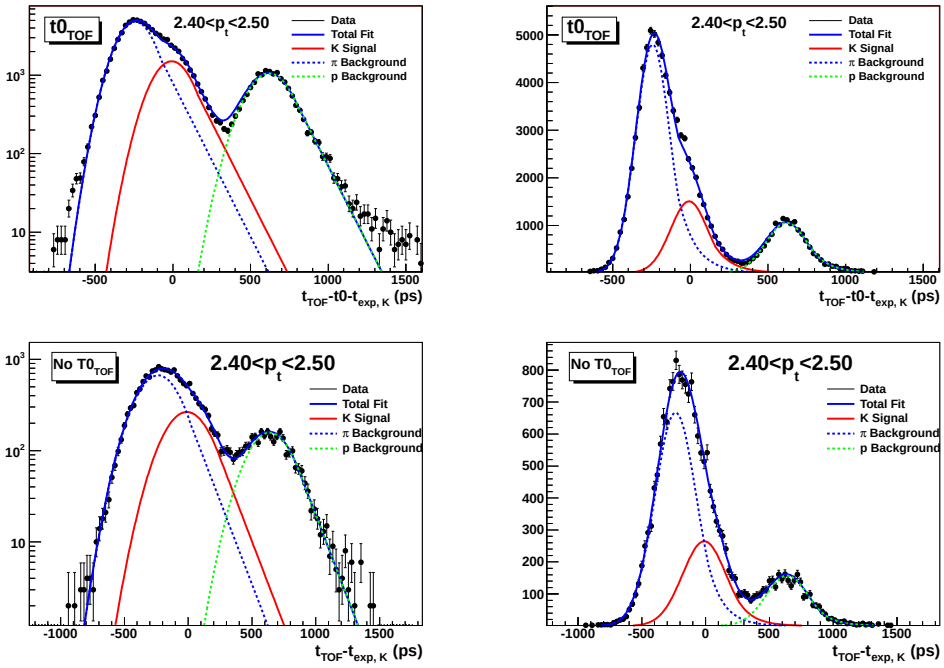

Figure 5.9: $t_{TOF} - t0 - t_{exp,K}$ distribution for tracks with (top) and without (bottom) $t0_{TOF}$, in logarithmic (left) and linear (right) scale. The $2.40 < p_t < 2.50$ GeV/c interval was considered. The red line corresponds to the fit of the signal, while the dotted blue and green lines are the fits of the background. Each fit function consists of a gaussian part and an exponential tail on its right-end side, see text for more details.

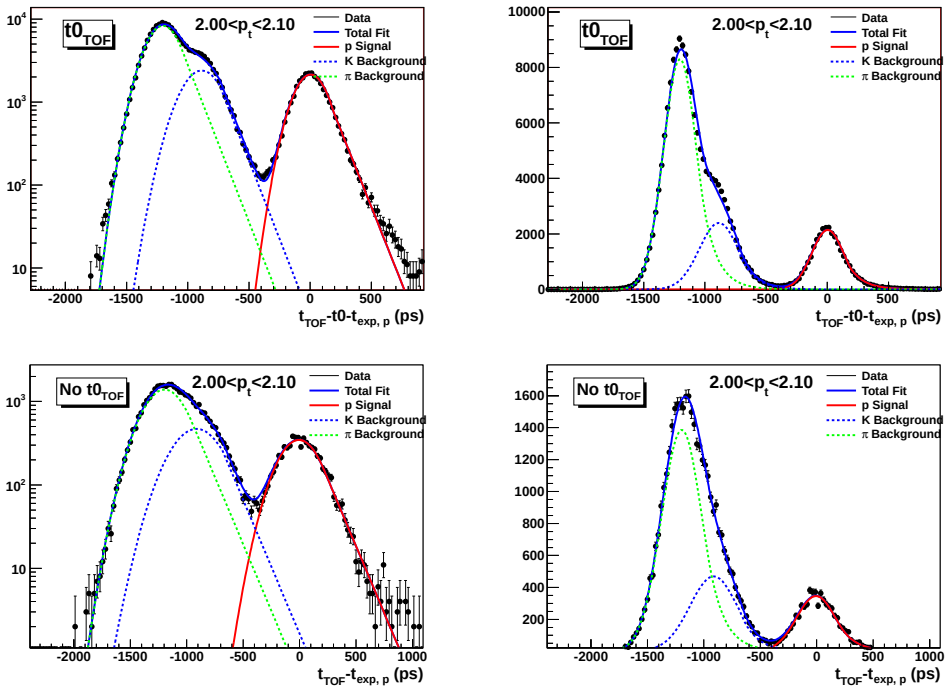

Figure 5.10: $t_{TOF} - t0 - t_{exp,p}$ distribution for tracks with (top) and without (bottom) $t0_{TOF}$, in logarithmic (left) and linear (right) scale. The $2.00 < p_t < 2.10$ GeV/c interval was considered. The red line corresponds to the fit of the signal, while the dotted blue and green lines are the fits of the background. Each fit function consists of a gaussian part and an exponential tail on its right-end side, see text for more details.

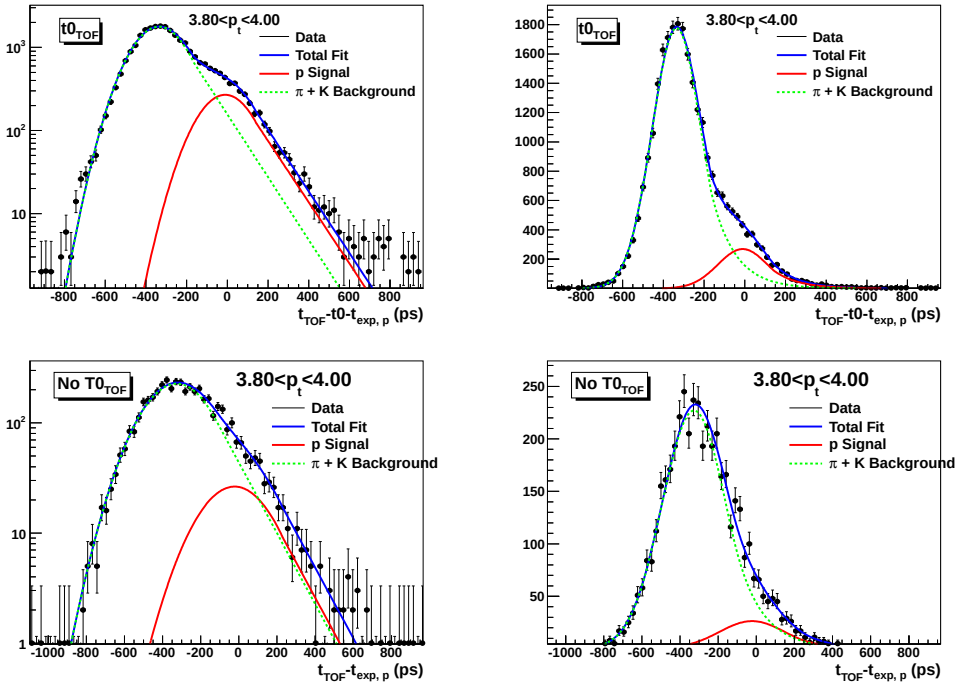

Figure 5.11: $t_{TOF} - t0 - t_{exp,p}$ distribution for tracks with (top) and without (bottom) $t0_{TOF}$, in logarithmic (left) and linear (right) scale. The $3.80 < p_t < 4.00$ GeV/c interval was considered. The red line corresponds to the fit of the signal, while the dotted green line is the fit of the background. Each fit function consists of a gaussian part and an exponential tail on its right-end side, see text for more details. We notice that, since in this momentum range pions and kaons can not be distinguished, I considered the background as made of only one single distribution.

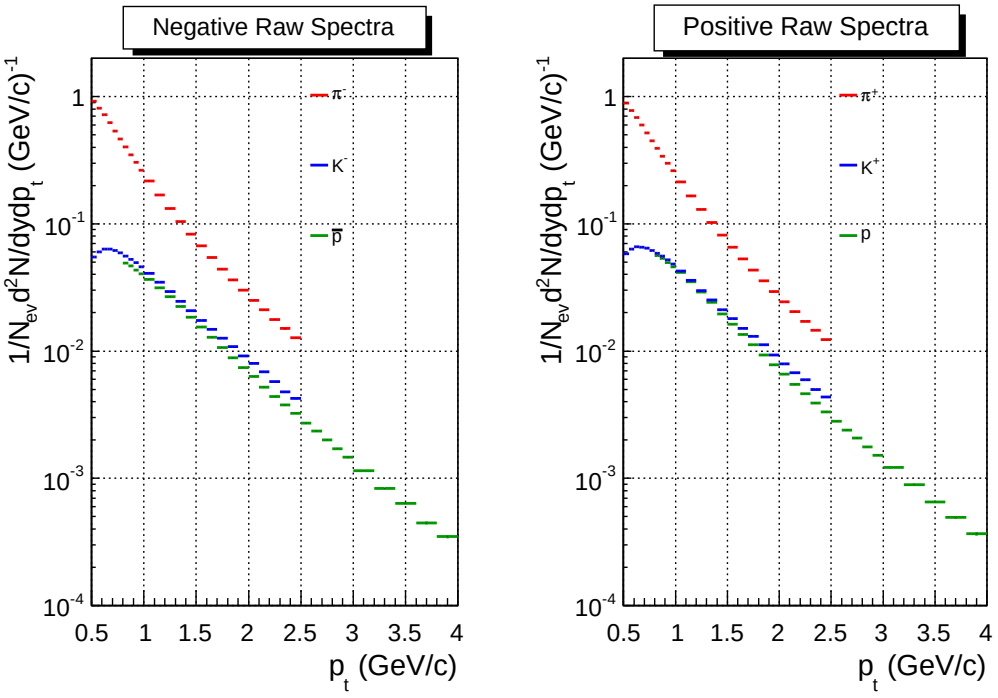

Figure 5.12: Total transverse momentum raw spectra for negative (left) and positive (right) pions (red), kaons (blue) and protons (green). The spectra were obtained by the combination of the results of the fit of the two samples with and without $t0_{TOF}$ performed separately. For both samples, three functions were used, resulting from the combination of a gaussian term and an exponential tail.

5.4 TOF Identified hadron spectra with the 3σ cut procedure

As a test of the robustness of the PID approach used in this thesis, a comparison of the spectra obtained with the unfolding procedure and a 3σ cut method was performed. I selected a subsample of events (~ 5 million events), I analyzed them with both the gaussian unfolding and the 3σ cut method and I compared the results. As it will be shown at the end of this section, the two yields differ by at most 5%.

This comparison was performed analyzing only the tracks with the time-zero computed by the TOF detector, corresponding to about 70% of the total to deal with a sample with a uniform time resolution. Equivalent results are expected to be obtained with the sample of tracks without $t0_{TOF}$: however, the former sample was chosen because it has a higher statistics and the comparison could be performed on a wider p_t range (thanks to the better time resolution).

5.4.1 The 3σ cut method

The basic separation variable used in the 3σ cut method is the difference between the observed time-of-flight ($t_{TOF} - t0$, where from the measured time-of-flight the $t0$ of the event is subtracted), and the expected time $t_{exp,i}$ for the three mass hypothesis π, K and p. This difference is calculated in terms of $n\sigma_i$ where σ is $\sigma_{PID,i}$ as defined in eq. 5.7:

$$n\sigma_i = \frac{t_{TOF} - t0 - t_{exp,i}}{\sigma_{PID,i}}. \tag{5.7}$$

In Fig. 5.13, 5.14 and 5.15 $t_{TOF} - t0_{TOF} - t_{exp,i}$ is shown for the π, K and p hypothesis as a function of transverse momentum. The horizontal bands centered at zero correspond to the tracks for which the mass hypothesis is correct. At low p_t the three bands from the three particle species are clearly distinguishable, while as p_t increases, they start to overlap due to the decreasing separation power of the TOF detector with increasing transverse momentum.

For the spectra analysis I used an "exclusive" 3σ cut method: for each track, once the $n\sigma_i$ is computed for all the three mass hypotheses ($i = \pi, K, p$), the identity j is assigned to the track if the number of sigma $n\sigma_j$ is smaller than 3 only for the hypothesis j. If this condition is satisfied by more than one mass hypothesis (i.e. the number of sigma is smaller than 3) the track is discarded and no indentity is assigned to it.

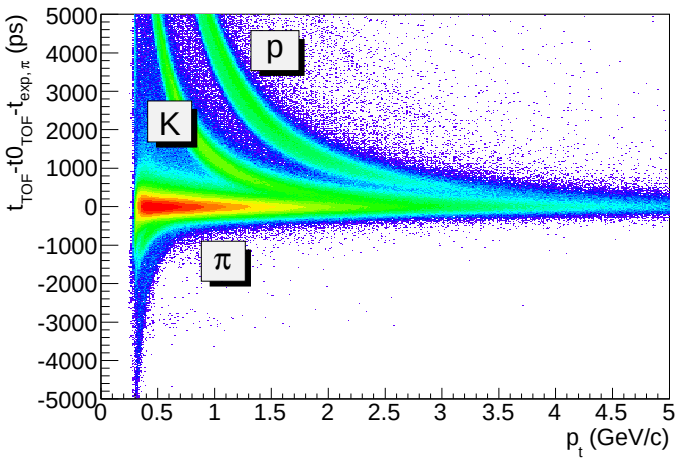

Figure 5.13: $t_{TOF} - t0_{TOF} - t_{exp,\pi}$ (pion hypothesis) for primary tracks matched with TOF and with the time-zero computed by the TOF detector.

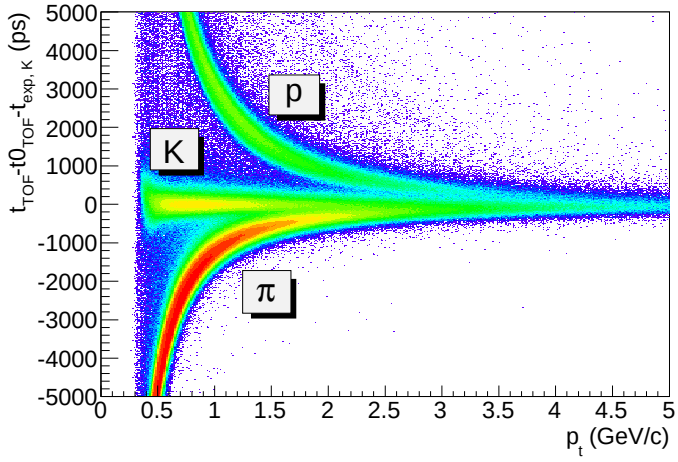

Figure 5.14: $t_{TOF} - t0_{TOF} - t_{exp,K}$ (kaon hypothesis) for primary tracks matched with TOF and with the time-zero computed by the TOF detector.

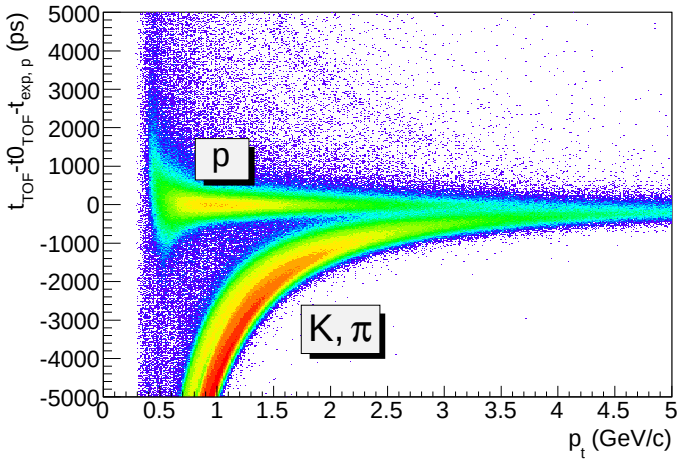

Figure 5.15: $t_{TOF} - t0_{TOF} - t_{exp,p}$ (proton hypothesis) for primary tracks matched with TOF and with the time-zero computed by the TOF detector.

In Fig. 5.16, 5.17 and 5.18 the number of sigma $n\sigma_i$ as a function of p_t is shown in the π, K and p hypothesis. The pink lines emphasize the $\pm 3\sigma$ region. From the plots one can easily see that, while at low p_t where the TOF separation power is high this method is highly performant at high p_t it becomes less efficient.

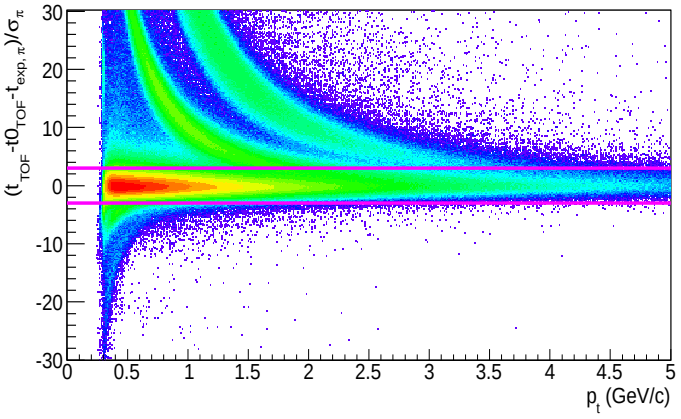

Figure 5.16: $(t_{TOF} - t0 - t_{exp,\pi})/\sigma_{PID,\pi}$ as a function of p_t. The pink lines identify the $\pm 3\sigma$ region.

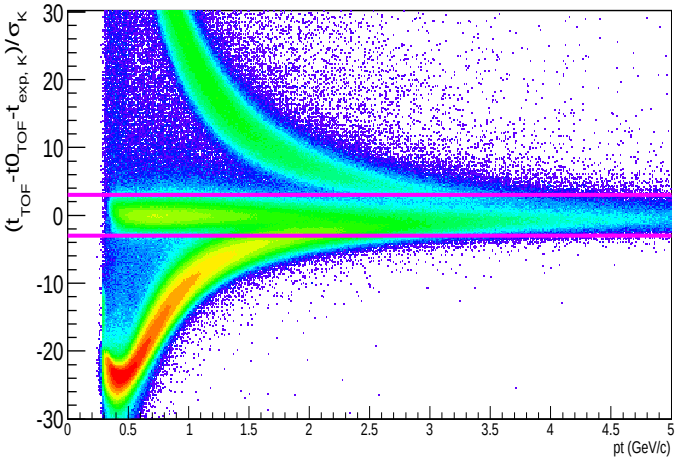

Figure 5.17: $(t_{TOF} - t0 - t_{exp,K})/\sigma_{PID,K}$ as a function of p_t. The pink lines identify the $\pm 3\sigma$ region.

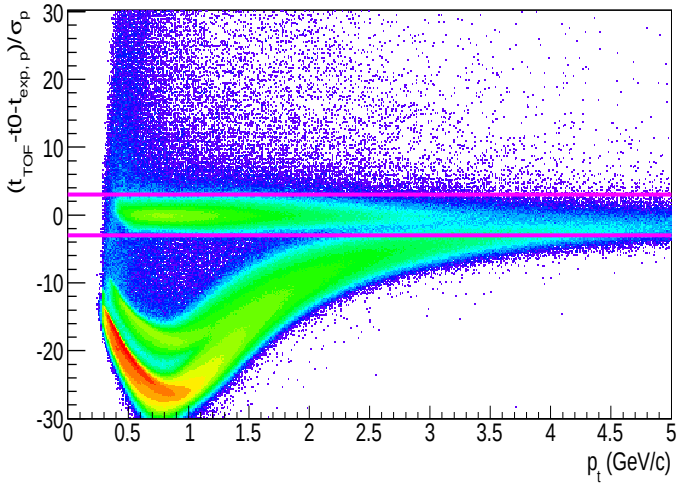

Figure 5.18: $(t_{TOF} - t0 - t_{exp,p})/\sigma_{PID,p}$ as a function of p_t. The pink lines identify the $\pm 3\sigma$ region.

Obviously, this method relies on the fact that the expected time is correctly reconstructed and that the $\sigma_{PID,i}$ is able to reproduce the resolution observed in the data in each momentum interval, if the right mass hypothesis is assumed. As a consequence the distribution of $(t_{TOF} - t0_{TOF} - t_{exp,i})/\sigma_{PID,i}$ for every p_t interval has to be centered around zero and have a standard deviation close to unity. This is actually the case, as can be seen in Fig. 5.19, 5.20 and 5.21 where $(t_{TOF} - t0_{TOF} - t_{exp,i})/\sigma_{PID,i}$ for the π, K, p hypothesis is drawn; the $1.10 < p_t < 1.20$ GeV/c range is considered, but equivalent results were obtained for the other p_t intervals.

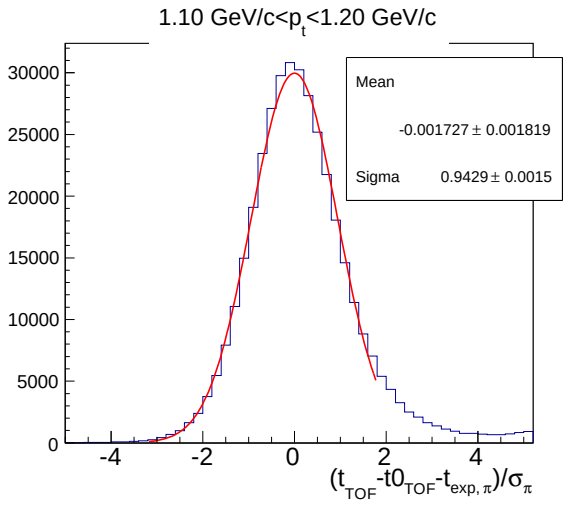

Figure 5.19: $(t_{TOF} - t0_{TOF} - t_{exp,\pi})/\sigma_{PID,\pi}$ for tracks with $1.10 < p_t < 1.20$ GeV/c. The gaussian fit to the distribution is superimposed and the mean and sigma shown.

As already said, the p_t reach of this approach is determined by the total time resolution. Considering only the tracks with the time-zero computed by the TOF detector algorithm, the expected separation for π/K and K/p defined as $(t_{exp,K} - t_{exp,\pi})/\sigma_{PID,K}$ and $(t_{exp,p} - t_{exp,K})/\sigma_{PID,p}$ as a function of p_t is shown in Fig. 5.22. A 3σ (2σ) separation is possible for π/K until 1.8 GeV/c (2.3 GeV/c) and for K/p until 3.2 GeV/c (4 GeV/c).

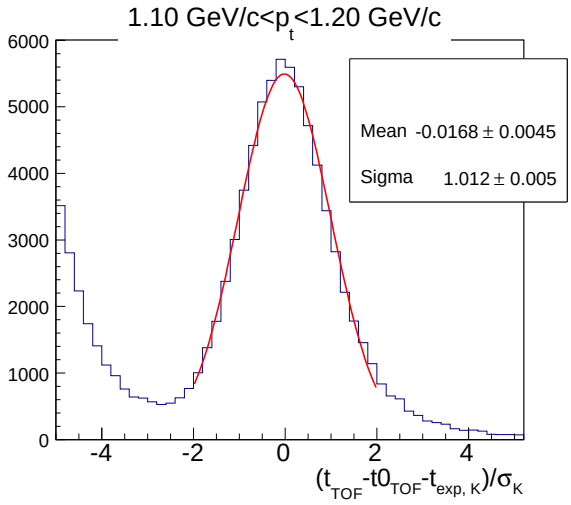

Figure 5.20: $(t_{TOF} - t0_{TOF} - t_{exp,K})/\sigma_{PID,K}$ for tracks with $1.10 < p_t < 1.20$ GeV/c. The gaussian fit to the distribution is superimposed and the parameters shown.

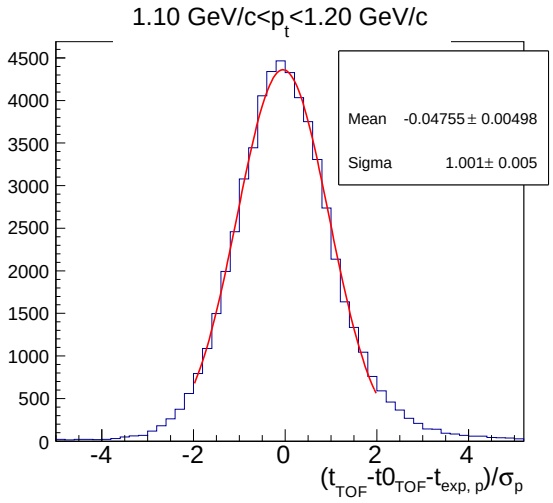

Figure 5.21: $(t_{TOF} - t0_{TOF} - t_{exp,p})/\sigma_{PID,p}$ for tracks with $1.10 < p_t < 1.20$ GeV/c. The gaussian fit to the distribution is superimposed and the parameters shown.

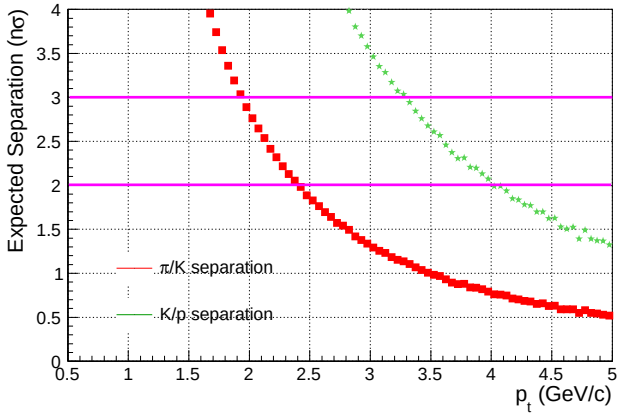

Figure 5.22: $(t_{exp,K} - t_{exp,\pi})/\sigma_{PID,K}$ (red squares) and $(t_{exp,p} - t_{exp,K})/\sigma_{PID,p}$ (green squares) as a function of p_t for primary tracks with the time-zero computed by the TOF detector.

5.4.2 The raw spectra

After applying the exclusive 3σ cut PID procedure a cut on the rapidity (see eq. 5.5) was applied so that only the tracks identified as primary π, K or p with $|y| < 0.5$ are selected.

In Fig. 5.23 the raw (i.e. non corrected) transverse momentum spectra for negative (left) and positive (right) selected primary pions (red), kaons (blue) and protons (green) are shown. These spectra are normalized to the number of analyzed events. Since the matching efficiency falls down for $p_t < 0.5$ GeV/c (see \$4.5), the results will be reported only for $p_t > 0.5$ GeV/c.

5.4.3 Correction for the PID method efficiency

In order to compare the spectra obtained with the unfolding method and with the 3σ cut procedure, the efficiency of the method for particle identification has to be taken into account. While this correction is strictly related to the PID method, all the others (e.g. the matching efficiency correction) are PID independent and won't therefore be included in the results hereafter. To compute the PID method efficiency the same PID analysis have to be carried out on Monte Carlo samples and the assigned identity of the particles has to be compared with the true one from Monte Carlo information. The feasibility of this approach relies on the fact that the resolution is consistent in data

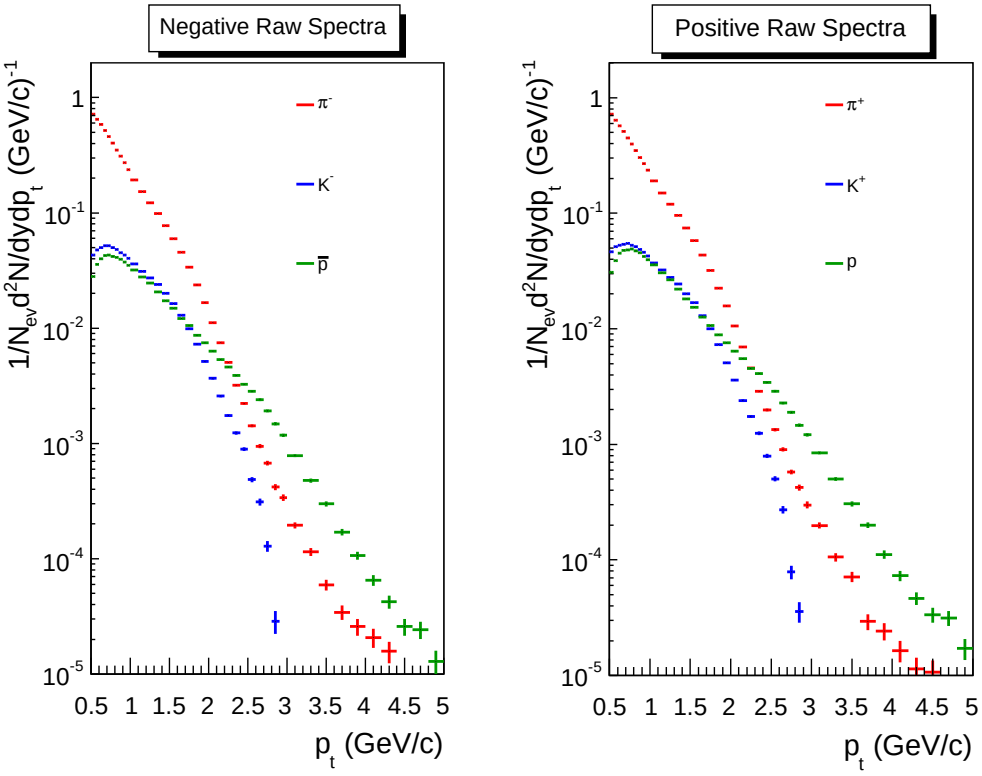

Figure 5.23: Transverse momentum raw spectra for negative (left) and positive (right) pions (red), kaons (blue) and protons (green) normalized to the number of analyzed events.

and Monte Carlo. Besides, choosing only the sample of tracks with $t0_{TOF}$, the different fraction of events with and without $t0_{TOF}$ in data and Monte Carlo is, as already said, of no importance[3].

In Fig. 5.24 the PID efficiency ε_{PID} for the 3σ cut method for negative (top) and positive (bottom) pions (red), kaons (blue) and protons (green) is shown as a function of p_t. In detail, $\varepsilon_{PID}(i)$ is defined as

$$\varepsilon_{PID}(i) = \frac{N^t_{id}(i)}{N(i)}, \tag{5.8}$$

where $N^t_{id}(i)$ is the number of tracks correctly identified as type i and $N(i)$ is the number of tracks of type i in the sample under study. In other words $N(i)$ is the number of the primary tracks reconstructed by TPC, matched with TOF, and with $|y| < 0.5$.

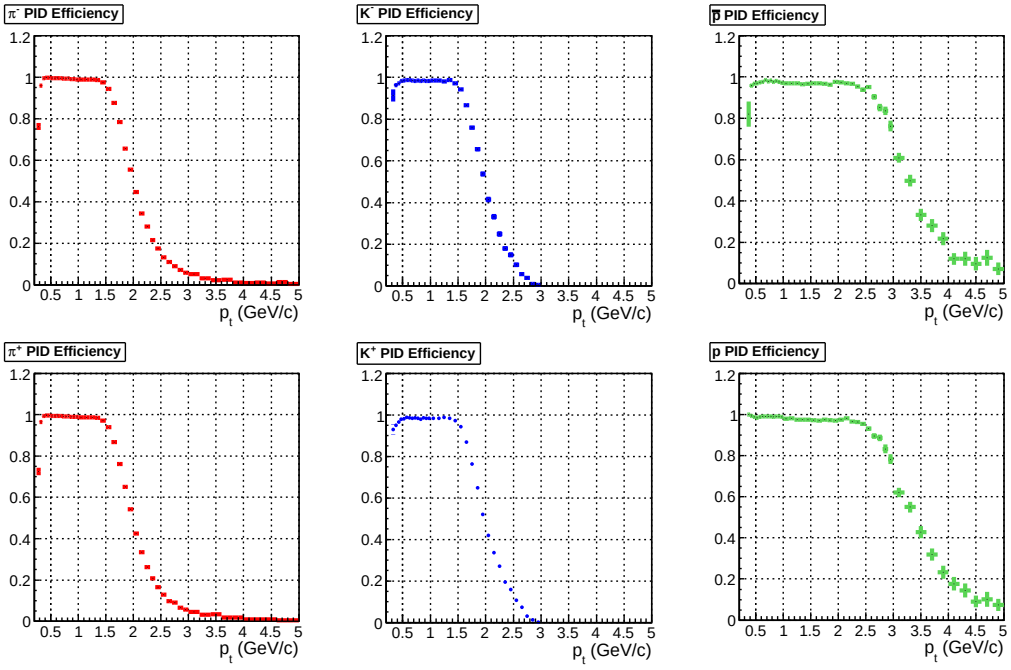

Figure 5.24: ε_{PID} for the 3σ cut method as a function of p_t for negative (top) and positive (bottom) pions (red), kaons (blue) and protons (green).

We can see that the efficiency is the same for negative and positive particles, as expected. To give a feeling of the p_t reach of the 3σ cut method we

[3]To compute the PID method efficiency I analyzed the Monte Carlo events reproducing the same detector conditions as in real data.

can conventionally take as a reference the transverse momentum at which the PID efficiency reaches 0.5. In this case one can see that the 3σ cut method can identify π and K up to $\sim$ 1.8 GeV/c and p up to $\sim$3.3 GeV/c. In Fig. 5.25 ε_{PID} is shown as function of p_t and η, while in Fig. 5.26 it is drawn as function of η and ϕ. In this plots an homogeneous behavior both in η and in ϕ can be observed.

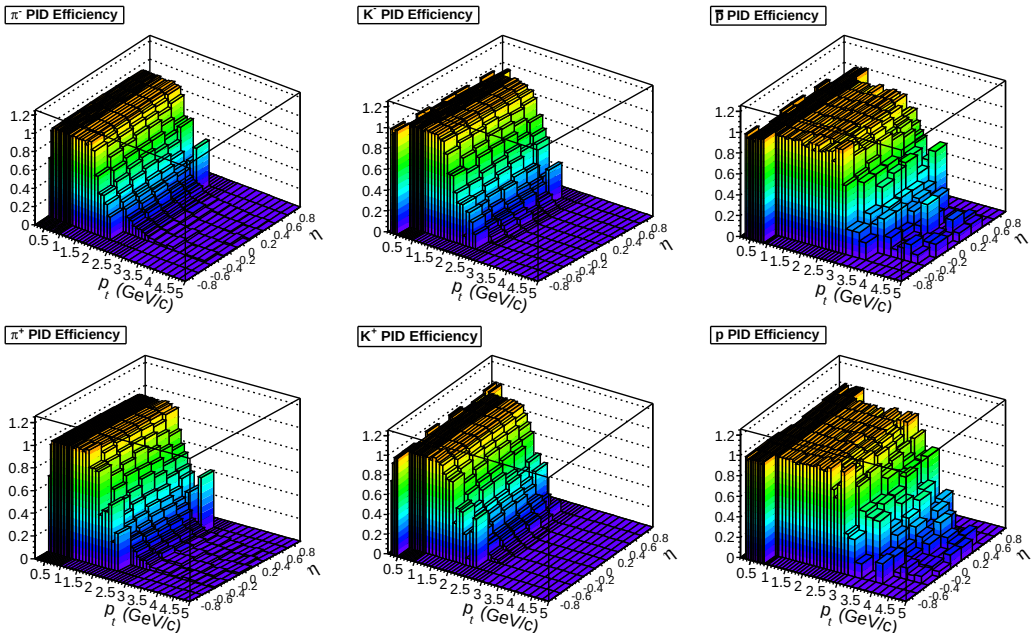

Figure 5.25: ε_{PID} for the 3σ cut method as a function of p_t and η for negative (top) and positive (bottom) pions (left), kaons (middle) and protons (right).

To correct the raw spectra we have also to take into account the PID contamination, that is the number of misidentified tracks defined as:

$$C_{PID}(i) = \frac{N^w_{id}(i)}{N^t_{id}(i) + N^w_{id}(i)}, \tag{5.9}$$

where $N^w_{id}(i)$ is the number of particles wrongly identified as type i, but that are in fact of type j. $N^t_{id}(i)$ is on the other hand the number of particles of type i correctly identified. Since we use an exclusive 3σ cut method, the contamination is expected to be low (of the order of few percent), as it can be seen from Fig. 5.27.

The spectra corrected for PID efficiency and contamination ($(dN/dydp_t)_{PID}$)

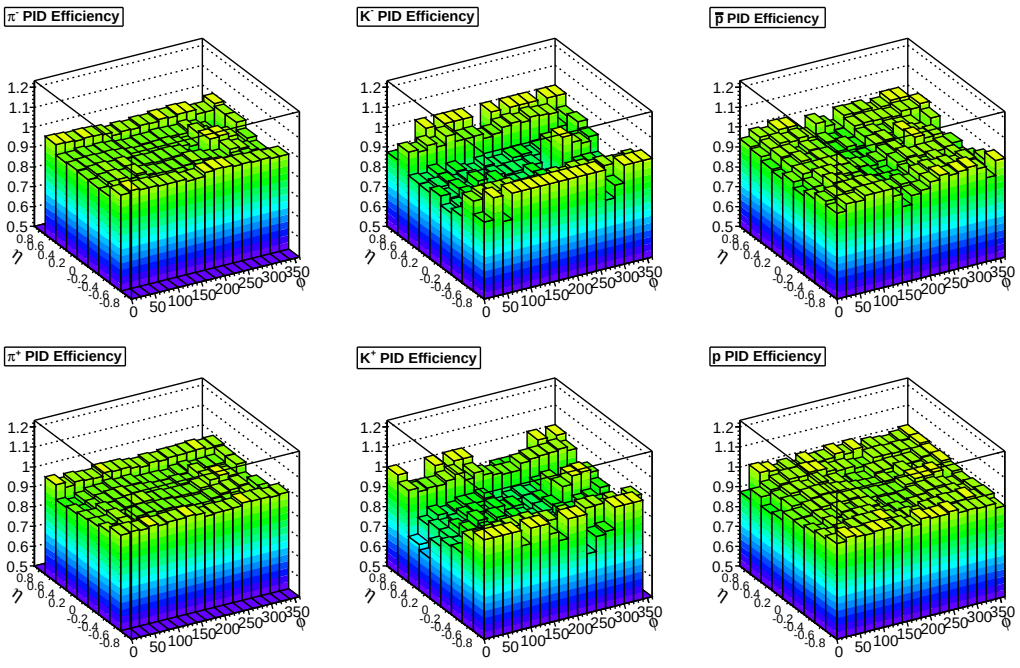

Figure 5.26: ε_{PID} for the 3σ cut method as a function of η and ϕ for negative (top) and positive (bottom) pions (left), kaons (middle) and protons (right).

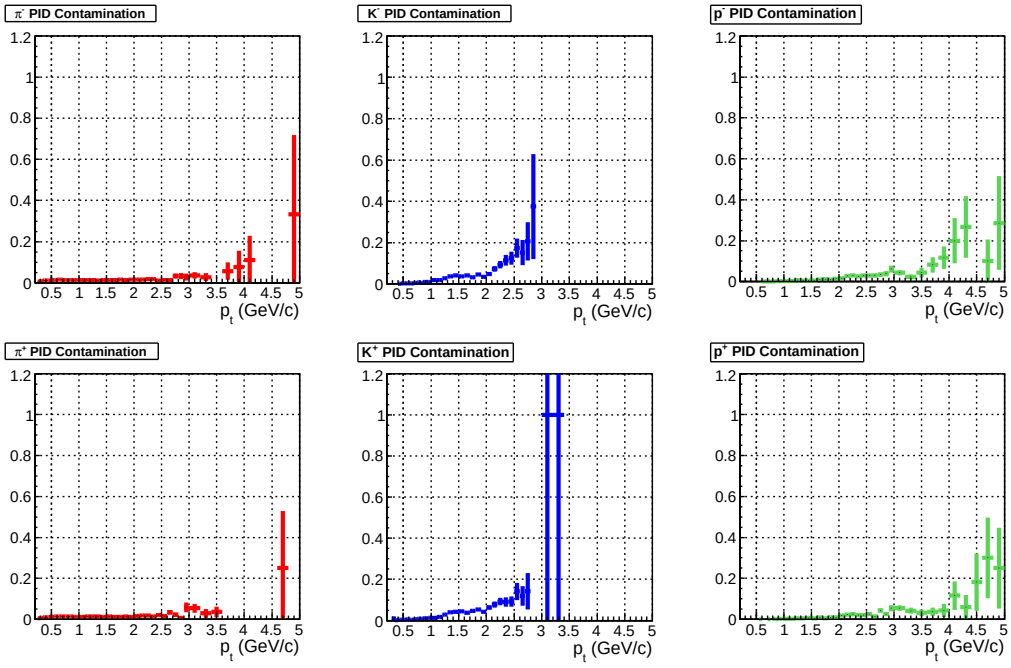

Figure 5.27: C_{PID} for the 3σ cut method as a function of p_t for negative (top) and positive (bottom) pions (red), kaons (blue) and protons (green).

can be obtained from the raw spectra ($(dN/dydp_t)_{raw}$) as:

$$(dN/dydp_t)_{PID} = \frac{(dN/dydp_t)_{raw}}{\varepsilon_{PID}}(1 - C_{PID}), \tag{5.10}$$

and are shown in Fig. 5.28.

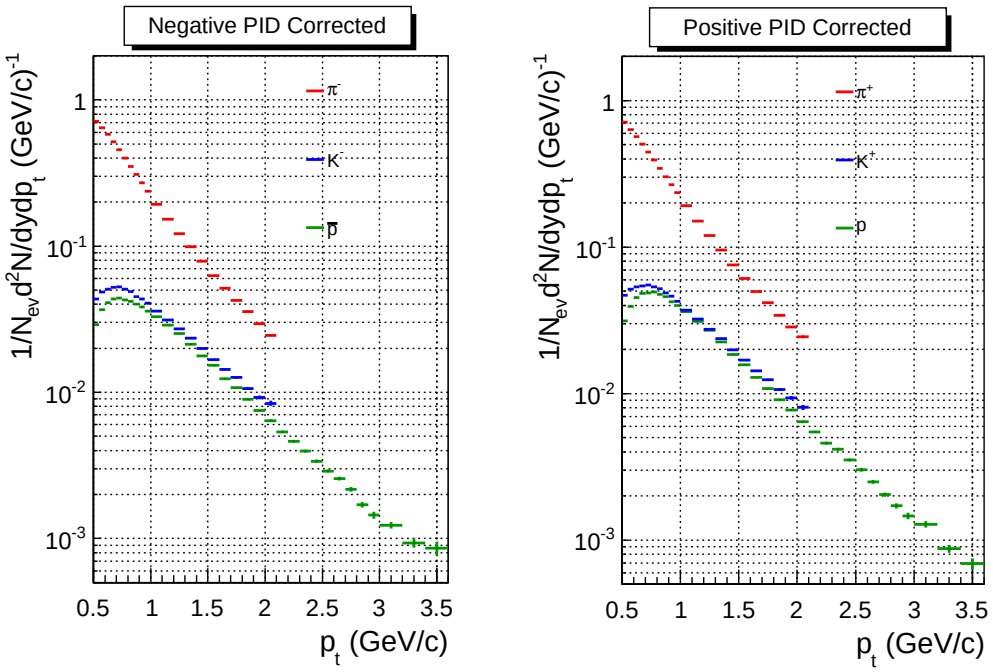

Figure 5.28: Negative (left) and positive (right) spectra of pions (red), kaons (blue) and protons (green) corrected for PID efficiency and contamination.

However, the PID contamination just defined in eq. 5.9 depends on the particle concentrations in the Monte Carlo sample, which may differ from those in the data. For this reason, a bias in the correction may be introduced. To avoid this problem, a correction matrix Eff_{PID} has to be used. Its components are the probabilities ε_{ij} to identify a particle of type j as a particle of type i, that is:

$$\varepsilon_{ij} = \frac{N_{id}(i;j)}{N(j)} \tag{5.11}$$

where $N_{id}(i;j)$ is the number of particles of type j from Monte Carlo information that are identified as type i and $N(j)$ is the number of particle of type j that undergo the PID procedure. The resulting correction matrix can

then be expressed as

$$\mathbf{Eff_{PID}} = \begin{pmatrix} \varepsilon_{\pi\pi} & \varepsilon_{\pi K} & \varepsilon_{\pi p} \\ \varepsilon_{K\pi} & \varepsilon_{KK} & \varepsilon_{Kp} \\ \varepsilon_{p\pi} & \varepsilon_{pK} & \varepsilon_{pp} \end{pmatrix}.$$

If we define $(dN/dydp_t)_{raw}$ the array with the raw spectra and $(dN/dydp_t)_{true}$ the array with the true ones, then:

$$(dN/dydp_t)_{raw} = Eff_{PID} \times (dN/dydp_t)_{true}. \tag{5.12}$$

Hence, to correct the raw spectra for the PID method efficiency the Eff_{PID} matrix has to be inverted and

$$(Eff_{PID})^{-1} \times (dN/dydp_t)_{raw} \tag{5.13}$$

computed to derive the corrected spectra. In Fig. 5.29 the ratio between the raw spectra corrected for PID efficiency with the matrix Eff_{PID} and as in eq. 5.10 is shown. The ratio for protons stops at 3 GeV/c since at higher p_t the efficiency matrix is not invertible due to the lack of statistics. As we can see the difference is less than 2%. Even if the two PID correction procedures

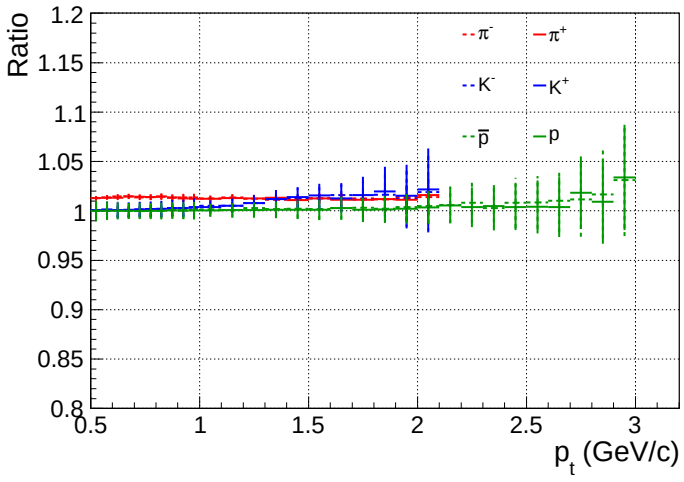

Figure 5.29: Ratio between the raw spectra corrected for PID efficiency with the matrix Eff_{PID} and in the traditional way, i.e. as in eq. 5.10.

produce very similar results, the correction of the raw spectra with the matrix efficiency should be preferred.

5.4.4 Comparison between the 3σ cut method and the unfolding procedure

If we analyze the same sample of data with the unfolding procedure described in $5.3.1, we obtain the raw spectra in Fig. 5.30.

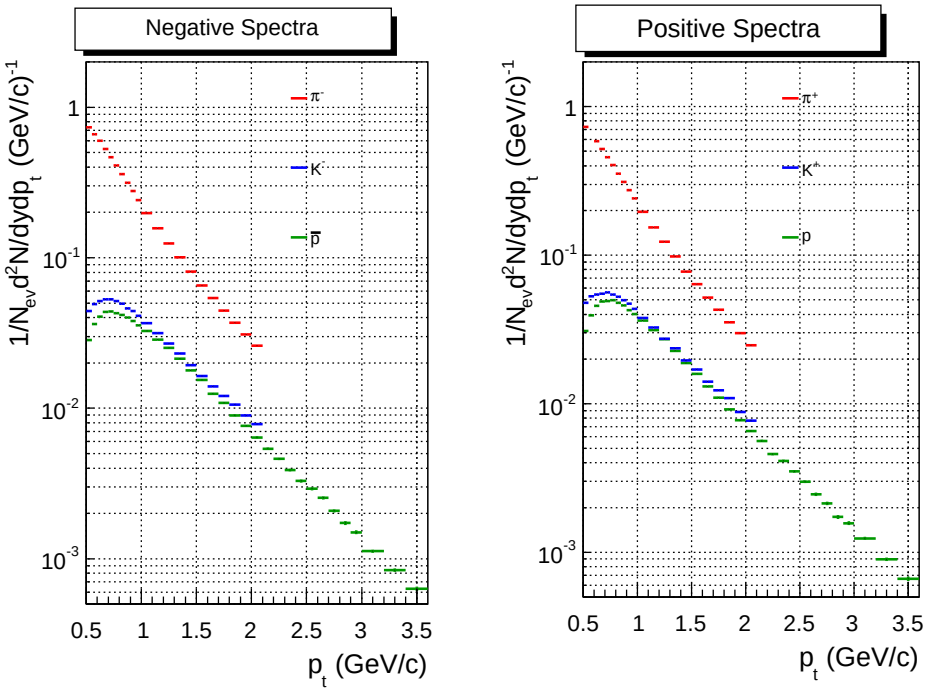

Figure 5.30: Transverse momentum raw spectra for negative (left) and positive (right) pions (red), kaons (blue) and protons (green) identified with the gaussian unfolding procedure normalized to the number of analyzed events.

For this PID method the PID efficiency is assumed to be 100% hence no PID corrections are needed. The ratio of the spectra measured with the 3σ cut method corrected with the matrix efficiency and the ones reconstructed with the unfolding procedure is shown in Fig. 5.31.

As we can see, the two methods provide the same results within 5%, except for the last two p_t intervals in the case of kaons. Here the separation power starts to be limitated and the 3σ cut PID efficiency is very low. Nevertheless, the unfolding procedure shows better performance in terms of p_t reach, so it provides the best approach to identify π, K and p in pp collisions at $\sqrt{s} = 7$ TeV. In addition it does not rely on any Monte Carlo information and simulation. It is anyway worth to underline that in the p_t range where

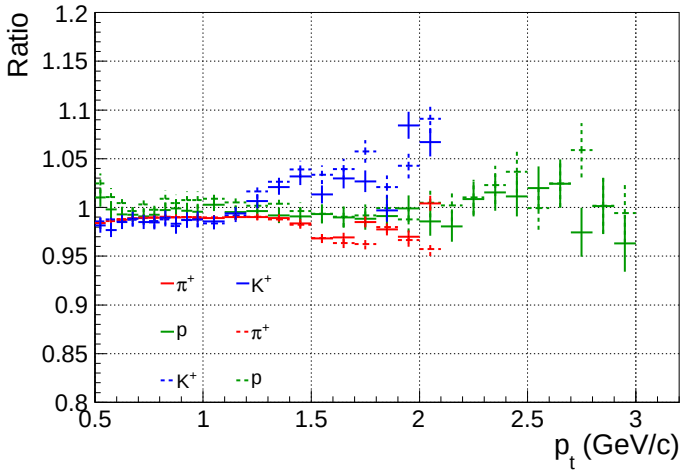

Figure 5.31: Ratio between the spectra computed with the 3σ cut method corrected with the matrix efficiency and the ones reconstructed with the gaussian unfolding procedure as a function of p_t.

both the methods can be applied, results from the unfolding procedure are compatible with the ones obtained with the 3σ cut method.

Chapter 6

Identified hadron spectra with the TOF detector: results

As we said in the previous chapters, to access the thermal parameters of the system created in heavy-ion collisions at the kinetic and chemical freeze-out, the measurement of identified particle transverse momentum spectra is one of the key tools. In the ALICE experiment, particle spectra are studied not only in Pb-Pb collisions, but also in pp interactions, since they provide the necessary reference for the understanding of heavy-ion data and are crucial to tune Monte Carlo models.

In the previous chapter, the technique used to identify primary hadrons with the TOF detector and to reconstruct their raw transverse momentum spectra in pp collisions at $\sqrt{s} = 7$ TeV was described. In particular, using an unfolding procedure, the momentum spectra have been measured in the range $0.5 < p_t < 2.5$ GeV/c for pions and kaons and in the range $0.8 < p_t < 4.0$ GeV/c for protons. This chapter is organized as follows:

In \$6.1 all the efficiency corrections (matching efficiency, tracking efficiency and GEANT/Fluka corrections) that have to be applied to the TOF Minimum Bias raw spectra will be described.

In \$6.2 studies on the sistematic uncertainties related to the track selection cuts, to the choice of the function used to fit the signal, and to the matching efficiency will be reported. In addition, a comparison with the spectra obtained with the unfolding procedure based on a slightly different fit function will be shown. This was meant to check the robustness of the TOF results within the unfolding method.

In \$6.3 the K/π and p/π ratios obtained from the TOF spectra will be reported and compared to the Monte Carlo predictions from different event generators and to the particle ratios obtained in pp collisions at $\sqrt{s} = 0.9$ TeV [75]. In the same section, also the final TOF results at $\sqrt{s} = 7$ TeV will

be compared to the Monte Carlo predictions.

In ALICE, the identified transverse momentum spectra analysis is based not only on TOF but makes also use of other PID detectors, techniques and tracking algorithms that are complementary to TOF in terms of momentum coverage. This allows to extend the particle identification on a wider p_t range. In addition, the p_t range where different analyses overlap can serve as a cross-check between them, proving the robustness of the results.

In \$6.4 a brief description of the ALICE spectra analyses and a comparison of their independent results will be provided showing, in particular, the excellent agreement between the TOF spectra and those from the others analyses in the p_t region where they overlap.

6.1 TOF transverse momentum spectra

In the previous chapter it was shown that the best way to identify π, K and p with the TOF detector is applying the unfolding technique since it allows to broaden the PID p_t coverage with respect to the other methods (e.g. 3σ cut). Besides, this approach does not rely on any Monte Carlo information and simulation for what concerns the PID efficiency and contamination. With this method we can identify pions and kaons up to $p_t = 2.5$ GeV/c and protons up to $p_t = 4.0$ GeV/c. Once the raw spectra are obtained, the efficiency corrections have to be applied. They include the correction due to the fact that not every primary track can be reconstructed (tracking efficiency) and that not every reconstructed track is matched with a TOF hit (matching efficiency). These corrections are obtained from the Monte Carlo simulations applying the same event and track cuts as in the data analysis.

6.1.1 Raw Spectra

Since in pp collisions the time-zero can be provided by the TOF detector only for a fraction of events, two subsamples of data can be defined. The first sample includes the 70% of the tracks for which the $t0_{TOF}$ measurement is available, with a resolution on the event time $\sigma t0 = \sigma t0_{TOF}$. The second sample is made out of the remaining 30% of the tracks, for which no time-zero information was available and $\sigma t0 = t0_{Spread}$. Since $\sigma t0_{TOF} < t0_{Spread}$, these two subsamples are characterized by a different total time resolution (see eq. 5.3). In order to deal with tracks with an uniform time resolution, the unfolding procedure was applied independently to each sample. In each subsample the $\Delta t_i = t_{TOF} - t0 - t_{exp,i}$ distributions, (one for each mass hypothesis, $i = \pi, K, p$), was fitted with three functions (see eq. 5.6), one for

the signal due to the particles for which the mass hypothesis i was correct, and two for the background deriving from particles belonging to the two other species. The raw yields of pions, kaons and protons were extracted from the integral of the signal fit function in both samples and summed up, to obtain the total raw spectra reported in Fig. 6.1. The spectra in the figure were normalized to the total number of analyzed events.

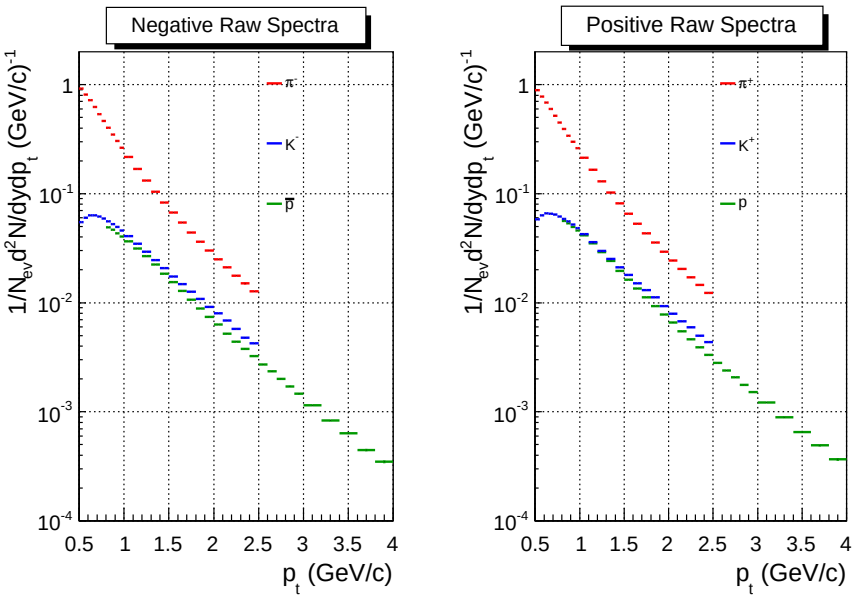

Figure 6.1: Total raw spectra obtained from the sum of the ones from the tracks for which the $t0_{TOF}$ measurement was available, and those from the tracks for which it was not. Negative (left) and positive (right) pions (red), kaons (blue) and protons (green) are shown.

As explained in \$4.5, due to the presence of the magnetic field which deflects the charged particles, Eff_{match} at $p_t < 0.5\,\mathrm{GeV/c}$ drops quickly and a little variation in the track momenta can cause a significant variation in Eff_{match}. To minimize the sensitivity of the analysis to imperfections in the simulation of the matching efficiency and to the uncertainty induced on the corresponding correction, only tracks with $p_t > 0.5\,\mathrm{GeV/c}$ were considered for the TOF analysis. Moreover, in the case of protons, p_t spectra are reported starting from $p_t = 0.8$ GeV/c since, below this threshold, the estimate of $t_{exp,p}$ suffers from imperfections in the corrections for energy loss in the material. This causes the signal distribution to be unsatisfactorily described by the fit function used in the procedure, and the result of the interpolation may

be not reliable. The PID efficiency of this method is assumed to be 100% by definition so no further corrections to be determined from Monte Carlo simulations are needed.

6.1.2 Matching Efficiency

The raw spectra have to be corrected for the matching efficiency (Eff_{match}) to take into account that only a fraction of the reconstructed primary tracks are matched with an hit on the TOF detector. Eff_{match} depends on the fraction of tracks that are lost during the propagation from TPC to TOF due to the geometrical acceptance, the decays and the interactions with the material. In addition it includes the probability to match a track reaching the TOF with a TOF hit. This depends on the TOF intrinsic detector efficiency, on the effect of dead channels and on the efficiency of the track-TOF signal matching procedure (for a detailed study of the matching efficiency see §4.5).

Eff_{match} is derived for each particle species from the Monte Carlo simulations. The matching efficiency, in the p_t range of interest for the analysis, for positive (line) and negative (dotted line) pions (red), kaons (blue) and protons (green) is reported in Fig. 6.2.

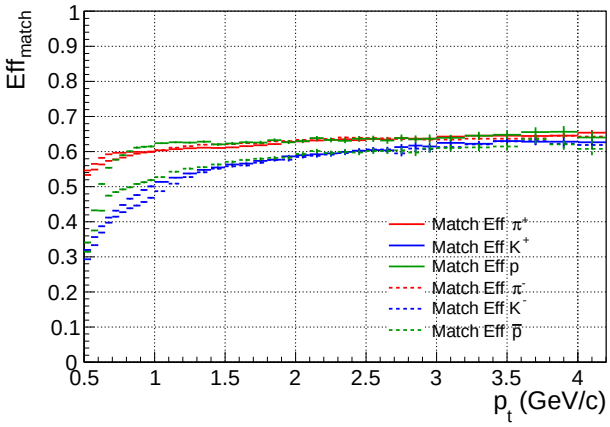

Figure 6.2: Matching efficiency for negative (dotted line) and positive (line) pions (red), kaons (blue) and protons (green). Only values for $p_t > 0.5$ GeV/c are shown.

The spectra corrected by the matching efficiency $(dN/dydp_t)_{Match}$ are obtained from the raw ones $(dN/dydp_t)_{Raw}$ as follows:

$$(dN/dydp_t)_{Match} = \frac{(dN/dydp_t)_{Raw}}{Eff_{match}} \tag{6.1}$$

From Fig. 6.2 it is clear that Eff_{match} for K^+ and p is higher than the one for K^- and $\overline{p}$, especially at low p_t. As already pointed out in \$4.5, a slight difference between protons and anti-protons and between kaons and anti-kaons is expected due to their different cross sections. This would anyway not explain the differences observed in Fig. 6.2 which was found to be due to the fact that the cross sections for $\overline{p}$ and K^- in GEANT3 (the ALICE simulation transport code) are not correctly reproduced, while Fluka is expected to provide a more accurate prediction. For this reason, a comparison between the GEANT3 and Fluka simulations was done and the two correction factors ($Corr_{Match}$) reported in Fig. 6.3 were extracted. To take into account also

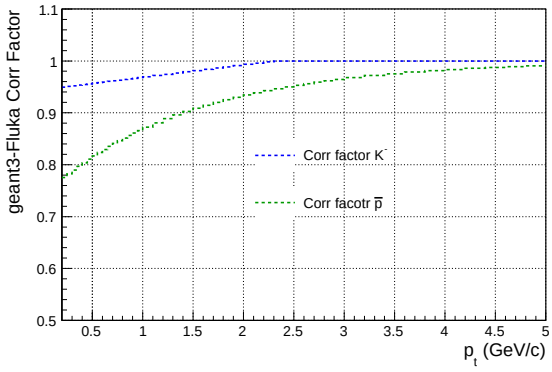

Figure 6.3: Correction factors for the matching efficiency of $\overline{p}$ and K^- extracted from the comparison between the GEANT3 and Fluka simulations.

the GEANT/Fluka correction, eq. 6.1 has to be modified as follows:

$$(dN/dydp_t)_{MatchMC} = \frac{(dN/dydp_t)_{Raw}}{Eff_{match}} \times Corr_{Match} \tag{6.2}$$

6.1.3 Tracking Efficiency

Once the corrections for the matching efficiency have been applied, we have to correct for the tracking efficiency (Eff_{track}), that is, for the fact that only a fraction of the primary tracks produced in the collisions are reconstructed by the TPC. Eff_{track} is calculated from Monte Carlo simulations comparing the number of reconstructed particles to the number of generated charged primary particles. In Fig. 6.4 the tracking efficiency for positive (line) and negative (dotted line) pions (red), kaons (blue) and protons (green) is shown.

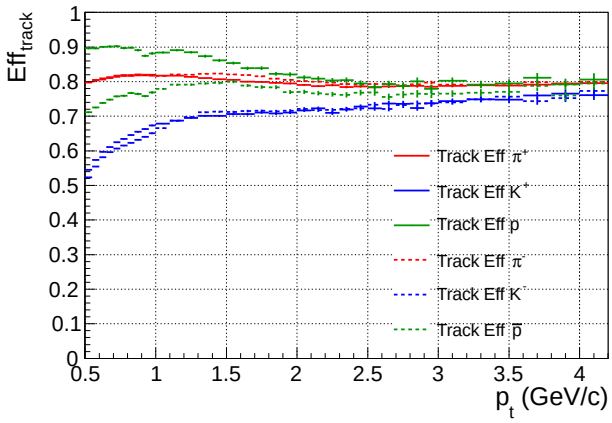

Figure 6.4: Tracking efficiency for negative (dotted line) and positive (line) pions (red), kaons (blue) and protons (green). Only values for $p_t > 0.5$ GeV/c are shown.

Eq. 6.3 combines the matching and tracking efficiency corrections that have to be applied to the raw spectra to get the corrected ones:

$$(dN/dydp_t)_{MatchMCTrack} = (dN/dydp_t)_{Raw} \frac{1}{Eff_{match}} \times Corr_{Match} \times \frac{1}{Eff_{track}} \tag{6.3}$$

The wrong simulation of the K^- and $\bar{p}$ cross sections in GEANT3 affects also the tracking efficiency. Also in this case, two correction factors ($Corr_{Track}$ reported in Fig. 6.5) have been extracted on the basis of the comparison between the GEANT3 and Fluka simulations.

The fully corrected spectra ($(dN/dydp_t)_{TOF}$) can finally be obtained as follows:

$$(dN/dydp_t)_{TOF} = (dN/dydp_t)_{Raw} \times \frac{1}{Eff_{match}} \times Corr_{Match} \times \frac{1}{Eff_{track}} \times Corr_{Track} \tag{6.4}$$

6.1.4 TOF Corrected Spectra

The primary spectra $(dN/dydp_t)_{TOF}$ reconstructed by the TOF detector and corrected for the matching and tracking efficiency and for the GEANT/Fluka factors as described in eq. 6.4 are reported in Fig. 6.6. Here only statistical errors are shown.

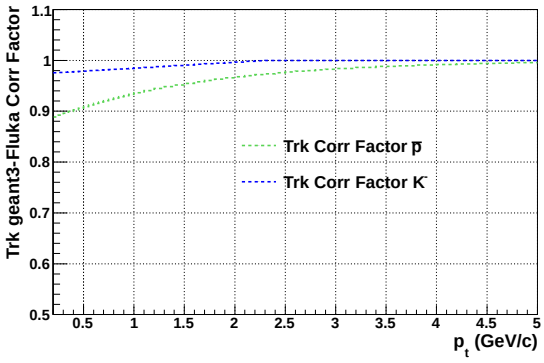

Figure 6.5: Tracking efficiency correction factors for $\overline{p}$ and K^- extracted from the comparison between the GEANT3 and Fluka simulations.

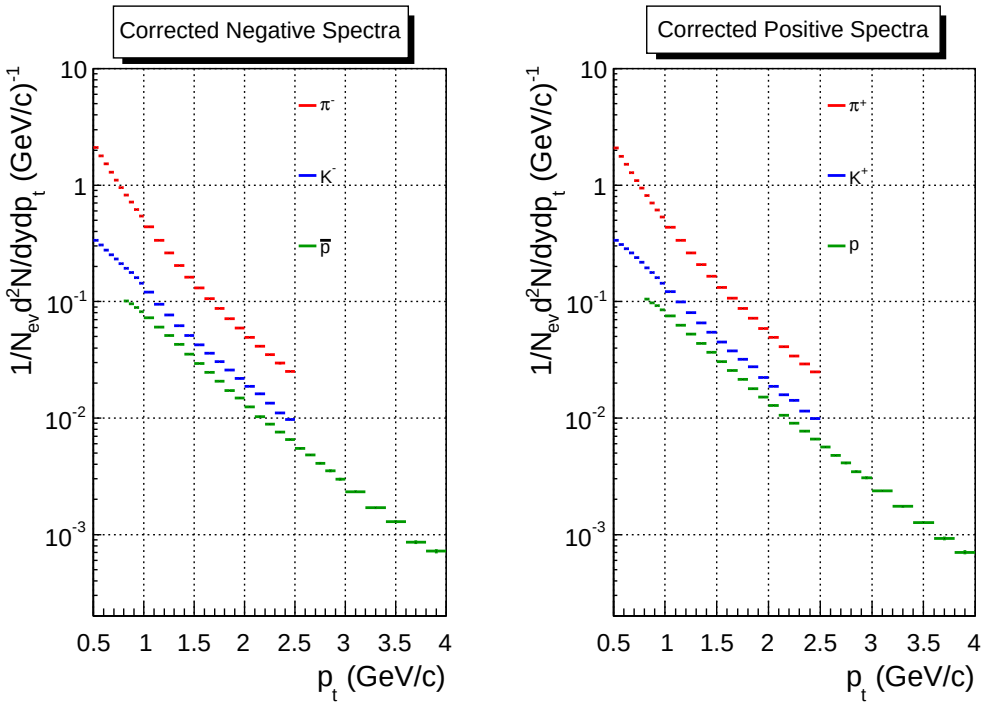

Figure 6.6: TOF spectra of negative (left) and positive (right) pions (red), kaons (blue) and protons (green) corrected for matching and tracking efficiency.

6.2 Systematic uncertainties

To evaluate the systematic uncertainties related to the track selection (see \$ 4.4), the same unfolding analysis was repeated varying one at a time the most significant track selection parameters. This was done within reasonable intervals according to the following table, both in data and Monte Carlo.

Parameter	Standard Value	Lower Value	Upper Value
min. TPC cluster	70	60	80
max. χ^2 per TPC cluster	4	3	5
max. DCAz (cm)	2	1	3

In Fig. 6.7 the ratios between the spectra obtained with the modified track cuts and the spectra obtained with the standard ones are shown. It can be seen that, for all the species, there is no dependence of the spectra on the value of the maximum χ^2 per TPC clusters and of the maximum DCAz required. On the contrary, especially for pions and kaons with $p_t < 1.8$ GeV/c, a variation up to $\sim$8% is present if the minimum number of TPC cluster varies from 70 to 60 or 80.

Moreover, another source of systematic uncertainty is related to the matching efficiency. This was evaluated during the spectra analysis on the $\sqrt{s} = 0.9$ TeV pp data [75], comparing, for each particle species, the matching efficiency obtained on Monte Carlo samples with the one obtained on the data using the dE/dx in the TPC to identify the particles. Good agreement was observed in the case of pions, kaons and protons, with deviations of the level of, at most, 3%, 6% and 4% respectively, over the full p_t range. The observed differences were assigned as systematic errors.

To check the systematic uncertainties related to the PID procedure, I performed the same unfolding analysis fitting the signal with a function made of a gaussian term plus an exponential tail on its right-end side, where all the parameters but one, were fixed to the values obtained during the standard analysis (see \$6.1.1). The remaining parameter was, on the contrary, increased or decreased by the 10% with respect to the "standard" value. During these fits only the yields for the signal and the background were left free. In Fig. 6.2 the ratios between the spectra obtained changing the fit parameters and the spectra in Fig. 6.1 are shown. The effect is less than 4% for each particle species.

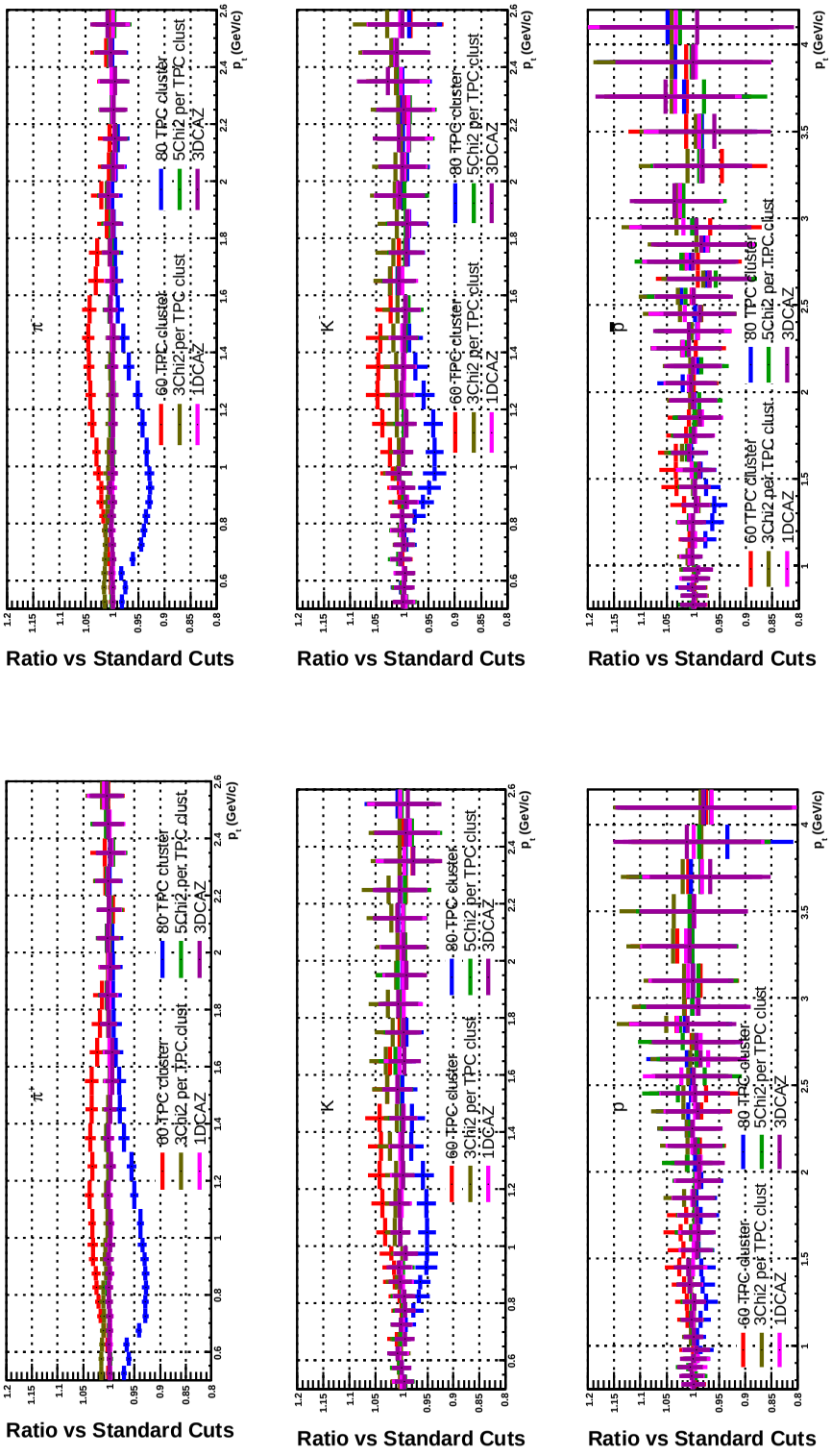

Figure 6.7: Ratios between the spectra obtained with the modified track cuts and those obtained with the standard cuts for positive (left) and negative (right) pions (top), kaons (middle) and protons (bottom).

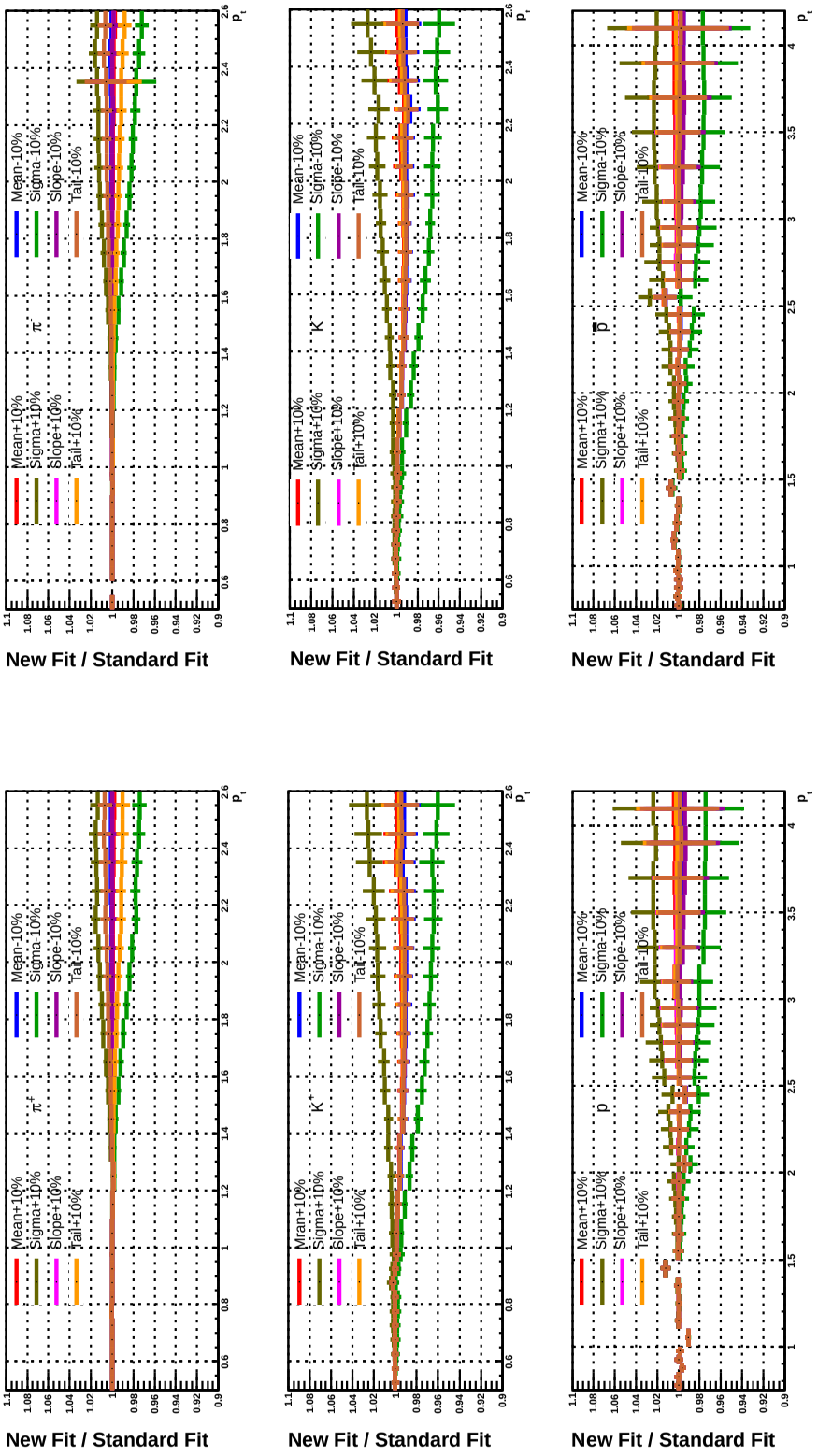

Figure 6.8: Ratios between the spectra obtained changing the fit parameters and those in Fig. 6.1 for positive (left) and negative (right) pions (top), kaons (middle) and protons (bottom).

In Fig. 6.9 the square sum of the three sources of systematic uncertainties described above is shown. We can see that the maximum value for all the particle species is ∼8%.

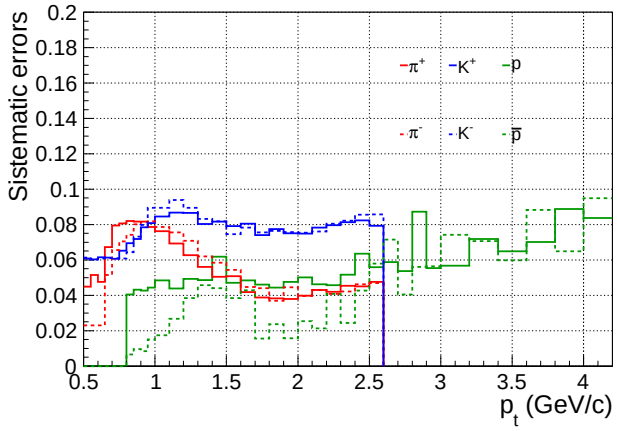

Figure 6.9: Overall systematic errors (due to the track selection, the PID procedure and the matching efficiency) for negative (dotted line) and positive (line) pions (red), kaons (blue) and protons (green).

In Fig. 6.10 the final TOF spectra (already shown in Fig. 6.6) are reported with both the statistical (stat) and the systematical (syst) errors (combined as $\sqrt{(syst)^2 + (stat)^2}$).

Checks on the fit function

To prove the robustness of the TOF results, I checked the dependence of the raw spectra on the fit function shape. In addition, I checked if the raw spectra obtained analyzing all the tracks together are compatible with the ones obtained analyzing the two samples of tracks with and without the $t0_{TOF}$ separately. For these purposes, I analyzed the same sample of events fitting the Δt_i distribution of the whole sample of tracks, regardless the availability of the $t0_{TOF}$, with three functions $f'(x)$ each of which defined by a gaussian term and two exponential tails, one on each end side of the gaussian function:

$$x \leq \overline{x} + t \quad \text{or} \quad x \geq \overline{x} - tsx \rightarrow f'(x) = Gaus(x, \overline{x}, \sigma) \tag{6.5}$$

$$x > \overline{x} + t \rightarrow f'(x) = Gaus(\overline{x} + t, \overline{x}, \sigma) \times Exp(-s(x - t - \overline{x}))$$

$$x < \overline{x} - t_{sx} \rightarrow f'(x) = Gaus(\overline{x} - t_{sx}, \overline{x}, \sigma) \times Exp(-s_{sx}(x + t_{sx} - \overline{x}))$$

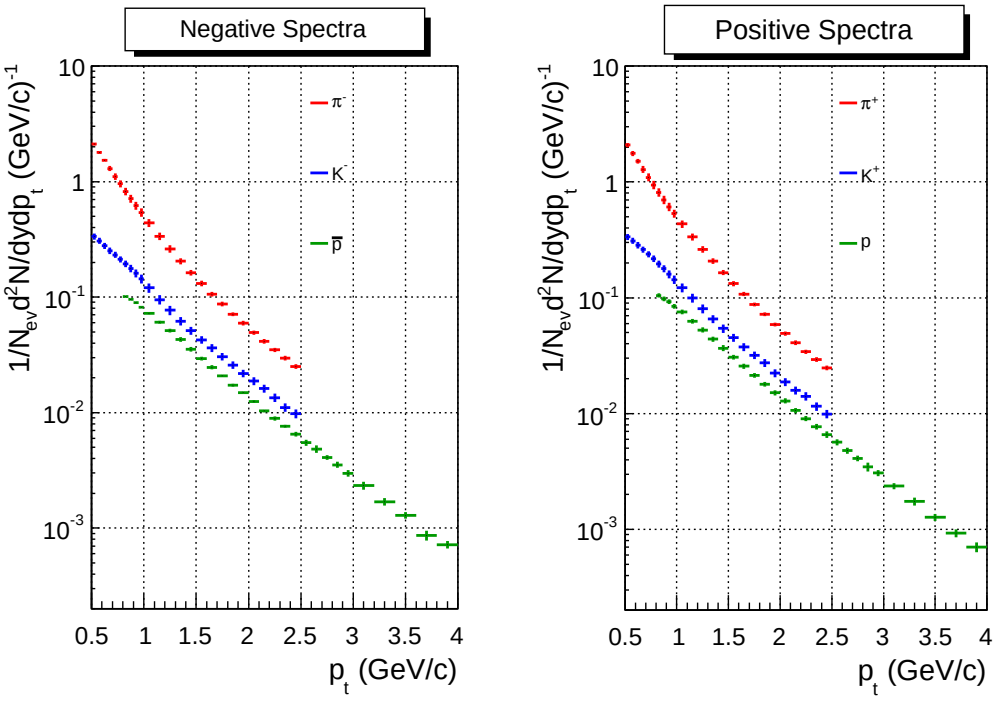

Figure 6.10: TOF spectra of negative (left) and positive (right) pions (red), kaons (blue) and protons (green) corrected for the matching and tracking efficiency. The error bars correspond to the combination of the statistical (stat) and systematical (syst) uncertainties ($\sqrt{(syst)^2 + (stat)^2}$).

Each function $f'(x)$ has 6 parameters: the mean ($\overline{x}$) and the sigma (σ) of the gaussian shape, the tails (t and t_{sx}) that are the points where the exponential tails start and their slopes (s and s_{sx}). t and s are the tail and the slope of the exponential tail on the right-end side of the gaussian shape while t_{sx} and s_{sx} are the tail and the slope of the exponential tail on the left-end side. Also in this case the exponential tails are supposed to have the same slope for the signal and the backgrounds due to the other two species. In Fig. 6.11, Fig. 6.12 and Fig. 6.13 an example of the fit for the pion, kaon and proton mass hypothesis is reported. In Fig. 6.14 the ratio between the raw spectra obtained fitting separately the two sub-sample of tracks using as fit functions a gaussian term and an exponential tail (see \$5.3.1), and fitting all the tracks together using as fit functions a gaussian term and two exponential tails is shown. It can be seen that the difference is less than 5% except for few p_t regions for kaons and protons where the $f'(x)$ functions are not able to accurately describe the data.

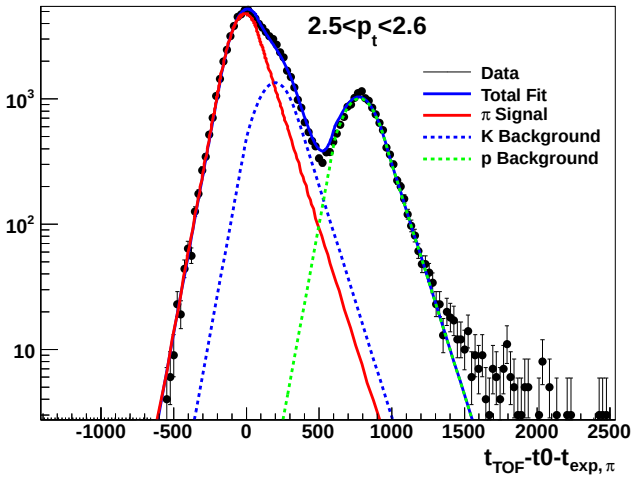

Figure 6.11: $t_{TOF} - t0 - t_{exp,\pi}$ distribution for all tracks. The $2.50 < p_t < 2.60$ GeV/c interval was considered. The red line corresponds to the fit of the signal, while the dotted blue and green lines are the fits to the background. Each fit function consists of a gaussian part and two exponential tails one on each side.

We have hence shown how the TOF results are stable with respect to the shape of the fit function and with respect to fitting all the tracks together regardless of which time-zero is present or the samples of tracks with and without $t0_{TOF}$ separately.

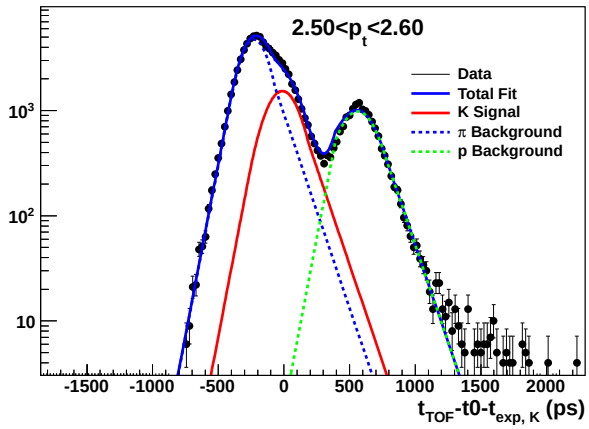

Figure 6.12: $t_{TOF} - t0 - t_{exp,K}$ distribution for all tracks. The $2.50 < p_t < 2.60$ GeV/c interval was considered. The red line corresponds to the fit of the signal, while the dotted blue and green lines are the fits to the background. Each fit function consists of a gaussian part and two exponential tails one on each side.

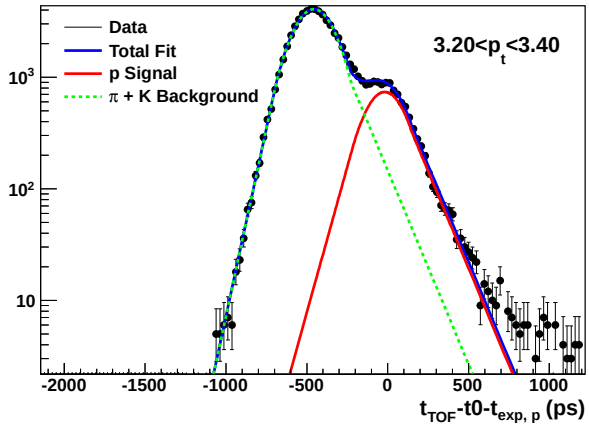

Figure 6.13: $t_{TOF} - t0 - t_{exp,p}$ distribution for all tracks. The $3.20 < p_t < 3.40$ GeV/c interval was considered. The red line corresponds to the fit of the signal, while the dotted green line is the fit to the background. Each fit function consists of a gaussian part and two exponential tails one on each side. We notice that, since in this momentum range pions and kaons can not be distinguished, I considered the background as made of only one single distribution.

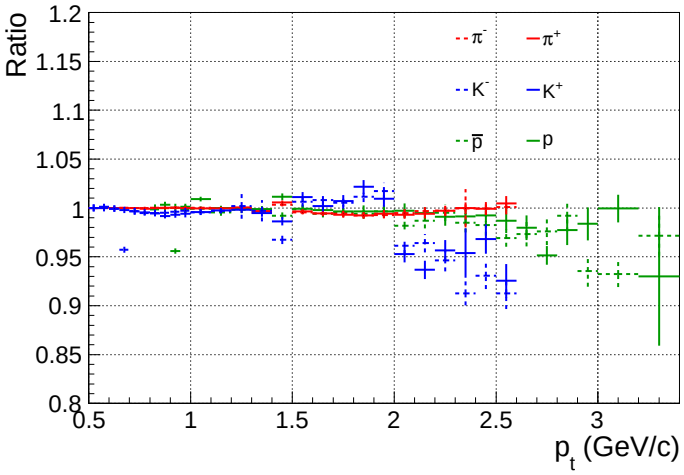

Figure 6.14: Ratios between the raw spectra obtained fitting the two subsample of tracks with three functions defined by a gaussian term plus an exponential tail and fitting all the tracks together with three functions consisting of a gaussian term plus two exponential tails.

6.3 TOF spectra: particle ratios and Monte Carlo comparison

The transverse momentum spectra in pp collisions provide a useful reference to tune Monte Carlo models. In Fig. 6.15, 6.16 and 6.17 the transverse momentum spectra of negative pions, kaons and protons reconstructed using the TOF PID are compared with the predictions of the most updated tunes of the Pythia event generator [76] and with Phojet [77]. The spectra are normalized to the number of inelastic collisions that is the sum of non diffractive, single-diffractive and double-diffractive interactions[1]. We can see that all the Monte Carlo generators do not provide a satisfactory description of the data. The one that reproduces the data in the best way is the Perugia tune (named Perugia 2011) which takes into account some of the first LHC results obtained from the analysis of pp collisions at $\sqrt{s} = 0.9$ and 7 TeV (e.g. multiplicity measurements and results on strange barion production). In detail, the Perugia 2011 tune is able to give a reasonable description of the K^- spectrum over the whole p_t range and of the $\overline{p}$ spectrum for $p_t > 1$ GeV/c. However, it deviates by ∼25% from the measured π^- spectrum. The

[1]For details on the normalization procedure see [78].

same conclusions can be drawn looking at the comparison between the Monte Carlo predictions and the measured spectra of positive pions, kaons and protons, (not reported here).

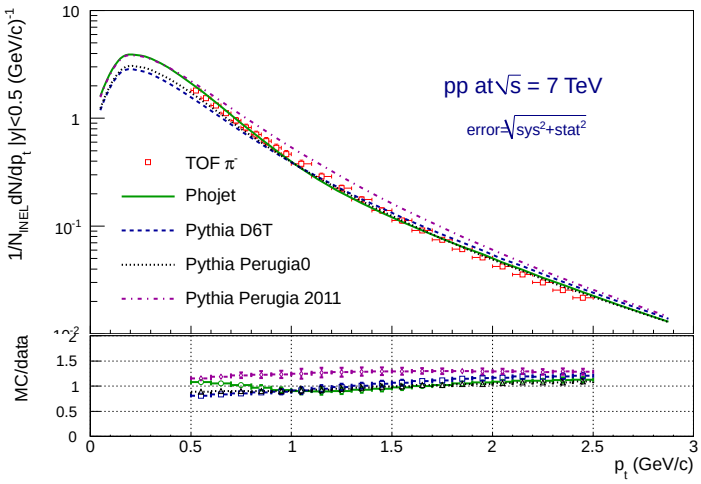

Figure 6.15: Top: comparison between the π^- spectrum reconstructed using the TOF PID in pp collisions at $\sqrt{s} = 7$ TeV and the predictions of the most updated event generators. Both statistical and systematical errors are shown. Bottom: ratios between the Monte Carlo predictions and the measured spectrum.

In Fig. 6.18 the $(K^+ + K^-)/(\pi^+ + \pi^-)$ ratio derived from the TOF spectra for pp collisions at $\sqrt{s} = 7$ TeV (red markers) is shown as a function of p_t. As a comparison, the predictions from the same Monte Carlo generators shown in the previous figures are reported. As expected, they are not able to give a reasonable description of the data, which lie above than any Monte Carlo prediction. In addition, the K/π ratio obtained from the ALICE spectra analysis of pp collisions at $\sqrt{s} = 0.9$ TeV (violet markers, see [75]) is shown. For $p_t < 1.3$ GeV/c the K/π ratio is independent from the collision energy while at higher momenta some differences are present. One should have in mind that, in the $\sqrt{s} = 0.9$ TeV analysis, results in the high p_t region were based on a very limited statistics. Nevertheless, further checks are ongoing to understand the origin of the discrepancy.

In Fig. 6.19 the $(p + \overline{p})/(\pi^+ + \pi^-)$ ratio derived from the TOF spectra for pp collisions at $\sqrt{s} = 7$ TeV (red markers) is shown as a function of p_t. In addition, the p/π ratio obtained from the ALICE spectra analysis of pp collisions at $\sqrt{s} = 0.9$ TeV (violet markers) (see [75]) and the Monte Carlo generators predictions at 7 TeV are reported. As far as the dependency on

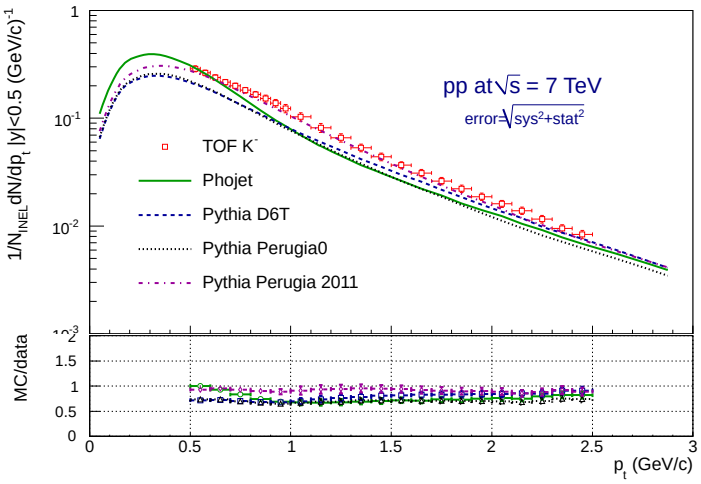

Figure 6.16: Top: comparison between the K^- spectrum reconstructed using the TOF PID in pp collisions at $\sqrt{s} = 7$ TeV and the predictions of the most updated event generators. Both statistical and systematical errors are shown. Bottom: ratios between the Monte Carlo predictions and the measured spectrum.

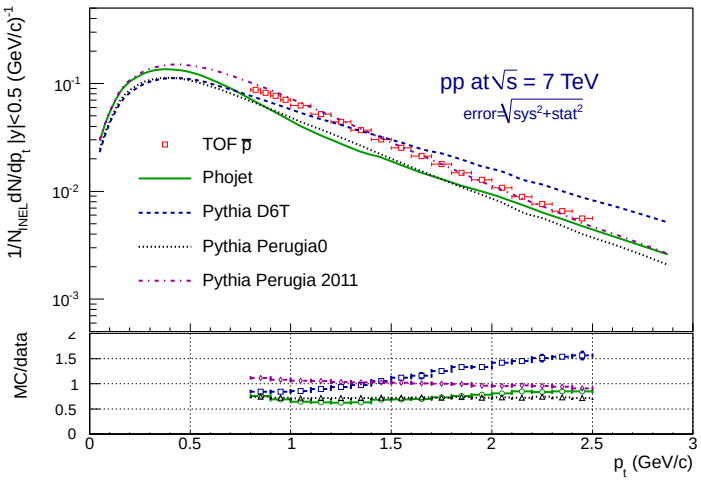

Figure 6.17: Top: comparison between the $\overline{p}$ spectrum reconstructed using the TOF PID in pp collisions at $\sqrt{s} = 7$ TeV and the predictions of the most updated event generators. Both statistical and systematical errors are shown. Bottom: ratios between the Monte Carlo predictions and the measured spectrum.

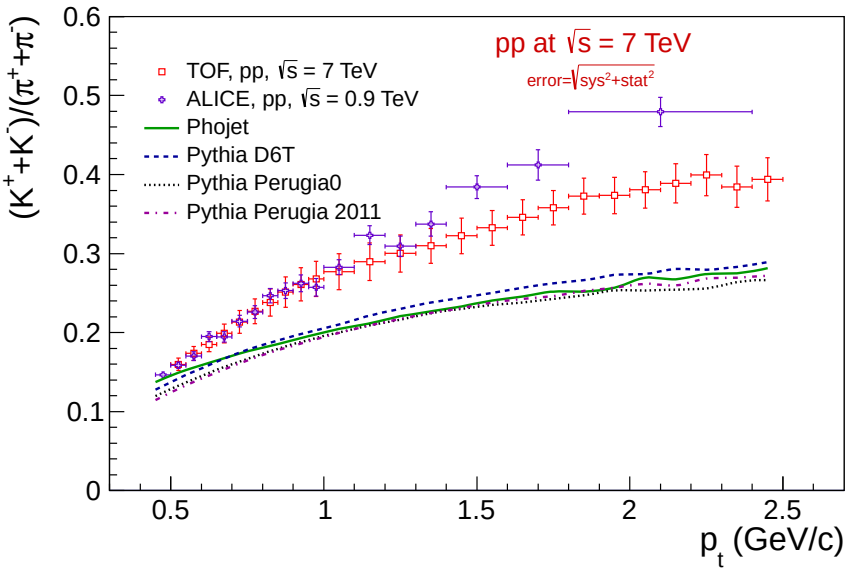

Figure 6.18: $(K^+ + K^-)/(\pi^+ + \pi^-)$ ratio as a function of p_t for pp collisions at $\sqrt{s} = 7$ TeV (red markers) and $\sqrt{s} = 0.9$ TeV (violet markers). For $\sqrt{s} = 7$ TeV data, both statistical and systematical uncertainties are shown, while for $\sqrt{s} = 0.9$ TeV data only the statistical ones are reported. The dashed and dotted curves refer to different Monte Carlo generators predictions.

the energy of the system is concerned, one can see that the $\sqrt{s} = 0.9$ TeV p/π ratio is higher than the one obtained from $\sqrt{s} = 7$ TeV data, being the difference rather constant for $p_t > 1.2$ GeV/c. Comparing with Monte Carlo results, one can see that at present, as it was for K/π, the p/π ratio can not be described in a satisfactory way by any Monte Carlo prediction, as expected.

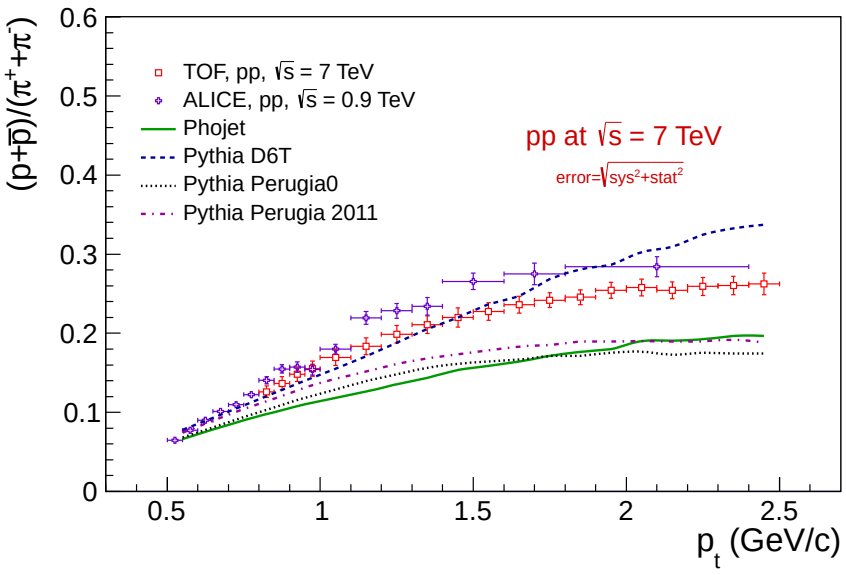

Figure 6.19: $(p + \overline{p})/(\pi^+ + \pi^-)$ ratio as a function of p_t for pp collisions at $\sqrt{s} = 7$ TeV (red markers) and $\sqrt{s} = 0.9$ TeV (violet markers). For $\sqrt{s} = 7$ TeV data, both statistical and systematical uncertainties are shown, while for $\sqrt{s} = 0.9$ TeV data only the statistical ones are reported. The dashed and dotted curves refer to different Monte Carlo generators predictions.

6.4 The ALICE spectra results

As mentioned before, in the ALICE collaboration, the identified transverse momentum spectra analysis is based not only on TOF, but makes use also of other PID detectors, techniques and tracking that are complementary to the TOF analysis in terms of momentum coverage. To extend the identified spectra on a wider p_t range, four independent analyses were performed. Namely:

- the so-called *ITSsa* analysis based on a nσ cut method applied on the ITS dE/dx signal. It uses only ITS stand-alone tracks (see \$3.2) to extend the spectra reconstruction at low p_t;
- the so-called *ITSTPC* analysis based on an unfolding method on the ITS dE/dx signal. It uses global tracks (see \$3.2);
- the so-called *TPCTOF* analysis based on a nσ cut method on both the TPC dE/dx signal and the TOF time signal. It uses global tracks;
- the so-called *TOF* analysis based on an unfolding method on the TOF time signal, as already described in this thesis. It uses global tracks.

In Tab. 6.1 the momentum coverage for each spectra analysis and each particle species is summarized.

	p_t ranges (GeV/c)			
	ITSsa	*ITSTPC*	*TPCTOF*	*TOF*
π	0.1-0.5	0.2-0.55	0.2-1.2	0.5-2.5
K	0.2-0.5	0.25-0.5	0.25-1.2	0.5-2.5
p	0.3-0.55	0.4-0.85	0.45-1.7	0.8-4.0

Table 6.1: Momentum coverage for each ALICE spectra analysis.

In Fig. 6.20 the comparison between the primary π^+ spectra obtained independently by the four analyses is shown. The spectra are normalized to the number of analyzed events and both systematical and statistical errors ($\sqrt{(syst)^2 + (stat)^2}$) are reported. As it can be seen from the bottom panels, where the ratios between the spectra from the different analyses are drawn using the *TPCTOF* one as a reference, the results are compatible within the errors in the p_t overlapping regions within 4%[2].

[2]We remind here that the primary particles are those directly produced in the collisions including the products of strong and electromagnetic decays but excluding weak decays of strange particles.

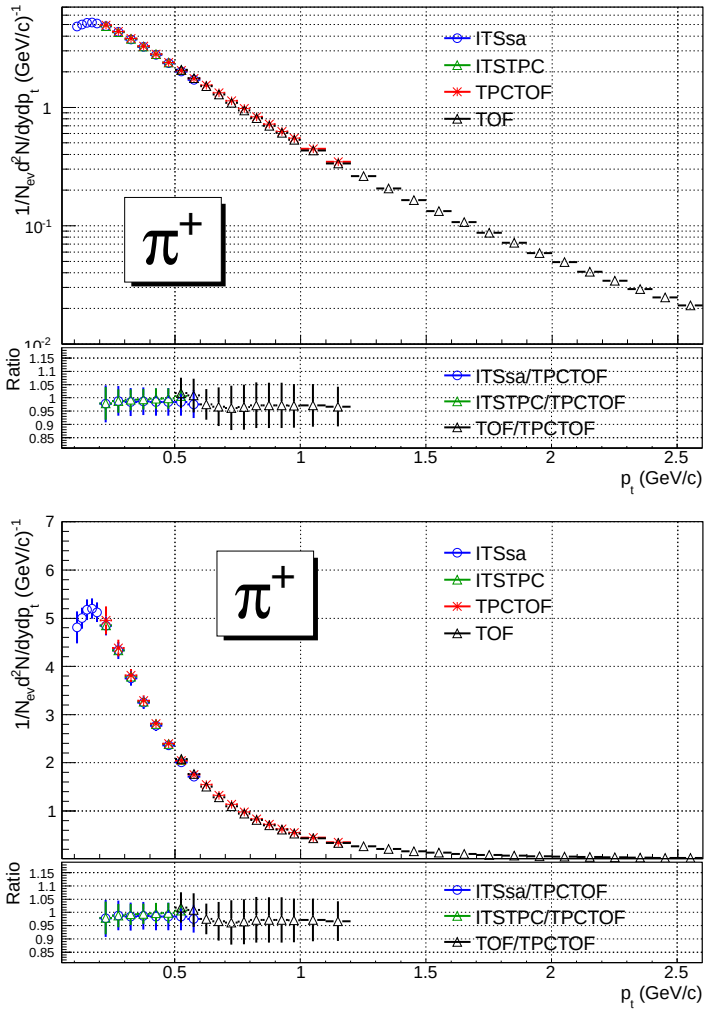

Figure 6.20: Comparison between the most updated π^+ spectra obtained independently by the *ITSsa*, *ITSTPC*, *TPCTOF*, *TOF* analyses in logarithmic (top) and linear (bottom) scale. The spectra are normalized to the number of analyzed events. Both systematical and statistical errors ($\sqrt{(syst)^2 + (stat)^2}$) are reported.

The same comparisons for primary K^+, p, π^-, K^- and $\overline{p}$ spectra are reported in Fig. 6.21, Fig. 6.22, Fig. 6.23, Fig. 6.24, and Fig. 6.25. Also for these spectra the results are compatible within the errors in the p_t overlapping regions within less that 6%

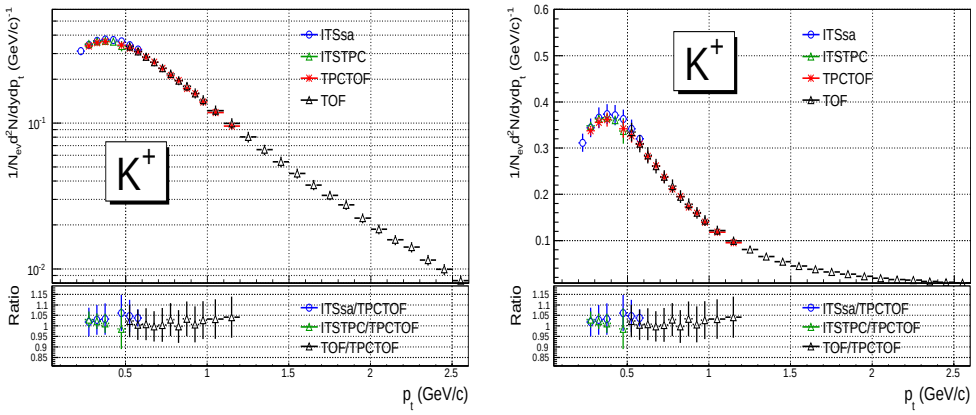

Figure 6.21: Comparison between the most updated K^+ spectra obtained independently by the *ITSsa*, *ITSTPC*, *TPCTOF*, *TOF* analyses in logarithmic (left) and linear (right) scale. Both systematical and statistical errors ($\sqrt{(syst)^2 + (stat)^2}$) are reported.

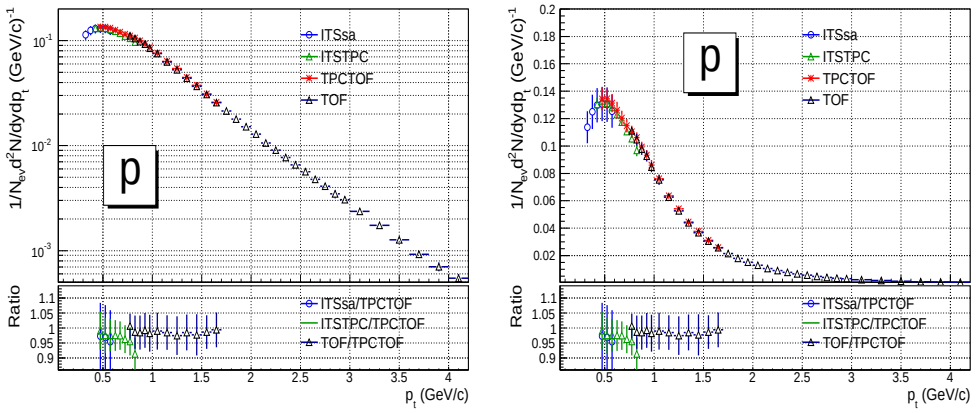

Figure 6.22: Comparison between the most updated p spectra obtained independently by the *ITSsa*, *ITSTPC*, *TPCTOF*, *TOF* analyses in logarithmic (left) and linear (right) scale. Both systematical and statistical errors ($\sqrt{(syst)^2 + (stat)^2}$) are reported.

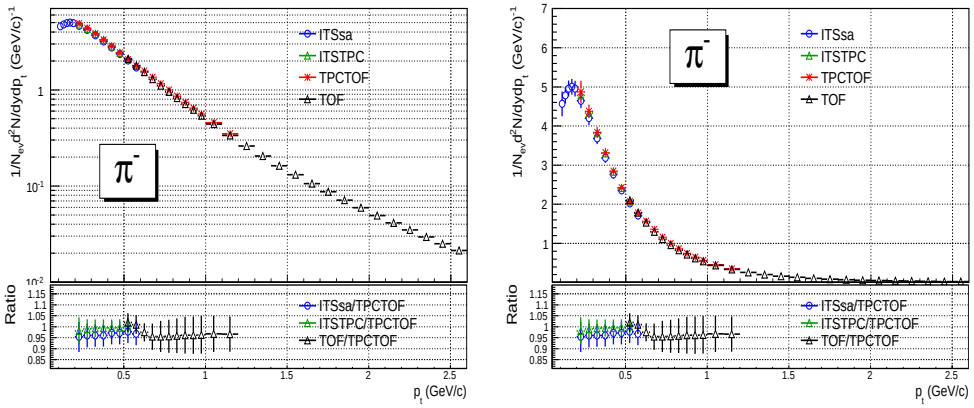

Figure 6.23: Comparison between the most updated π^- spectra obtained independently by the *ITSsa*, *ITSTPC*, *TPCTOF*, *TOF* analyses in logarithmic (left) and linear (right) scale. Both systematical and statistical errors ($\sqrt{(syst)^2 + (stat)^2}$) are reported.

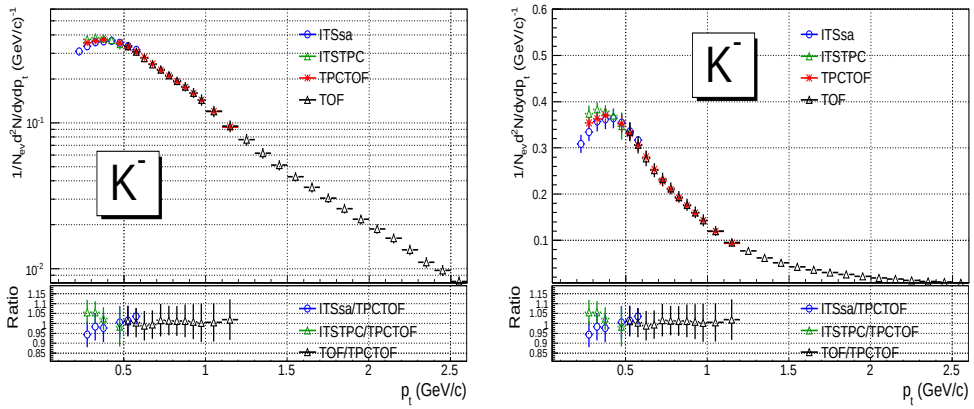

Figure 6.24: Comparison between the most updated K^- spectra obtained independently by the *ITSsa*, *ITSTPC*, *TPCTOF*, *TOF* analyses in logarithmic (left) and linear (right) scale. Both systematical and statistical errors ($\sqrt{(syst)^2 + (stat)^2}$) are reported.

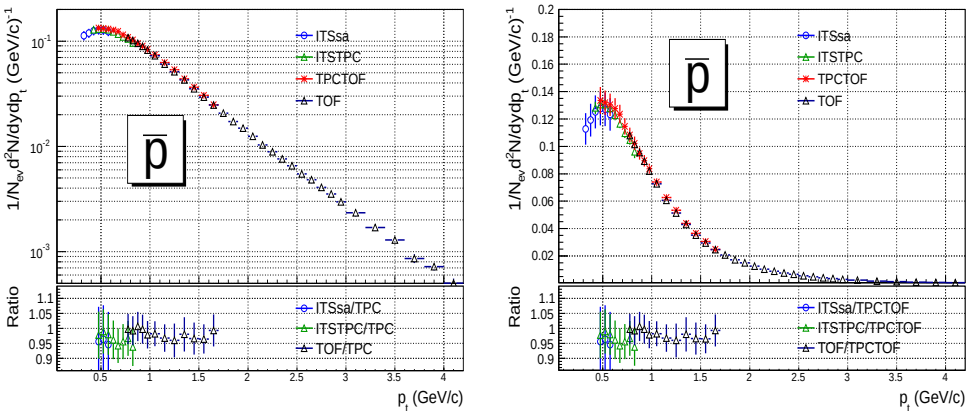

Figure 6.25: Comparison between the most updated $\overline{p}$ spectra obtained independently by the *ITSsa*, *ITSTPC*, *TPCTOF*, *TOF* analyses in logarithmic (left) and linear (right) scale. Both systematical and statistical errors ($\sqrt{(syst)^2 + (stat)^2}$) are reported.

Thanks to the fact that the spectra from the *ITSsa*, *ITSTPC*, *TPCTOF* and *TOF* analyses agree within the errors, they can be combined to cover the widest p_t range. This combination of spectra in pp collisions at $\sqrt{s} = 7$ TeV was already done with the first preliminary ALICE results shown at the 2011 Quark Matter conference (23-28 May 2011 Annecy, France). Since the TOF spectra analysis was not yet finalized, the TOF p_t coverage was limited to a safe region, that was $p_t < 1.6$ GeV/c for pions and kaons and $p_t < 2.5$ GeV/c for protons. Small differences with respect to the most updated spectra shown in the previous figures were present also for the other analyses. However, the current and Quark Matter spectra are compatible within errors.

In Fig. 6.26 the combined spectra shown at Quark Matter obtained averaging the four independent analyses using the systematic errors as weights are shown for negative (top) and positive (bottom) particles.

The combined spectra were fitted with the Lévy-Tsallis function ([79]):

$$\frac{d^2N}{dp_t dy} = p_t \frac{dN}{dy} \frac{(n-1)(n-2)}{nC(nC + m_0(n-2))} \left(1 + \frac{m_t - m_0}{nC}\right)^{-n} \qquad (6.6)$$

where C, n and the yield dN/dy are the parameters of the fit. This function is able to describe the data within few percent. For this reason it was used to extract the total yields and the mean p_t ($< p_t >$). As it can be seen, the p_t coverage at the time of the Quark Matter conference was $0.1 < p_t < 1.6$ GeV/c for pions, $0.2 < p_t < 1.6$ GeV/c for kaons and $0.3 < p_t < 2.5$ GeV/c for protons.

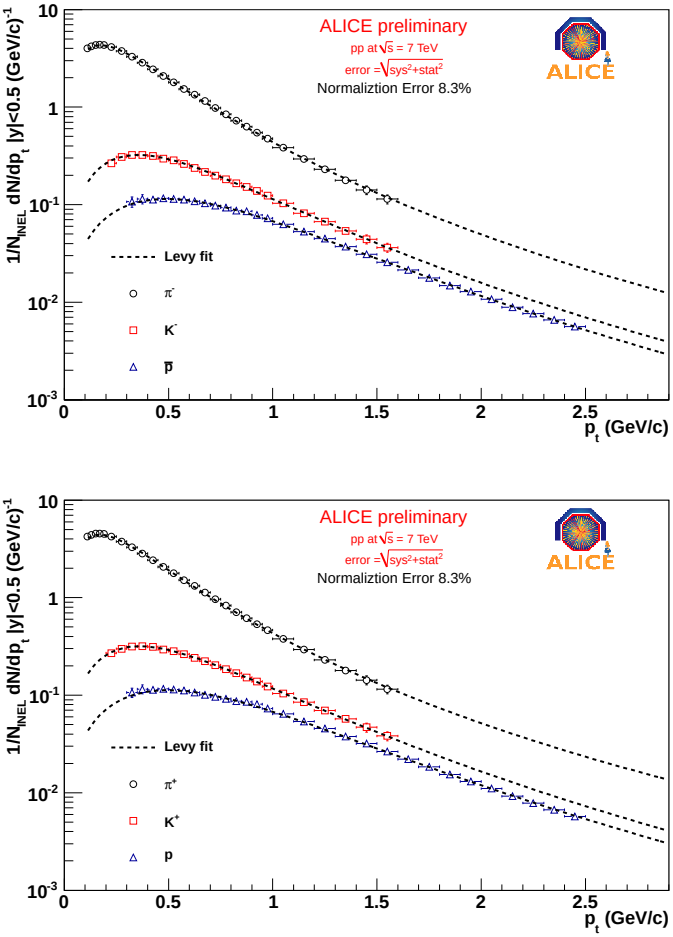

Figure 6.26: Minimum-Bias combined transverse momenutm spectra for positive (top) and negative (bottom) pions, kaons and protons in pp collisions at $\sqrt{s} = 7$ TeV shown at the Quark Matter conference. The fits to the data with the Lévy-Tsallis function are reported.

With the latest results, a better agreement within the analyses was reached and the p_t coverage extended up to $p_t = 2.5$ GeV/c for pions and kaons and up to $p_t = 4.0$ GeV/c for protons. Anyway, this results are still in the process of being finalized and their combination is still ongoing. For this reason hereafter I will show the results on integrated K/π and p/π ratios and on $< p_t >$ that were obtained with the preliminary spectra shown at the Quark Matter conference (see [80] and [81]).

In Fig. 6.27 the ratio of integrated yields K/π is shown for different collision energies. This ratio does not seem to vary going from the 0.9 TeV (see [75]) to the 7 TeV ALICE data, while at lower centre-of-mass energies it shows a slight increase.

In Fig. 6.28 the p/π ratio is shown for separate charges to point out how the baryon/antibaryon asymmetry vanishes at the LHC energy (as already reported in [82]) leading to a constant value of about 0.05.

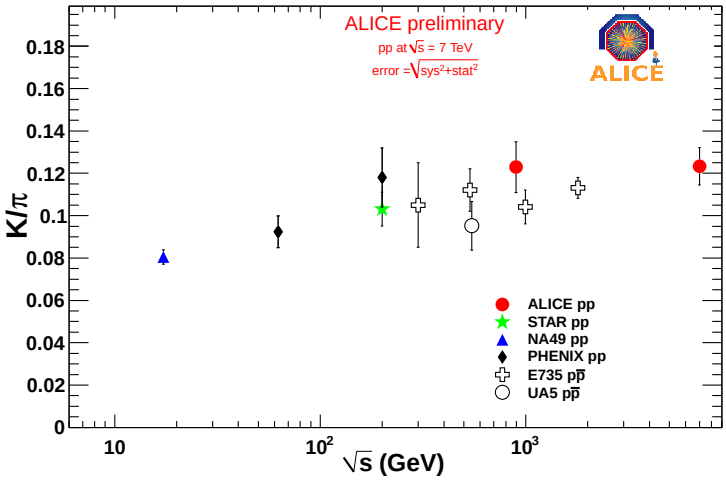

Figure 6.27: K/π integrated yield ratios in pp collisions as a function of the collision energy.

In Fig. 6.29 the mean p_t for π, K and p at different collision energies is reported. An increase as a function of the mass of the particles is visible. Moreover, as one can seen, the $< p_t >$ increases with the collision energy hinting at the fact that harder spectra are created at higher energies.

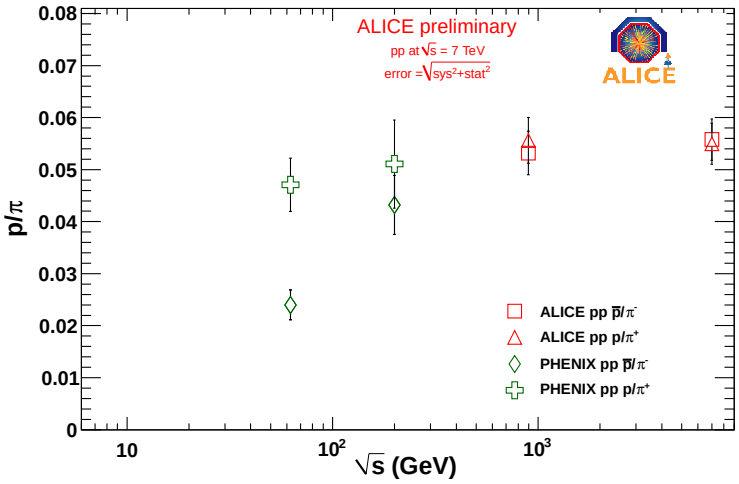

Figure 6.28: p/π integrated yield ratios in pp collisions as a function of the collision energy.

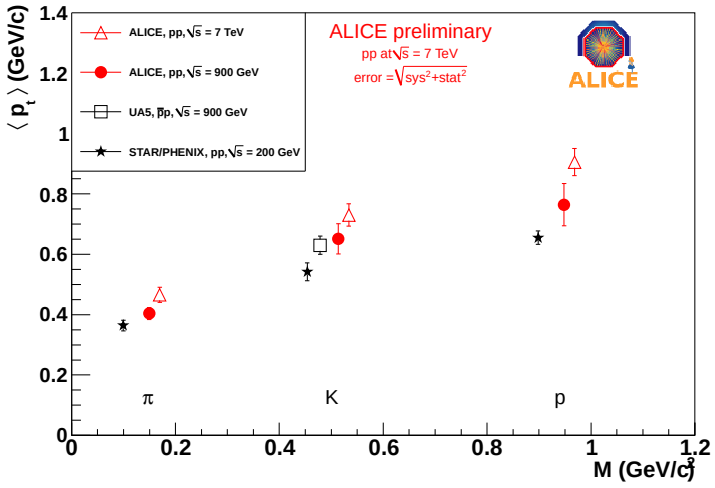

Figure 6.29: Mean p_t for π, K and p at different collision energy in pp collisions.

Conclusions

In this thesis the analysis to reconstruct the transverse momentum (p_t) spectra for pions, kaons and protons identified with the TOF detector of the ALICE experiment in pp Minimum Bias collisions at $\sqrt{s} = 7$ TeV was reported.

After a detailed description of all the parameters which influence the TOF PID performance (time resolution, calibration, alignment, matching efficiency, time-zero of the event) the method used to identify the particles, the unfolding procedure, was discussed. With this method, thanks also to the excellent TOF performance, the pion and kaon spectra can be reconstructed in the $0.5 < p_t < 2.5$ GeV/c range, while the protons can be measured in the interval $0.8 < p_t < 4.0$ GeV/c. To prove the robustness of these results, a comparison with the spectra obtained with a more traditional approach, a 3σ cut PID procedure, was reported, showing an agreement within 5%. In addition, the estimation of the systematic uncertainties (related to the track selection, the PID procedure and the matching efficiency), was described.

The reported spectra provide very useful information to tune the Monte Carlo generators that, as was shown, are not able to describe π, K and p production over the full momentum range. The same limitation for the theoretical models in describing the data was observed when comparing with the Monte Carlo predictions the K/π and p/π ratios, as obtained with the TOF analysis.

Finally, the comparison between the TOF results and the spectra obtained with analyses that use other ALICE PID detectors and techniques to extend the identified spectra to a wider p_t range was reported, showing an agreement within 6%. Since all these ALICE analyses on the identified spectra are compatible within the errors, they were combined and fitted with a Lévy-Tsallis function to extract the total yields and the mean p_t. These results represent a fundamental reference for the understanding of Pb-Pb data.

Bibliography

[1] E. Andersen et al. (WA97 Collaboration), *Strangeness enhancement at mid-rapidity in Pb-Pb collisions at 158 A GeV/c*, Phy. Lett. B 449 (1999) 401-406

[2] H. Caines, *Using strange hadrons as probes of dense matter*, J. Phys.G: Nucl. Part. Phys. 32 (2006) S171-S178

[3] M.A.C. Lamont,*Recent Results on Strangeness and Heavy Flavour at RHIC*, J. Phys:Conference Series 50 (2006) 192-200

[4] F. Antinori et al. (NA57 Collaboration), *Enhancement of hyperon production at central rapidity in 158 A GeV/c Pb-Pb collision*, J. Phys.G: Nucl. Part. Phys. 32 (2006) 427-441

[5] H. Caines, *Strange hadrons as dense matter probes*; Proceedings of the Strange Matter Conference 2006

[6] T. Matsui, H. Satz, J/ψ *suppression by quark-gluon plasma formation*; Phys. Lett. B178(1986) 416

[7] M.C. Abreu et al. (NA50 Collaboration), *Evidence for deconfinement of quarks and gluons from the* J/ψ *suppression pattern measured in Pb-Pb collisions at the CERN-SPS*, Physics Letter B 477, (2000) 28

[8] A. A. P. Suaide, *Heavy Flavor Measurements at RHIC*, Brazilian Journal of Physics, vol. 37, no. 2C, June, 2007

[9] R. Granier de Cassagnac, J/ψ *production in PHENIX*, arXiv:nucl-ex/0608041v1

[10] S.S. Adler et al., *Centrality Dependence of Direct Photon Production in* $\sqrt{s_{NN}} = 200\,\mathrm{GeV}$ *in* $Au - Au$ *Collision*, arXiv:nucl-ex/0503003 (2005)

[11] S. S. Adler et al., *Centrality Dependence of Charm Production from a Measurement of Single Electrons in Au − Au Collisions at* $\sqrt{s_{NN}} =$ 200 GeV, Phys. Rev. Lett. PRL 94, 082301 (2005)

[12] M. Kaneta, N. Xu, *Centrality Dependence of Chemical Freeze-out in Au+Au Collision at RHIC*, arXiv:nucl-th/0405068v1 (2004)

[13] B. Mohanty, *Results from STAR experiment at RHIC*

[14] O. Brannikova, *Bulk properties at RHIC: systematic study*, J. Phys. G:Nucl. Part. Phys. 31 (2005) S93-S99

[15] S.S Adler et al., (PHENIX Collaboration), *Absence of Suppression in Particle Production at Large Transverse Momentum in* $\sqrt{s_{NN}} =$ 200 GeV *d+Au Collisions*, Phys. Rev. Lett. 91 (2003) 072303

[16] D. d'Enterria, *Jet quenching: RHIC result and phenomenology*, arXiv:nucl-ex/0510062v1

[17] C. Klein-Bosing, *Systematic Study of Particle Production at High* p_t *with the PHENIX Experiment*, arXiv:nucl-ex/0606013v1 6 Jun (2006)

[18] G. Agakishiev et al. (CERES Collab.), Phys. Lett. B 422, 405 (1998)

[19] D. Adamova, et al., Phys. Rev. Lett. 91 (2003) 042301

[20] http://aliceinfo.cern.ch/ArtSubmission/publications

[21] ALICE Collaboration, Phys. Rev. Lett. 105, 252301 (2010), DOI:10.1103/PhysRevLett.105.252301

[22] ALICE Collaboration, Phys. Rev. Lett. 106, 032301 (2011), DOI: 10.1103/PhysRevLett.106.032301

[23] ALICE Collaboration, Phys. Lett. B 696 (2011) 30-39, DOI:10.1016/j.physletb.2010.12.020

[24] J.Y. Ollitrault, Phys.Rev.D 46, 229 (1992)

[25] S. Voloshin and Y. Zhang, Z. Phys C 70,665 (1996)

[26] ALICE Collaboration, Phys. Rev. Lett. 105, 252302 (2010), DOI:10.1103/PhysRevLett.105.252302

[27] ALICE Collaboration, Phys Rev Lett Vol.105, No.7, (2010)

[28] STAR Collaboration, Phys.Rev. C 79, 034909 (2009)

[29] PHENIX Collaboration, Phys.Rev. C 69, 034909 (2004)

[30] BRAHMS Collaboration, Phys.Rev. C 72, 014908 (2005)

[31] E. Schnedermann, J. Sollfrank, U. Heinz, Phys.Rev. C 48, 2462 (1993)

[32] A. Kalweit,*Global properties of strange particle production in pp and Pb-Pb collisions with the ALICE detector* at Strangeness in Quark Matter, 18-24 September 2011, Crakow, Poland

[33] *The CERN Large Hadron Collider: Accelerator and Experiments vol.1*, Journal of instrumentation

[34] *The CERN Large Hadron Collider: Accelerator and Experiments vol.2*, Journal of instrumentation

[35] http://lhc.web.cern.ch/lhc/.

[36] J. Rossbach, P. Schmuser, *Basic course on accelerator optics.*

[37] S. Baird, *Accelerators for pedestrians*, AB-Note-2007-014 OP, CERN February 2007.

[38] ALICE Collaboration, *The ALICE experiment at the CERN LHC*, 2008, JINST, 3, S08002

[39] ALICE Collaboration, *ALICE: Physics Performance Report, Volume I*, J. Phys. G: Nucl. Part. Phys. **30** 1517–1763.

[40] K. Aamodt et al. (ALICE Collaboration), J. Instrum. 3, S08002 (2008)

[41] J. Alme et al., Nucl. Instrum. Methods Phys. Res. A 622, 316 (2010)

[42] CERN/LHCC 2001-021, ALICE TDR 9, 3 October 2001, *ALICE TRD Technical Design Report*

[43] CERN/LHCC 2000-012, ALICE TDR 8, 16 February 2000, *ALICE TOF Technical Design Report*

[44] CERN/LHCC 98-19, ALICE TDR 1, 14 August 1998, *ALICE HMPID Technical Design Report*

[45] CERN/LHCC 99-4, ALICE TDR 2, 5 March 1999, *ALICE PHOS Technical Design Report*

[46] CERN/LHCC 2006-014, *ALICE electromagnetic calorimeter: addendum to the lice TECHNICAL PROPOSAL*

[47] CERN/LHCC 99-22, ALICE TDR 5, 13 August 1999, *ALICE Muon Spectrometer Technical Design Report*

[48] CERN/LHCC 99-5, ALICE TDR 3, 5 March 1999, *ALICE ZDC Technical Design Report*

[49] CERN/LHCC 99-32, ALICE TDR 6, 30 September 1999, *ALICE PMD Technical Design Report*

[50] CERN/LHCC 2002-016, Addendum to ALICE TDR 8, 24 April 2002, *Addendum to ALICE TDR 8*

[51] E. Cerron-Zeballos et al., *A new type of resistive plate chamber: The Multigap RPC*, 1996, Nucl. Instr. and Meth. A 374, 132

[52] A.V. Akindinov et al., *Results from a large sample of MRPC-strip prototypes for the ALICE TOF detector*, 2004, Nucl. Instr. and Meth. A 532, 611

[53] A.V. Akindinov et al., *Latest results on the performance of the multigap resistive plate chamber used for the ALICE TOF*, 2004, Nucl. Instr. and Meth. A 533, 74

[54] A.V. Akindinov et al., *The ALICE Time-of-Flight system: construction, assembly and quality tests*, 2009, Il Nuovo Comento Vol 124 B, N.2

[55] A. Akindinov et al., EPJC (2010) 68:601-607 *Results of the ALICE time-of-flight detector from the 2009 cosmic-ray data taking*

[56] A.V. Akindinov et al., *Final test of the MRPC production for the ALICE TOF detector*, 2009, Nucl. Instr. and Meth. A 602, 709

[57] A.V. Akindinov et al., *Construction and test of the MRPC detectors fot TOF in ALICE*, 2009, Nucl. Instr. and Meth. A 602, 658

[58] A.V. Akindinov et al., *A topological trigger based on the Time-of-Flight detector for the ALICE experiment*, 2009, Nucl. Instr. and Meth. A 602, 372

[59] A.V. Akindinov et al., *Space charge limited avalanche growth in multigap resistive plate chambers*, 2004, Eur. Phys. J. C 34, 325

[60] P.Hristov, *AliRoot Primer*, http://aliceinfo.cern.ch/Offline/AliRoot/Manual.html

[61] http://root.cern.ch

[62] X.N. Wang and M. Gyulassy, Phys. Rev. D44(1991) 3501. X.N. Wang and M. Gyulassy, Comput. Phys. Commun. 83 (1994) 307-331. http://www-nsdth.lbl.gov/∼xnwang/hijing

[63] http://sroesler.web.cern.ch/sroesler/dpmjet3.html

[64] Torbjorn Sjostrand, A Brief Introduction to PYTHIA 8.1, arXiv:0710.3820, CERN-LCGAPP-2007-04, LU TP 07-28, FERMILAB-PUB-07-512-CD-T, October 2007

[65] B. Andersson et al., Phys. Rep. 97 (1983),31

[66] http://wwwasdoc.web.cern.ch/wwwasdoc/geant_html3/geantall.html

[67] S. Agostinelli et al., *Geant4, a simulation toolkit*, Nucl. Instrum. Meth A506 (2003) 250, CERN-IT-2002-003, http://cdsweb.cern.ch/record/602040

[68] A. Fass et al., *FLUKA: present status and futur developments*, Proceeding of the IV International Conference on Calorimeters and their Application, World Scientific, Singapore (1994)

[69] P. Billoir; NUM A225 (1984) 352,
P. Billoir et al. NIM A241 (1985) 115,
R. Fruhwirth NIM A262 (1987) 444
P. Billoir CPC (1989) 390

[70] E.Crescio, A. Dainese, M. Masera, F. Prino *Performance of the ITS stand-alone tracker in pp collisions*, ALICE Internal Note, ALICE-INT-2009-046

[71] R.Fruhwirth, A.Strandlie, W.Waltenberger, J.Wroldsen, *A rewiew of fast circle and helix fitting, Nuclear Instruments and Methods in Physics Research*, A 502 (2003) 705-707

[72] A. Strandlie, *Error analysis of the track fit on the Riemann sphere*, Nuclear Instruments and Methods A 480 (2002) 734.

[73] A. Strandlie, J. Wroldsen, R. Frhwirth and B. Lillekjendlie, *Particle Tracks fitted on the Riemann sphere*, Computer Physics Communications 131 (2000) 95.

[74] F.James, MINUIT, *Function Minimization and Error Analysis, Reference Manual, Version 94.1*, Computing and Networks Division, CERN, Geneva

[75] ALICE Collaboration *Production of pions, kaons and protons in pp collisions at sqrt(s)= 900 GeV with ALICE at the LHC*, The European Physical Journal C (2011)

[76] P. Z. Skands, *Tuning Monte Carlo Generators: The Perugia Tunes*, Phys.Rev.D82:074018, (2010)

[77] R. Angel, J. Ranft, S.Roesler, Phys. Rev. D52, 1459 (1995)

[78] K. Aamodt at al. (ALICE Collaboration), Eur. Phys. J. C 68, 98 (2010)

[79] C. Tsallis, J. Stat. Phys. 52, 479 (1988)

[80] M. Floris, *Identified particles in pp and Pb-Pb collisions at LHC energies with the ALICE detector*,J.Phys.G:Nucl.Part.Phys. 38 (2011)

[81] Chojnacki M (ALICE Collaboration) 2011 J. Phys. G: Nucl. Part. Phys. 38 124074

[82] Aamodt K et al (ALICE Collaboration) 2010 Phys. Rev. Lett. 105 072002 (arXiv:1006.5432 [hep-ex])